Results of the LOCA bundle test QUENCH-L5 with pre-hydrogenated optimised ZIRLO™ claddings (SR-7738)

J. Stuckert, M. Große, C. Rössger, M. Steinbrück, M. Walter

KIT

Karlsruher Institut für Technologie

Karlsruher Institut für Technologie

in der Helmholtz-Gemeinschaft

Wissenschaftliche Berichte

QUENCH – LOCA – REPORTS Nr. 6

Results of the LOCA bundle test QUENCH-L5 with pre-hydrogenated optimised ZIRLO™ claddings. (SR-7738)

J. Stuckert*, M. Große*, C. Rössger*, M. Steinbrück*, M. Walter**

Institut für Angewandte Materialien:

* Angewandte Werkstoffphysik (IAM-AWP)

** Werkstoff- und Biomechanik (IAM-WBM)

Programm Nukleare Entsorgung und Sicherheit

Karlsruher Institut für Technologie

Mai 2018

Zusammenfassung

Ergebnisse des unter Bedingungen eines LOCA-Störfalls ausgeführten Versuches QUENCH-LOCA-5 mit hydrierten opt. ZIRLO™-Hüllrohren

Der QUENCH-L5-Bündelversuch wurde im Rahmen der QUENCH-LOCA-Testserie durchgeführt. Das Ziel der Testreihe ist die Untersuchung von Dehnung, Bersten, Oxidation und sekundärer Hydrierung der Hüllrohre unter repräsentativen Auslegungsstörfallbedingungen sowie der Einfluss dieser Parameter auf die mechanischen Eigenschaften dieser Rohre. Mit den Versuchen dieser Serie wird das Verhalten von verschiedenen Hüllrohrmaterialien mit und ohne Vorhydrierung untersucht. Für den QUENCH-L5-Versuch wurden opt. ZIRLO-Hüllrohre (Außendurchmesser: 10,75 mm) mit etwa 300 wppm Wasserstoff vorbelastet. Die Bündelkonfiguration und das Testprotokoll waren ähnlich dem Referenztest QUENCH-L3, der mit nicht vorbehandelten opt. ZIRLO-Hüllrohren durchgeführt wurde. Spezifisches Ziel des QUENCH-L5-Tests war die Untersuchung des Verhaltens der vorhydrierten Hüllrohre, mit speziellem Fokus auf die Auswirkungen des Hydrierens auf die Dehnungs- und Berst-Parameter, sowie die Hüllrohrintegrität während des Abschreckens. Der Test wurde am Karlsruher Institut für Technologie (KIT) am 10. Februar 2016 erfolgreich durchgeführt.

Zu Beginn des Experiments wurde zunächst die Teststrecke stabilisiert. Hierzu wurde das Bündel erwärmt mit einer elektrischen Leistung von 3,25 kW, einer Gasströmung von 6 g/s Argon sowie 2 g/s überhitzten Dampfes bis eine Hüllrohrtemperatur von höchstens etwa 800 K erreicht war. Während dieser Stabilisierungsphase (mit einer Dauer von 1700 s) wurden die Stäbe bis auf 55 bar mit Krypton beaufschlagt. In der sich anschließenden Aufheizphase wurde die elektrische Leistung auf 60 kW erhöht; diese Testphase dauerte 76 s. Während dieser Zeit stiegen die Temperaturen von ihren Anfangswerten (d.h. denen am Ende der Stabilisierungsphase) bis zu einem Maximum von 1205 K. Die durchschnittliche Aufheizgeschwindigkeit betrug 6 K/s. Die erhöhte Duktilität der erwärmten Hüllrohre führte zu deren fortschreitender Dehnung und anschließendem Bersten aller Rohre. Die Bersttemperatur betrug 1087 ± 36 K (*etwa 35 K niedriger als im QUENCH-L3-Test*). Das Experiment wurde mit einer Leistungsreduzierung auf 3,5 kW (Modellierung der Zerfallswärme) und Einführung von Dampf bei einem Nennwert von 20 g/s fortgesetzt (Abkühlphase). In dieser Phase fand eine Abkühlung auf etwa 930 K statt. Die darauf folgende Abschreckphase erfolgte vom Bündelfuß aus mit einer Wassereinspeisung von bis zu 100 g/s (entspr. 3,3/g/s/Effektivstab). Das vollständige Abschrecken wurde nach 290 s erreicht.

Aufnahmen nach dem Versuch mit einem Videoskop vom Bündelinneren zeigen Ballooning-Bereiche typischerweise in den heißesten Bündelebenen zwischen 850 und 1000 mm. Das Bündel wurde demontiert und die geometrischen Parameter aller Stäbe wurden mit einem Laserscanner bestimmt; die gemessenen Hüllrohr-Umfangsdehnungen im Berstbereich lagen zwischen 21% und 33%. Das ist etwas höher als für die QUENCH-L3-Hüllrohre; ebenso war die axiale Ausdehnung der Balloonings-Region größer für QUENCH-L5 als für QUENCH-L3. Einige Hüllrohre bildeten bis zur drei Ballooning-Regionen. Die maximale Blockade des Kühlkanals (25%) wegen des Balloonings war etwas höher im Vergleich zu QUENCH-L3 (21%). Bei allen Stäben konnten kleine Verbiegungen in den radialen Ebenen, die durch die Berstöffnungen gingen, festgestellt werden. Mit Ultraschallmessungen wurde die Verminderung der Hüllrohrwandstärke in der Nähe der Berstöffnungen bestimmt. Die axiale und radiale Verteilung sowie die Stärke von Oxidschichten an den Hüllrohren wurden durch Wirbelstromverfahren ermittelt; die maximale Dicke von ZrO_2 - in Kombination mit α-Zr(O) -Schichten - betrug etwa 15 µm (weniger im Vergleich zu QUENCH-L3 aufgrund niedrigerer Temperaturen). *Beim Quenchen nach der Hochtemperaturphase wurde keine Fragmentierung der Hüllrohre beobachtet, weder für QUENCH-L3 noch für QUENCH-L5 (Restfestigkeiten oder Duktilität sind ausreichend).* Wegen der relativ kurzen Dauer (nur ca. 30 s) der Versuchsphase im Temperaturbereich von über 850 °C (bei QUENCH-L3 dauerte diese nahezu 100 s) fand keine sekundäre Hydrierung der Hüllrohre statt (T > 850 °C: komplette Umwandlung zu β-Zr-Phase). Die Messung der mechanischen Eigenschaften und die Bestimmung der Restduktilität wurden durch Zugversuche bei Raumtemperatur an Hüllrohrsegmenten von ca. 800 mm bewerkstelligt; Sprödbrüche bei Spannungen von etwa 540 MPa (ca. 40 MPa mehr als für QUENCH-L3) fanden

hauptsächlich aufgrund der Spannungskonzentration an den Spitzen von Berstöffnungen statt. Die restlichen Hüllrohre versagten durch Einschnürung in weitem Abstand von der Berstöffnung.

Abstract

The QUENCH-L5 experiment was performed in the framework of the QUENCH-LOCA test series. The overall objective of this bundle test series is the investigation of ballooning, burst, degree of oxidation and secondary hydrogen uptake of the cladding under representative design-basis accident conditions and their influence on the mechanical properties. The various experiments of the series examine the behavior of different cladding materials and the effect of pre-hydriding. For the QUENCH-L5 test, opt. ZIRLO™ claddings pre-loaded with approximately 300 wppm hydrogen and with an outside diameter of 10.75 mm have been used. Like in all experiments of the QUENCH-LOCA series, the fuel rod simulators were separately pressurized with krypton to 55 bar. Bundle configuration and test protocol were similar to the reference test QUENCH-L3 with as-received opt. ZIRLO claddings. Specific objectives of QUENCH-L5 were to provide information about the behavior of pre-hydrided opt. ZIRLO alloy on the response to a best-estimate large-break LOCA sequence, with special focus on the impact of hydrided claddings on their ballooning and burst parameters, as well as cladding integrity during quenching. The test was successfully conducted at the Karlsruhe Institute of Technology (KIT) on February 10, 2016.

The experiment started by stabilizing the bundle conditions with an application of electrical bundle power of 3.25 kW (linear heat rate of approx. 0.9 W/cm) and gas flows of 6 g/s argon plus 2 g/s superheated steam resulting in maximum bundle temperatures of about 800 K. During this stabilization phase (lasting 1700 s) the rods were refilled with krypton to 55 bar. The transient stage was initiated by increasing of electrical power to 60 kW and lasted 76 s. During this period the peak cladding temperature increased from their initial values to a maximum of 1205 K. The average heatup rate at the maximum temperature location was 6 K/s. The increased ductility of the heated cladding resulted in a progressive ballooning and consequent burst of all rods. The burst temperature is 1087 ± 36 K (*about 35 K lower in comparison to the QUENCH-L3 test* performed without pre-hydrogenation). The experiment continued with power decrease to 3.5 kW to simulate decay heat and injection of steam at a nominal of 20 g/s (cool-down stage). In this stage mostly steady cooling to about 930 K occurred. The cooling phase was followed by up to 100 g/s (3.3 /g/s/effective rod) water injection from bundle bottom (quench stage). Complete quench was achieved at about 290 s.

Post-test videoscope inspections showed typical ballooning pictures at the hottest bundle elevations between about 850 and 1000 mm. The bundle was dismounted and geometric parameters of all rods were determined by laser scanning; the range of circumferential strains measured was between 21% and 33%. It is slightly higher as for the QUENCH-L3 claddings; as well as the axial extension of ballooning region for each cladding was larger for QUENCH-L5 in comparison to QUENCH-L3. Some rods have up to three ballooning regions for both tests QUENCH-L5 and -L3. The maximum blockage ratio of the cooling channel (25%) due to ballooning was slightly higher in comparison to QUENCH-L3 (21%). A small bending of all rods was detected in the plane going radially through the burst opening. Ultrasound measurements were used to determine thinning of cladding wall in vicinity of burst openings. Axial and radial distribution of oxidation rate was measured by eddy current methods; maximal combined thickness of ZrO_2 and α-Zr(O) layers was about 15 µm (lower in comparison to QUENCH-L3 due to lower temperatures). *During quenching, following the high-temperature phase, no fragmentation of claddings was observed for both QUENCH-L3 and QUENCH-L5 (residual strengths or ductility is sufficient).* No secondary hydrogenation was indicated for the QUENCH-L5 claddings due to relative short high temperature period: less of 30 s above 850 °C (complete transition to β-Zr phase) in comparison to almost 100 s for QUENCH-L3. Measurement of mechanical properties and determination of residual ductility were carried out by tensile tests with cladding tube segments (about 800 mm length) at room temperature and showed fracture of claddings at engineering stress of about 540 MPa (about 40 MPa higher in comparison to the QUENCH-L3 test) mostly due to stress concentration at burst opening tips. Residual part of claddings was fractured due to necking far away from the burst.

Contents

List of Tables

List of Figures

Introduction

Under the licensing procedures for pressurized water reactors (PWR) evidence must be given that the impacts of all pipe ruptures, hypothetically occurring in the primary loop and implying a loss of coolant, can be controlled when the other cooling lines are not available. The double-ended break of the main coolant line between the main coolant pump and the reactor pressure vessel is considered to constitute the design basis for the emergency core cooling system (ECCS) in a loss-of-coolant accident (LOCA). The break of a coolant line leads to the loss of coolant in the primary circuit of a PWR and the decrease in system pressure from 15.5 MPa to eventually around 0.32 MPa (boiling point corresponding to 135 °C). Consequently, the remaining coolant in the core as well as the emergency cooling water fed into the reactor core evaporate, the temperature of the fuel elements rapidly rises and the fuel rods start to balloon since they contain pressurized filling gas and fission gas products. At temperatures above 700 °C, the load within the metallic wall reaches a critical value and the most ballooned cladding tubes finally burst.

Upon rupture of the reactor coolant line the reactor is shut down. However, as the production of decay heat will be continued, reliable sustainment of the reactor core rod geometry and long-term emergency cooling of the core are required. The cladding embrittlement increasing during oxidation in steam has to be limited to an acceptable value to retain the core rod geometry. The current LOCA criteria and their safety goals are applied worldwide with minor modifications since the NRC release in 1973 [1, 2]. The criteria are given as limits on peak cladding temperature ($T_{pct} \leq 1200$ °C) and on oxidation level ECR (equivalent cladding reacted) calculated as a percentage of cladding oxidized (ECR ≤ 17% using the Baker-Just oxidation correlation). These two items constitute the criterion of cladding embrittlement due to oxygen uptake and, according to the RSK (Reactor Safety Commission) Guidelines, are also included in the current German LOCA criteria [3].

The results elaborated worldwide in the 1980's on the Zircaloy-4 (Zry-4) cladding tubes behaviour (oxidation, deformation and bundle coolability) under LOCA conditions constitute a reliable data base and an important input for the safety assessment of LWRs. With respect to the LOCA conditions for German LWRs, different out-of-pile with more prototypical internal heating [4, 8] and outer heating [5, 6], the FR2 in-pile [7] single rod as well as the REBEKA out-of-pile bundle tests [9, 10] were performed. It was concluded that the ECC-criteria established by licensing authorities are conservative and that the coolability of an LWR and the public safety can be maintained in a LOCA [11]. In-pile test data (with burn-up up to 35 MWd/kgU) were consistent with the out-of-pile data and did not indicate an influence of the nuclear environment on cladding deformation.

Due to major advantages in fuel-cycle costs, optimised reactor operation, and waste management, the current trend in the nuclear industry is to increase fuel burn-up. At high burn-up, fuel rods fabricated from conventional Zry-4 often exhibit significant oxidation, hydriding, and oxide spallation. Thus, fuel vendors have developed and proposed the use of new cladding alloys, such as Duplex DX-D4, M5®, ZIRLO™ and other. Therefore, it is important to verify the safety margins for high burn-up fuel and fuel claddings with advanced alloys. In recognition of this, LOCA-related behaviour of new types of cladding is being actively investigated in several countries [12, 13]. Due to long cladding hydriding period for the high fuel burn-up, post-quench ductility is not only influenced by oxidation, but also significantly depending on the hydrogen concentration. Consequently, the 17% ECR limit is inadequate to ensure post-quench ductility at hydrogen concentrations higher than ≈500 wppm [14]. Due to so-called secondary hydriding (during oxidation of inner cladding surface after burst), which was firstly observed by JAERI [15], the hydrogen content can reach 4000 wppm in Zircaloy cladding regions around the burst [16].

Particularly to investigate the influence of the secondary hydriding phenomena on the applicability of the embrittlement criteria for the German nuclear reactors, it was decided to perform the QUENCH-LOCA bundle test series in the QUENCH facility of KIT, supported by the association of the German utilities (VGB). Additionally, the QUENCH-LOCA bundle tests could support experiments performed in-pile and in-cell, respectively, e.g. single-rod tests as those planned in the OECD SCIP-2 project [17]. Compared to single-rod

experiments, bundle tests have the advantage to study the mutual interference of rod ballooning among fuel rod simulators as well as to take into account the local coolant channel blockages in this more realistic arrangement.

The first test QUENCH-L0 was performed with Zry-4 cladding tubes not pre-oxidised on July 22, 2010 as commissioning test and terminated with reflood immediately after the transient phase [18, 19]. The QUENCH-L1 test was performed on February 02, 2012 as reference test, using a similar bundle compared to the QUENCH-L0 test but including a cool-down phase between transient and reflood [20, 21]. The experiment QUENCH-L2 with as-received M5$^{®}$ claddings was conducted on July 30, 2013 [22]. Similar test scenario was used also for the QUENCH-L3 test (March 17, 2015) with as-received optimised ZIRLO™ claddings [23]. To check the influence of hydrogen absorbed in claddings during the reactor operation, the QUENCH-L5 with optimised ZIRLO™ claddings pre-hydrogenated to about 300 wppm was conducted on February 10, 2016. The hydrogen concentration was increased in comparison to the QUENCH-L4 test with M5® claddings, which were pre-hydrogenated to 100 wppm [24].

1 Description of the Test Facility

The QUENCH facility was constructed 1997 at KIT for the investigation of the hydrogen source term during reflood, i.e. of the measurement of hydrogen release during the reflood of an overheated reactor core. Since then 17 bundle tests were performed as under severe accident conditions (Table 1). The main components of the QUENCH test facility are presented in Fig. 1. The test section is enclosed by a safety containment with a wall thickness of 5.6 mm and an inner diameter of 801.8 mm. The facility can be operated in two modes: a forced-convection mode depicted in the flow diagram of Fig. 2 and a boil-off mode. In the forced-convection mode (relevant for QUENCH-L5) superheated steam from the steam generator and superheater together with argon as a carrier gas enter the test bundle at the bottom (Figs. 3 and 4). The system pressure in the test section for the QUENCH-LOCA tests is about 0.3 MPa. The argon, steam and hydrogen produced in the zirconium-steam reaction flow upward inside the bundle and from the outlet at the top through a water-cooled off-gas pipe to the condenser where the remaining steam is separated from the non-condensable gases argon and hydrogen. The water cooling circuits for bundle head and off-gas pipe are temperature-controlled to guarantee that the steam/gas temperature is high enough so that condensation at the test section outlet and inside the off-gas pipe can be avoided. The temperature of the cooling water in the bundle head is kept at 348 K, and the water flow rate is 250 g/s.

The off-gas pipe consists of water-cooled pipes with a counter-current flow (flow rate of 370 g/s) and inner pipe. The inlet temperature of cooling water is controlled at 393 K. Between the off-gas pipe and inner pipe there is stagnant off-gas. The main dimensions of the tubes that make up the off-gas pipe are:

·   Inner pipe: outer diameter 139.7 mm, wall thickness 4.5 mm; total length 3256 mm, material: stainless steel;

·   Inner cooling pipe: outer diameter 154 mm, wall thickness 2 mm, material: stainless steel;

·   Outer cooling pipe: outer diameter 168.3 mm, wall thickness 5 mm, material: stainless steel.

The quenching water is injected into the bundle through a separate line marked "bottom quenching" in Fig. 4.

1.1 The test bundle

The design characteristics of the test bundle are given in Table 2. The test bundle is made up of 21 fuel rod simulators, each with a length of approximately 2.5 m, and of four corner rods (see cross section in Fig. 5). Insertion of four corner rods avoids an atypically large flow cross section at the outer positions and hence helps to obtain a rather uniform radial temperature profile. The fuel rod simulators (Fig. 6) are held in their positions by five grid spacers made of ZIRLO. This bundle design is applied with a pitch of 14.3 mm. All test rods are heated electrically over a length of 1900 mm (thereof 1024 mm in the middle with W heater and residual length with Mo heaters at rod ends).

1.1.1 Claddings

Unlike the QUENCH-L3 experiment with fresh optimised ZIRLO claddings, the QUENCH-L5 test was performed with *pre-hydrogenated* (to hydrogen concentration of 300 wppm) optimised ZIRLO claddings. The properties of fresh cladding are listed in Table 3. Before manufacture of hydrogenated tubes for the bundle test, one prototype cladding was prepared by AREVA and tested at KIT. The prototype was welded from three segments: 500 mm hydrogenated, 1200 mm hydrogenated and 500 mm not hydrogenated (Fig. 7). The hydrogenation parameters are shown in Fig. 8. The hydrogen axial distribution in the welding zone is pictured

in Fig. 9. The resulting hydrides inside the cladding are to be seen in Fig. 10. The XRD analysis revealed only small peak corresponding the γ-hydrides (Fig. 11).

Two samples with lengths of 300 mm and welded joint in the axial middle of each sample were cut from his prototype: first sample from the upper prototype part for the tensile test, second sample from the lower prototype part for burst experiment in tensile machine equipped with furnace. Fig. 12 shows results of tensile test with the first sample at room temperature: the sample was fractured relatively early in comparison to tubes without welded joint. The second sample was installed in the tensile machine, slightly axially loaded with tensile force of 10 N, pressurized with Kr to 30 bar and heated with 10 K/min. The sample has burst inside the hydrogenated part at 710 °C (Fig. 13).

Similar to the prototype, to extend the claddings to required length, the hydrogenated samples were welded to not hydrogenated cladding segments at bundle elevations 50 and 1250 mm (Fig. 14). Whereas the fresh ZIRLO cladding of the fuel rod simulator has an outside diameter of 10.75 mm and a wall thickness of 0.725 mm (see also Table 2), the outside diameter of hydrogenated tubes will be increased. This material property was used to determine the hydrogen concentration at each elevation of the pre-hydrogenated segment for each cladding (Figs. 15 - 18).

1.1.2   Heaters

Tungsten (chemically clean tungsten) heating elements of 4.6 mm diameter are installed in the center of rods (Fig. 6). W heaters with this small diameter were used for the first time in the QUENCH-L2 experiment. Their higher electrical resistance in comparison to tungsten heaters of 6 mm diameter (used for commissioning test QUENCH-L0) results in higher maximum heating rates, especially during the first transient phase and hence to a more prototypical test conduct. The tungsten heaters with a diameter of 4.6 mm produce a similar heat amount as the tantalum heaters with a diameter of 6 mm (used for the QUENCH-L1 test), but they are more rigid at high temperatures. These heaters are surrounded by annular yttria-stabilized ZrO_2 pellets. The physical properties of the ZrO_2 pellets are described in Table 4.

The tungsten heaters are connected to molybdenum heater (chemically clean molybdenum) and copper electrode (material 2.1293 with Cr 0.8, Zr 0.08 and balance Cu) at each end of the W heater. The molybdenum and copper parts are joined by high-frequency/high-temperature brazing under vacuum ($2x10^{-3}$ mbar) using an AuNi 18 powder (particle size <105 μm). For electrical insulation the surfaces of both Mo and Cu parts are plasma-coated with 0.2 mm ZrO_2. To protect the copper electrodes and the O-ring-sealed wall penetrations against excessive heat, they are water-cooled (lower and upper cooling chambers filled with demineralized water).

The copper electrodes are connected to the DC electric power supply by means of special sliding contacts at the top and bottom. The total heating power is limited by a maximal current of 7200 A and voltage of 9 V. Two DC-generators were used for two groups of rods connected in parallel: 1) 9 internal rods #1 - #9 and rod #15; 2) 11 external rods: #10 - #14 and #16 - #21. The electrical resistance of the rod heating system, combined of W and Mo heaters and copper electrodes, was measured before (at the end of bundle assembling) and after the test (Table 5). The electric resistance of a single heater (W+Mo+Cu sections) measured at room temperature was about 5 mΩ before and after the test. The additional resistance of the external electric circuit between the axial end of the single heater and the connection to the generator (sliding contacts, cables, and bolts) is 3.75 mΩ for the inner rod group and 4.05 mΩ for the outer rod group. These values can be taken as constant because the external electric circuit remains at ambient temperature throughout the experiment.

1.2   Bundle surroundings

The bundle is surrounded by a 3.17 mm thick shroud (79.66 mm ID) made of the Zr702 alloy. This part has two functions: 1) The shroud acts as steam and gas guide tube; 2) It simulates an adiabatic surrounding of the

reactor core. The consideration of heated rod claddings, corner rods and shroud, manufactured from similar zirconium alloys, results in the surface of 30.6 effective rod simulators. The shroud is surrounded by a 36 mm thick ZrO_2 fiber insulation (physical properties are given in Table 6) and an annular cooling jacket made of Inconel 600 (inner tube) and stainless steel (outer tube; see Fig. 5). The annulus between shroud and cooling jacket was filled (after several cycles of degasing) with stagnant argon of about 0.3 MPa (Fig. 31) and was connected to a flow-controlled argon feeding system in order to prevent steam access to the annulus after possible shroud failure. The 6.7 mm annulus of the cooling jacket is cooled by an argon flow. Above the W heater, i.e. above the 1024 mm elevation there is no ZrO_2 fibre insulation to allow for higher radial heat losses. This region of the cooling jacket is cooled by a water flow (Figs. 3 and 4). Both, the lack of ZrO_2 insulation above the W heaters and the water cooling, force the axial temperature maximum downward.

The lower boundary for the lower cooling chamber is a sealing plate made of stainless steel with plastic inlays for electrical insulation, sealed toward the system by O-shaped rings. The upper boundary of the lower cooling chamber is a sealing plate of stainless steel. An insulation plate made of plastic (PEEK) forms the top of the upper cooling chamber, and a sealing plate of Al_2O_3, functioning as a heat-protection shield, is the lower boundary of the upper cooling chamber (see Fig. 6).

In the region below the upper Al_2O_3 plate the copper electrode is connected firmly to the cladding. This is done by rotary swaging the cladding onto the electrode. In the swaging region a sleeve of boron nitride is put between electrode and cladding for electrical insulation. The axial position of the fuel rod simulator in the test bundle is fixed by a groove and a locking ring in the top Cu electrodes. Referred to the test bundle the fixing point of the fuel rod simulators is located directly above the upper edge of the upper insulation plate. So, during operation the fuel rod simulators are allowed to expand downwards. Clearance for expansion of the test rods is provided in the region of the lower sealing plate. Also in this region, relative movement between cladding and internal heater/electrode can take place.

1.3   Rod pressurization

All fuel rod simulators were separately pressurized. The gas supply system (Fig. 19) for individual pressurization of rods consists of pressure controller, 21 valves, 21 pressure transducers, and 21 justified compensation volumes for simulation of prototypic plenum volumes of 31.5 cm³. The gas supply is connected with capillary tubes (with inner diameter 1 mm, length ca. 1.2 m) to each rod at its lower end via drill axial holes in the copper electrodes (Fig. 20). The gas gap between the cladding and the coated Cu/Mo parts and the W-heater/ZrO_2-pellets is 0.15 mm and 0.075 mm, respectively.

Before gas filling, the rods and the gas supply system were evacuated. At the beginning of experiment, the fuel rod simulators were backfilled with Kr gas to 30 bar. Then, before the transient, they were separately pressurized to the target pressure of 55 bar as shown in Fig. 21.

2   Test Bundle Instrumentation

A list of all instruments for the experiment QUENCH-L5, which were installed in the test section and at the test loop is given in Table 7. The distribution of the thermocouples along the bundle is shown in Table 8. No failed thermocouples were detected during the test.

2.1 Thermocouples

The test bundle was instrumented with sheathed thermocouples (TC) attached to the rod claddings (<u>Fig. 22</u>) at 17 different elevations between -250 mm and 1350 mm and at different orientations according to <u>Figs. 23 and 24</u>. The NiCr/Ni thermocouples (1 mm diameter, stainless steel sheath 1.4541 (X6CrNiTi18-10), MgO insulation) are used for temperature measurement at rod cladding and shroud outer surfaces. The TC tip is held in place by a Zr ferrule welded to the surface. The cables of the rod-thermocouples from the -250 mm to the 850 mm level leave the test section at the bottom whereas those of the TCs above 850 mm are routed out on the top of the test section to prevent TC cables passing the hot zone. For the same reason the cables of the shroud-thermocouples in this region are routed outside the insulation. The thermocouples are designated as following:

- "TFS" for the thermocouples attached to the outer surface of the rod claddings;

- "TSH" for the shroud thermocouples mounted at the outer surface between -250 mm and 1250 mm;

- "TIT" for the thermocouples installed inside the Zry-4 instrumentation rods at the three corner positions of the bundle (positions A, C and D) (see <u>Fig. 25</u>);

- "TCI" for the thermocouples at the cooling jacket are installed inside the wall of the inner cooling tube (from 550 mm to 950 mm, designation).

2.2 Gas Measurement System

The flow rates of noble gases (Ar, Kr) are regulated with the BRONKHORST flow controllers. Steam and water flows are controlled with the SIEMENS flow controllers. Numerous pressure transmitters from WIKA measure absolute and differential pressures along the gas supply system, at inlet and outlet of the test section.

The outlet steam and released hydrogen are analyzed by a Balzers mass spectrometer (MS) "GAM 300" (<u>Fig. 26</u>). Due to its location at the off-gas pipe in the facility the mass spectrometer responds almost immediately (less than 10 s). The "BALZERS GAM 300" is a completely computer-controlled quadrupole MS with an 8 mm rod system which allows reliable quantitative measurement of gas concentrations down to about 10 ppm. For the MS measurement a sampling tube is inserted in the off-gas pipe located approx. 2.7 m downstream from the test section outlet (see Fig. 2 and 4). It has several holes at different elevations to guarantee that the sampling of the gas to be analyzed is representative (see <u>Fig. 27</u>). To avoid steam condensation in the gas pipes between the sampling position and the MS the temperature of the gas at the MS inlet is controlled by heating tapes to about 150 °C (the upper operating temperature of the MS inlet valves). This allows the MS to analyze the steam production rate. Besides, the concentrations of the following species were continuously measured by the mass spectrometer during all test phases: argon, hydrogen, steam, nitrogen, oxygen, and krypton. The fuel rod simulators are filled with krypton which can be used as an indicator for cladding failure. Additionally, the MS is used to control the atmosphere in the facility, e.g., to monitor the gas composition at the beginning of the test.

The temperature and pressure of the analyzed gas are measured near to the inlet valve of the MS. The MS is calibrated for hydrogen with well-defined argon/gas mixtures and for steam with mixtures of argon and steam supplied by a BRONKHORST controlled evaporator mixing (CEM) device. The MS off-gas is released into the atmosphere because the amount of sampling gas taken out of the system is negligible. A heated measuring gas pump was used to ensure a continuous flow of the steam-gas mixture from the off-gas pipe to the mass spectrometer.

For the MS the mass flow rate of each gas specious is calculated by referring the measured gas concentration to the known argon mass flow rate according to equation (1):

$$n\&_G = \frac{M_G}{M_{Ar}} \cdot \frac{C_G}{C_{Ar}} \cdot n\&_{Ar} \tag{1}$$

with M representing the molecular masses, C the concentrations in vol% and $n\&$ the mass flow rates of the corresponding gases

3 Data Acquisition and Process Control

A LabView-based control and data acquisition system is used in the QUENCH facility. Data acquisition, data storage, online visualization as well as process control, control engineering and system protection are accomplished by three computer systems that are linked in a network.

During the QUENCH-L5 test the data acquisition system recorded all measurement channels at a frequency of 5 Hz per channel. The experimental data and the date and time of the data acquisition are stored as raw data in binary format. After the experiment the raw data are converted into SI units and stored as ASCII data.

For process control, a system flow chart with the most important actual measurement values is displayed on the computer screen. Furthermore, the operating mode of the active components (pumps, steam generator, superheater, DC power system, valves) is indicated. Blocking systems and limit switches ensure safe plant operation. Operating test phases, e.g. heating or quenching phases, are pre-programmed and can be started on demand during the experiment. The parameter settings of the control circuits and devices can be modified online.

Online visualization allows to observe and to document the current values of selected measurement positions in the form of tables or line graphs. Eight diagrams with six curves each can be displayed as graphs. This means that altogether 48 measurement channels can be selected and displayed online during the course of the experiment.

The data of the main data acquisition system and of the mass spectrometers are stored on different computers. Both computers are synchronized. The data of the mass spectrometer data are recorded at a frequency of approx. 0.8 Hz during the entire test.

4 Test Performance and Results of Online Measurements

The test procedure was based on pre-test calculations for the QUENCH-LOCA series performed by the Paul Scherrer Institute (PSI, Villigen). According to the planned LOCA scenario, the transient phase should be performed with 8 K/s followed by slow cool-down phase and quenching.

The sequence of the test events is represented in Table 9. The experiment started by stabilizing the bundle conditions with an application of electrical bundle power of 3.25 kW (corresponding to a linear heat rate of approx. 0.9 W/cm) in 6 g/s (specific rate 0.2 g/s/(effective rod)) argon plus 2 g/s (specific rate 0.07 g/s/(effective rod)) superheated steam resulting in maximum bundle temperatures of approximately 800 K (Fig. 28). During this stabilization phase the rod internal pressure was increased to 55 bar. The bundle was kept at this peak cladding temperature and pressure for 386 s before the start of the transient. The current and voltage progression during the test are depicted in Fig. 29.

The peak cladding temperature was decreased in comparison to QUENCH-L3 during the pre-conditioning test stage (800 K instead 850 K) to avoid the accelerated dissolution of hydrides at T > 550 °C (823 K). The surrounding of hydrides at these temperatures is β-Zr. For T < 550 °C the hydrides are surrounded by α-Zr. The diffusion coefficient of hydrogen in β-Zr is at least four times higher than the one in α-Zr near to 550 °C. So, the T = 800 K during the QUENCH-L5 bundle preconditioning stage before the start of the heat-up phase allowed to reduce the possibility of not prototypical rapid dissolution of hydrides. Additionally, multiple phase transformations during the dissolution of hydrides were avoided during the test preconditioning stage.

The transient was initiated (at t=0 s) by rapidly increasing the electrical power to about 40 kW (linear heat rate ≈9 W/cm) reached after 3.6 s followed by steady increase to 60 kW (linear heat rate ≈13 W/cm) within the next 50 s, and stayed at that level for the rest of the transient (until 75.6 s after transient start). During this period the peak cladding temperature increased from their initial values to 1205 K. Due to limitation of the maximal electrical current of the DC generators the average heatup rate at the maximum temperature location was 6 K/s. The experiment continued with a power decrease to 3.5 kW at 74 s to simulate decay heat and injection of steam at a nominal of 20 g/s. The cladding temperatures increased to a maximum of 1257 K at 82 s, followed by steady cooling to about 930 K. The cooling phase was terminated at 214 s by quenching with up to 100 g/s water injection. There was a period of about 40 s while the lower volume was being filled during which time the temperatures increased somewhat in the absence of significant flow. The first quench occurred at the bottom of the bundle at 238 s. Quenching progressed readily toward the top, and the first quench in the ballooned region occurred at 270 s (Table 10). Complete quench was achieved at 287 s.

Oscillation of the gas pressures during the whole test are presented in Figs. 30, 31. Fig. 32 shows the water flow characteristics. Mass spectrometer data on steam registration (during steam supply and evaporation phases), hydrogen production (due to oxidation of bundle and shroud) and krypton release (due to failure of claddings) are presented in Fig. 33.

The readings of thermocouples at each bundle elevation are shown in Figs. 34 – 50. For each bundle elevation there is also a radial temperature gradient due to two reasons: 1) radial heat flux to the shroud, 2) electrical power supplied to the internal rod group was higher than the power for the external group because both DC generators reached their current limit (≈ 3600 A) but the electrical resistance of the 11 external rods connected in parallel is lower than for the 10 internal rods. The temperatures of the cooling jacket were practically not changed during the whole test (Fig. 51). The axial temperature profile in the bundle has a pronounced maximum between 850 and 1050 mm (Figs. 52 – 55). Fig. 56 compares the QUENCH-L5 thermocouple readings at the hottest elevations with corresponding readings during the QUENCH-L3 test at the first cladding burst and at the end of transient. Due to start of transient at lower temperatures for the QUENCH-L5 test, the QUENCH-L5 bundle was colder until end of transient. However, the lower burst temperatures attributed not to this fact, but depend on other mechanical properties of hydrogenated claddings. Similar influence of hydrogenation was also indicated during comparison of QUENCH-L2 and -L4 tests with fresh and pre-hydrogenated M5® claddings [22, 24].

Two additional (in comparison to the reference test QUENCH-L1) thermocouples TFS 7/12i and TFS 7/13i installed at the cladding surface of rod #7 at the azimuthal position adjacent to the central rod #1 (i.e. opposite to thermocouples TFS 7/12 and TFS 7/13) allowed the registration of radial temperature gradients at the hottest elevations (Fig. 57). According to the REBEKA burst criterion [9], the azimuthal temperature difference has the dominant influence on the circumferential burst strain. Significant azimuthal temperature difference can be developed during the transient not only due to global radial temperature gradient across the bundle (heat loss through the shroud), but also due to a not coaxial positioning of pellets and cladding [4]. The highest temperature achieved at the contact between pellet and cladding (absence of gas gap with relatively low heat conductivity). The temperature difference between this contact position and opposite cladding side increased during the ballooning process, which occurred in such manner that the gas gap at the cold side increased whereas no gas gap formed at the hot side before burst. This effect was detected by in-situ X-ray observation [4, 11] and confirmed by QUENCH-L5 post-test neutron tomography.

Both the increasing ductility and decreasing creep strength of the heated cladding resulted in a progressive ballooning and consequent burst of all rods (Tables 11, 12). During the ballooning development at the hottest elevation, ballooning can be developed before the cladding burst also at higher and lower bundle positions due to achievement of temperature threshold for ballooning onset (Figs. 58 - 59), which phenomenon was observed also for QUENCH-L3 [23]. The first burst occurred 50.6 s after transient initiation for inner rod #01 at about 1057 K, according to the thermocouple reading at the adjacent rod #07. All rods failed within the next 22 s (Fig. 60). The time frame of rod failures as indicated by internal pressure readings correlated with the time frame of the krypton signal measured in the off-gas by mass spectrometer (Fig. 33).

There was a small amount of oxidation during the experiment, resulting in approximately 0.45 g hydrogen released during the high temperature period, including the period of rod burst and shortly after (Fig. 33). Some of the hydrogen produced is expected to have been taken up by inner surface of the cladding after burst.

5 Posttest Examinations

Posttest Examinations (PTE) included nondestructive methods (optical bundle observations, laser profilometry of all claddings, ultrasound cladding wall thickness measurements, eddy current measurements of outer layers of claddings, neutron radio- and tomography) as well as destructive investigations (tensile tests, metallography, fractography, XRD).

5.1 Optical Observation of Cladding Surfaces

First observations of burst positions were performed after the test by means of an OLYMPUS videoscope. The camera of the videoscope (diameter 6 mm, total cable length 9 m) was introduced through the bundle bottom at positions of withdrawn corner rods (Figs. 61 - 64). For the peripheral rods only very local contacts between adjacent claddings due to ballooning were observed. All observed thermocouples remained intact after the test.

The bundle was withdrawn from the shroud for further investigations. No noticeable changes of bundle geometry were indicated (Figs. 65 and 66). Grid spacers were removed for the separation of the single rods. No rod bending was observed in the plane with overhead view to burst opening. For the plane with the side view of openings only negligible rod bending was observed for the inner rods (Fig. 67) and some of the outer rods (Fig. 68) with values less of 3 mm deviation from the original rod axis.

The shape of burst openings of all rods is quite similar among each other, whereas their dimensions vary widely. The lengths of openings varied between 12 and 18 mm, the width between 2.7 and 4.9 mm, and the opening areas determined by image analyses are 19 - 52 mm² (Table 13). The tangential burst positions of all rods correspond to the hottest rod region and are directed mostly to the bundle centre (Fig. 69). All bursts are axially located between 860 and 1010 mm (Fig. 70). No global blockage was formed due to relatively small cladding strengths and due to the variation of the ballooning positions.

Observations of the cladding surface were performed with a Keyence digital microscope equipped with a macroscopic objective. The shapes of burst openings are shown in Figs. 71 - 76. Fig. 77 illustrates the structure of oxidized cladding surfaces near to the opening of rod #1. It can be seen that the cladding surface is covered with a network of crossed longitudinal cracks developed during the ballooning process. A large-scale crack cells network is located near to the burst opening, whereas small-scale cells are typical for the cladding side opposite to burst. The cell sizes change not only circumferentially, but also longitudinally: they decrease with increasing distance to the burst location. The cell size strongly depends on strain: the higher the strain the larger are the cells.

The inner surface of cladding #3 was investigated by videoscope (Fig. 78). Typical traces of contact between pellet and cladding slightly below the burst opening were observed. Similar observations were made previously also for some claddings of the QUENCH-L2 [22], -L3 [23] and -L4 [24] bundles and confirmed the early suggestions [4] that relatively often the burst occurs at the position of contact between pellet and cladding. Due to absence of the gas gap, the heat transport from pellet to cladding is the highest at this circumferential position. Concerning the gas penetration to these contact spots, the corresponding surface areas were not oxidised because access of steam was not possible to this area. Because the metal in these areas is not covered by oxide layer, the hydrogen, which has a higher diffusivity than steam, can be absorbed by cladding at these contacts between pellet and claddings.

5.2   Profilometry of Claddings with Laser Scanner

5.2.1   Linear Laser Scanning

The profilometry of the rods was performed with a Linear Laser Scanner made by ANT Antriebstechnik GmbH for quantifying the deformations produced on the rods as a result of the QUENCH-LOCA experiments. The ballooned parts of the bundle rods exposed to LOCA scenarios acquire a variety of shapes and sizes due to different temperature conditions. Therefore a precise method to detect the local variations in diameter along the rods was required.

5.2.2   Main Characteristics of the Measuring Device and Procedures

The measuring mechanism is based upon photocells which compare the amount of laser light blocked by the rod in relation to the portion of light that reaches the sensors. The equipment is mounted vertically and supported on a wall of the experimental hall in order to minimize the effects of shocks and vibrations propagated by the floor. The rod to be measured is placed vertically and linked to a step motor which ensures the precise turning of the rod according to a given number of measurements that should be made during a rotation of 360°. A resolution of 0.25° is provided. The laser scanner itself moves a predetermined length up or down the driving rails in order to cover a specific section of the examined rod. The smallest vertical step is 100 μm and the maximum length which the scanner can handle is 2000 mm.

Automatic settings allow the scanner to work for many hours without the need of supervision. For safety reasons and because of mechanical limitations, the data gathering is quite slow. A total of approximately 5700 points are measured each hour. This means that a scanning of a 1500 mm rod section takes roughly 4 days considering a measurement every 1 mm and 1°.

All data generated can be processed in various ways in order to determine different information. For instance, it allows the exact location and orientation of each burst, determination of radial strain, calculation of cross-section area reduction and thus blockage. Also, a digital 3D rendered image is generated as a record and for further analysis, since every rod is sooner or later damaged by mechanical testing or cut for metallographic examination.

5.2.3   Results of the Scans

The evaluation of the scans can be divided into azimuthal and longitudinal analysis.

The azimuthal plots (Figs. 79 - 99, bottom) clearly show the orientation of the bursts and also give an idea of the shape. It was revealed that the bursts were oriented to the centre of the bundle, mainly because of the radial thermal gradient which was established in the test section. The maximal cladding diameter was observed in the burst plane, the minimal diameter – in the perpendicular plane. It is also to seen, that immediately below and above the burst opening the maximal diameter was measured in the plane

perpendicular to the burst plane. All azimuthal plots illustrate this fact: the neighboring elevations lower the burst evident the maximal diameter in the plane perpendicular to the burst. I.e. during ballooning and immediately before burst, the cladding extends here more in the directions perpendicular to the burst plane.

The shape of the bursts varies widely, neither size nor symmetry have any apparent correlation to burst temperature.

Also based on these scans, the circumferential strains can be determined (Table 14), which are depicted on Figs. 79 - 99, top. There is a clear correlation of the burst location (position with a largest strain) and the temperature distribution on the longitudinal axis. Maximum strain of 33% was observed on the outer rod #21, minimum strain of 21% was observed on the outer rod #13. Comparison with corresponding results of the QUENCH-L3 test shows that the circumferential strain values in ballooning regions outside of burst opening are remarkably higher for the QUENCH-L5 (marked with red arrows in top plots of Figs. 79 - 99). A possible reason could be different mechanical properties of hydrogenated claddings.

For all rods the deformation starts at elevations about 250 mm and ends at 1250 mm. The axial extension of cladding region with more than 5% strain is usually shorter than 185 mm. It is worth to notice that besides the main strain maximum some of the rods (#2, #4, #5, #8, #9, #11, #12, #17, #20, #21) have a second (or sometimes even third) strain maximum located ≈100 mm (or ≈200 mm) below or above main maximum too. I.e. the ballooning was initiated at many axial locations inside the hot zone. A second balloon region was observed also for several rods of the QUENCH-L3 tests. The intensity and extension of ballooning were comparable for both bundle tests.

The blockage is the quotient of total increase of the rod cross-sections divided by initial empty area inside the inner surface of the shroud. Since the burst locations are scattered between elevations 870 and 1002 mm, the blockage wasn´t too significant. As shown in Fig. 100, the maximum blockage occurs at about 940 mm and reaches 25% of area reduction. If, hypothetically, all burst were located at the same level, the blockage would be 32%.

5.3 Nondestructive Eddy Current and Ultrasound Measurements

Before cutting the cladding tubes for further investigations, some analyses had to take place. The oxidation degree of each cladding was measured by means of the eddy current measurement device ISOSCOPE FMP30 from Helmut Fischer GmbH. The device was calibrated with two plastic foils of 24.3 and 99.3 μm thicknesses, which were disposed at the surface of pre-hydrogenated opt. ZIRLO prototype tube. At least 20 circumferential measurements at each axial position were used to achieve the averaged result. The axial step width was 20 mm. The device shows the distance between the gauge and the internal metallic layer; i.e. the measured values correspond to the sum of the thicknesses of ZrO_2 and α-Zr(O) layers. The comparison of eddy current results with metallographic results confirms this assumption.

Fig. 101 shows results of eddy current measurements for the central rod and one rod of the inner group in comparison with corresponding results for the QUENCH-L3 tests. The decreased oxidation of QUENCH-L5 claddings attributed to lower bundle temperatures. The most oxidized region is between 750 and 1000 mm for both tests, what corresponds to the axial temperature profile. Fig. 102 illustrates clearly the existence of a circumferential temperature gradient caused by shifting of pellet from the central position (Fig. 57) and moderate bending of cladding [4]. Irregular thickness changes were observed inside the axial zone with the pronounced ballooning due to variations of the cladding thickness from the cladding thickness for the original calibration sample.

The thinning of the cladding wall along the line of the burst opening in the ballooned region of the central rod was proved by ultrasound measurements (Fig. 103) performed by the Echometer device from Karl Deutsch GmbH. The wall thickness increases from 350 μm in vicinity of the opening tip to the regular thickness of 725 μm at a distance of about 50 mm.

5.4 Results of Neutron Radiography and Tomography; Analysis of Absorbed Hydrogen.

5.4.1 Basic Principles

Neutron radiography is a powerful tool for the determination of hydrogen concentration and distribution in zirconium alloys [25-29]. Hydrogen can be quantitatively and non-destructively determined with a spatial resolution of up to 20 μm. The method was applied for the post-test hydrogen analysis of selected QUENCH-L5 cladding tubes.

Firstly, a short introduction into neutron radiography will be given. The sample is positioned into a parallel neutron beam. The intensity distribution behind the sample is measured for each pixel. From the intensity the transmission *T* can be calculated:

$$T(x, y) = \frac{I(x, y) - I_B(x, y)}{I_0(x, y) - I_B(x, y)} \tag{2}$$

where *x* and *y* are the coordinates of the pixel position. *I*, I_0 and I_B are the intensities behind and before the sample and the background intensity, respectively. From the neutron transmission the total macroscopic neutron cross section Σ_{total} can be calculated:

$$\Sigma_{total}(x, y) = \frac{-\ln(T(x, y))}{s(x, y)} \tag{3}$$

where *s* is the neutron path length through the material. The total macroscopic neutron cross section is the sum of the total microscopic cross section *σ* of the isotopes *i* multiplied with their number density *N*:

$$\Sigma_{total}(x, y) = \sum_i \sigma_i \cdot N_i = \underbrace{N_{Zry}(x, y)\, \overline{\sigma_{Zry}}}_{\Sigma_{sample\,as\,received}} + N_O(x, y)\, \sigma_O + N_H(x, y)\, \sigma_H \tag{4}$$

In the case of steam oxidation of cladding materials it can be assumed that only the amount of oxygen and hydrogen is changed whereas the amount of zirconium and the alloying elements is not influenced significantly.

In order to reconstruct the specimen three-dimensionally, radiography projections have to be taken from different orientations. According to the sampling theorem, the number *n* of projections is connected with the spatial resolution (pixel size) *d* and the radius R of the object circle that fully encompasses the object formed by the rotating of the sample:

$$n = \sqrt{2\pi}\, \frac{R}{d} \tag{5}$$

5.4.2 Technique

The neutron radiography measurements were performed at the CONRAD facility of HZB Berlin. The investigations were performed using a pixel distance of 33 μm. Two rods were measured at once. The detector field of view (FOV) was 67 mm x 67 mm. The samples were scanned through the FOV with a step width of 60 mm. Illumination times per image was 40 s. The measurements were repeated 27 times. From these images the median image was determined in order to improve the counting statistics (and with it the resolution in the hydrogen concentration) with supressing gamma spots at once.

The neutron tomography experiments were performed at the ANTARES facility at the FRM2 research reactor in Garching. Each of the 875 projections per tomogram was measured three times with a pixel size of 20 μm and an illumination time of 19 s. For the further data treatment, the median of the three measurements per projection were determined. The dimensions of the FOV were 43 mm (axial direction) x 51 mm (radial direction). Three rods were measured at once.

5.4.3   Results of Radiography

The investigations comprise measurements of all rods of the QUENCH-L5 test. Because of the uncertainties of the tube wall thickness caused by the plastic deformation as well as the contribution of front and back side of the tube, quantitative information cannot be extracted from one single radiograph alone. However, the radiographies could give information about the occurrence of hydrogen enrichments and their positions. Fig. 104 shows the radiographs taken from inner rods, whereas Fig. 105 reveals depicted results for outer rods. For both cladding groups no regions with visible hydrogen content were indicated. In order to obtain quantitative information about the relative low hydrogen concentrations in the claddings, neutron tomography investigations were performed.

5.4.4   Results of Tomography: Hydrogen Content

For the sample reconstruction the Muhrec3 software of PSI Villigen was used. The reconstructed data set was analyzed for each slice (axial cut) using the macro "Background correction" developed at KIT in the software package ImageJ. The different steps of the analysis are

o   Sample identification by background correction (definition of threshold value at which it is assumed that the voxel is part of the sample, dilatation of the marked volume to close the sample area, shrinking of the marked volume by the same numbers).

o   Additional shrinking of the sample to neglected sample surface positions with increased cross section as an artefact or surface effects like total reflection and refraction.

o   Determination of minimum, mean and maximum values in the marked sample volume.

Due to fixed space positions of individual slices it is possible to analyse the geometrical parameters (bending, strain etc.) of a whole cladding tube. Fig. 106 illustrates such approach to deformation determination of the central cladding in the ballooning region. This figure gives proof of ballooning and burst details at the hottest axial elevation described in [4]: the circumferential hottest position of cladding stays continuously in contact with fuel pellet and finally cladding bursts here, whereas the cladding site opposite to burst goes more and more away from the pellet and will be colder.

For the determination of the hydrogen content the following correlation was determined:

$$\Sigma_{total} = 0.204 \; cm^{-1} + 2.327 \; cm^{-1} \frac{H}{Zr} \tag{6}$$

The statistical analysis of the tomography data allows determining the axial distribution of hydrogen concentration in the vicinity of burst openings. The resolution of this distribution is very high due to small pixel size (20 μm). Figs. 107 - 112 depict distribution of mean and maximal concentrations calculated for each cross section (width of cross section is 20 μm) of six investigated claddings. The maxima of both curves for each measured rod are represented in Table 15. The mean values deviate not significantly from pre-hydrogenated concentration level of 300 wppm.

5.5 Mechanical Tests

Tensile tests on relevant cladding sections were performed at room temperature to determine the residual strength and ductility of QUENCH-LOCA tested claddings, particularly to identify the embrittlement in dependence of the different quench test conditions. Previously, the mechanical properties of axially homogeneously hydrogenated ZIRLO claddings by this method were described in [30].

5.5.1 Tensile Test Set-up

The tensile tests were carried out using a universal testing machine from INSTRON (type 4505, 50 kN load cell), equipped with specially developed grip holders. The experiments were performed displacement-controlled with a displacement rate of 2 mm/min at room temperature (RT). Exact fitting end plugs were mounted to clamp the tubes without deforming their end sections. Since a cladding tested in a QUENCH experiment usually shows an inhomogeneous ZrO_2/α-$Zr(O)$ layer thickness along the main tube axis, the specimens were optically subdivided with paint markers to determine both the global and the local axial elongation during a test by using a CCD-camera measurement system. Three cameras were used for the tests to increase the resolution of the optical measurement device. Generally, the initial gauge length l_0 of a specimen was 750 mm and a sample was prepared in that way, that the ballooning section was positioned in the axial center. After the tests, the strain was calculated from the captured pictures by using the Digital Image Correlation and Tracing program provided by MATLAB [31] and the stress was calculated by using average values of the measured initial inner and outer diameters from the ends of a tube.

5.5.2 Results of the Tensile Tests

One inner rod failed at the positions of thermocouple, the failure of other three rods was due to stress concentration at opening middle, whereas others failed after necking. During the tensile tests with outer rods also typical fracture after necking with fracture surfaces perpendicular to the load direction was observed for several rods. However, mostly was observed fracture from (pre)crack tip to (pre)crack tip at which the final crack propagates around a sample. This fracture mode doesn't occur abruptly. In fact one can observe that the onset of failure is driven by strong local deformations, starting at the (pre)crack tips. It is interesting to note, that only claddings from the outer area of the bundle failed in this mode, in parts with remarkable elongations at fracture up to more than 5%.

In general, the elongation at fracture of all QUENCH-L5 tested claddings varies between 3.3 and 12.3%, and the strength at fractures was on average 448 for necking and 541 MPa for stress concentration. Both values are more than 7% higher than corresponding values for the not pre-hydrogenated claddings of the QUENCH-L3 bundle. An overview of all determined mechanical properties is given in Table 16. Fig. 113 and Fig. 114 depict the stress-strain curves of all inner and outer specimens, respectively.

6 Summary and Conclusions

The QUENCH-LOCA-5 test with pre-hydrogenated opt. ZIRLO™ claddings was performed according to a temperature/time-scenario typical for a LBLOCA in a German PWR with similar test parameters as the QUENCH-LOCA-3 test with as-received opt. ZIRLO™ claddings: similar time schedule, maximal heat-up rate 8 K/s, cooling phase lasted 120 s and terminated with 3.3 g/s/rod water flooding.

The maximum peak cladding temperature at the end of the heat-up phase at elevation 950 mm was 1250 K. It is lower in comparison to 1350 K for QUENCH-L3 because of lower temperatures at the transient start. Due to local radial pellet shift up to contact with cladding, the circumferential temperature gradient measured across a cladding varied at different elevations (e.g. about 20 K at 950 mm and 90 K at 850 mm at the burst onset). The oxidation degree of QUENCH-L5 claddings (max. 16 μm for ZrO_2 and α-Zr(O) layer thicknesses) was decreased in comparison to QUENCH-L3 (max. 25 μm) by reason of lower bundle temperatures. The integral oxidation of the QUENCH-L5 bundle was indicated by a release of 0.45 g hydrogen during the whole test, almost 0.2 g less in comparison to QUENCH-L3 (correspondingly to the lower temperatures in QUENCH-L5).

The averaged maximal strain of the QUENCH-L5 claddings (26.2%) is slightly higher than this parameter for the QUENCH-L3 claddings (25.5%), and the axial extension of ballooning region for each cladding is larger for QUENCH-L5 in comparison to QUENCH-L3. The reason could be the onset of ballooning at lower temperatures. Some rods have up to three ballooning regions for both tests; the reason is successive onset of ductile temperature threshold at different elevations. Another parameter calculated, based on profilometry measurements, is the bundle blockage. The maximum blockage ratio of the cooling channel due to ballooning (25% at 940 mm) was slightly higher in comparison to QUENCH-L3 (21% at 918 mm). Because of moderate blockage good bundle coolability was kept for both bundles.

Cladding wall thinning from 725 μm to 450 μm due to ballooning was observed at the burst side along 50 mm below and above burst opening (ultrasound measurement). The cladding bursts occurred at temperatures between 1027 and 1151 K (QUENCH-L3: 1064 and 1188 K). The average burst temperatures of 1081 K (808 °C) for QUENCH-L5 is lower than for QUENCH-L3 (1117 K or 844 °C) because of lower α-Zr→β-Zr phase transition temperature. The average burst opening parameters were: width 3.8 ± 0.6 mm; length 14.3 ± 1.8 mm (similar to QUENCH-L3 with not pre-hydrogenated claddings). I.e. the sizes of openings are relatively small and only small fragments of fuel pellets in the reactor case can be released from the claddings.

No secondary hydrogenation was observed for the QUENCH-L5 claddings due to relative short high temperature period: only about 30 s above 850 °C (complete transition to β-Zr phase) in comparison to nearly 100 s for QUENCH-L3.

During quenching, following the high-temperature phase, no fragmentation of claddings was observed for both QUENCH-L3 and QUENCH-L5 (residual strengths or ductility is sufficient).

Tensile tests at room temperature showed cladding fracture mostly as a result of stress concentration in the region of burst opening.

7   Acknowledgments

8   References

[1]   Atomic Energy Commission Rule-Making Hearing, Opinion of the Commission, Docket RM-50-1, 28 December, 1973.

[2]   G. Hache and H. M. Chung, "The History of LOCA Embrittlement Criteria," NUREG/CP-0172, May 2001, pp. 205-237.

[3]   RSK-Leitlinien für Druckwasserreaktoren. Ursprungsfassung (3. Ausgabe vom 14. Oktober 1981) mit Änderungen vom 15.11.1996. http://www.rskonline.de/downloads/8110dwr.pdf

[4]   K. Wiehr, He. Schmidt, Out-of-pile-Versuche zum Aufblähvorgang von Zirkaloy-Hüllen. Ergebnisse aus Vorversuchen mit verkürzten Brennstabsimulatoren. Wissenschafliche Berichte, KFK-2345. Karlsruhe, 1977. http://bibliothek.fzk.de/zb/kfk-berichte/KFK2345.pdf

[5]   P. Hofmann, S. Raff. Verformungsverhalten von Zircaloy-4-Hüllrohren unter Schutzgas im Temperaturbereich zwischen 600 und 1200°C. Wissenschaftliche Berichte, KFK-3973, Karlsruhe, 1981. http://bibliothek.fzk.de/zb/kfk-berichte/KFK3168.pdf

[6]   L. Schmidt, H. Lehning, D. Piel. Berstversuche an Zircaloy-Huellrohren unter kombinierter mechanisch-chemischer Beanspruchung (FABIOLA). In: Projekt Nukleare Sicherheit. Jahresbericht 1982. KFK-3350 (Juli 83) S.4200/69-4200/70. http://quench.forschung.kit.edu/img/fabiola_kfk_1980_1983_schmidt.pdf

[7]   E. H. Karb, M. Prüßmann, L. Sepold, P. Hofmann, G. Schanz. LWR Fuel Rod Behavior in the FR2 ln-pile Tests Simulating the Heatup Phase of a LOCA. Final Report. Wissenschaftliche Berichte, KFK-3346, Karlsruhe, 1983. http://bibliothek.fzk.de/zb/kfk-berichte/KFK3346.pdf

[8]   M. E. Markiewicz, F. J. Erbacher. Experiments on Ballooning in Pressurized and Transiently Heated Zircaloy-4 Tubes. Wissenschaftliche Berichte, KFK-4343, Karlsruhe, 1988. http://bibliothek.fzk.de/zb/kfk-berichte/KFK4343.pdf

References

[9] K. Wiehr. REBEKA-Bündelversuche Untersuchungen zur Wechselwirkung zwischen aufblähenden Zircaloyhüllen und einsetzender Kernnotkühlung. Abschlußbericht. Wissenschaftliche Berichte, KFK-4407, Karlsruhe, 1988. http://bibliothek.fzk.de/zb/kfk-berichte/KFK4407.pdf

[10] F. J. Erbacher, H. J. Neitzel, K. Wiehr. Cladding Deformation and Emergency Core Cooling of a Pressurized Water Reactor in a LOCA. Summary Description of the REBEKA Program. Wissenschaftliche Berichte, KFK-4781, Karlsruhe, 1990. http://bibliothek.fzk.de/zb/kfk-berichte/KFK4781.pdf

[11] F. J. Erbacher, S. Leistikow. A Review of Zircaloy Fuel Cladding Behavior in a Loss-of-Coolant Accident. Wissenschaftliche Berichte, KFK-3973, Karlsruhe, 1985. http://bibliothek.fzk.de/zb/kfk-berichte/KFK3973.pdf

[12] J.-C. Brachet, V. Vandenberghe-Maillot, L. Portier, D. Gilbon, A. Lesbros, N. Waeckel, and J.-P. Mardon, Hydrogen Content, Preoxidation, and Cooling Scenario Effects on Post-Quench Microstructure and Mechanical Properties of Zircaloy-4 and M5$^{®}$ Alloys in LOCA Conditions. J. ASTM Intl., Vol. 5, No. 5 (2008). Available online as JAI101116 at www.astm.org.

[13] T. Chuto, F Nagase and T. Fuketa. High Temperature Oxidation of Nb-containing Zr Alloy Cladding in LOCA Conditions. Nuclear Engineering and Technology, Vol.41, No.2, March 2009.

[14] Hee M. Chung. Fuel Behavior under Loss-of-Coolant Accident Situations. Nuclear Engineering and Technology, Vol.37 No.4, August 2005.

[15] H. Uetsuka, T. Furuta and S. Kawasaki. Zircaloy-4 Cladding Embrittlement due to Inner Surface Oxidation under Simulated Loss-of-Coolant Condition. Journal of Nuclear Science and Technology, 18[9], pp. 705~717 (September 1981).

[16] M. Billone, Y. Yan, T. Burtseva, R. Daum. Cladding Embrittlement During Postulated Loss-of-Coolant Accidents, NUREG/CR-6967, July 2008.

[17] OECD SCIP-2 Project: http://www.oecd-nea.org/jointproj/scip-2.html

[18] J. Stuckert, M. Große, C. Rössger, M. Steinbrück, M. Walter. Results of the commissioning bundle test QUENCH-L0 performed under LOCA conditions. KIT Scientific Reports, KIT-SR 7571 (March 2013).

[19] J. Stuckert, M. Große, C. Rössger, M. Klimenkov, M. Steinbrück, M. Walter. QUENCH-LOCA program at KIT on secondary hydriding and results of the commissioning bundle test QUENCH-L0. Nuclear Engineering and Design, 255(2013), pp. 185-201. DOI:10.1016/j.nucengdes.2012.10.024.

[20] J. Stuckert, M. Große, C. Rössger, M. Steinbrück, M. Walter. Results of the LOCA reference bundle test QUENCH-L1 with Zircaloy-4 claddings. KIT Scientific Reports, KIT-SR 7651 (2013).

[21] J. Stuckert, M. Große, C. Rössger, M. Steinbrück, M. Walter. Influence of the temperature history on secondary Hydriding and mechanical properties of zircaloy-4 claddings - An analysis of the QUENCH-LOCA bundle tests. Proceedings of 22nd International Conference on Nuclear Engineering (ICONE 2014); Vol. 3, Paper 30792; July 7-11, 2014, Prague. DOI: 10.1115/ICONE22-30792. http://proceedings.asmedigitalcollection.asme.org/proceeding.aspx?articleid=1937123, Presentation: http://bibliothek.fzk.de/zb/veroeff/96364.pdf.

[22] J. Stuckert, M. Große, C. Rössger, M. Steinbrück, M. Walter. Results of the LOCA bundle test QUENCH-L2 with M5$^{®}$ claddings. KIT Scientific Reports, KIT-SR 7677 (2015).

References

[23] J. Stuckert, M. Große, C. Rössger, M. Steinbrück, M. Walter. Results of the LOCA bundle test QUENCH-L3 with optimised ZIRLO™ claddings. KIT Scientific Reports, KIT-SR 7737 (2017).

[24] J. Stuckert, M. Große, A. Pshenichnikov, C. Rössger, M. Steinbrück, M. Walter. Results of the LOCA reference bundle test QUENCH-L4 with pre-hydrogenated M5® claddings. KIT Scientific Reports, KIT-SR 7712 (2016).

[25] M. Grosse, E. Lehmann, P. Vontobel, M. Steinbrueck: "Quantitative determination of absorbed hydrogen in oxidised Zircaloy by means of neutron radiography", Nucl. Instr. & Methods in Phys. Res. A 566 (2006), 739.

[26] M. Große, G. Kühne, M. Steinbrück, E. Lehmann, P. Vontobel, J. Stuckert. Determination of the hydrogen uptake of steam-oxidised zirconium alloys by means of quantitative analysis of neutron radiographs. J. Phys.: Condens. Matter 20 (2008), 104263.

[27] M. Grosse, E. Lehmann, M. Steinbrueck, G. Kühne, J. Stuckert. Influence of oxide layer morphology on hydrogen concentration in tin and niobium containing zirconium alloys after high temperature steam oxidation. J. Nucl. Mater. 385 (2009), 339.

[28] J. Stuckert, J. Birchley, M. Grosse, B. Jaeckel, M. Steinbrück. Experimental and calculation results of the integral reflood test QUENCH-14 with M5 cladding tubes. Annals of Nuclear Energy, 37(2010) S.1036-47, DOI:10.1016/j.anucene.2010.04.015.

[29] M. Grosse, M. Van den Berg, C. Goulet E. Lehmann, B. Schillinger. In-situ neutron radiography investigations of hydrogen diffusion and absorption in zirconium alloys. Nuclear Instruments and Methods in Physics Research Section A: Accelerators, Spectrometers, Detectors and Associated Equipment, Volume 651, Issue 1, 21 September 2011, Pages 253–257.

[30] J. Stuckert, M. Große, M. Walter. Mechanical properties of pre-hydrogenated (600 – 5000 wppm) cladding segments. 16th International QUENCH-Workshop, Karlsruhe, November 2010, ISBN 978-3-923704-74-3.

[31] C. Eberl, D.S. Gianola, K. J. Hemker. Mechanical Characterization of Coatings Using Microbeam Bending and Digital Image Correlation Techniques. Experimental Mechanics, January 2010, Volume 50, Issue 1, pp 85-97.

Tables and Figures

Table 1 QUENCH Test Matrix 1997 – 2016

Test	Quench medium and injection rate	Temp. at onset of flooding or cool-down[1]	Max. ZrO$_2$ before transient[2]	Max. ZrO$_2$ (*X s*) before flooding[2]	Posttest average ZrO$_2$ thickness[3]	H$_2$ production before / during cooldown, g	Remarks, objectives
QUENCH-00 Oct. 9 - 16, 97	Water 80 g/s	≈ 1800 K			completely oxidized		Commissioning tests.
QUENCH-01 Febr. 26, 98	Water 52 g/s	≈ 1830 K	312 μm		500 μm at 913 mm	36 / 3	COBE Project; partial fragmentation of pre-oxidized cladding.
QUENCH-02 July 7, 98	Water 47 g/s	≈ 2400 K			completely oxidized	20 / 140	COBE Project; no additional pre-oxidation; quenching from high temperatures.
QUENCH-03 Jan. 20, 99	Water 40 g/s	≈ 2350 K			completely oxidized	18 / 120	No additional pre-oxidation, quenching from high temperatures.
QUENCH-04 June 30, 99	Steam 50 g/s	≈ 2160 K	82 μm		280 μm	10 / 2	Cool-down behavior of slightly pre-oxidized cladding by cold steam injection.
QUENCH-05 March 29, 2000	Steam 48 g/s	≈ 2020 K	160 μm		420 μm	25 / 2	Cool-down behavior of pre-oxidized cladding by cold steam injection.
QUENCH-06 Dec. 13, 2000	Water 42 g/s	≈ 2060 K	207 μm[5]	300 μm, (60 s), SVECHA modeling	670 μm[4] (60% metal converted to outer ZrO$_2$)	32 / 4	OECD-ISP 45; prediction of H$_2$ source term by different code systems.
QUENCH-07 July 25, 2001	Steam 15 g/s	≈ 2100 K	230 μm		completely oxidized	66 / 120	COLOSS Project; impact of B$_4$C absorber rod failure on H$_2$, CO, CO$_2$, and CH$_4$ generation.
QUENCH-09 July 3, 2002	Steam 49 g/s	≈ 2100 K			completely oxidized	60 / 400	As QUENCH-07, steam-starved conditions prior to cooldown.
QUENCH-08 July 24, 2003	Steam 15 g/s	≈ 2090 K	274 μm		completely oxidized	46 / 38	As QUENCH-07, no absorber rod.

Test	Quench medium and injection rate	Temp. at onset of flooding or cool-down[1]	Max. ZrO_2 before transient[2]	Max. ZrO_2 (X s) before flooding[2]	Posttest average ZrO_2 thickness[3]	H_2 production before / during cooldown, g	Remarks, objectives
QUENCH-10 July 21, 2004	Water 50 g/s	≈ 2200 K	514 µm	613 µm (at 850 mm)	completely oxidized	48 / 5	LACOMERA Project; Air ingress.
QUENCH-11 Dec. 08, 2005	Water 18 g/s	≈ 2040 K		170 µm	completely oxidized	9 / 132	LACOMERA Project; Boil-off.
QUENCH-12 Sept. 27, 2006	Water 48 g/s	≈ 2100 K	160 µm, breakaway	300 µm, (110 s) breakaway	completely oxidized	34 / 24	ISTC Project No. 1648.2; VVER bundle with E110 claddings.
QUENCH-13 Nov. 7, 2007	Water 52 g/s	≈ 1820 K		400 µm, after AgInCd rod failure	750 µm	42 / 1	SARNET; impact of AgInCd absorber rod failure on aerosol generation.
QUENCH-14 July 2, 2008	Water 41 g/s	≈ 2100 K	170 µm[6]	470 µm[6], (30 s)	840 µm[4] (74% metal converted to outer ZrO_2)	34 / 6	ACM series: M5[®] cladding.
QUENCH-15 May 27, 2009	Water 48 g/s	≈ 2100 K	145 µm[6]	380 µm[6], (30 s)	630 µm[4] (70% metal converted to outer ZrO_2)	41 / 7	ACM series: ZIRLO[TM] cladding.
QUENCH-L0 July 22, 2010	*Water, 100 g/s*	*1330 K*	*1 µm*	*≈ 18 µm*	*20 µm (central rod)*	*0.748/0.3*	*VGB Project; Commissioning test with Zry-4.*
QUENCH-16 July 27, 2011	Water 53 g/s	≈ 1870 K	135 µm	130 µm at 450-950 mm, breakaway	1075 µm at 550-650 mm	16 / 128	LACOMECO Project; Air ingress.
QUENCH-L1 Feb. 02, 2012	*Water, 100 g/s*	*1373 K*	*1 µm*	*≈ 19 µm*	*22 µm (central rod)*	0.718/0.01	*VGB Project; Reference test.*
QUENCH-17 Jan. 31, 2013	Water 10 g/s	≈ 1800 K		completely oxidized	completely oxidized	110 / 1	SARNET-2; Debris formation and coolability.
QUENCH-L2 July 30, 2013	*Water, 100 g/s*	*1373 K*	*1 µm*	*n.a.*	*13 µm (central rod)*	*0.4 total*	*VGB Project; M5[®] claddings.*
QUENCH-L3HT March 21, 2014	*Water, 100 g/s*	*1623 K*	*1 µm*	*n.a.*	*70 µm (central rod)*	*1 total*	*VGB Project; Opt. ZIRLO claddings.*

Test	Quench medium and injection rate	Temp. at onset of flooding or cool-down[1]	Max. ZrO₂ before transient[2]	Max. ZrO₂ (X s) before flooding[2]	Posttest average ZrO₂ thickness[3]	H₂ production before / during cooldown, g	Remarks, objectives
QUENCH-L4 *July 30, 2014*	*Water,* *100 g/s*	*1385 K*	*1 μm*	*n.a.*	*13 μm* *(central rod)*	*0.8 total*	*VGB Project;* *Pre-hydrogenated (100 wppm) M5®* *claddings.*
QUENCH-L3 *March 17, 2015*	*Water,* *100 g/s*	*1346 K*	*1 μm*	*n.a.*	*14 μm* *(central rod)*	*0.6 total*	*VGB Project;* *Optimised ZIRLO claddings.*
QUENCH-L5 *Febr 10, 2016*	*Water,* *100 g/s*	*1257 K*	*1 μm*	*n.a.*	*8 μm* *(central rod)*	*0.45 total*	*VGB Project;* *Pre-hydrogenated (300 wppm)* *optimised ZIRLO claddings.*

[1] Maximum measured bundle temperature at 950 mm elevation. [2] Measured (or calculated for LOCA tests) at the withdrawn corner rod at 950 mm elevation.
[3] Measured posttest at the bundle elevation of maximum temperature, i.e. 950 mm. [4] Some claddings were completely oxidized at 950 mm elevation.
[5] Oxide thickness during transient phase. [6] Zircaloy-4 corner rods.   Revised: August 2017

Table 2   Design characteristics of the QUENCH-L5 test bundle

Bundle type		PWR
Bundle size		21 heated rods
Effective number of rods	(considering surface of heated rods, shroud and corner rods)	30.6 rods (21 + 7.4 from shroud + 2.2 from corner rods)
Pitch		14.3 mm
Coolant channel area		29.65 cm^2
Hydraulic diameter		11.5 mm
Cladding material		pre-hydrogenated opt. ZIRLO (300 wppm H) in middle part (1200 mm), not hydrogenated end sections (645 and 435 mm)
Cladding outside diameter		10.75 mm
Cladding thickness		0.725 mm
Cladding length	(position in the bundle)	2278 mm (between -593 and 1685 mm)
Rod length	(elevations)	2480 mm (-690 to 1790 mm)
Internal rod pressure (gas)		5.5 MPa abs. (Kr)
Material of middle heater		Tungsten (W)
	surface roughness	Ra=1.6 µm
Tungsten heater length		1024 mm (between 0 and 1024 mm)
Tungsten heater diameter		4.6 mm
Annular pellet	material	ZrO_2;Y_2O_3-stabilized
	dimensions	$\varnothing$ 9.15/4.75 mm; L=11 mm
	surface roughness	Ra=0.3 µm
Pellet stack		0 mm to ~1020 mm
Corner rod (4)	material	Zircaloy-4
	instrumented (A, C, D)	tube $\varnothing$ 6x0.9 (bottom: -1140 mm)
		rod $\varnothing$ 6 mm (top: +1300 mm)
	not instrumented (B)	rod $\varnothing$ 6 mm (-1350 to +1155 mm)
Grid spacer (cutout of 16x16 spacer)	material	low tin ZIRLO
	length	59 mm
	sheet thickness	0.6 mm
	elevation of lower edge	-100, 150, 550, 1050, 1410 mm
Shroud	material	Zirconium 702 (flange: Zry-4)
	wall thickness	3.17 mm
	outside diameter	86.0 mm
	length (extension)	1600 mm (-300 mm to 1300 mm)
Shroud insulation	material	ZrO_2 fiber
	insulation thickness	≈ 36 mm
	elevation	-300 to ≈1000 mm
Molybdenum heaters and copper electrodes	length of upper part	766 mm (576 Mo, 190 mm Cu)
	length of lower part	690 mm (300 Mo, 390 mm Cu)
	outer diameter:	
	prior to coating	8.6 mm
	after coating with ZrO_2	9.0 mm
	coat. surface roughness	Ra=6-12 µm
	borehole of Cu-electrodes	diameter 2 mm, length 96 mm
Cooling jacket	Material: inner/outer tube	Inconel 600 (2.4816) / SS (1.4571)
	inner tube	$\varnothing$ 158.3 / 168.3 mm
	outer tube	$\varnothing$ 181.7 / 193.7 mm

Table 3   Properties of opt. ZIRLO cladding tubes

Table 3.1.   Chemical composition of opt. ZIRLO in weight-%

Element	Symbol	*Measured value*
Tin	Sn	*0.7*
Niobium	Nb	*1.1*
Iron	Fe	*0.11*
Oxygen	O	*0.12*

Table 3.2.   Mechanical properties of opt. ZIRLO at RT in tension

Element	*Measured value*
0.2 Yield strength Rp 0.2	520 MPa
Ultimate tensile stress Rm	700 MPa
Elongation at fracture A_{50} mm	25%

Table 3.3.   Microstructure of opt. ZIRLO

Grain size: 4.5 µm	Nr. 13.0 according to ASTM E 112 (acceptable average grain size shall be < Nr. 10, i.e. < 13 µm)
Surface Conditions:	Roughness (out- and inside): Ra = 0.35 µm

Table 4   Main characteristics of the ZrO$_2$ pellet material, yttria-stabilized (type FZY)

Property		Data*
Density		5.5-5.8 g/cm^3
Open porosity		0
Mean grain size		50 µm
Hardness (Knoop, 100 g)		17000 N/mm^2
Yield strength under compression		2000 N/mm^2
Bending strength		350 N/mm^2
Elastic modulus		165 GPa
Specific heat at 20 °C		400 J/(kg·K)
Thermal conductivity at 100 °C		2.5 W/(m·K)
Linear expansion, 20-1000 °C		10.5 x 10^{-6}/K
Specific electric resistance	at 20 °C	10^{10} Ω cm
	at 500 °C	5000 Ω cm
	at 1000 °C	50 Ω cm
*According to FRIATEC, Mannheim		

Table 5 QUENCH-L5; Electrical resistances of rods [mΩ] at 20 °C

Table 5.1. Internal circuit with 9+1 rods

rod	1	2	3	4	5	6	7	8	9	15	*Average*	*10 rods parallel*
pre-test	4.7	4.7	4.7	4.7	4.8	4.7	4.7	4.6	4.7	4.7	*4.7*	*0.47*
post-test	4.6	4.6	4.7	4.6	4.6	4.6	4.6	4.6	4.6	4.7	*4.6*	0.46

Note: Measured values include the resistance of slide contacts R_s=0.75 mΩ

Table 5.2. External circuit with 11 rods

rod	10	11	12	13	14	16	17	18	19	20	21	*Average*	*11 rods parallel*
pre-test	4.8	4.7	4.7	4.7	4.7	4.7	4.8	4.7	4.7	4.8	4.8	*4.7*	*0.43*
post-test	4.7	4.7	4.6	4.6	4.6	4.6	6.6	4.7	4.6	4.8	4.8	*4.8*	*0.44*

Note: Measured values include the resistance of slide contacts R_s=0.75 mΩ

Each circuit connected to the DC generator with 4 parallel bonded cables. The resistance of each cable is R_c=1.2 mΩ. Therefore, the external (outside) resistance corresponding to each heated rod (indicated by SCDAP/RELAP as fxwid) is $R_{ie}=R_s+10·R_c/4=3.75$ mΩ for the inner rod group and $R_{oe}=R_s+11·R_c/4=4.05$ mΩ for the outer rod group.

Table 6   Properties of zirconia fiber insulating boards

Table 6.1.   Chemical composition*

Oxide	ZrO_2	Y_2O_3	HfO_2	TiO_2	SiO_2	CaO	MgO	Fe_2O_3	Al_2O_3	Na_2O
typical wt%	88	10	2	0.14	0.12	0.09	0.03	0.04	0.01	0.01

Table 6.2.   Physical properties*

bulk density	porosity	shrinkage		thermal expansion coefficient at 298-1453K	melting point	max. service tempe-rature	flexural strength	compressive strength at 10% compression
		(1 hour at 1925 K)	(24 hours at 1925 K)					
g/cm³	%	%		1/K	K	K	MPa	MPa
0.48	92	1.2	2.8	$10.7*10^{-6}$	2866	2500	0.59	0.29

Table 6.3.   Thermal conductivity*

temperature, K	673	1073	1373	1673	1923
conductivity, W/(m·K)	0.08	0.11	0.14	0.19	0.24

Table 6.4.   Specific heat capacity*

temperature, K	366	2644
specific heat capacity, J/(kg·K)	544	754

According to specifications of manufacturer ZIRCAR PRODUCTS on the ZYFB3 material

Table 7   List of instrumentation for the QUENCH-L5 test

Chan	Desig-nation	Instrument, location	Unit
0	P rod 13	Internal pressure of rod #13	bar
1	P rod 14	Internal pressure of rod #14	bar
2	P rod 15	Internal pressure of rod #15	bar
3	P rod 12	Internal pressure of rod #12	bar
4	P rod 03	Internal pressure of rod #03	bar
5	P rod 04	Internal pressure of rod #04	bar
6	P rod 05	Internal pressure of rod #05	bar
7	P rod 16	Internal pressure of rod #16	bar
8	P rod 11	Internal pressure of rod #11	bar
9	P rod 02	Internal pressure of rod #02	bar
10	P rod 01	Internal pressure of rod #01	bar
11	P rod 06	Internal pressure of rod #06	bar
12	P rod 17	Internal pressure of rod #17	bar
13	P rod 10	Internal pressure of rod #10	bar
14	P rod 09	Internal pressure of rod #09	bar
15	P rod 08	Internal pressure of rod #08	bar
16	P rod 07	Internal pressure of rod #07	bar
17	P rod 18	Internal pressure of rod #18	bar
18	P rod 21	Internal pressure of rod #21	bar
19	P rod 19	Internal pressure of rod #19	bar
20	P rod 20	Internal pressure of rod #20	bar
21..31		20 mA, Reserve	
32..34		TC (W/Re), Reserve	
35	TSH 15/0	TC (NiCr/Ni), shroud outer surface, 1150 mm, 21°, feed cable outside of shroud insulation.	K
36	TSH 14/270	TC (NiCr/Ni), shroud outer surface, 1050 mm, 289°, feed cable outside of shroud insulation.	K
37		TC (W/Re), Reserve	K
38	TFS 15/13	TC (NiCr/Ni), surface of fuel rod simulator 15, group 5, 950 mm	K
39	TFS 19/12	TC (NiCr/Ni), surface of fuel rod simulator 19, group 5, 850 mm	K

Chan	Desig-nation	Instrument, location	Unit
40..41		TC (W/Re), Reserve	
42	TFS 7/12	TC (NiCr/Ni), surface of fuel rod simulator 7, group 3, 850 mm	K
43	TFS 15/12	TC (NiCr/Ni), surface of fuel rod simulator 15, group 5, 850 mm	K
44	TFS 2/12	TC (NiCr/Ni), surface of fuel rod simulator 2, group 2, 850 mm	K
45	TFS 4/12	TC (NiCr/Ni), surface of fuel rod simulator 4, group 2, 850 mm	K
46	TFS 19/13	TC (NiCr/Ni), surface of fuel rod simulator 19, group 5, 950 mm	K
47..57		TC (W/Re), Reserve	K
58	TFS 7/10	TC (NiCr/Ni), surface of fuel rod simulator 7, group 3, 650 mm	K
59..60		TC (W/Re), Reserve	K
61	TFS 11/12	TC (NiCr/Ni), surface of fuel rod simulator 11, group 4, 850 mm	K
62	P 206	Reserve	
63	F 206	Reserve	
64	T 402 b	TC (NiCr/Ni), Ar super heater	K
65..67		TC (W/Re), Reserve	
68	T 512	TC (NiCr/Ni), gas temperature at 1360 mm (bundle outlet) between rod #20 and shroud	K
69..70		TC (W/Re), Reserve	K
71	*Ref. T01*	*Temperature of measuring crate 1 (reference temperature)*	K
72	TFS 11/13	TC (NiCr/Ni) surface of fuel rod simulator 11, group 4, 950 mm	K
73	TFS 7/13	TC (NiCr/Ni), surface of fuel rod simulator 7, group 3, 950 mm	K
74	TFS 2/13	TC (NiCr/Ni), surface of fuel rod simulator 2, group 2, 950 mm	K
75	TFS 4/13	TC (NiCr/Ni), surface of fuel rod simulator 4, group 2, 950 mm	K
76	TFS 15/11	TC (NiCr/Ni), surface of fuel rod simulator 15, group 5, 750 mm	K
77	TFS 19/11	TC (NiCr/Ni), surface of fuel rod simulator 19, group 5, 750 mm	K
78	TFS 11/11	TC (NiCr/Ni) surface of fuel rod simulator 11, group 4, 750 mm	K
79	TFS 7/11	TC (NiCr/Ni), surface of fuel rod simulator 7, group 3, 750 mm	K
80	TFS 2/11	TC (NiCr/Ni) surface of fuel rod simulator 2 group 2, 750 mm	K
81	TSH 12/90	TC (NiCr/Ni), shroud outer surface, 850 mm, 109°	K
82	TFS 2/10	TC (NiCr/Ni); surface of fuel rod simulator 2, group 2, 650 mm	K
83	TSH 10/270	TC (NiCr/Ni), shroud outer surface, 650 mm, 289°	K
84	TSH 9/180	TC (NiCr/Ni), shroud outer surface, 550 mm, 191°	K

Chan	Desig-nation	Instrument, location	Unit
85	TSH 8/90	TC (NiCr/Ni), shroud outer surface, 450 mm, 109°	K
86	TSH 7/0	TC (NiCr/Ni), shroud outer surface, 350 mm, 11°	K
87	TSH 6/270	TC (NiCr/Ni) shroud outer surface, 250 mm, 281°	K
88	TSH 5/180	TC (NiCr/Ni), shroud outer surface, 150 mm, 191°	K
89	TSH 4/90	TC (NiCr/Ni), shroud outer surface, 50 mm, 109°	K
90	TSH 11/0	TC (NiCr/Ni), shroud outer surface, 750 mm, 11°	K
91	TCI 9/270	TC (NiCr/Ni), cooling jacket inner tube wall, 550 mm, 270°	K
92	TCI 10/270	TC (NiCr/Ni), cooling jacket inner tube wall, 650 mm, 270°	K
93	TCI 11/270	TC (NiCr/Ni), cooling jacket inner tube wall, 750 mm, 270°	K
94	TCI 13/270	TC (NiCr/Ni), cooling jacket inner tube wall, 950 mm, 270°	K
95	TFS 4/11	TC (NiCr/Ni), surface of fuel rod simulator 4, group 2, 750 mm	K
96	TFS 15/10	TC (NiCr/Ni), surface of fuel rod simulator 15, group 5, 650 mm	K
97	TFS 19/10	TC (NiCr/Ni), surface of fuel rod simulator 19, group 5, 650 mm	K
98	TFS 11/10	TC (NiCr/Ni), surface of fuel rod simulator 11, group 4, 650 mm	K
99	TSH 13/180	TC (NiCr/Ni), shroud outer surface, 950 mm, 191°, feed cable outside of shroud insulation.	K
100	TSH 3/0	TC (NiCr/Ni), shroud outer surface, -50 mm, 11°	K
101	TFS 4/10	TC (NiCr/Ni), surface of fuel rod simulator 4, group 2, 650 mm	K
102	TFS 15/14	TC (NiCr/Ni), surface of fuel rod simulator 15, group 5, 1050 mm	K
103	TFS 19/14	TC (NiCr/Ni), surface of fuel rod simulator 19, group 5, 1050 mm	K
104	TFS 11/14	TC (NiCr/Ni), surface of fuel rod simulator 11, group 4, 1050 mm	K
105	TFS 7/14	TC (NiCr/Ni), surface of fuel rod simulator 7, group 3, 1050 mm	K
106	TFS 2/14	TC (NiCr/Ni), surface of fuel rod simulator 2, group 2, 1050 mm	K
107	TFS 4/14	TC (NiCr/Ni), surface of fuel rod simulator 4, group 2, 1050 mm	K
108	TFS 15/9	TC (NiCr/Ni), surface of fuel rod simulator 15, group 5, 550 mm	K
109	TFS 11/9	TC (NiCr/Ni), surface of fuel rod simulator 11, group 4, 550 mm	K
110	TFS 7/9	TC (NiCr/Ni), surface of fuel rod simulator 7, group 3, 550 mm	K
111	TFS 4/9	TC (NiCr/Ni), surface of fuel rod simulator 4, group 2, 550 mm	K
112	TFS 15/15	TC (NiCr/Ni), surface of fuel rod simulator 15, group 5, 1150 mm	K
113	TFS 19/15	TC (NiCr/Ni), surface of fuel rod simulator 19, group 5, 1150 mm	K
114	TFS 11/15	TC (NiCr/Ni), surface of fuel rod simulator 11, group 4, 1150 mm	K

Chan	Desig-nation	Instrument, location	Unit
115	TFS 7/15	TC (NiCr/Ni), surface of fuel rod simulator 7, group 3, 1150 mm	K
116	TFS 2/15	TC (NiCr/Ni), surface of fuel rod simulator 2, group 2, 1150 mm	K
117	TFS 4/15	TC (NiCr/Ni), surface of fuel rod simulator 4, group 2, 1150 mm	K
118	TFS 11/8	TC (NiCr/Ni), surface of fuel rod simulator 11, group 4, 450 mm	K
119	TFS 7/8	TC (NiCr/Ni), surface of fuel rod simulator 7, group 3, 450 mm	K
120	TFS 4/8	TC (NiCr/Ni), surface of fuel rod simulator 4 group 2, 450 mm	K
121	TFS 11/16	TC (NiCr/Ni), surface of fuel rod simulator 11, group 4, 1250 mm	K
122	TFS 7/16	TC (NiCr/Ni), surface of fuel rod simulator 7, group 3, 1250 mm	K
123	T 601	Temperature off-gas, 2660 mm from test section outlet (flange)	K
124	TFS 11/7	TC (NiCr/Ni), surface of fuel rod simulator 11, group 4, 350 mm	K
125	TFS 7/12i	TC (NiCr/Ni), surface of fuel rod simulator 7, group 3, 850 mm, near to rod #1	K
126	TFS 7/7	TC (NiCr/Ni), surface of fuel rod simulator 7, group 3, 350 mm	K
127	TFS 4/7	TC (NiCr/Ni), surface of fuel rod simulator 4, group 2, 350 mm	K
128	T 104	Temperature quench water	K
129	T 201	Temperature steam generator heating pipe	K
130	TIT C/12	TC (NiCr/Ni), center line of corner rod C, 850 mm	K
131	T 205	Temperature upstream steam flow instrument location 10 g/s	K
132	T 301A	Temperature downstream superheater	K
133	T 302	Temperature superheater heating pipe	K
134	T 303	Temperature upstream total flow instrument location	K
135	T 401	Temperature upstream Ar flow instrument (orifice) location	K
136	T 403	Temperature of Ar at inlet cooling jacket	K
137	T 404	Temperature of Ar at outlet cooling jacket	K
138	T 501	Temperature in containment (near from bundle head)	K
139	TFS 7/6	TC (NiCr/Ni), surface of fuel rod simulator 7, group 3, 250 mm	K
140	TFS 4/6	TC (NiCr/Ni), surface of fuel rod simulator 4, group 2, 250 mm	K
141	TFS 7/17	TC (NiCr/Ni), surface of fuel rod simulator 7, group 3, 1350 mm	K
142	TFS 7/5	TC (NiCr/Ni), surface of fuel rod simulator 7, group 3, 150 mm	K
143	TFS 7/4	TC (NiCr/Ni), surface of fuel rod simulator 7, group 3, 50 mm	K
144	TFS 7/3	TC (NiCr/Ni), surface of fuel rod simulator 7, group 3, -50 mm	K

Chan	Desig-nation	Instrument, location	Unit
145	TFS 7/2	TC (NiCr/Ni), surface of fuel rod simulator 7, group 3, -150 mm	K
146	TFS 7/1	TC (NiCr/Ni), surface of fuel rod simulator 7, group 3, -250 mm	K
147	TFS 7/13i	TC (NiCr/Ni), surface of fuel rod simulator 7, group 3, 950 mm, near to rod #1	K
148	T 511	Gas temperature at bundle inlet	K
149	TIT D/11	TC (NiCr/Ni), center line of corner rod D, 750 mm	K
150	TIT A/13	TC (NiCr/Ni), center line of corner rod A, 950 mm	K
151	*Ref. T02*	*Temperature of measuring crate 2 (reference temperature)*	K
152	P 201	Pressure steam generator	bar
153	P 204	Pressure at steam flow instrument location 50 g/s	bar
154	P 205	Pressure at steam flow instrument location 10 g/s	bar
155	P 303	Pressure upstream total flow instrument (orifice) location	bar
156	P 401	Pressure upstream gas flow instrument location	bar
157	P 511	Pressure at bundle inlet, L501 low leg	bar
158	P 512	Pressure at bundle outlet	bar
159	P 601	Pressure upstream off-gas flow instrument (orifice) F 601	bar
160	P 901	Pressure at bundle inlet, L501 upper leg	bar
161	L 201	Liquid level steam generator	mm
162	L 501	Liquid level quench water	mm
163	L 701	Liquid level condensation vessel	mm
164	Fm 401	Argon (carrier gas) mass flow rate (Bronkhorst device)	g/s
165	P 411	Reserve (Pressure Kr supply for heated rods)	bar
166	P 403	Pressure Ar cooling of cooling jacket	bar
167	P 406	Pressure insulation shroud/cooling jacket	bar
168	Fm 104	Flow rate quench water	g/s
169	Fm 204	Flow rate steam (flow control up to 50 g/s)	g/s
170	Fm 205	Flow rate steam (flow control up to 10 g/s)	g/s
171	F 303	Flow rate at bundle inlet (steam + argon), orifice	mbar
172	F 401	Argon (carrier gas) volumetric flow rate	Nm³/h
173	Fm 403	Mass flow rate of cooling gas (Ar)	g/s
174	F 601	Flow rate off-gas (orifice), 2000 mm from test section outlet (flange)	mbar

Chan	Desig-nation	Instrument, location	Unit
175	Fm 406	Flow rate argon into room between shroud and cooling jacket	g/s
176	E 201	Electric current steam generator	A
177	E 301	Electric current superheater	A
178	E 501	Electric current of left group of fuel rod simulators	A
179	E 502	Electric current of right group of fuel rod simulators	A
180	E 503	Electric voltage of left group of fuel rod simulators	V
181	E 504	Electric voltage of right group of fuel rod simulators	V
182	Hub_V302	Gas supply valve lift	%
183	*Ref. T03*	*Temperature of buffer amplifier (reference temperature)*	K
184…..199		Binary inputs	
200…..215		Analog outputs	
250	E 505	Electric power inner ring of fuel rod simulators	W
251	E 506	Electric power outer ring of fuel rod simulators	W
252	EP	Gross electrical power	kW

Indications:

TFS - TC at the rod surface;

TIT - TC at the inside of corner rods;

TSH - TC at outer surface of shroud.

Groups of the rods for modeling:

central groups

group 1: rod 1;

group 2: rods 2, 4, 6, 8;

group 3: rods 3, 5, 7, 9;

peripherical groups

group 4: rods 11, 14, 17, 20;

group 5: rods 10, 12, 13, 15, 16, 18, 19, 21.

Table 8 QUENCH-L5; Rod thermocouple positions

Elevation, mm	-250	-150	-50	50	150	250	350	450	550	650	750	850	950	1050	1150	1250	1350
Rod/Elevation	1	2	3	4	5	6	7	8	9	10	11	12	13	14	15	16	17
1																	
2										X	X	X	X	X	X		
3																	
4						X	X	X	X	X	X	X	X	X	X		
5																	
6																	
7	X	X	X	X	X	X	X	X	X	X	X	X, Xi	X, Xi	X	X	X	X
8																	
9																	
10																	
11							X	X	X	X	X	X	X	X	X	X	
12																	
13																	
14																	
15										X	X	X	X	X	X		
16																	
17																	
18																	
19										X	X	X	X	X	X		
20																	
21																	
No. per elevation	1	1	1	1	1	2	3	3	4	6	6	6+1	6+1	6	6	2	2

TFS (rod surface, shroud direction), indicated as **X** in table above	**56**
TFS (rod surface, central rod direction), indicated as **Xi** in table above	**2**
TIT (inside corner rods)	*3*
TSH (outer shroud surface)	*13*

← TCs to bundle bottom | TCs to bundle top →
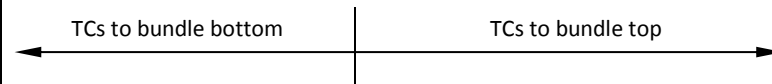
Table 9   QUENCH-L5; Sequence of events

Time [s]	Event
-1503 (10:26:24; 10.02.2016)	Start data recording, Tmax = TFS 7/13i = 789 K, el. power at 3.24 kW. L 701 = 1245 mm. L 501 = -404 mm. System pressure 3 bar. Hot Ar 6 g/s (heated in superheater), superheated steam 2 g/s.
-1503… -386	Pressurization of rods from 35 to 55 bar.
0	Start of transient with max electrical power increase rate.
3.6; 27; 54	Electrical power 39.4; 55; 60 kW.
40…60	**Sequential onset of ballooning from inner rod #1 to peripheral rod #18.**
50.6…73	**Sequential onset of burst for rods from inner rod #1 to peripheral rod #18.** See burst table (Table 11).
74…75.6	Reduction of the electrical power from max 59.7 kW to decay heat of 3.5 kW. Initiation of rapid steam supply line (20 g/s) additionally to carrier argon (6 g/s). Switch-off of slow steam supply (2 g/s). Tmax = TFS 7/12i = 1205 K.
82	Cladding surface temperature maximum reached. Maximal hydrogen production rate. **Tmax = TFS 7/13i = 1257 K.**
82…209	*Cool-down* of bundle in steam. Decrease of TFS 4/13 reading from 1257 K to 930 K.
209…213.8	Increase of maximal bundle temperatures to TFS 4/13≈953 K due to switch-off of the steam cooling.
213.8	Initiation of *quench* water supply. Switch of argon to bundle top supply.
236.6	Maximal quench rate (about 100 g/s) reached.
238…286	Wetting of cladding surface thermocouples (TFS) at elevations between -250 and 1350 mm at temperatures between 523 K (TFS 7/1; -250 mm) and 822 K (TFS 19/12; 850 mm). (Table 10).
257…296	Maximal water evaporation rate (25…30 g/s). Collapsed water front at 124…… 860 mm.
367	Bundle completely filled with water (L 501 = 1307 mm).
491	Electrical power switched off. Tmax = TFS 19/15 = 317 K.
683.2	End of data recording.

Table 10   QUENCH-L5; Wetting of TFS thermocouples

Bundle elevation, mm	Wetting time, s	Collapsed water front on wetting, mm
-250	238	-250
-150	242.4	-250
-50	247.6	-100
50	248	-90
150	254.8	55
250	255..256.4	85
350	256.8..257.6	112
450	257.8..260.2	205
550	259.2..260.4	205
650	263..270.8	320
750	263.2..275.4	235..486
850	263..277	235..520
950	270..284.8	380..630
1050	261.4...286.8	300..682
1150	279..285.6	550..660
1250	278.2..284.4	540..638
1350	259.6*	190

* Condensation of stagnant steam inside the bundle head due to injection of cold Argon.

Table 11 QUENCH-L5; Burst parameters

rod	burst time, s	interpolated burst T, K	burst azimuth. position, °	burst middle elev., mm	max burst width, mm	burst length, mm	burst area, mm²
1	**50.6**	**1057**	244	938	3.4	12	24
2	**53.4**	**1056**	231	942	4.4	15.5	35
3	**54.4**	**1100**	127	953	3.3	13	23
4	**52**	**1068**	236	913	3.9	14.5	29
5	**54.2**	**1080**	203	894	3.0	13	21
6	**52.4**	**1063**	232	946	3.6	14	27
7	**56.2**	**1077**	196	935	4.9	17.5	46
8	**52.6**	**1041**	147	902	3.2	13	21
9	**56**	**1040**	237	931	3.9	13.5	28
10	67.4	1121	108	952	4.0	14	31
11	69.8	1134	160	879	3.7	14	27
12	69	1126	175	939	4.9	18	52
13	65.2	1106	180	894	2.7	13	19
14	64.2	1100	212	901	2.8	13	20
15	*58.2*	1064	182	939	4.6	18	40
16	70.4	1151 (Max)	237	940	3.1	14	24
17	68.6	1096	265	941	4.5	16	41
18	73	1119	228	934	4.1	14.5	34
19	68	1027 (Min)	280	890	3.5	14.5	29
20	67	1047	99	870	3.6	14	29
21	70.6	1028	317	1002	3.8	12	28
average		*1081*		*926*	*3.8*	*14.3*	*30*
standard deviation		*±36*		*±31*	*±0.6*	*±1.8*	*±8.7*

Table 12 Burst time and temperature of all rods for the experiments: QL3 (left) and QL5 (right).

Rod group	Rod #	Burst time, s	Burst temperature, interpolated, K
Inner rods	1	47.8	1103
	2	51.6	1140
	3	53	1111
	4	55	1108
	5	52	1109
	6	51.8	1112
	7	53.6	1124
	8	49.6	1107
	9	53.2	1132
Outer rods	10	68	1188 (Max)
	11	65.6	1126
	12	65.8	1175
	13	61.8	1138
	14	59.4	1124
	15	*54.4*	1105
	16	62	1142
	17	60	1094
	18	63	1114
	19	66.2	1073
	20	64	1064 (Min)
	21	67.2	1073
QL3: average burst T: 1117 ± 30 K = 844 ± 30 °C			

Rod group	Rod #	Burst time, s	Burst temperature, interpolated, K
Inner rods	1	50.6	1057
	2	53.4	1056
	3	54.4	1100
	4	52	1068
	5	54.2	1080
	6	52.4	1063
	7	56.2	1077
	8	52.6	1041
	9	56	1040
Outer rods	10	67.4	1121
	11	69.8	1134
	12	69	1126
	13	65.2	1106
	14	64.2	1100
	15	*58.2*	1064
	16	70.4	1151 (Max)
	17	68.6	1096
	18	73	1119
	19	68	1027 (Min)
	20	67	1047
	21	70.6	1028
QL5: average burst T: 1081 ± 36 K = 808 ± 36 °C			

Table 13   Burst geometrical parameters: QL3 (left) and QL5 (right).

rod group	rod	max burst width, mm	burst length, mm	burst area, mm²
Inner rods	1	4.7	16	36
	2	3.2	11.5	21
	3	4.6	15	37
	4	3.9	12	26
	5	4.8	18	44
	6	6.2	20	67
	7	4.6	14	36
	8	2.9	12	20
	9	4.7	16	43
Outer rods	10	3.4	13	24
	11	4.1	14.5	33
	12	3.3	14	24
	13	2.7	12	18
	14	3.6	15	27
	15	3.3	13.5	24
	16	3.9	15	29
	17	3.6	14	28
	18	2.6	12.5	17
	19	2.8	12	18
	20	4.5	15.5	39
	21	4.1	17.5	40

QL3 average sizes of burst openings: **width 3.9 ± 0.9 mm;**
length 14.4 ± 2.2 mm;   area: 31.0 ± 12 mm²

rod group	rod	max burst width, mm	burst length, mm	burst area, mm²
Inner rods	1	3.4	12	24
	2	4.4	15.5	35
	3	3.3	13	23
	4	3.9	14.5	29
	5	3.0	13	21
	6	3.6	14	27
	7	4.9	17.5	46
	8	3.2	13	21
	9	3.9	13.5	28
Outer rods	10	4.0	14	31
	11	3.7	14	27
	12	4.9	18	52
	13	2.7	13	19
	14	2.8	13	20
	15	4.6	18	40
	16	3.1	14	24
	17	4.5	16	41
	18	4.1	14.5	34
	19	3.5	14.5	29
	20	3.6	14	29
	21	3.8	12	28

QL5 average sizes of burst openings: **width 3.8 ± 0.6 mm;**
length 14.3 ± 1.8 mm;   area: 30.0 ± 8.7 mm²

Table 14 QUENCH-L5; Strain parameters

rod group	rod #	elevation of burst *middle,* mm	max strain %	max outer diameter, mm	*at azimuth* °	min outer diameter, mm	*at azimuth* °
central group	1	938	23	14.17	50	12.40	150
	2	942	29	15.00	30	12.83	137
	3	953	23	14.27	112	12.37	35
	4	913	25	14.57	36	12.50	135
	5	894	22	14.07	44	12.38	125
	6	946	24	14.38	68	12.52	146
	7	935	32	15.64	45	12.97	118
	8	902	24	14.18	131	12.52	52
	9	931	29	14.89	41	12.94	149
peripherical group	10	952	28	14.89	91	12.64	11
	11	879	25	14.68	136	12.60	50
	12	939	31	15.11	13	12.94	84
	13	894	21	13.87	165	12.20	84
	14	901	22	14.12	14	12.27	110
	15	939	24	14.43	23	12.38	99
	16	940	24	14.34	69	12.36	150
	17	941	28	14.83	68	12.55	174
	18	934	30	15.28	69	12.85	150
	19	890	26	14.99	124	12.50	30
	20	870	27	15.04	72	12.72	162
	21	1002	33	15.56	159	13.22	66
Average		**926±31**	**26.2±3.5**	**14.7±0.5**		**12.6±0.3**	

Table 15 QUENCH-L5; Content of hydrogen in cladding (n^0-tomography): axial maximum averaged for cross section and axial absolute local maximum

rod #	C_H above burst opening (H-band), wppm		elevation, mm		C_H below burst opening (H-spot), wppm		elevation, mm	
	averaged	absolute	aver.	abs.	averaged	absolute	aver.	abs.
1	**390±5**	1335±25	**957**	965	**360±5**	1340±25	**909**	909
3	**345±5**	1300±25	**984**	984	**328±5**	1350±25	**930**	925
5	**238±5**	1240±25	**920**	922	**303±5**	1250±25	**873**	875
7	**327±5**	1202±25	**968**	965	**276±5**	1206±25	**918**	911
9	**285±10**	1250±30	**963**	962	**314±10**	1236±30	**902**	902
21	**293±10**	1154±120	**1016**	1017	**347±20**	1295±120	**978**	975

Table 16   QUENCH-L5; Results of tensile tests

rod	ultimate tensile strength [MPa]	fracture stress [MPa]	elongation at fracture [%]	rupture based on
01	566	566	5	stress concentration in opening middle
02	543	543	4.4	TC stress concentration (TFS 2/13)
03	547	422	6.9	fracture after necking
04	542	542	2.8	TC stress concentration (TFS 4/12)
05	570	442	7.1	fracture after necking
06	545	430	6.8	fracture after necking
07	541	540	4.8	stress concentration in opening middle
08	553	449	9	fracture after necking
09	561	442	7.8	fracture after necking
10	561	559	10.6	stress concentration at opening tips
11	533	531	4.3	stress concentration at opening tips
12	554	554	7.6	stress concentration at opening tips
13	548	546	5.1	stress concentration at opening tips
14	535	535	4.7	stress concentration at opening tips
15	521	521	3.3	stress concentration at opening tips
16	554	434	11.7	fracture after necking
17	557	428	12.3	fracture after necking
18	536	424	9.2	fracture after necking
19	517	510	4.9	stress concentration at opening tips
20	553	551	7.2	stress concentration at opening tips
21	553	552	7.9	stress concentration at opening tips
QL5 avrg stress	542±16	541±17	5.5±1.5	stress concentration
QL5 avrg necking	554±8	448±45	9.0±2.2	fracture after necking
QL3 avrg stress	514±10	501±22	9.2±2.1	stress concentration
QL3 avrg necking	521±5	385±8	11.0±2.6	fracture after necking
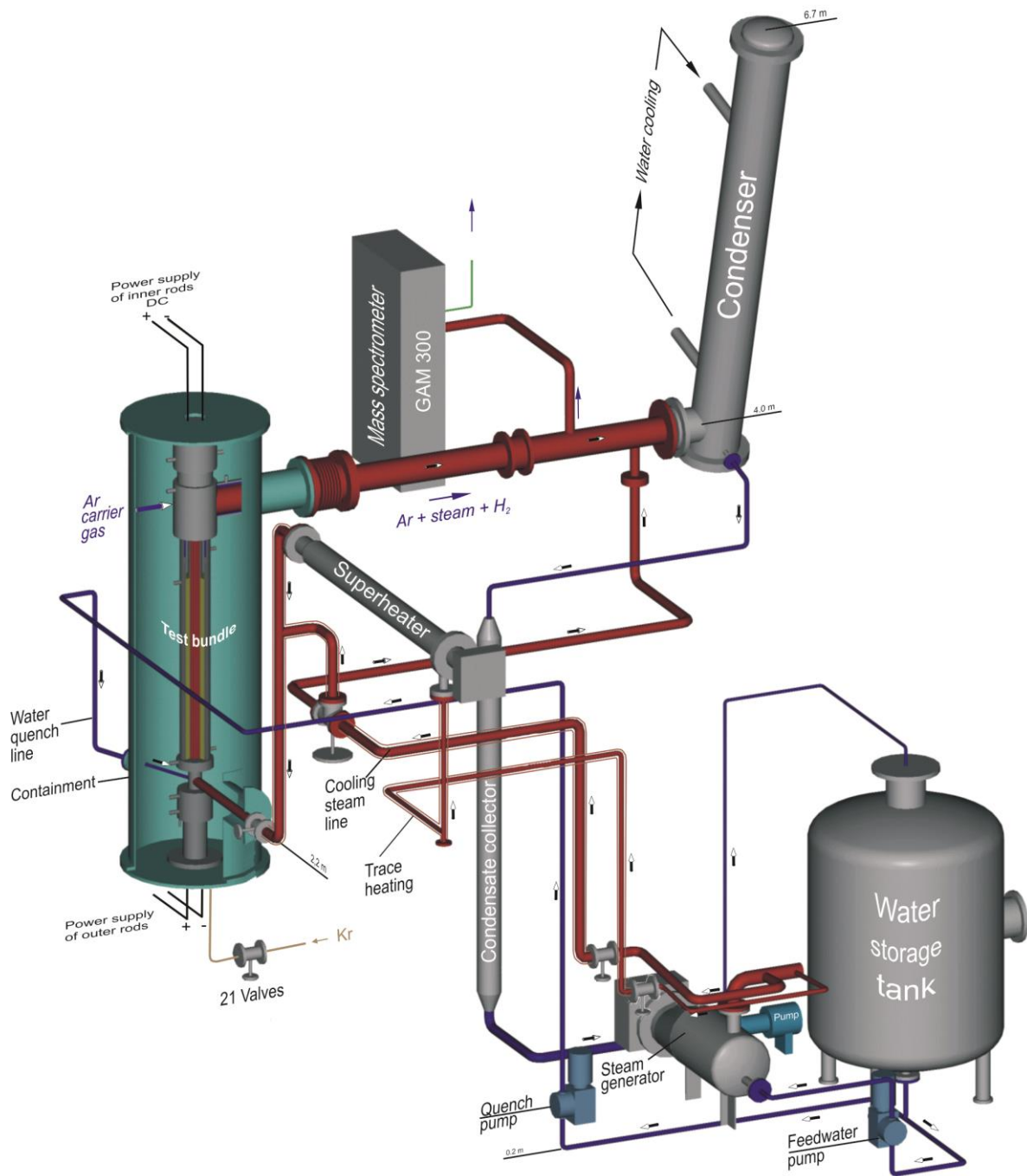
Figure 1   QUENCH Facility - Main components.
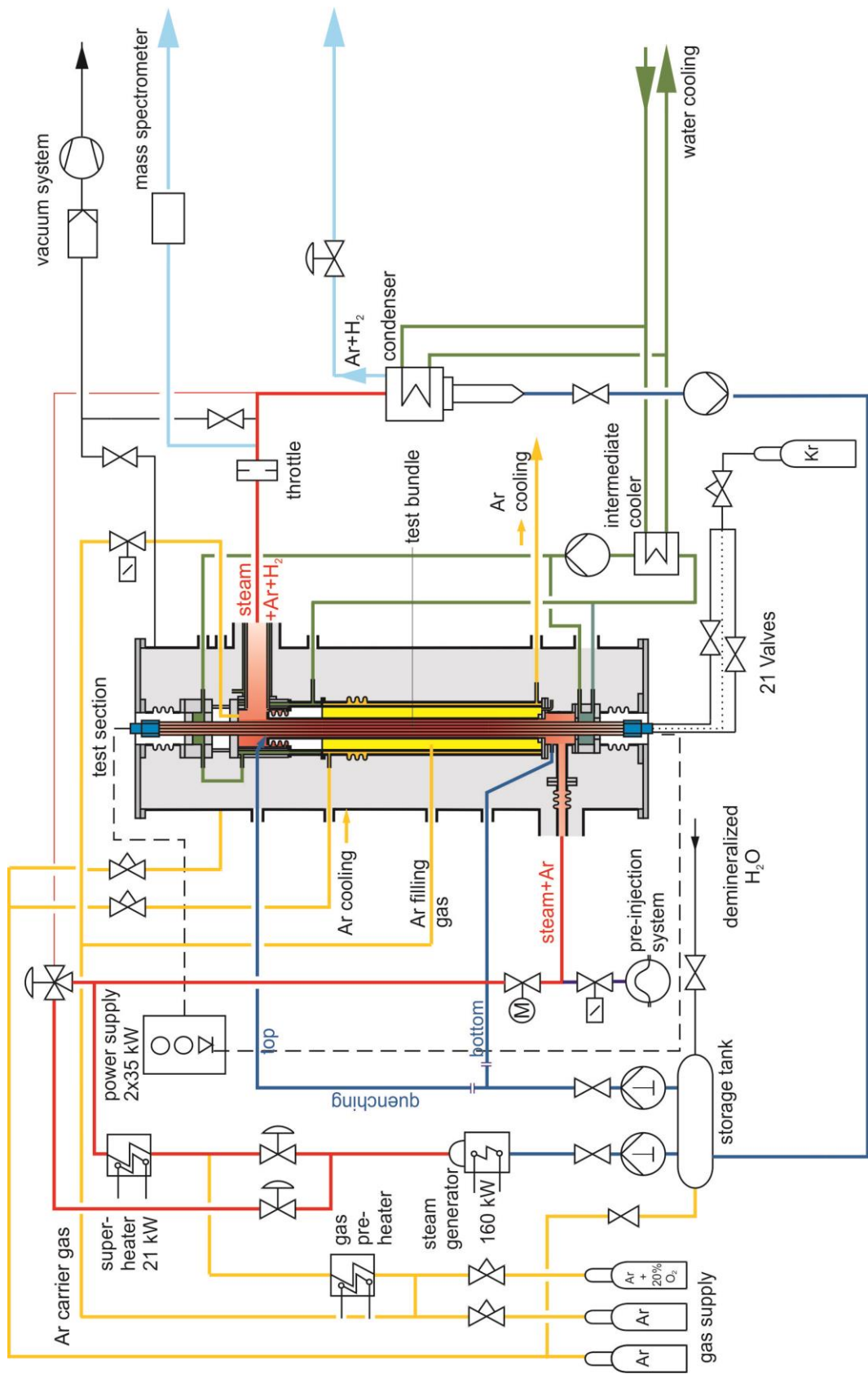
Figure 2 Flow diagram of the QUENCH test facility.
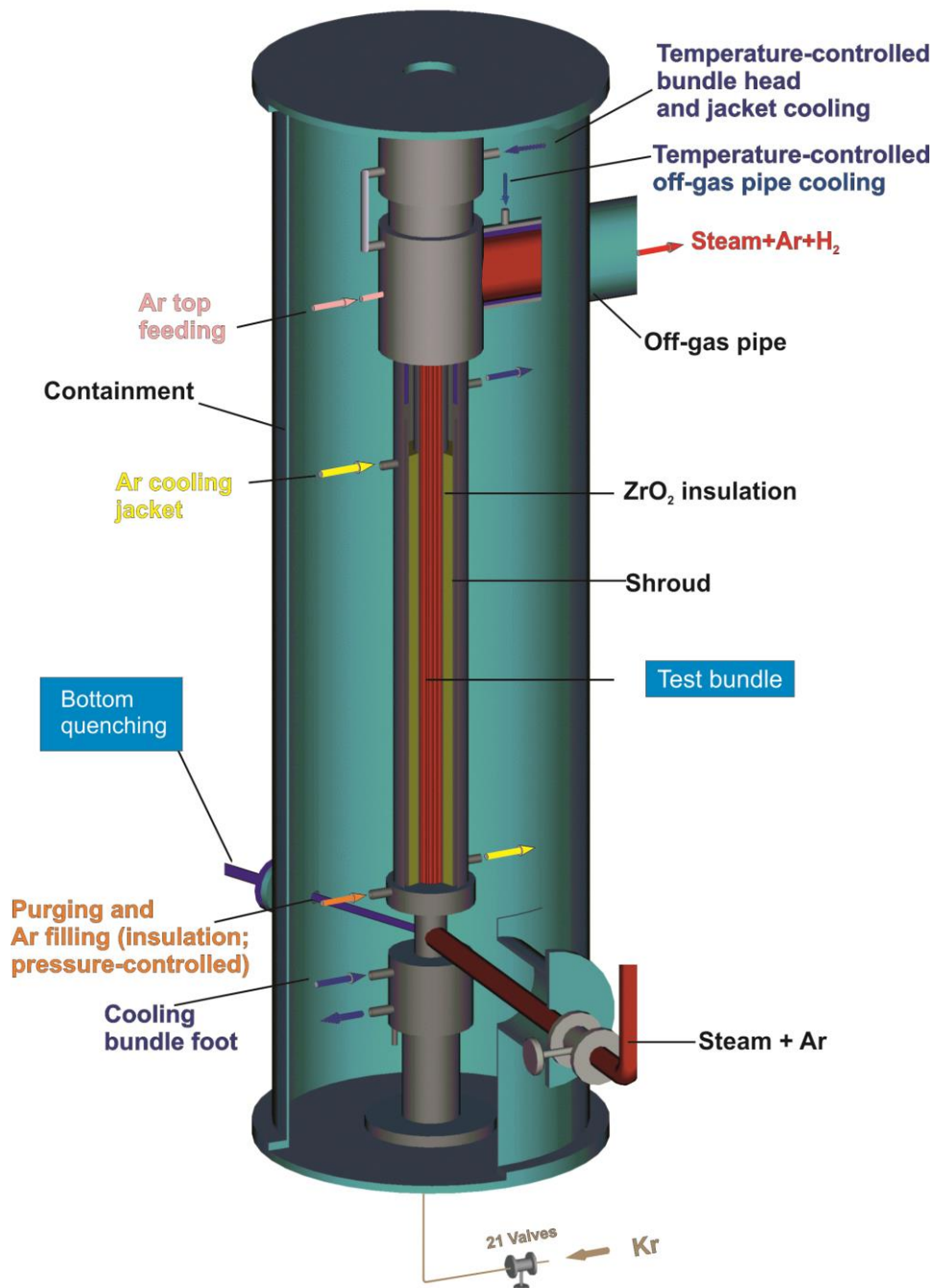
Figure 3   QUENCH Facility; Containment and test section.
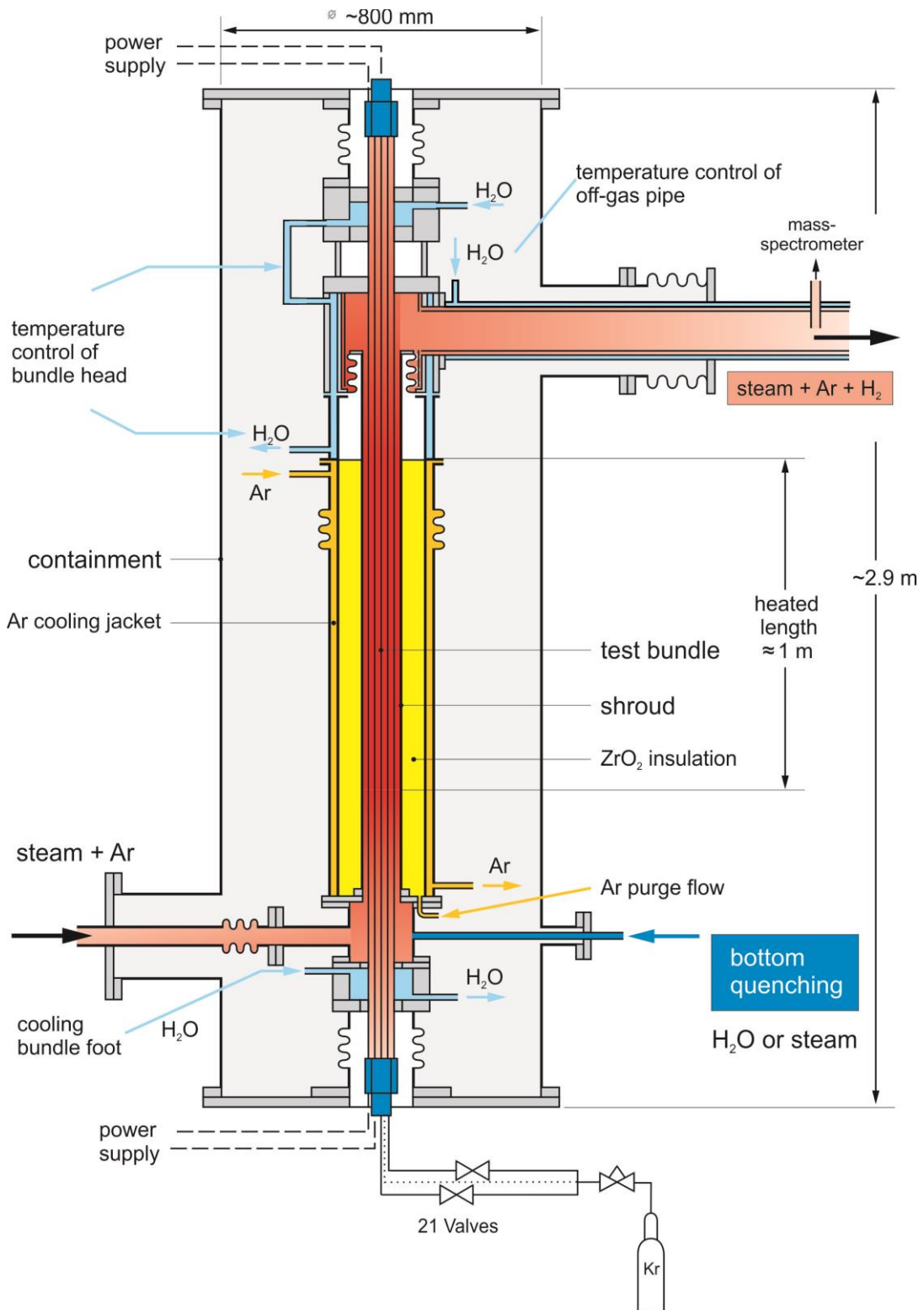
Figure 4   QUENCH-L5; Test section with flow lines.

S

0 ° Zr 702 shroud
Ø 79.66/86.0 mm

|14.3| Stainless steel tube
Ø181.7/193.7 mm

Inconel 600 tube
Ø158.3/168.3 mm

A 5 4 5 B

B:
Zry-4 rod
Ø6 mm
removable

5 3 2 3 5

O 270 ° 4 2 1 2 4 90 ° W

5 3 2 3 5

D 5 4 5 C

Heated rod
Ø 10.75 mm
(Tungsten heater,
ZrO$_2$ annular pellet,
hydrogenated optimized
ZIRLO cladding)

180 °
N

A,C,D:
Zry-4 rod (top),
Zry-4 tube (bottom)
Ø 6 mm, central TC

Ar cooling
gap 6.7 mm

ZrO$_2$ fiber
insulation
36 mm
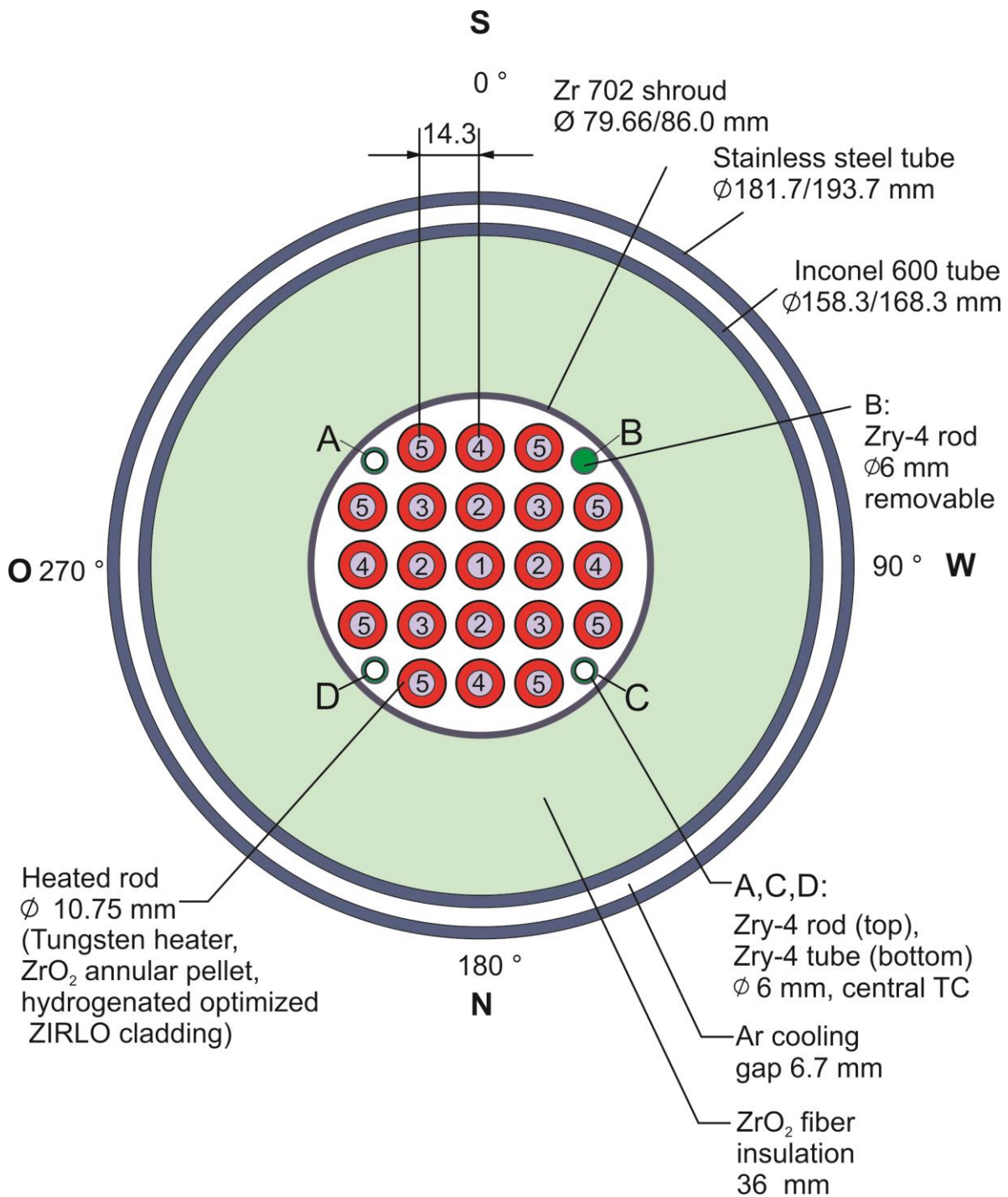
Figure 5   QUENCH-L5; Fuel rod simulator bundle (cross section, top view) including rod type indications corresponding to table "List of Instrumentation".
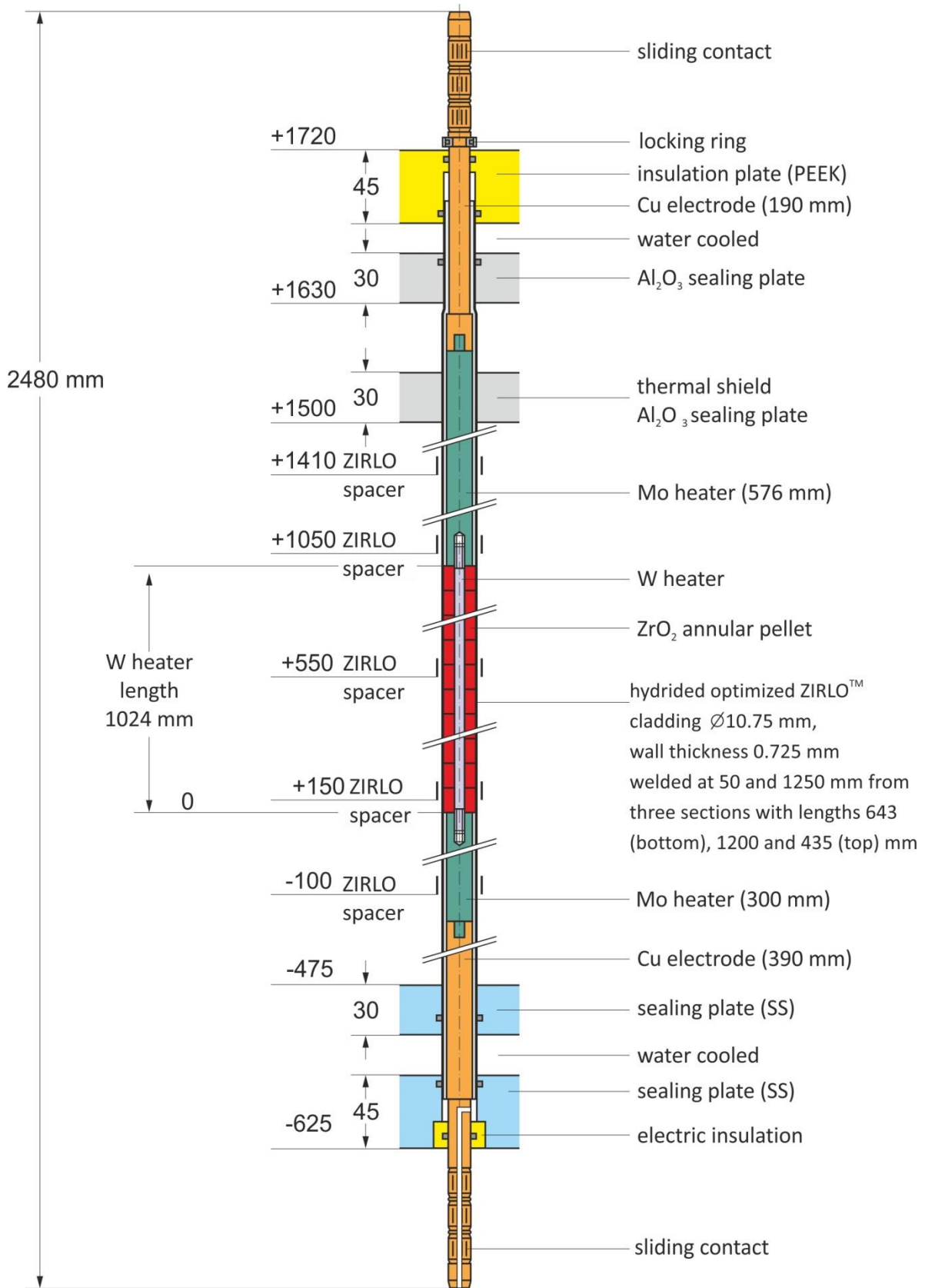
Figure 6   QUENCH-L5; Heated fuel rod simulator.
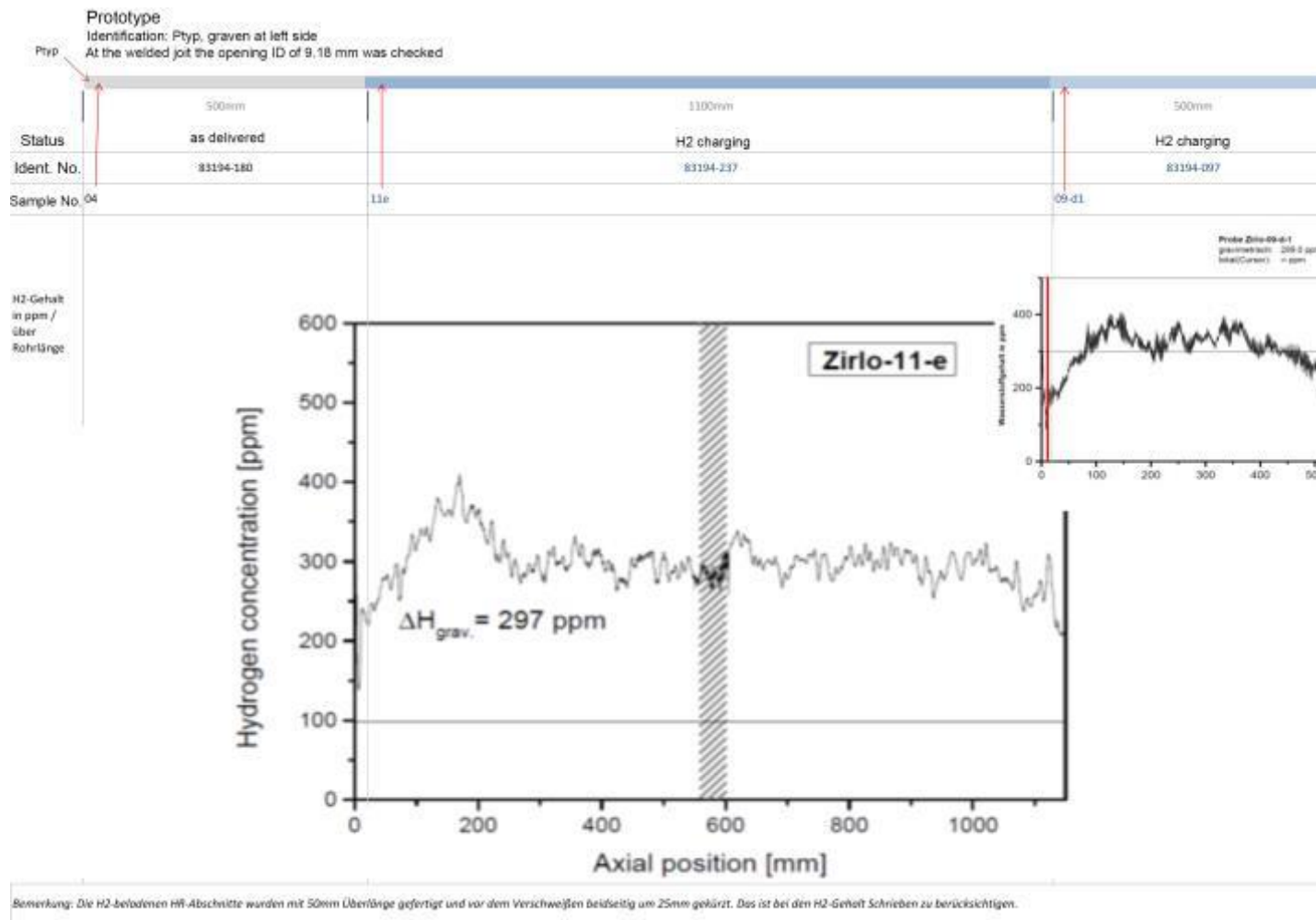
Figure 7 QUENCH-L5; scheme of prototype.
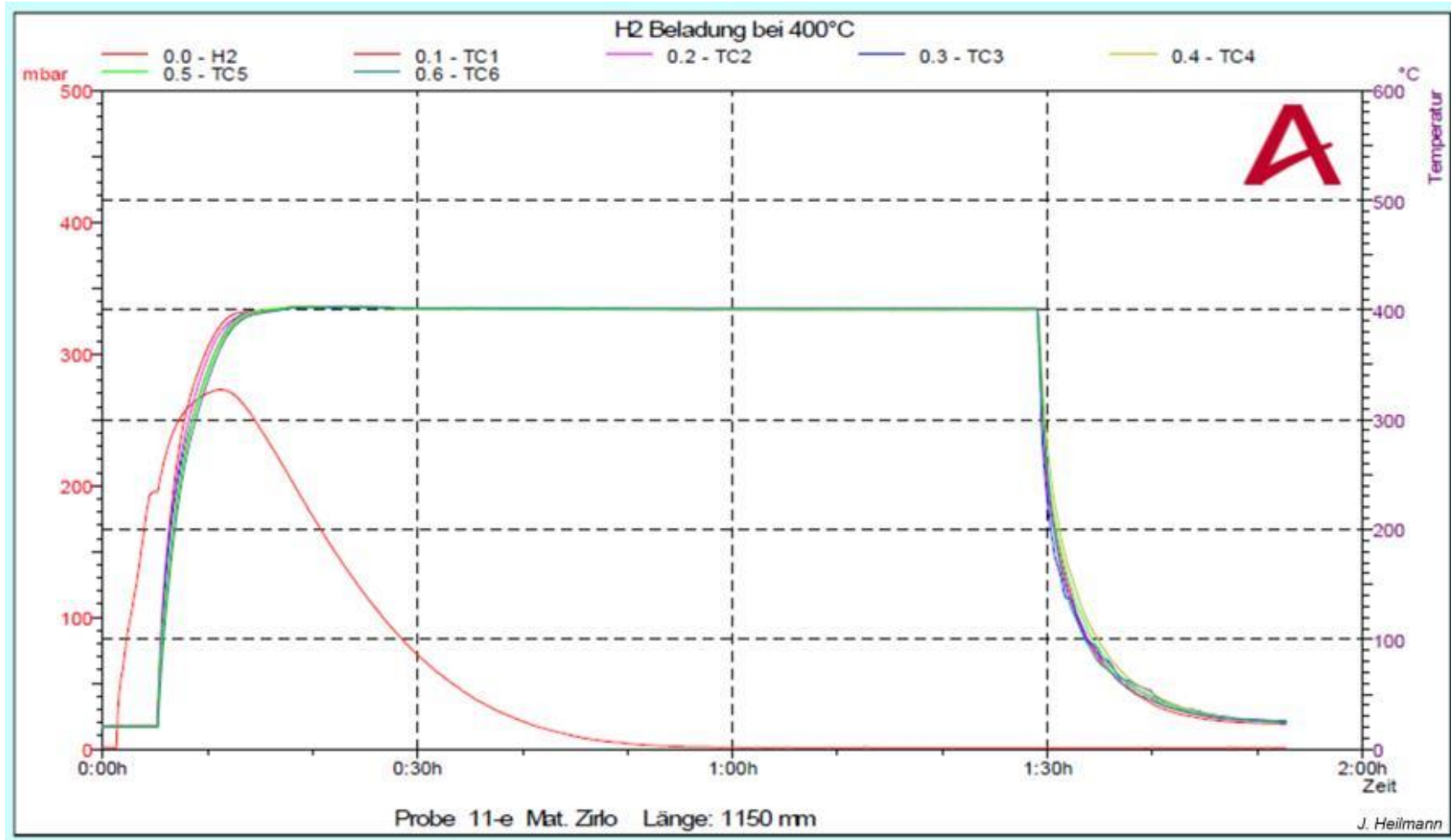
Figure 8   QUENCH-L5; parameters of hydrogen charging of the prototype central part.
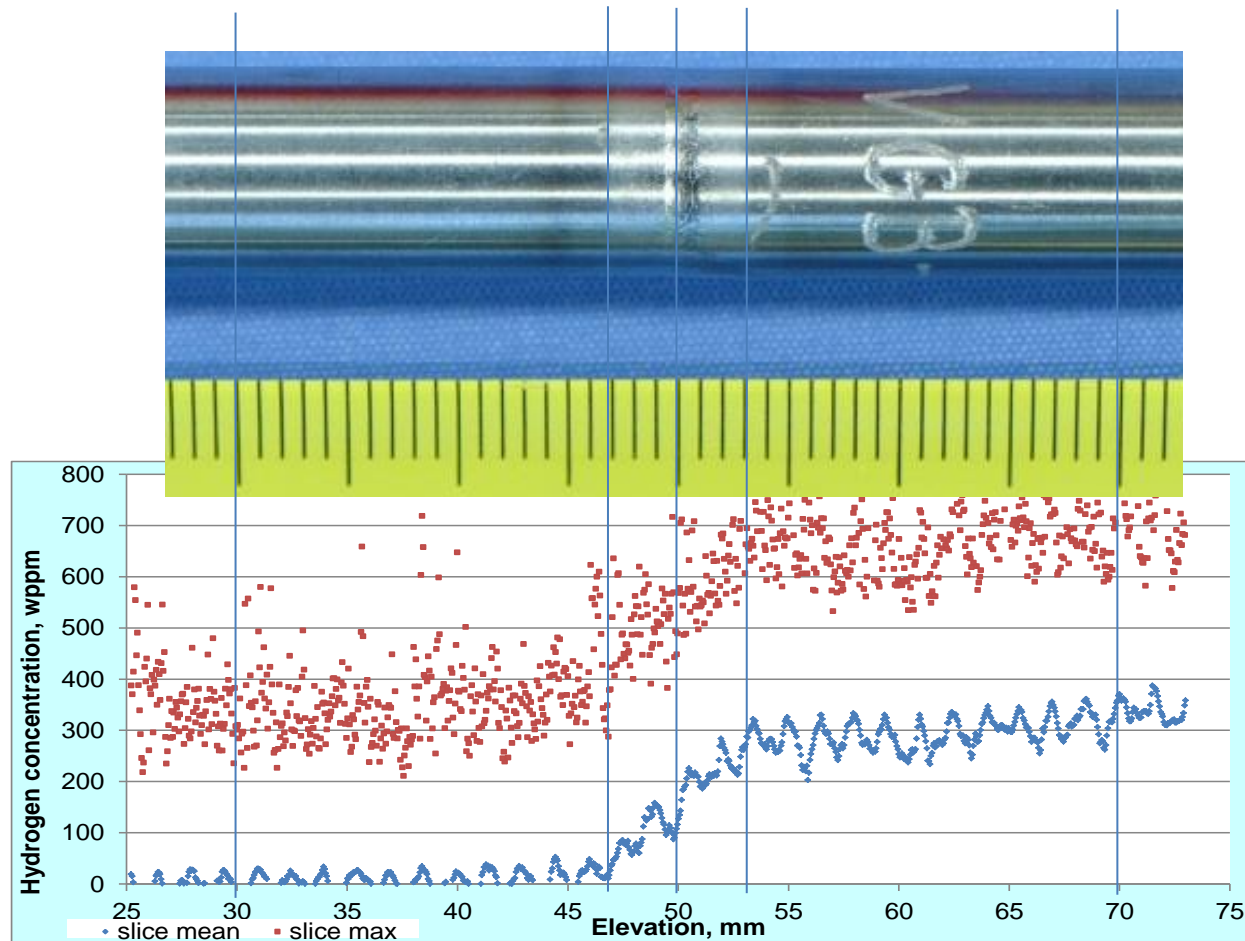
Figure 9 QUENCH-L5; axial distribution of hydrogen near to welded joint of the prototype sample: mean and maximal values determined by neutron tomography for each cross section slice of 47 μm width.

cladding cross section

middle of cladding

hydrides: 5% of area
to compare: QL4 with 100 wppm has 2%
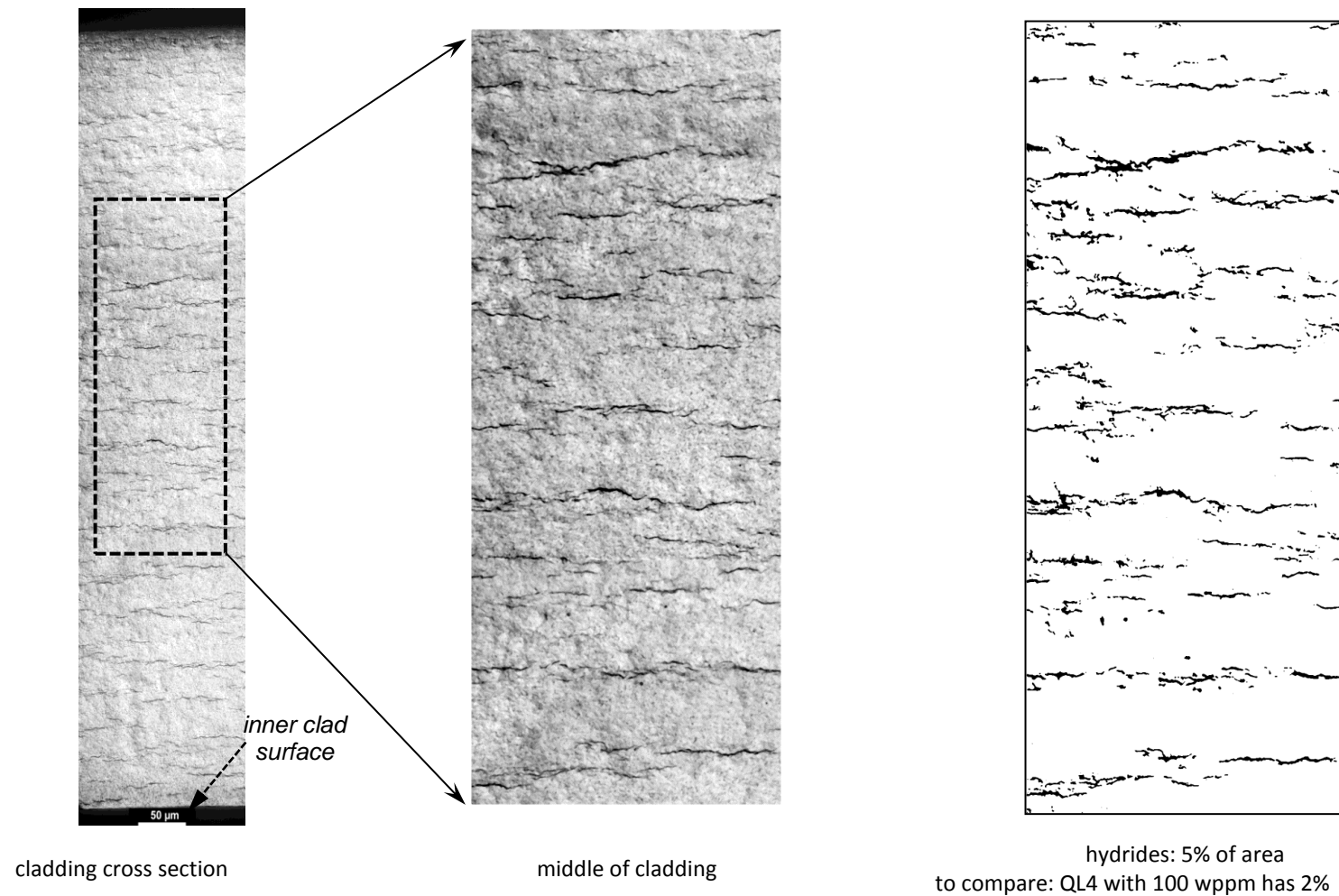
Figure 10   QUENCH-L5; hydrides inside the prototype cladding with 300 wppm H (as etched).
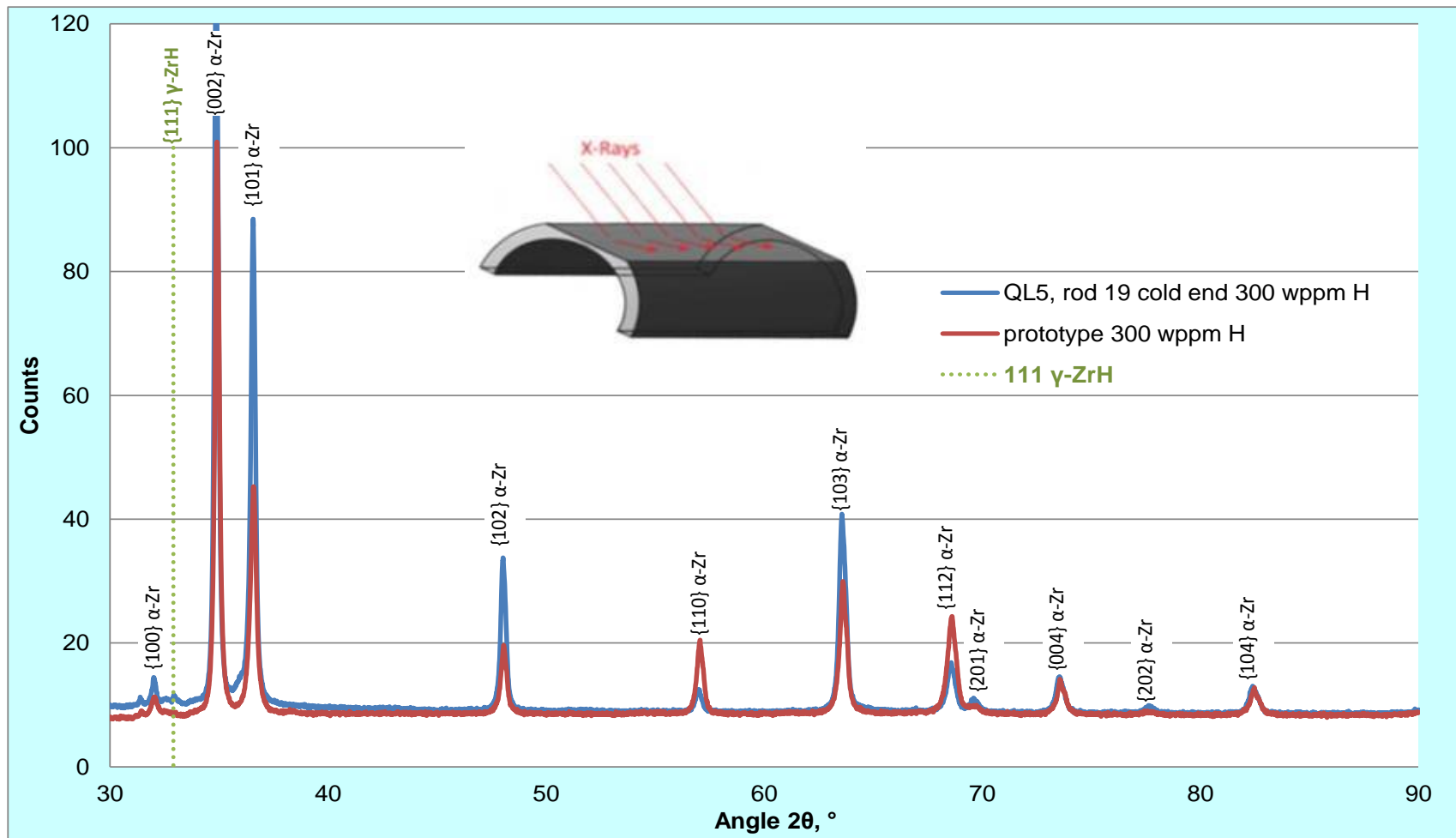
Figure 11 QUENCH-L5; XRD analysis of cladding parts with original hydriding of 300 wppm: indication of γ hydrides.
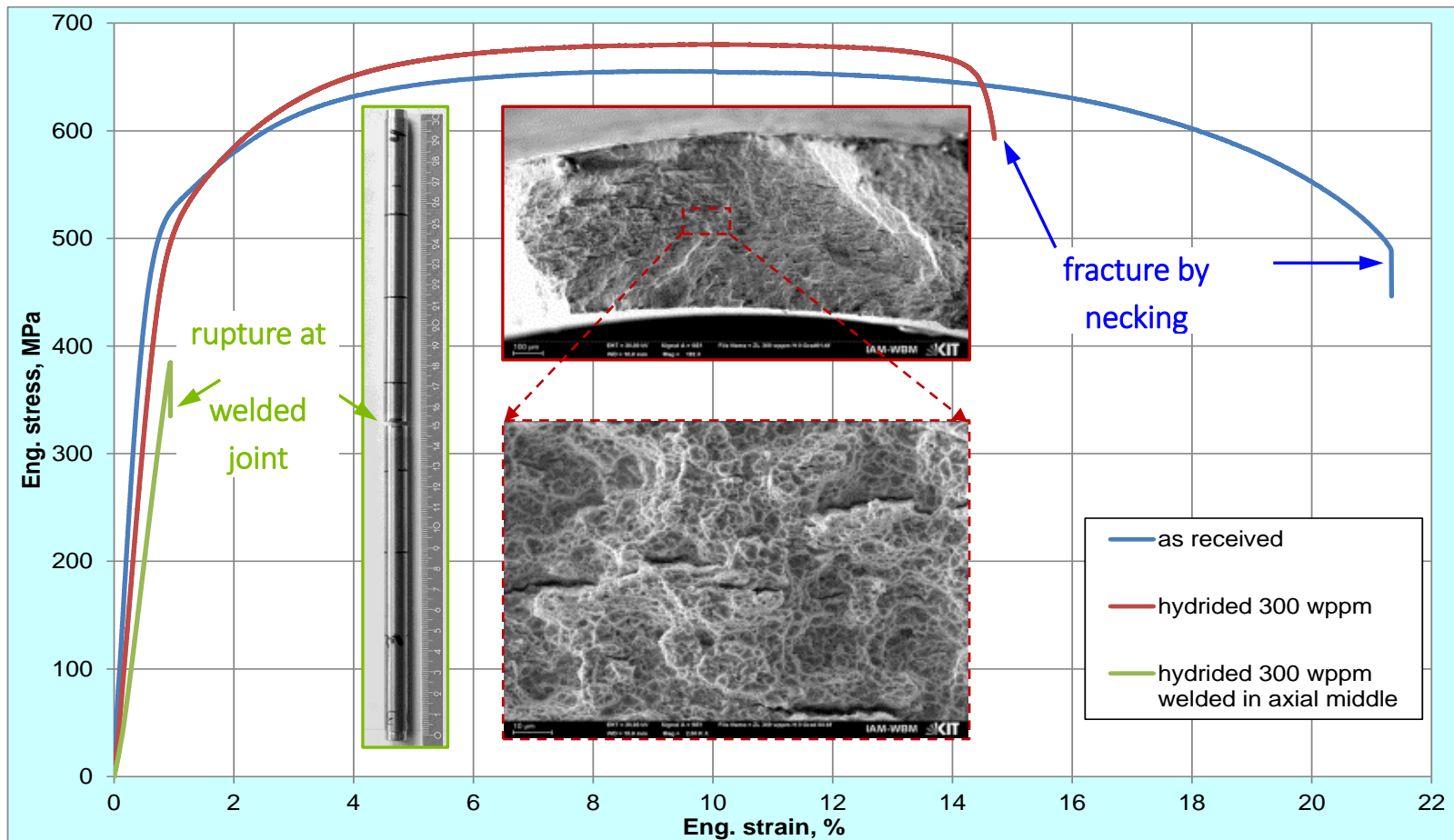
Figure 12 QUENCH-L5; tensile tests at room temperature with fresh and pre-hydrogenated opt. ZIRLO tubes (length 700 mm); fractography of pre-hydrogenated sample.
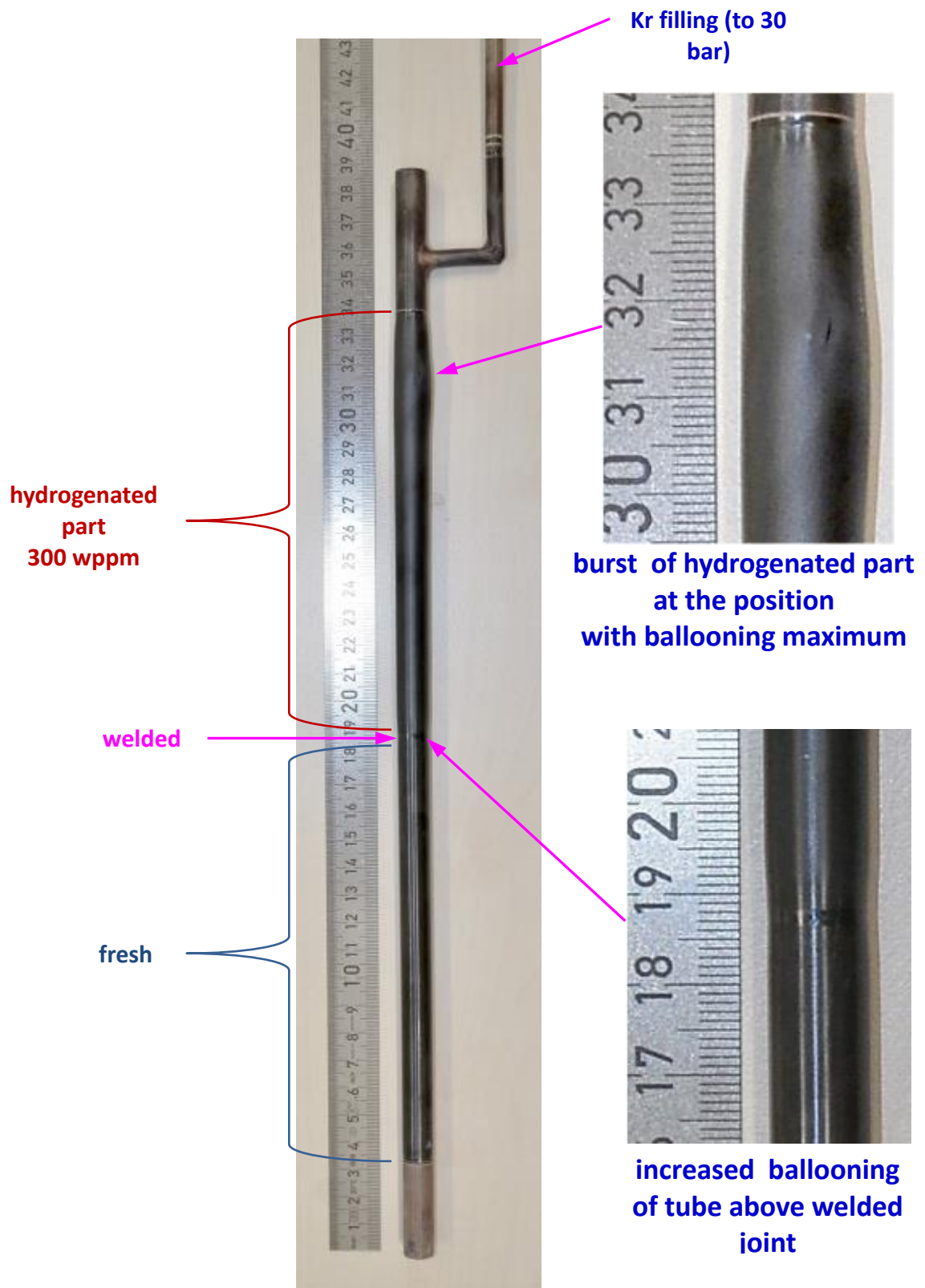
Figure 13 QUENCH-L5: ballooning of welded opt. ZIRLO prototype tube during heating in a tube furnace (10 K/min) from room temperature to burst temperature of 710 °C.

ZIRLO spacer
1410 mm

ZIRLO spacer
1050 mm

ZIRLO spacer
550 mm

ZIRLO spacer
150 mm

ZIRLO spacer
-100 mm

21 pre-hydrogenated tubes (300 wppm H),
each welded from 3 segments (645, 1200, 435 mm)

welded joints
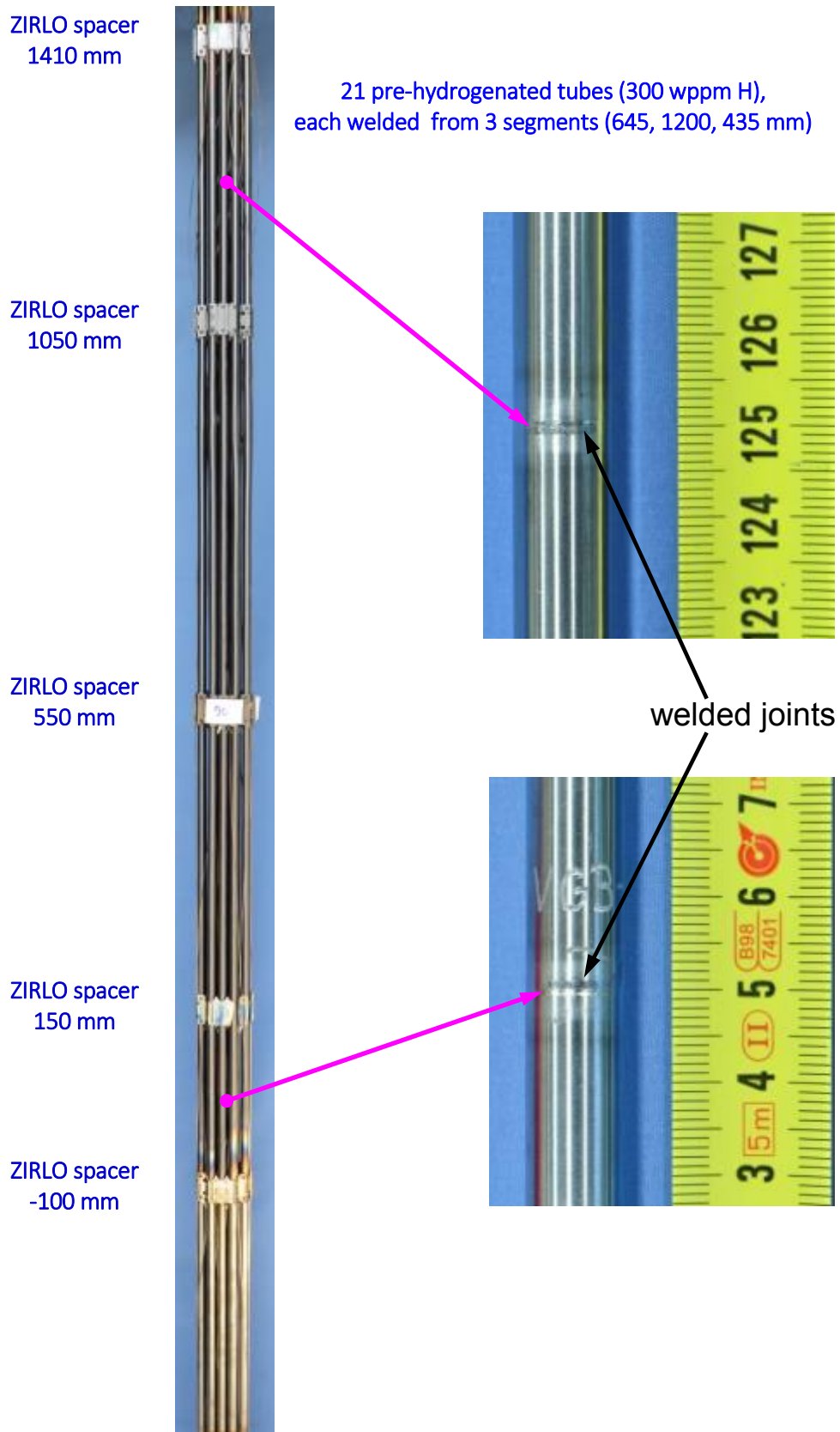
Figure 14 QUENCH-L5; Welding of pre-hydrogenated claddings.
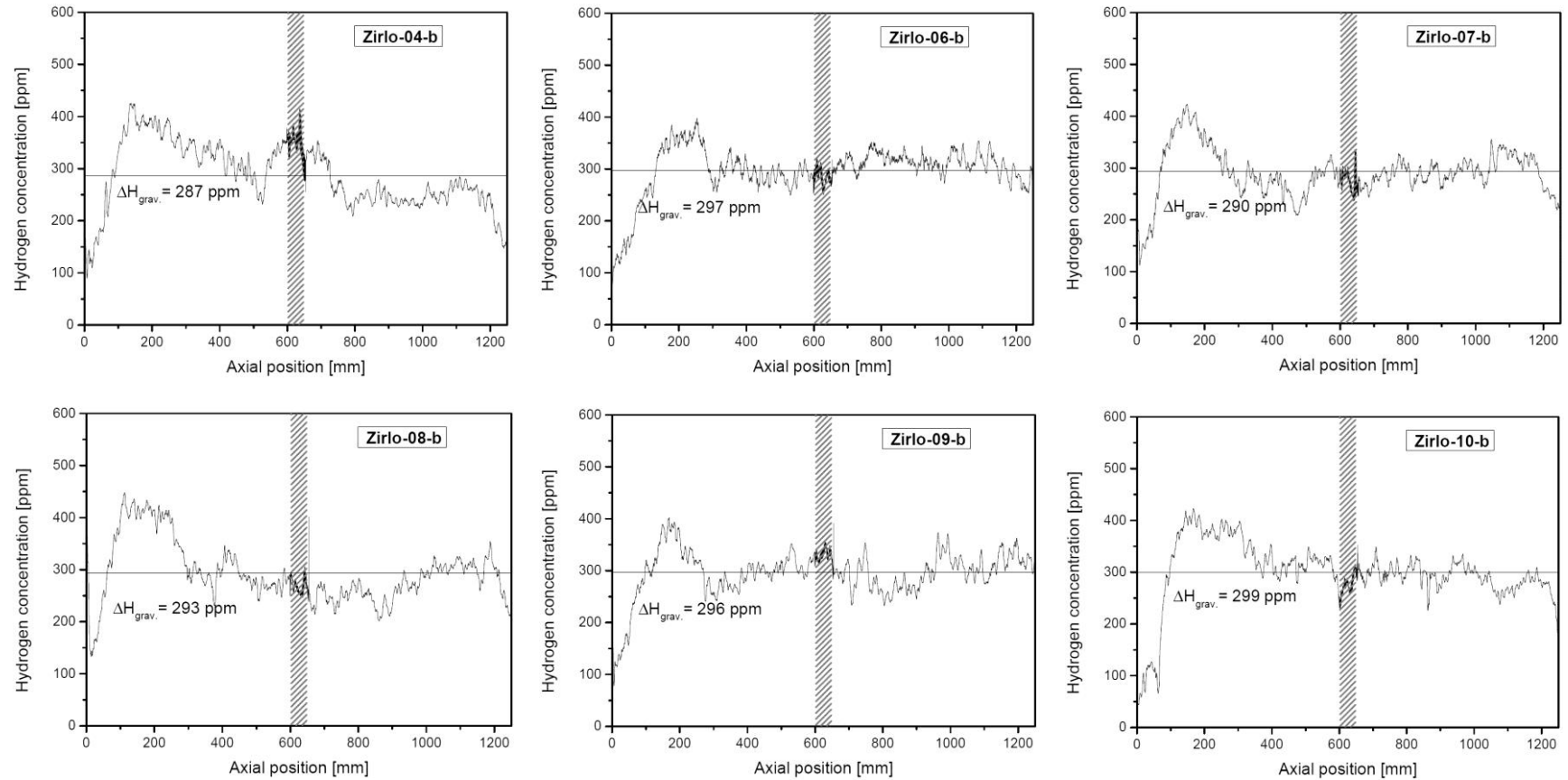
Figure 15   QUENCH-L5; axial distribution of hydrogen of pre-hydrogenated central part (50 – 1250 mm) of claddings #1 - #6 estimated by cladding diameter change. (Please note: sample numbers do not match the rod numbers).
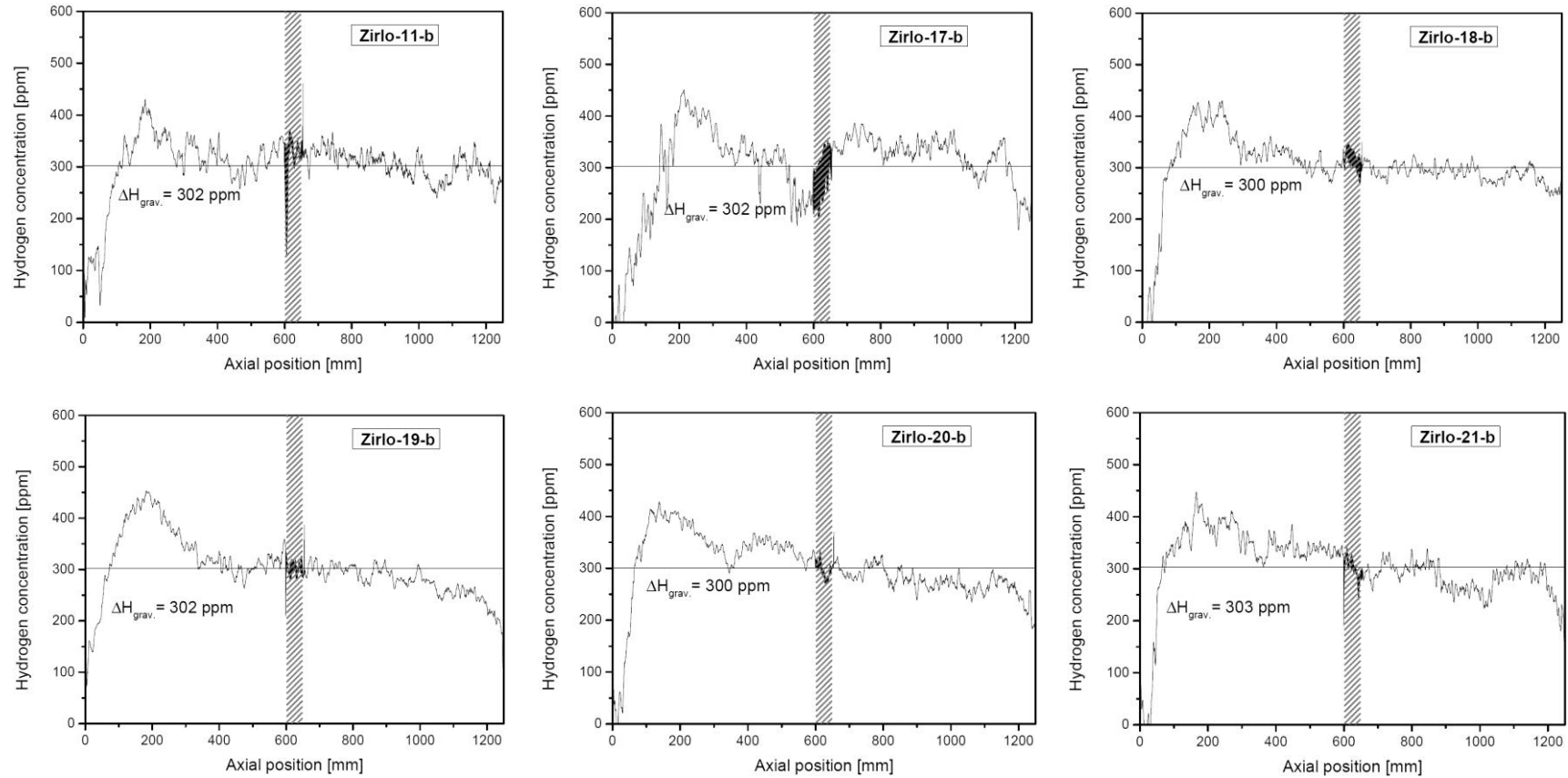
Figure 16   QUENCH-L5; axial distribution of hydrogen of pre-hydrogenated central part (50 – 1250 mm) of claddings #7 - #12 estimated by cladding diameter change. (Please note: sample numbers do not match the rod numbers).
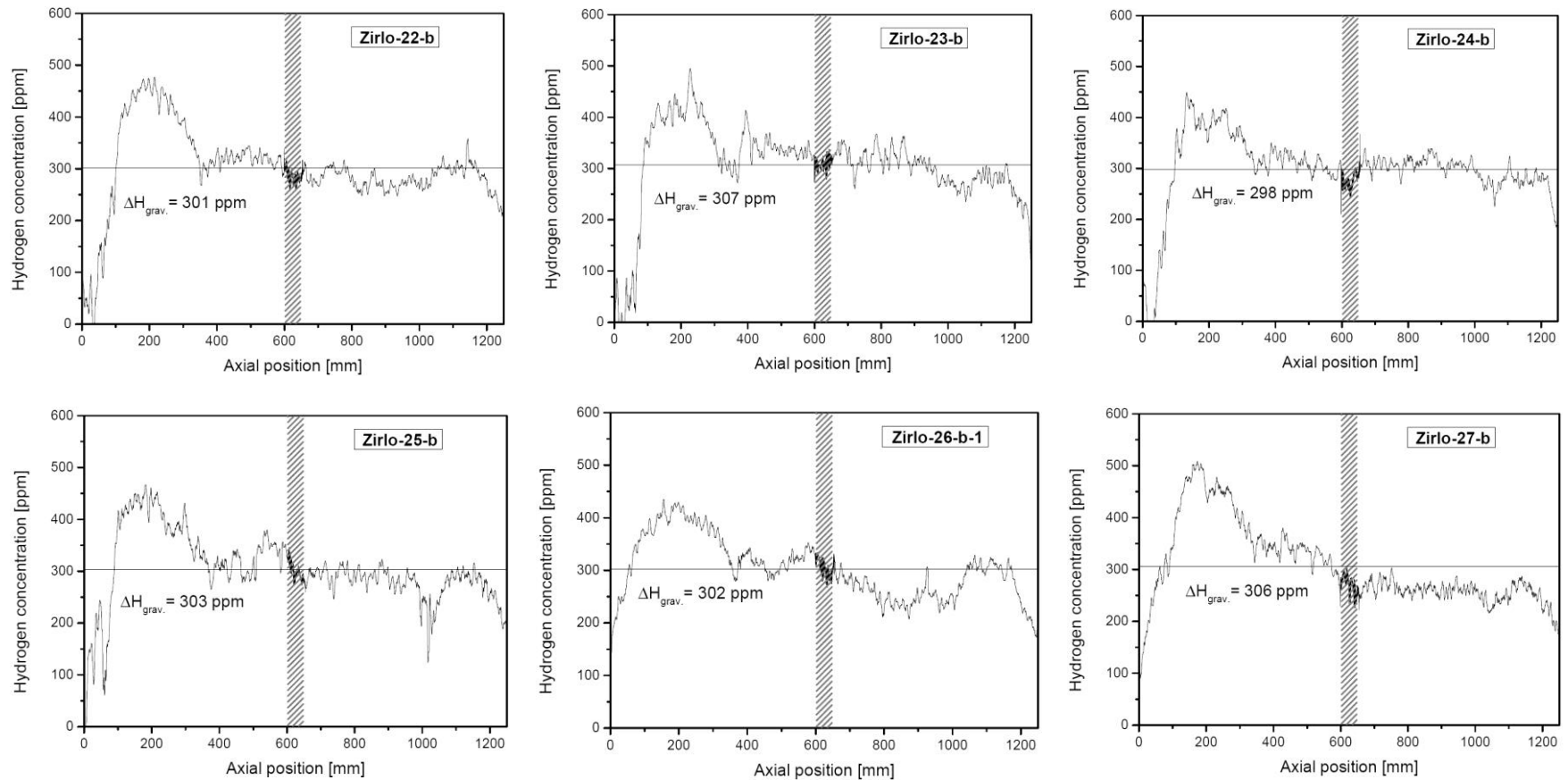
Figure 17 QUENCH-L5; axial distribution of hydrogen of pre-hydrogenated central part (50 – 1250 mm) of claddings #13 - #18 estimated by cladding diameter change. (Please note: sample numbers do not match the rod numbers).
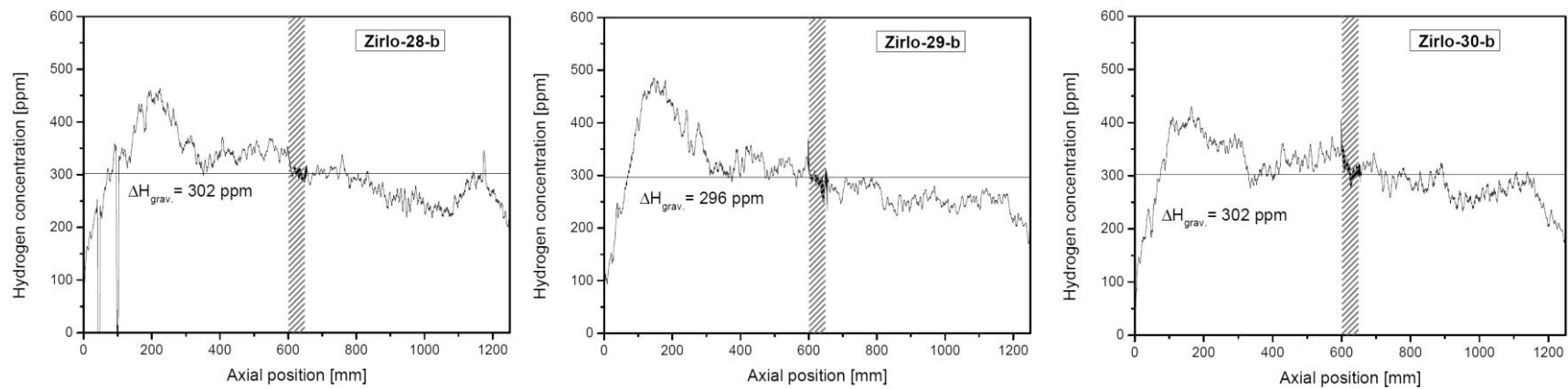
Figure 18 QUENCH-L5; axial distribution of hydrogen of pre-hydrogenated central part (50 – 1250 mm) of claddings #19 - #21 estimated by cladding diameter change. (Please note: sample numbers do not match the rod numbers).
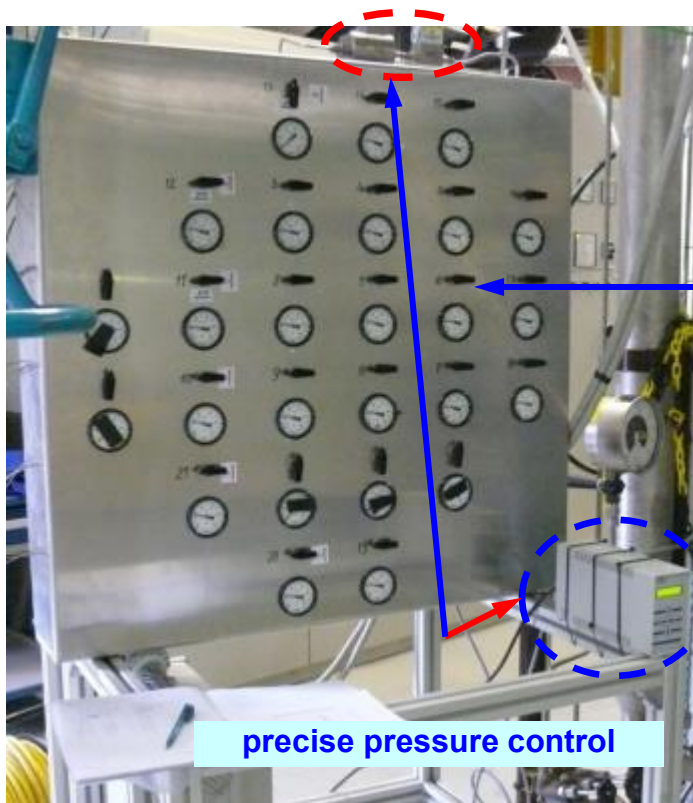
Front side view

21 pressure valves

precise pressure control

Rear side view

21 capillary tubes to test bundle

21 pressure transducers

21 adjustable compensation volumes to setting of original volume value of 31.5 cm^3

Figure 19   QUENCH-L5; Rod pressure control and measurement panel.

bundle top

475 mm

625 mm

2 m

bundle bottom

Mo electrode

Rod cladding

Cu electrode

O-seals

Ø 2 mm

Kr filling for rod internal pressurisation

boreholes
through bottom Cu-electrodes
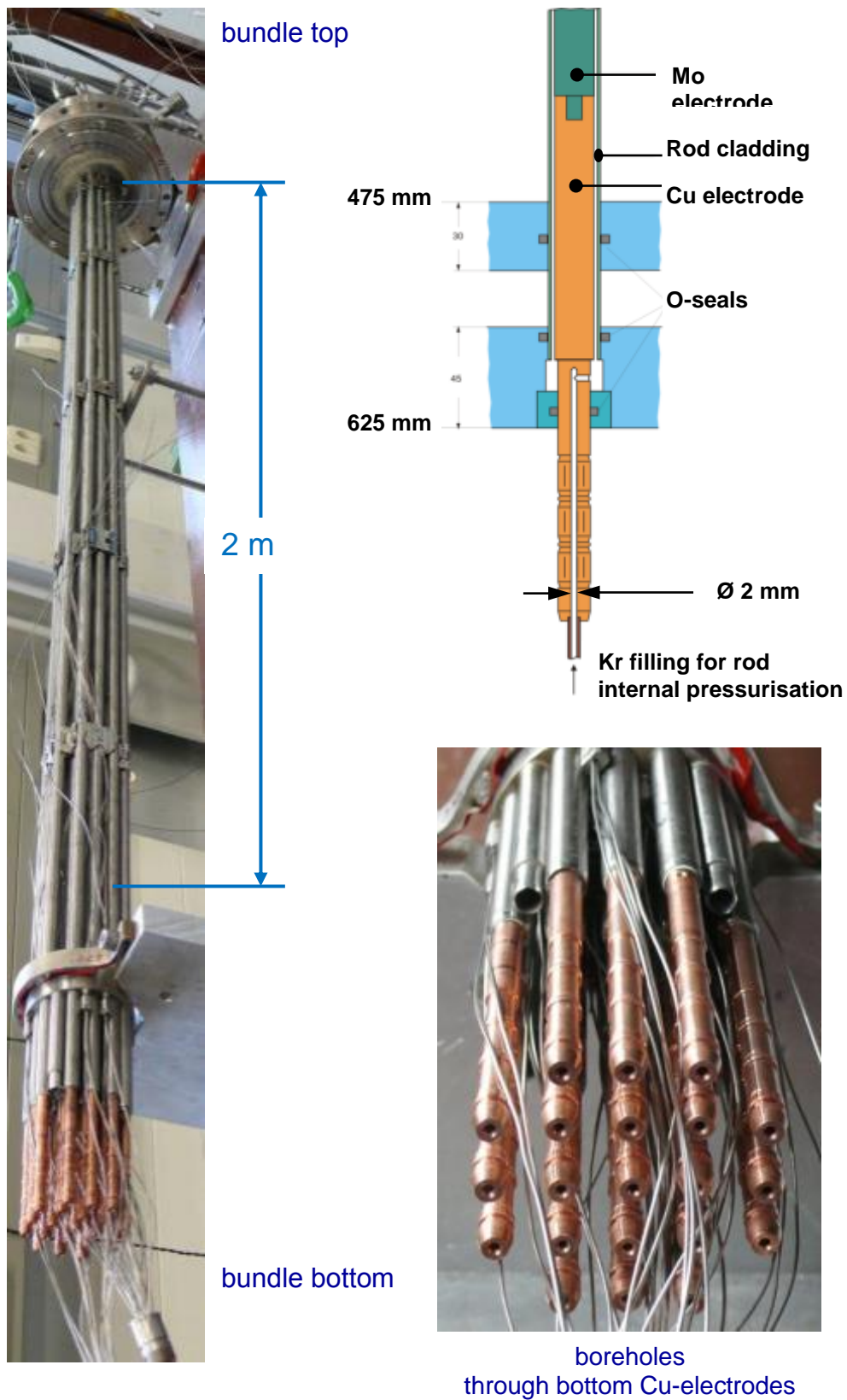
Figure 20   QUENCH-L5; Rod pressurization
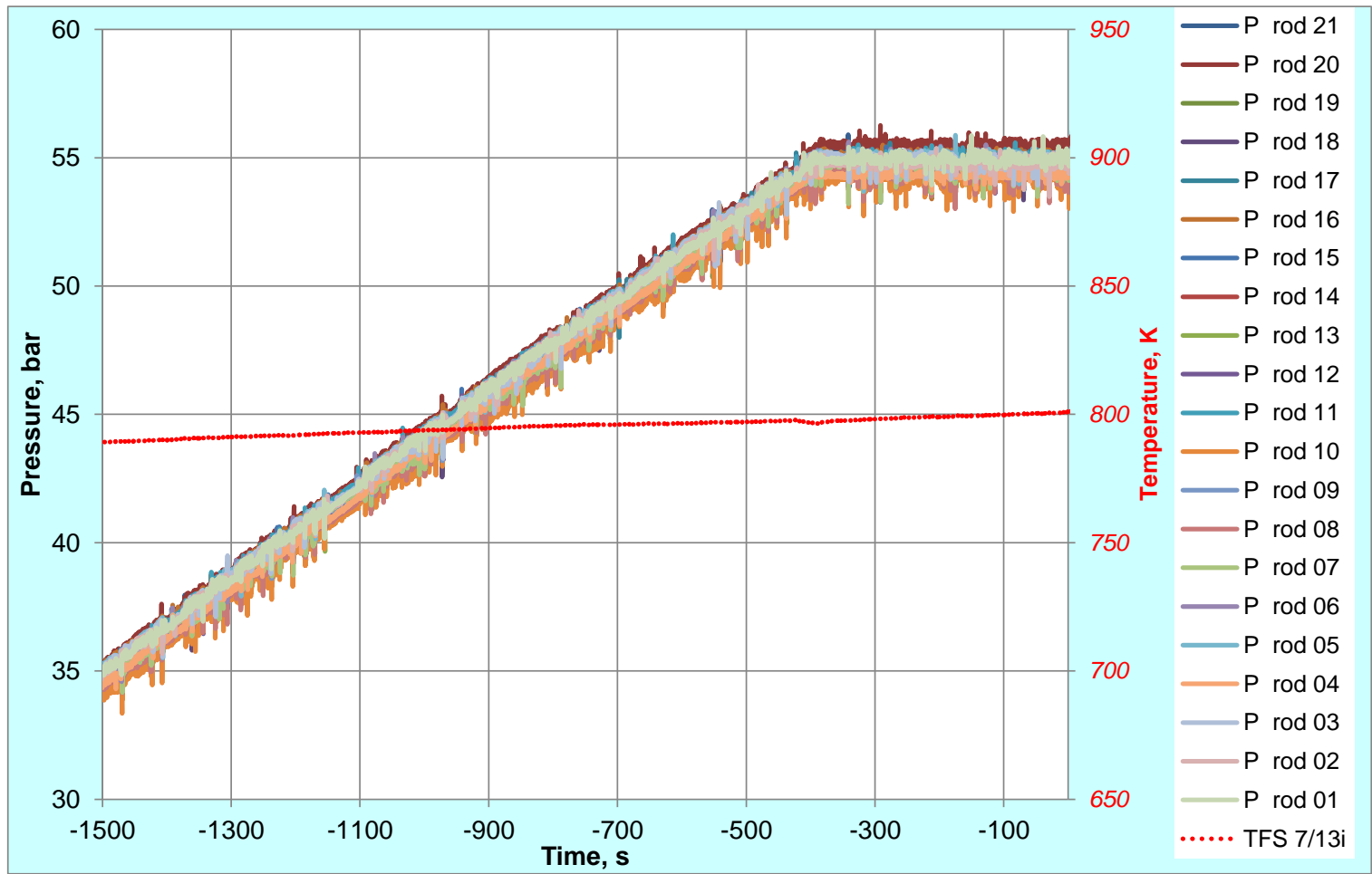
Figure 21   QUENCH-L5; Rod pressurization process at Tpct=800 K.
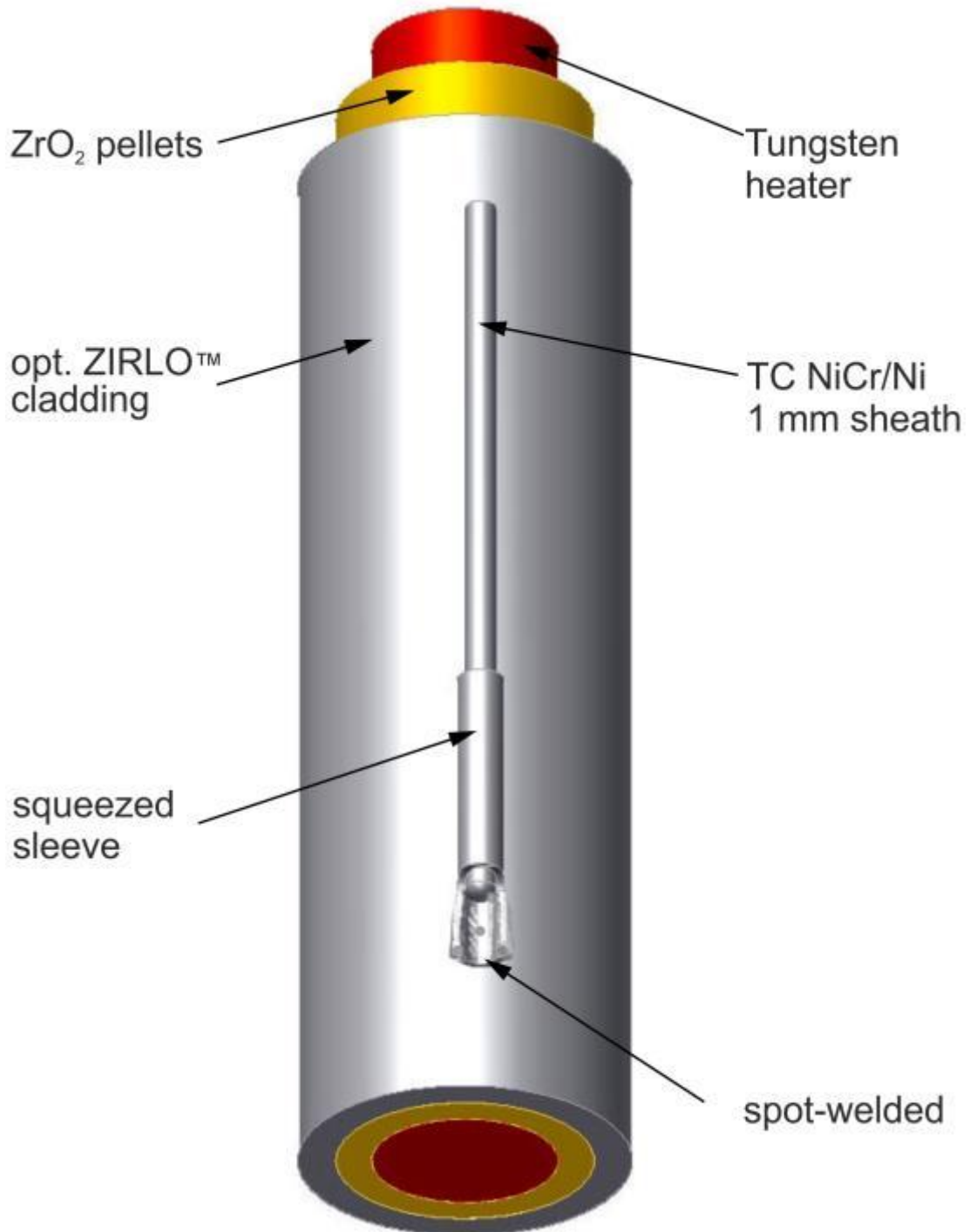
Figure 22   QUENCH-L5; Concept for TC fastening at the test rod.
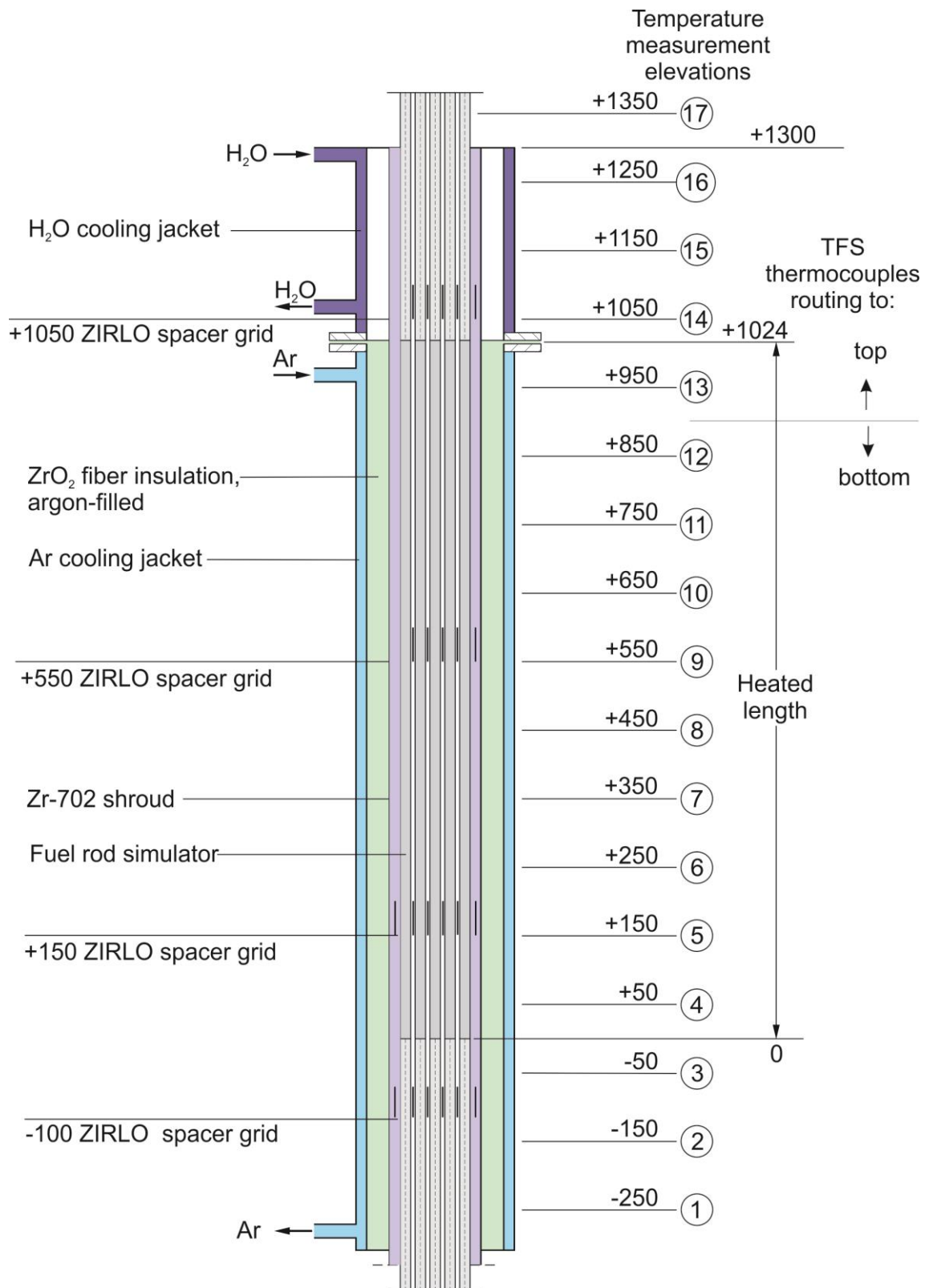
Figure 23 Axial temperature measurement locations in the QUENCH-L5 test section.
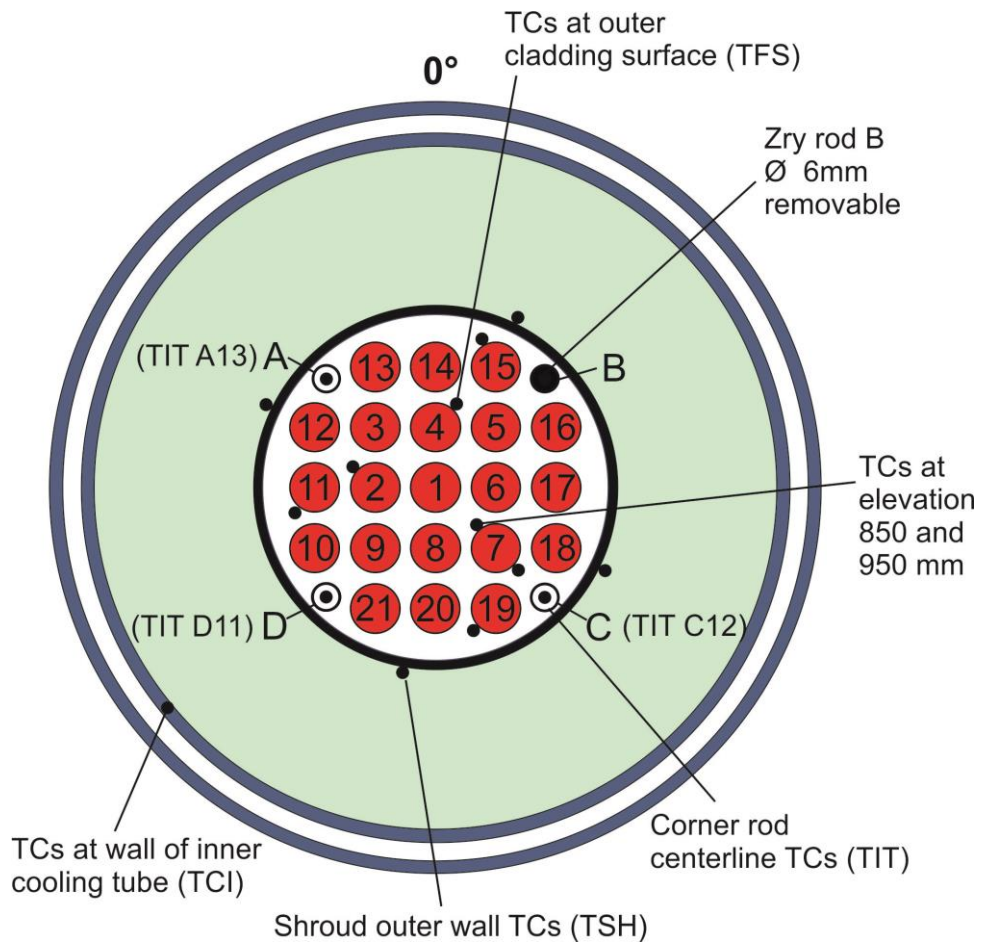
Figure 24   QUENCH-L5; Test bundle; TC instrumentation and rod designation (top view).
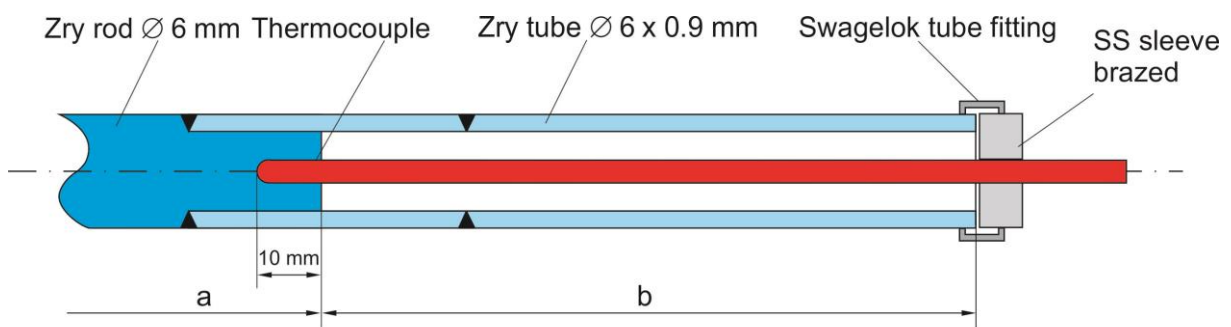
Rod A: TIT A13 (950 mm),   a = 360 mm, b = 2080 mm

Rod C: TIT C12 (850 mm),   a = 460 mm, b = 1980 mm

Rod D: TIT D11 (750 mm),   a = 560 mm, b = 1880 mm

Figure 25   QUENCH-L5; Arrangement of the thermocouples inside the corner rods.
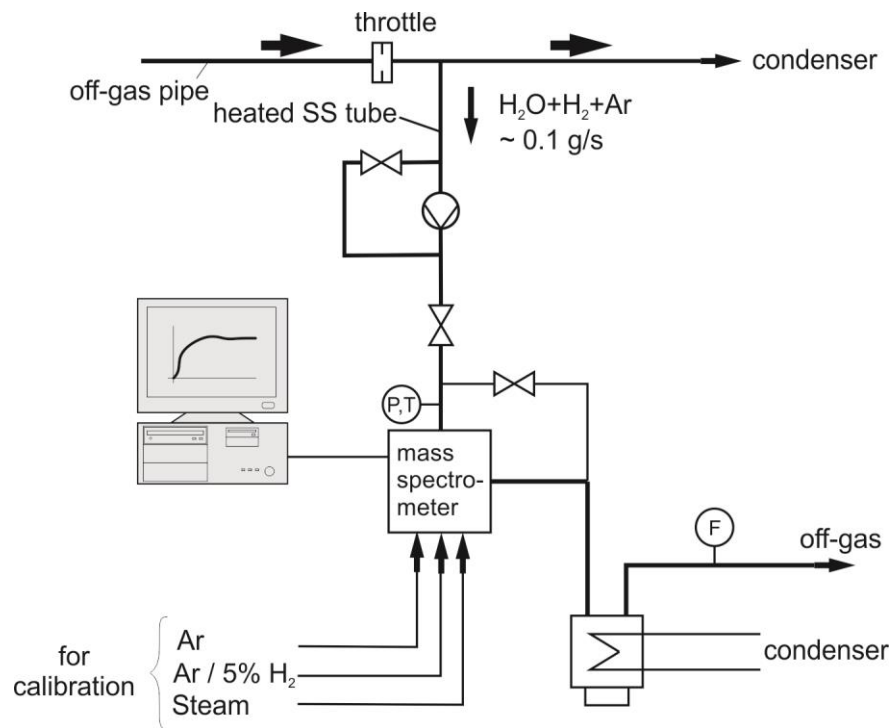
Figure 26   QUENCH Facility; H2 measurement with the GAM 300 mass spectrometer.
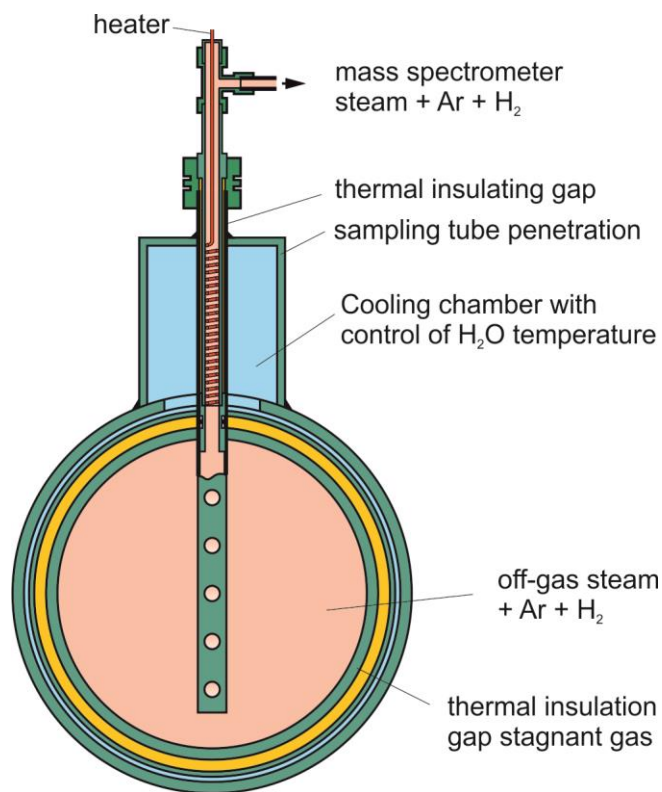
Figure 27   Mass spectrometer sampling position at the off-gas pipe of the QUENCH test facility.
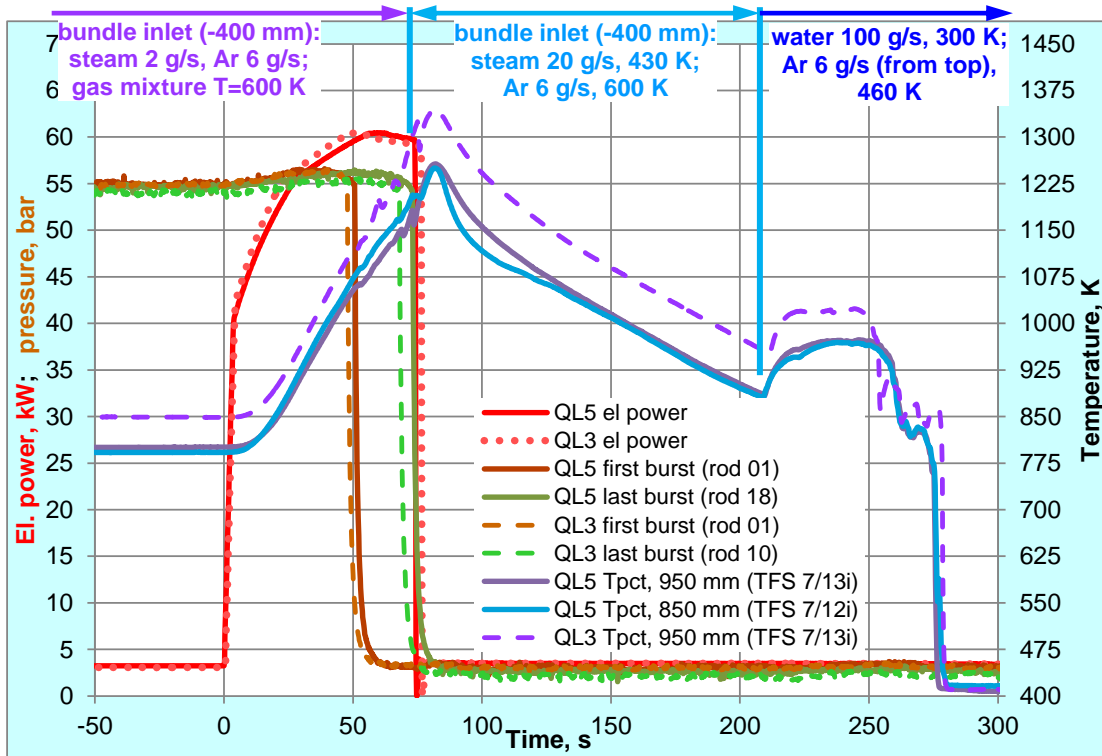
Figure 28   QUENCH-L5; test progress, comparison with QUENCH-L3.
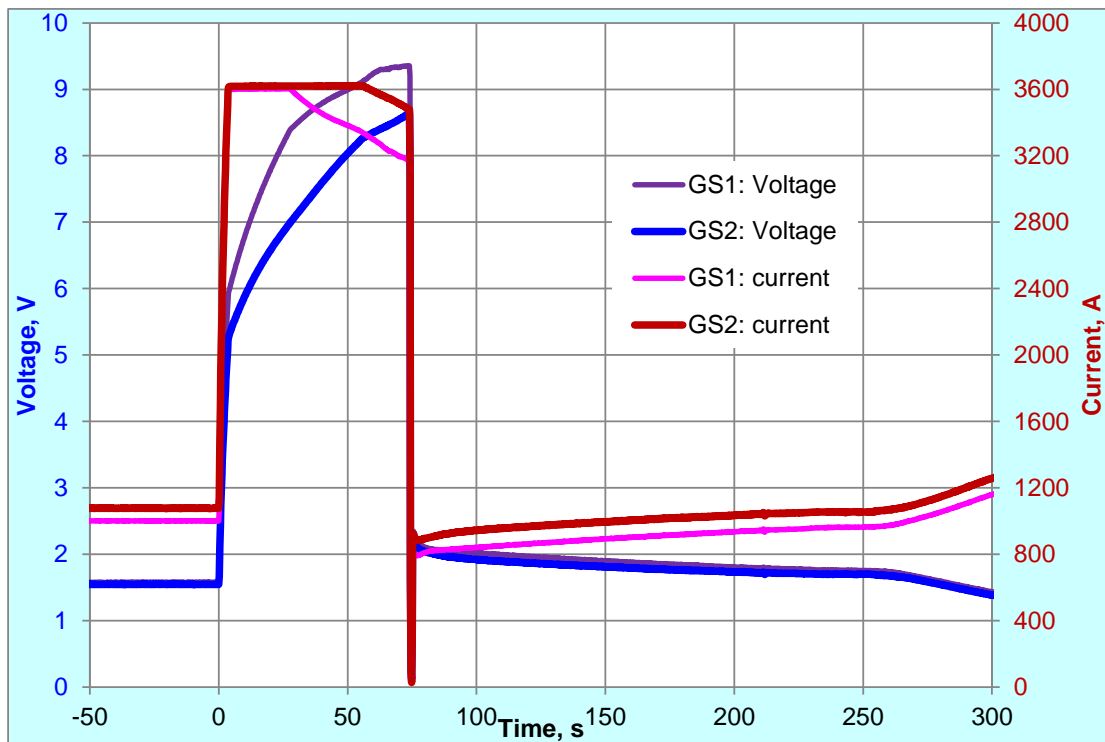
Figure 29   QUENCH-L5; voltage and current of two DC-generators.
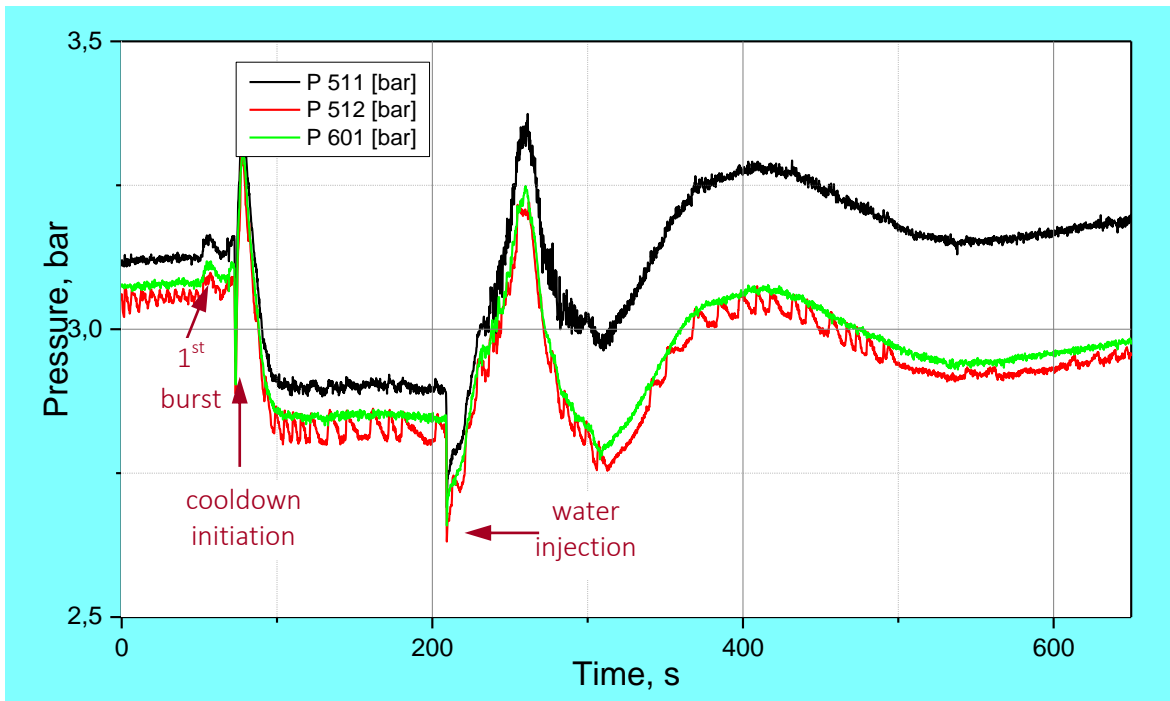
Figure 30 QUENCH-L5; System pressure measured at test section inlet P 511, at outlet P 512, and in the off-gas pipe P 601.
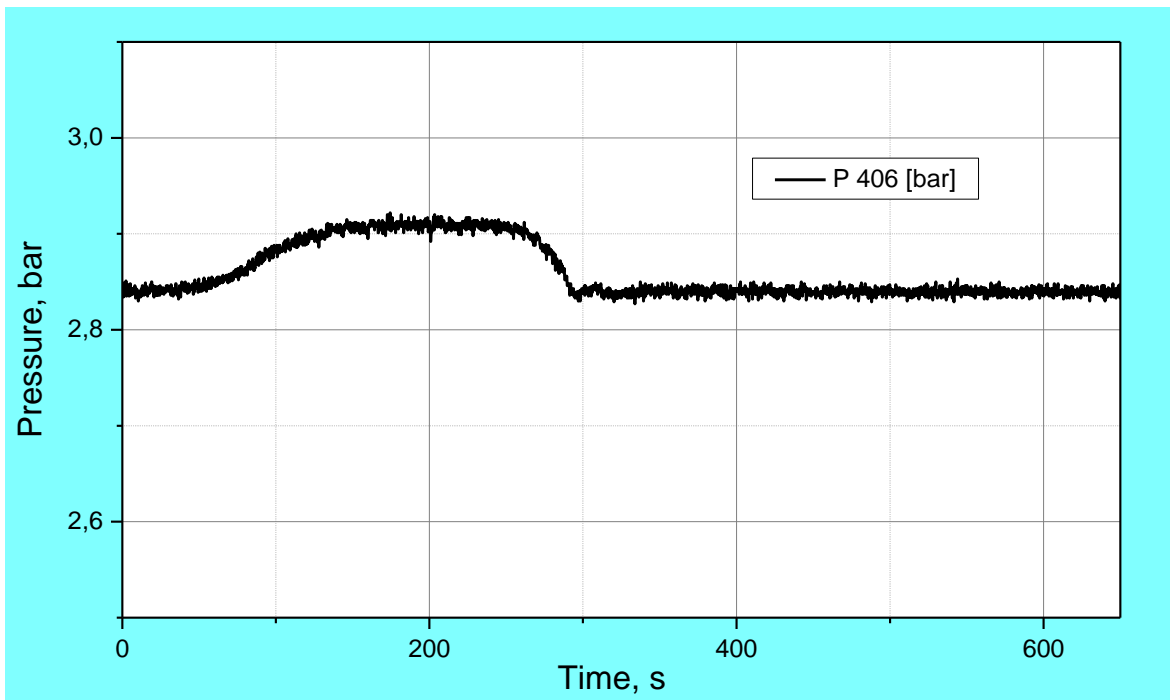
Figure 31 QUENCH-L5; Argon pressure between shroud and cooling jacket P 406 demonstrates tightness of the shroud.
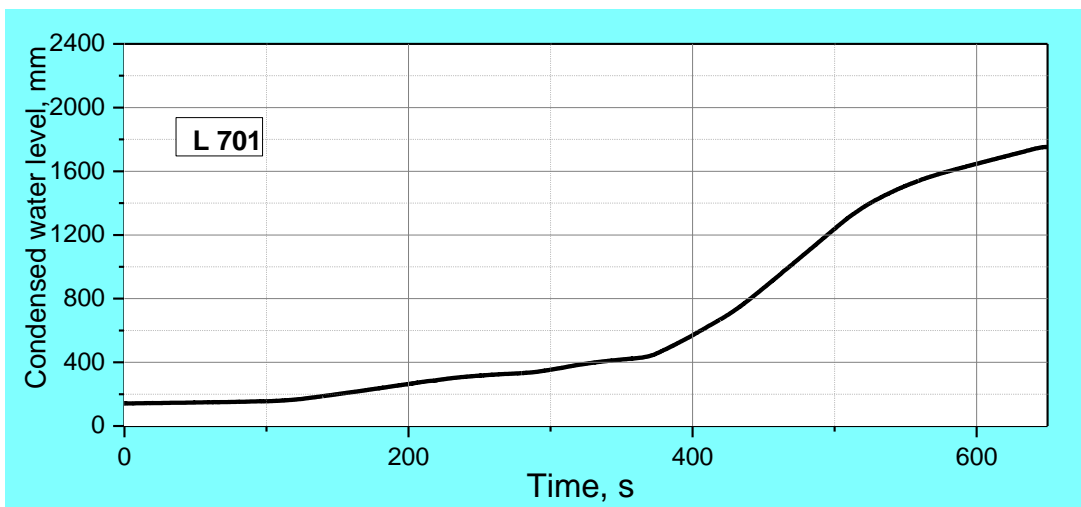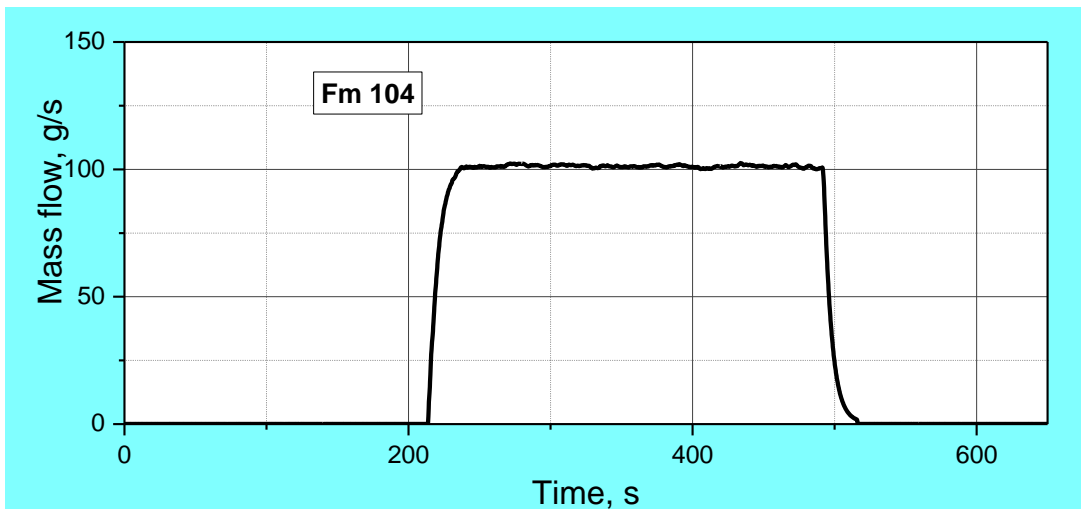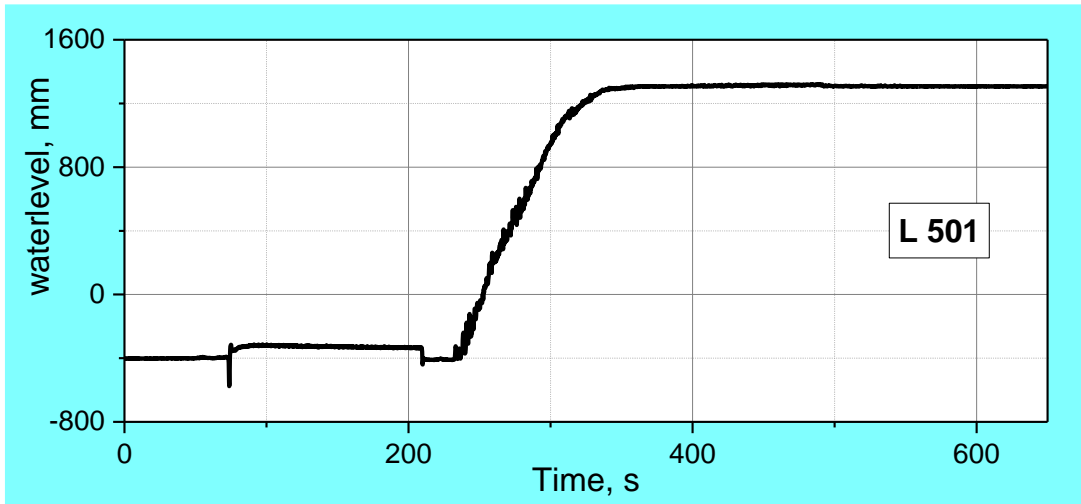
Figure 32 QUENCH-L5; Quench measurement of collapsed water level (L 501), top, water mass flow rate (Fm 104), center, condensed water (L 701), bottom.
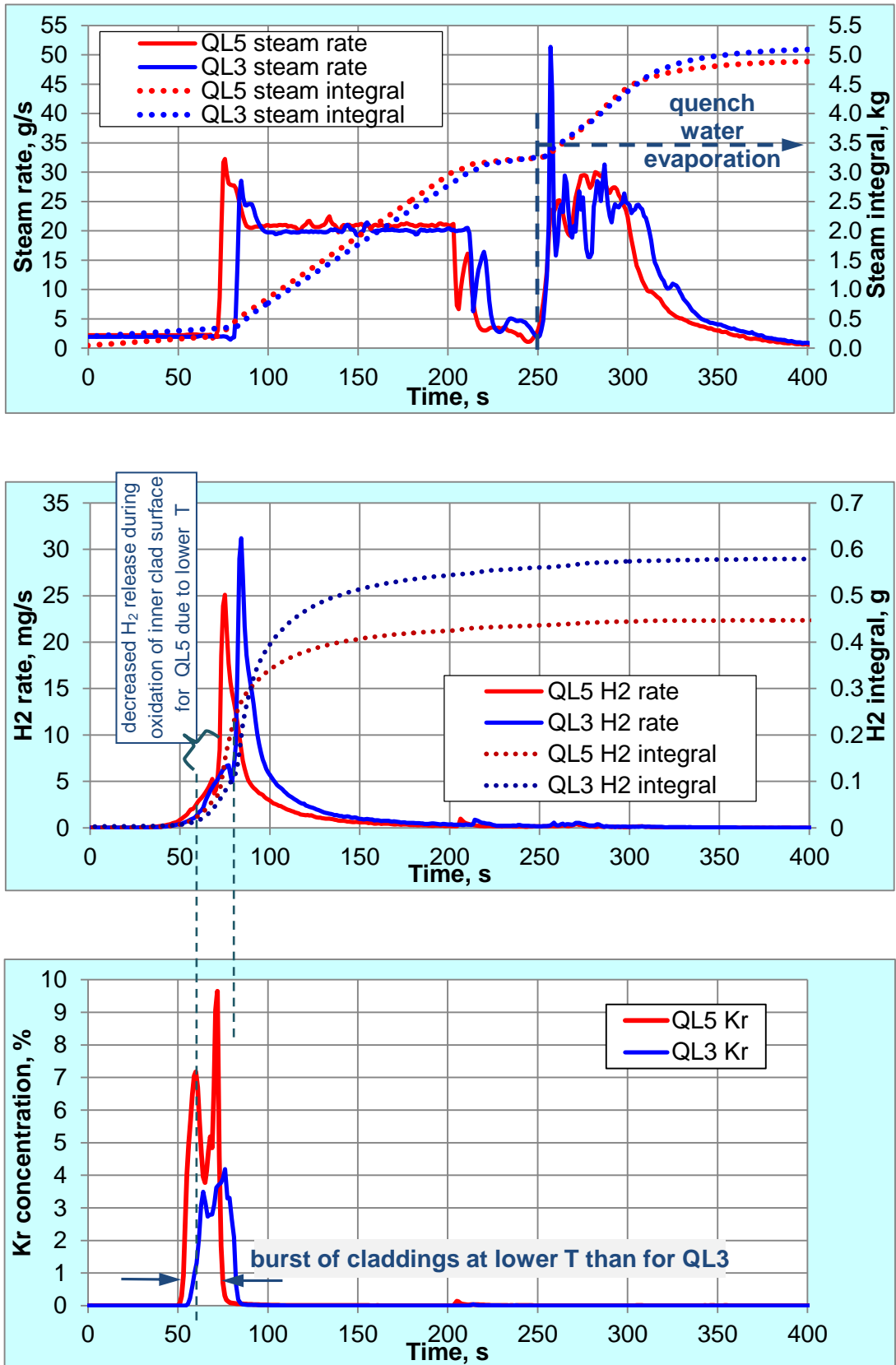
Figure 33 QUENCH-L5; steam, top; hydrogen, center; krypton, bottom, measured by mass spectrometry (MS).
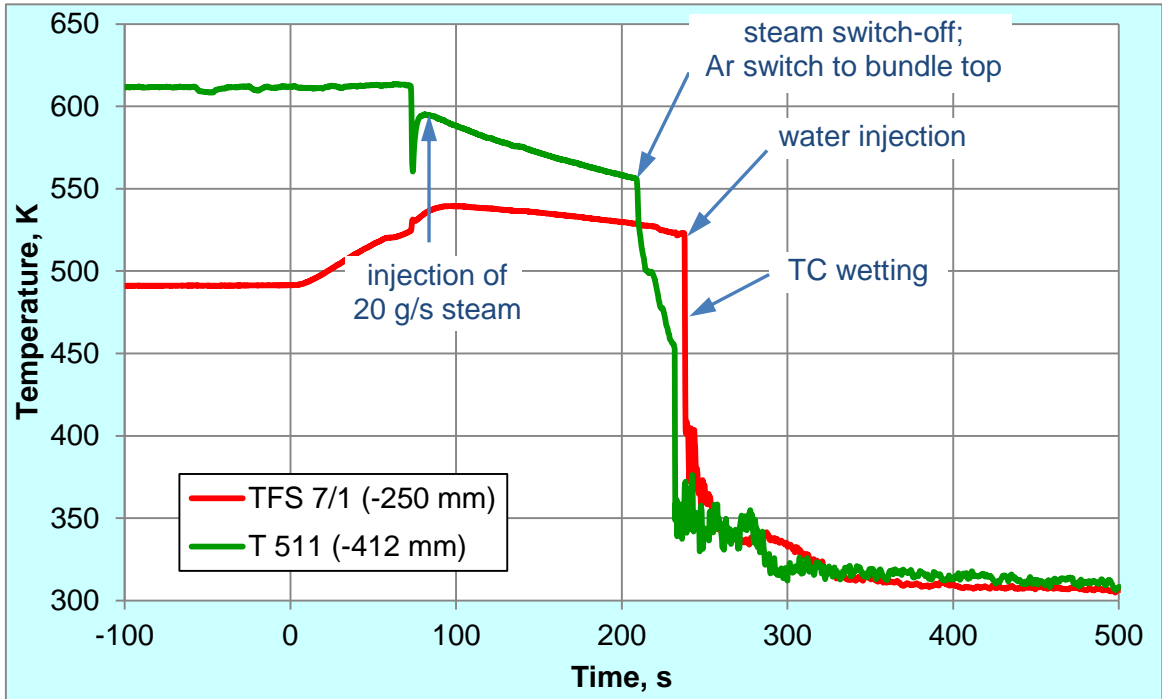
Figure 34 QUENCH-L5; Temperatures measured by gas inlet thermocouple (T 511) at -412 mm and rod cladding thermocouple at -250 mm elevation(TFS 7/1).
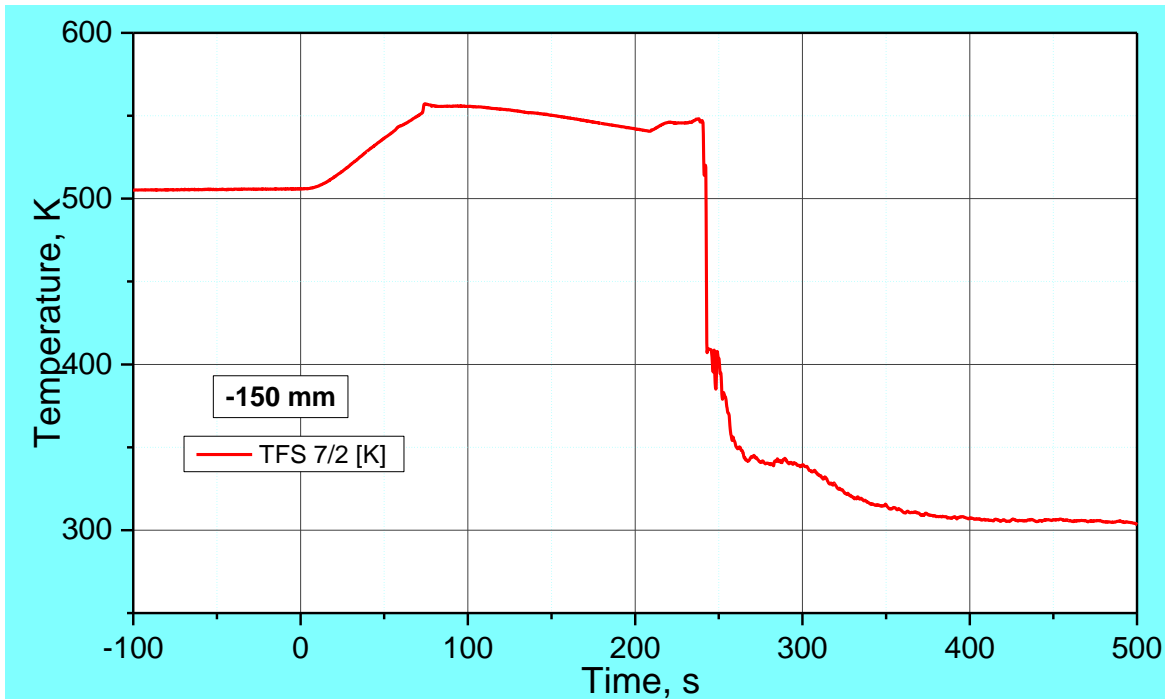
Figure 35 QUENCH-L5; Temperatures measured by rod cladding (TFS 7/2) thermocouple at -150 mm elevation.
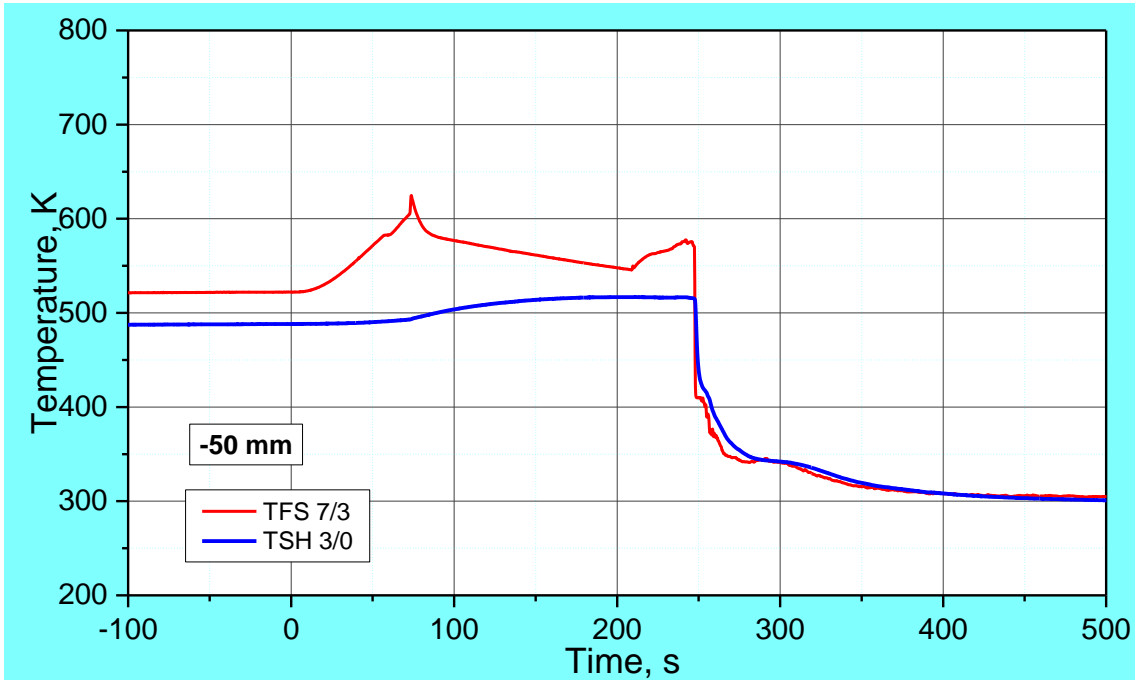
Figure 36   QUENCH-L5; Temperatures measured by rod cladding (TFS 7/3) and shroud (TSH 3/0) thermocouples at -50 mm elevation.
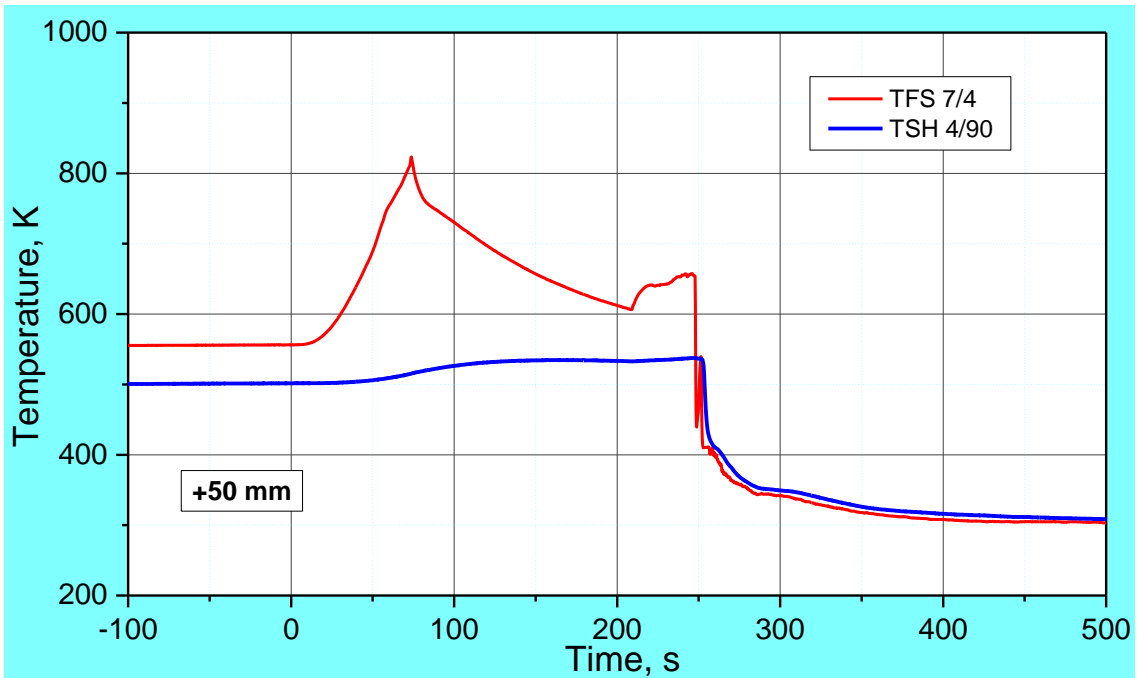
Figure 37   QUENCH-L5; Temperatures measured by rod cladding (TFS 7/4) and shroud (TSH 4/90) thermocouples at 50 mm elevation.
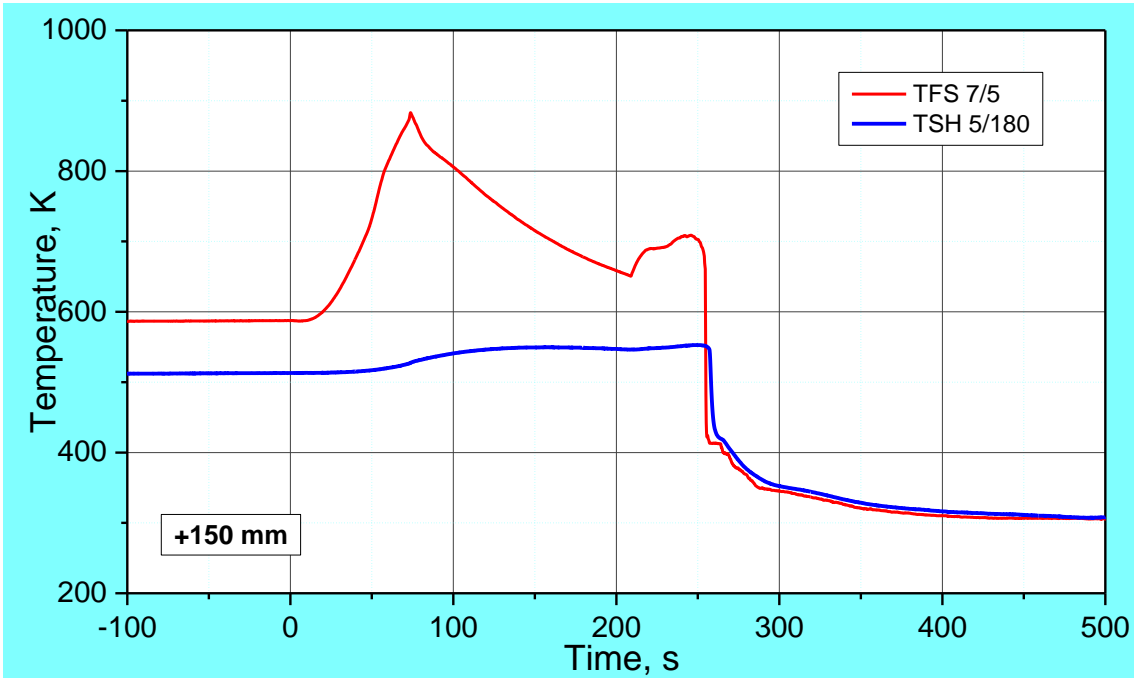
Figure 38   QUENCH-L5; Temperatures measured by rod cladding (TFS 7/5) and shroud (TSH 5/180) thermocouples at 150 mm elevation.
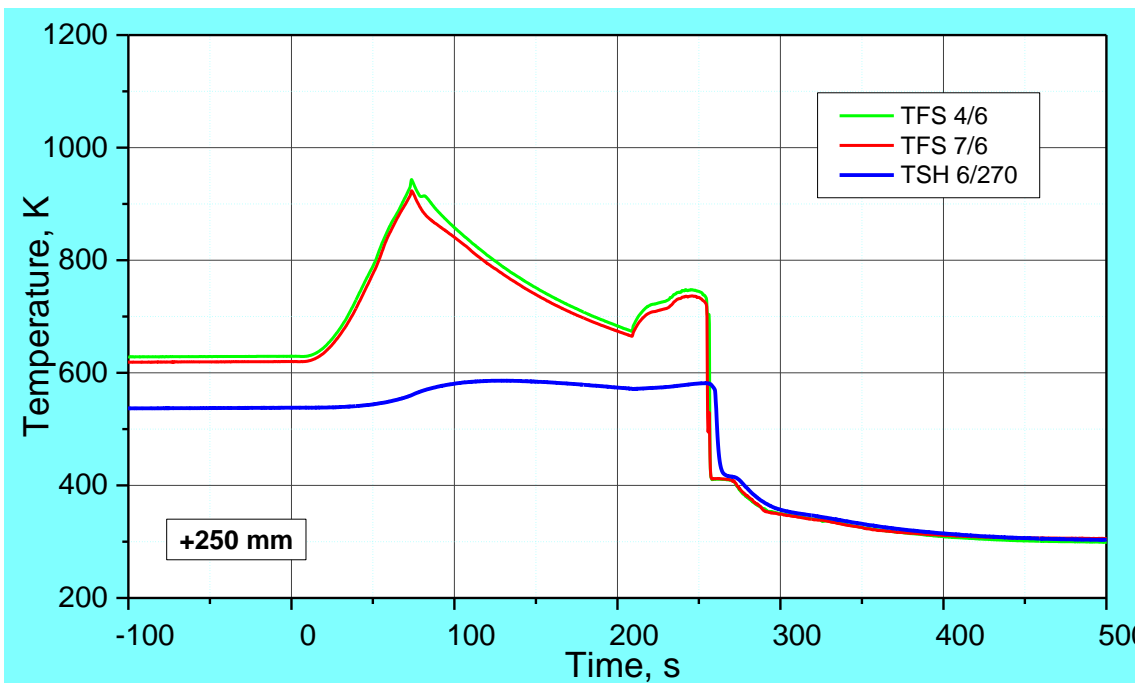
Figure 39   QUENCH-L5; Temperatures measured by rod cladding (TFS) and shroud (TSH 6/270) thermocouples at 250 mm elevation.
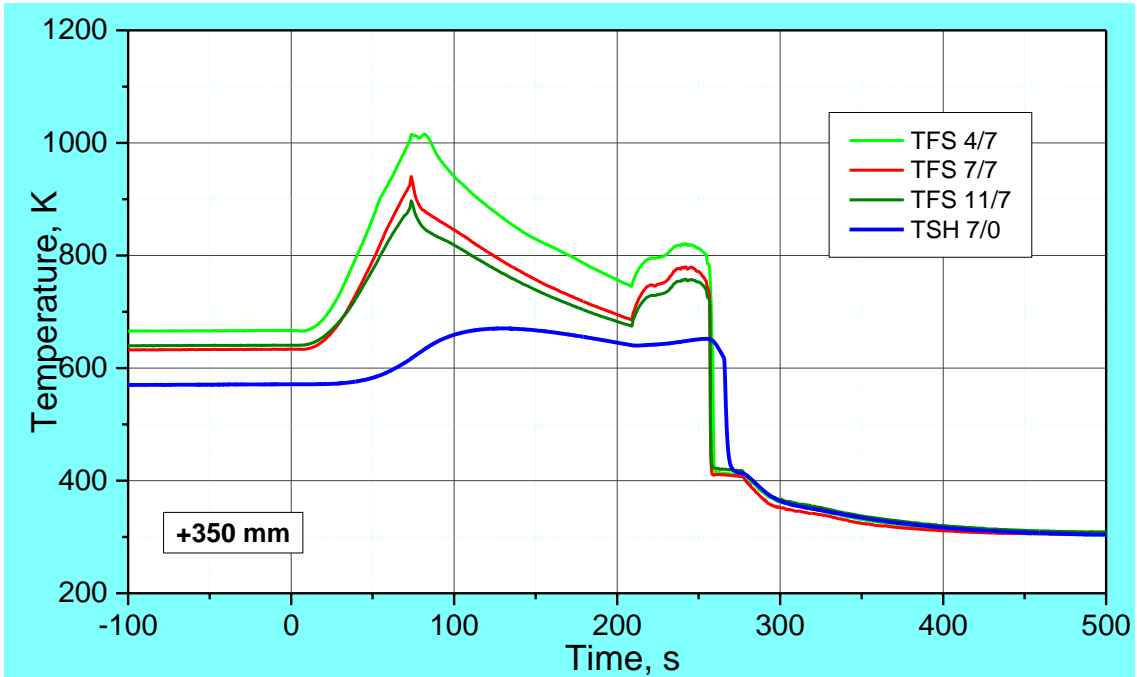
Figure 40   QUENCH-L5; Temperatures measured by rod cladding (TFS) and shroud (TSH 7/0) thermocouples at 350 mm elevation.
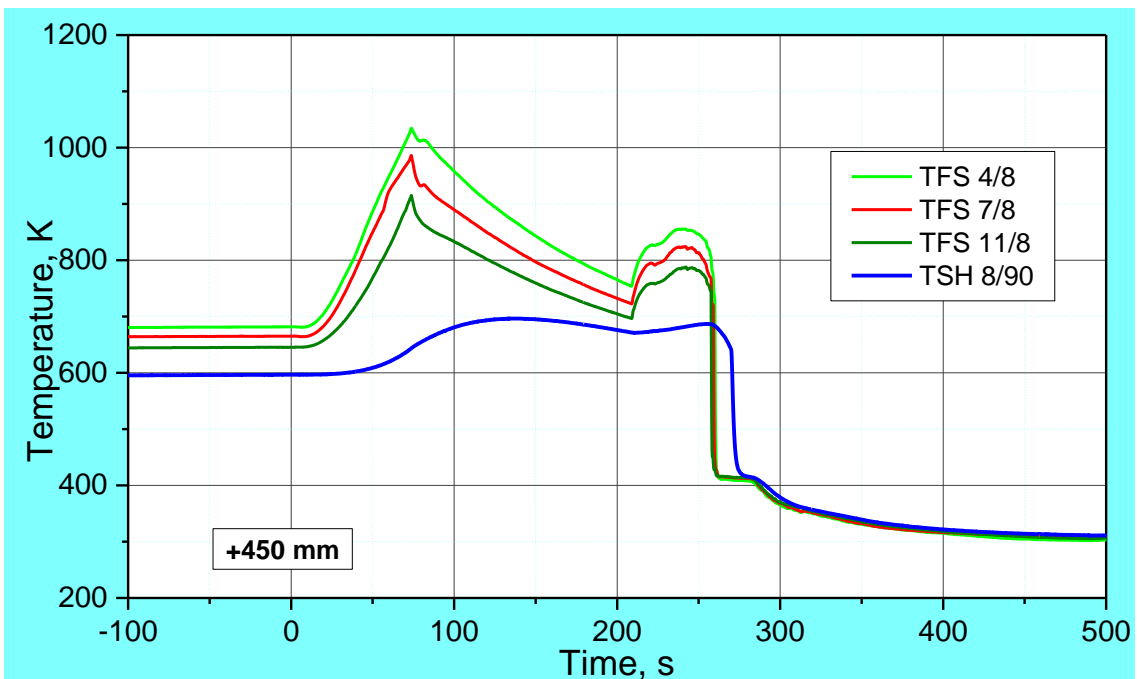
Figure 41   QUENCH-L5; Temperatures measured by rod cladding (TFS) and shroud (TSH 8/90) thermocouples at 450 mm elevation.
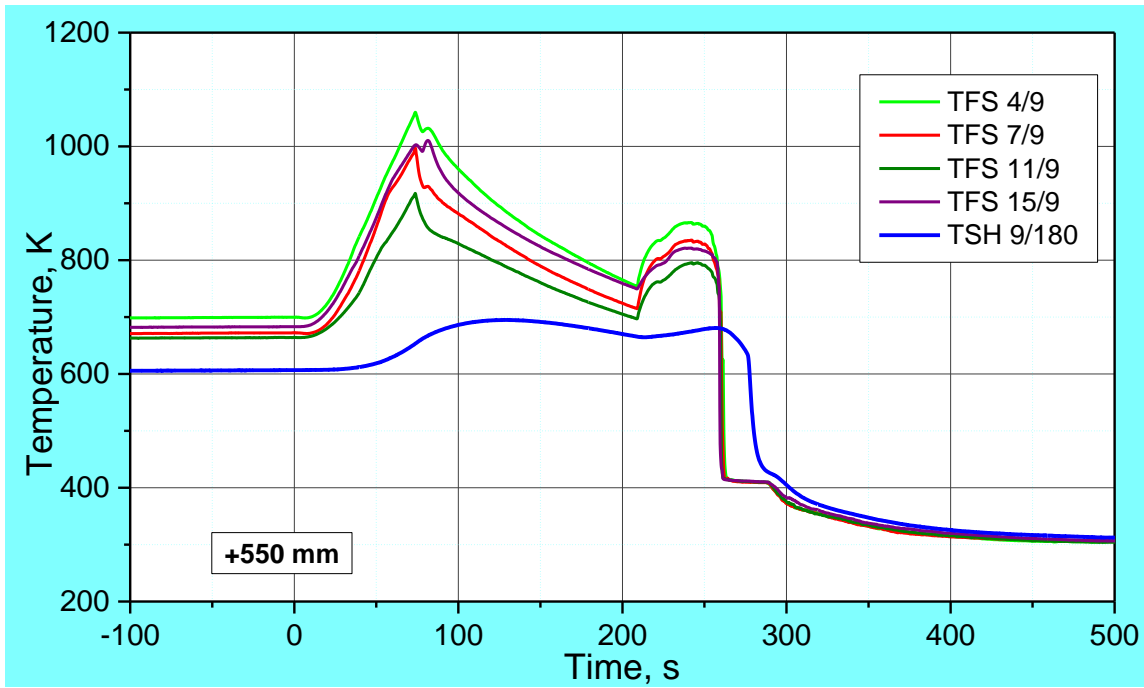
Figure 42 QUENCH-L5; Temperatures measured by rod cladding (TFS) and shroud (TSH 9/180) thermocouples at 550 mm elevation.
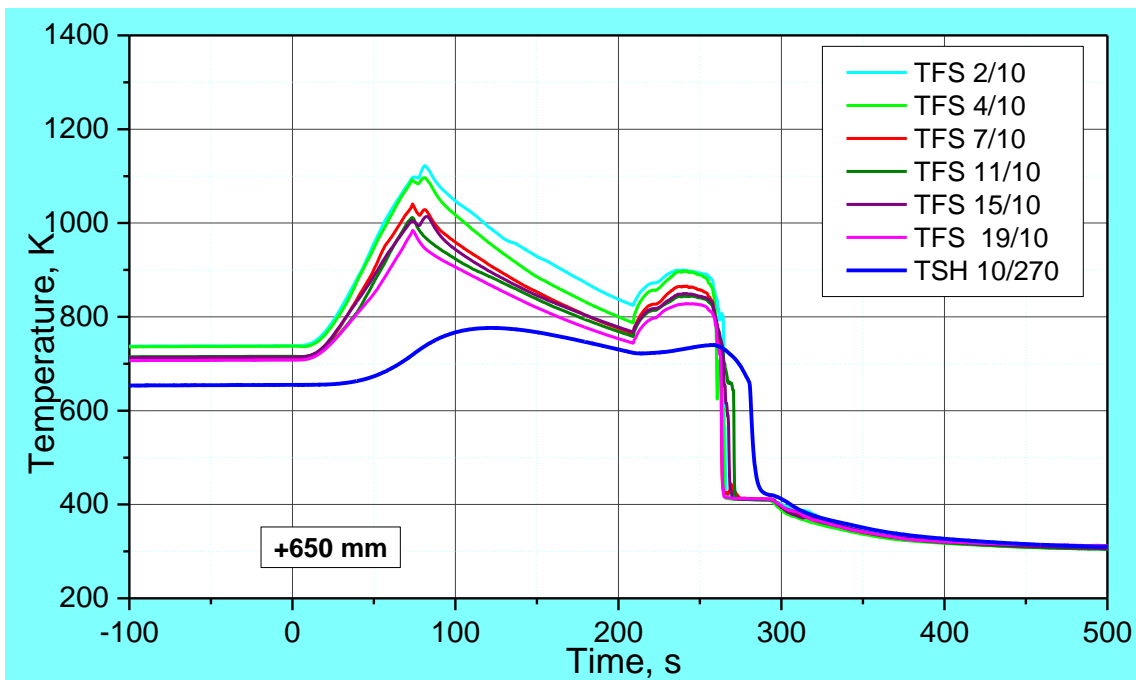
Figure 43 QUENCH-L5; Temperatures measured by rod cladding (TFS) and shroud (TSH 10/270) thermocouples at 650 mm elevation.
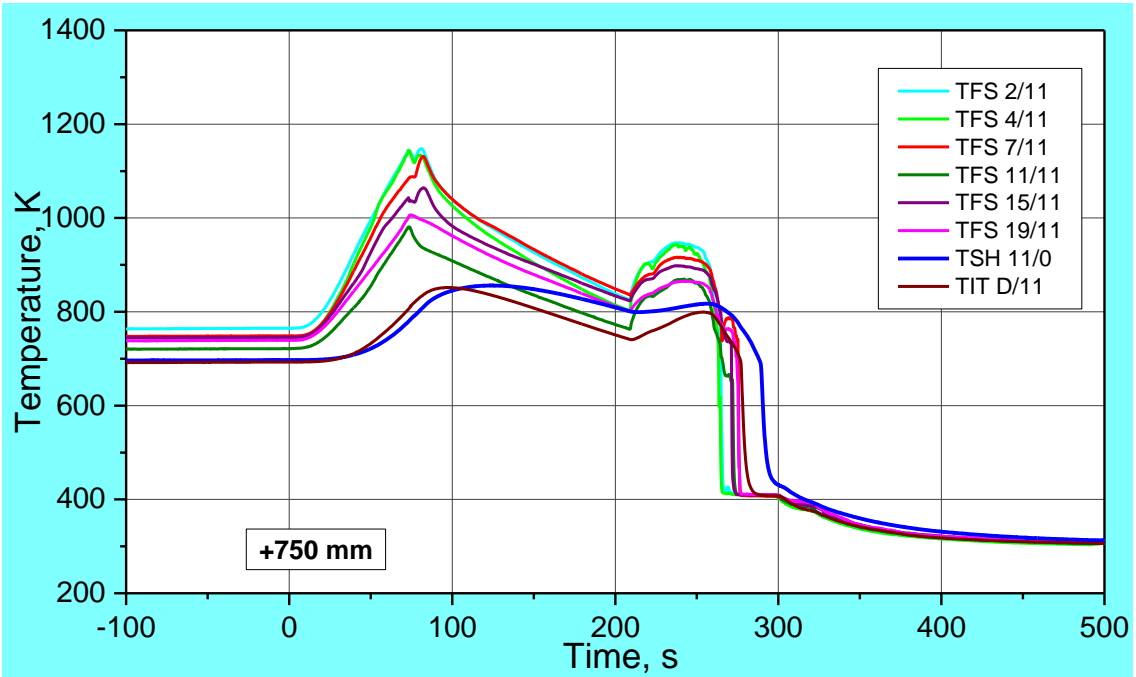
Figure 44 QUENCH-L5; Temperatures measured by rod cladding (TFS) and shroud (TSH 11/0), and corner rod internal (TIT D/11) thermocouples at 750 mm elevation.
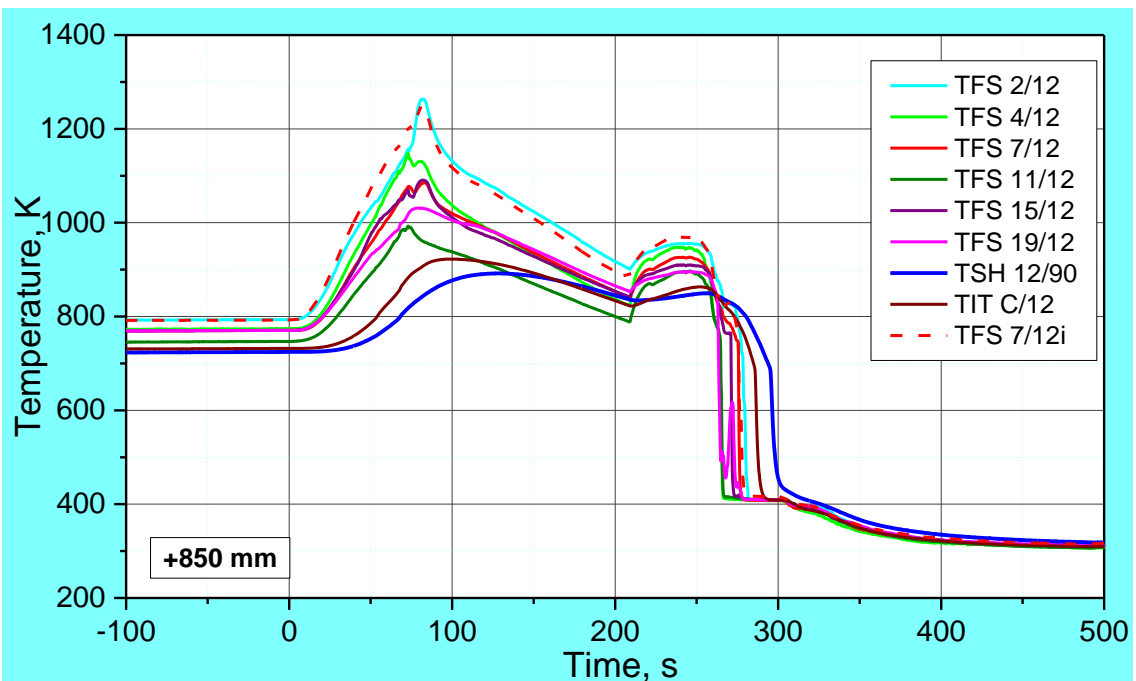
Figure 45 QUENCH-L5; Temperatures measured by rod cladding (TFS) and shroud (TSH 12/90), and corner rod internal (TIT C/12) thermocouples at 850 mm elevation.
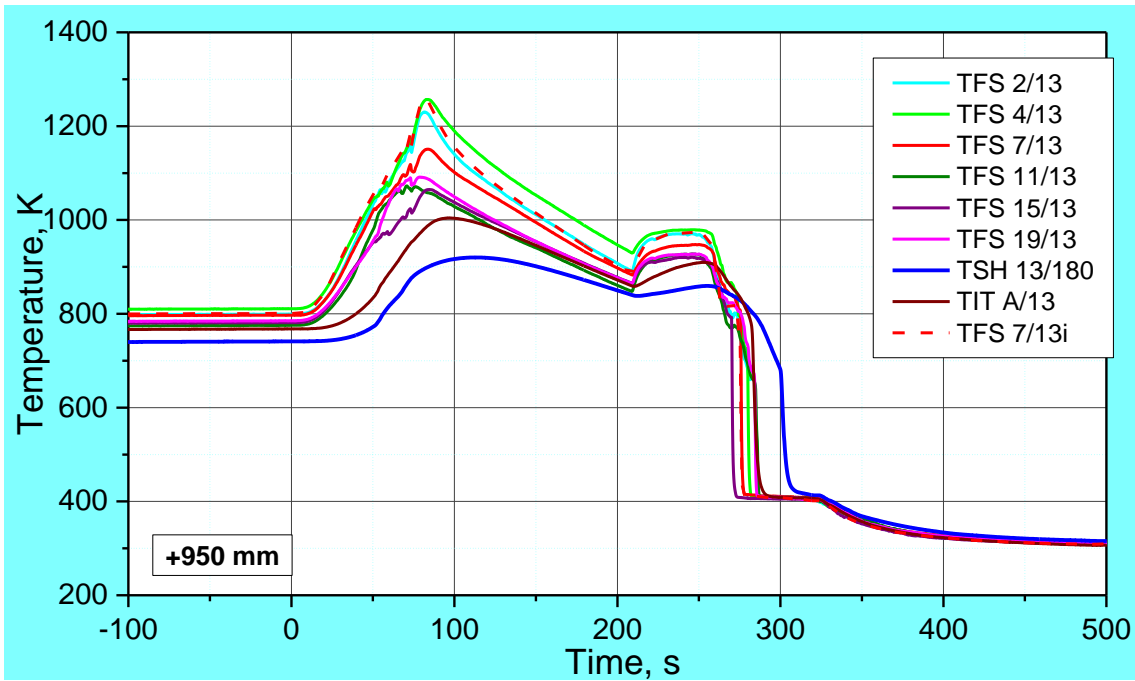
Figure 46 QUENCH-L5; Temperatures measured by rod cladding (TFS) and shroud (TSH 13/180), and corner rod internal (TIT A/13) thermocouples at 950 mm elevation.
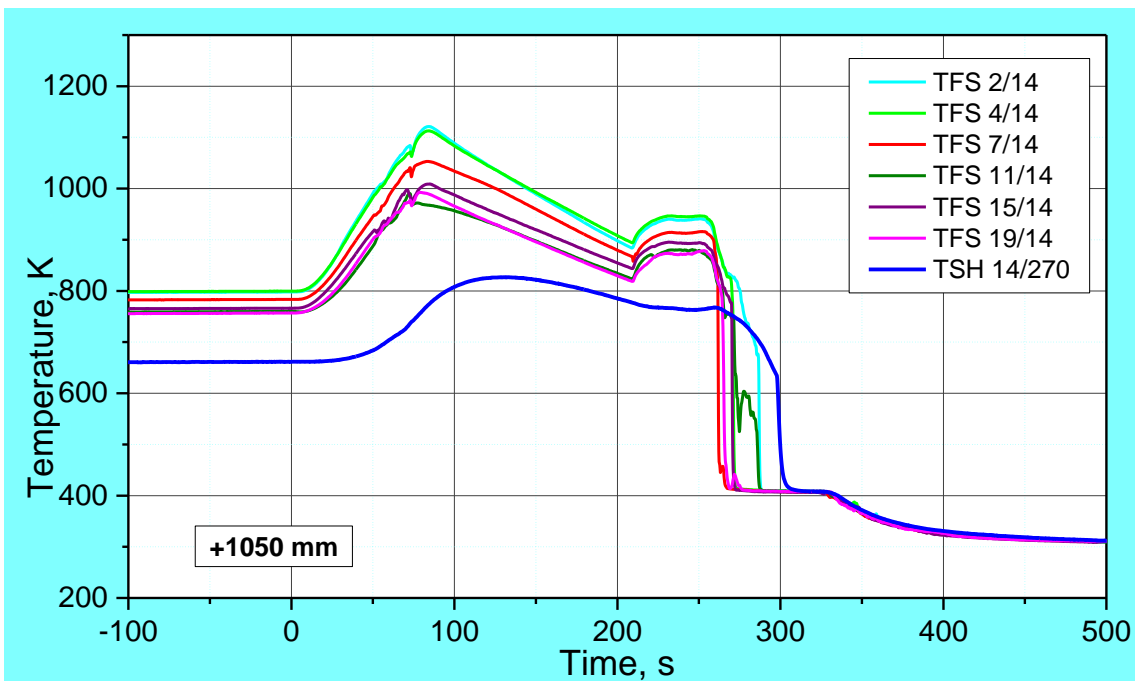
Figure 47 QUENCH-L5; Temperatures measured by rod cladding (TFS) and shroud (TSH 14/270) thermocouples at 1050 mm elevation.
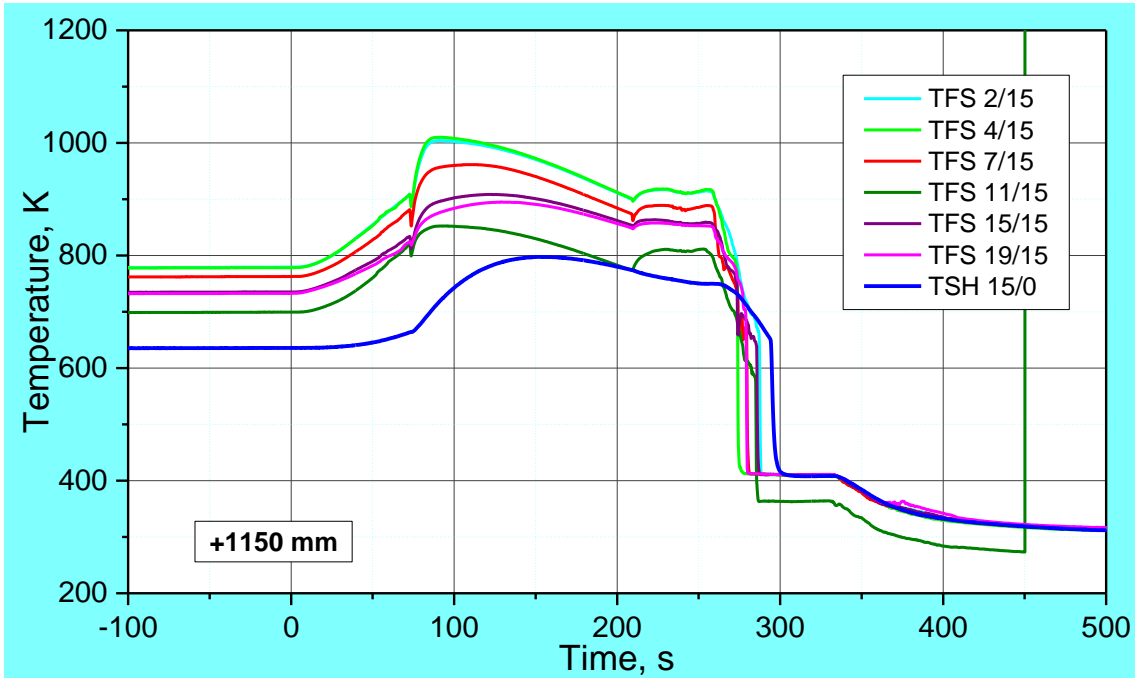
Figure 48   QUENCH-L5; Temperatures measured by rod cladding (TFS) and shroud (TSH 15/0) thermocouples at 1150 mm elevation.
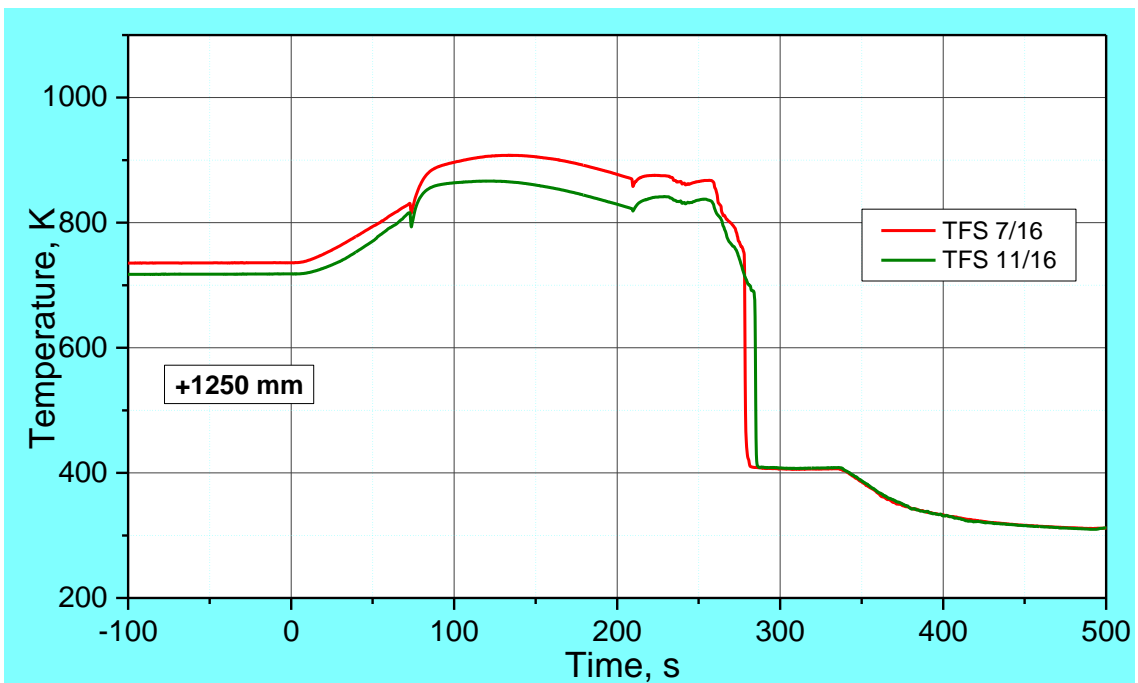
Figure 49   QUENCH-L5; Temperatures measured by rod cladding (TFS) thermocouples at 1250 mm elevation.
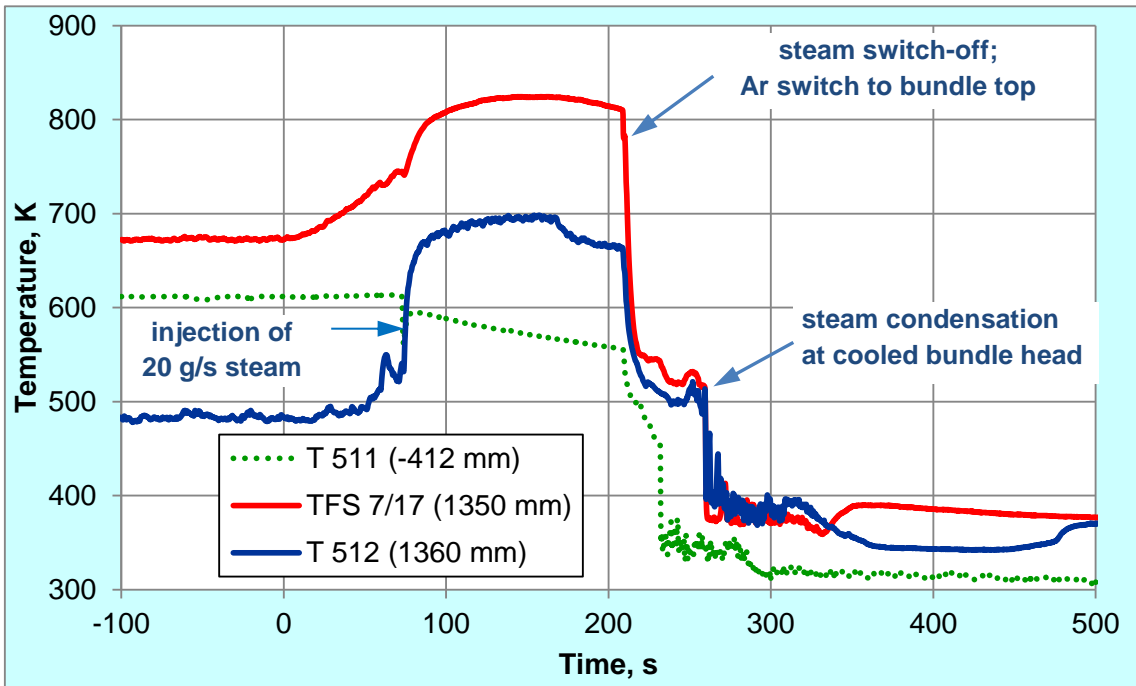
Figure 50   QUENCH-L5; Temperature measured by rod cladding thermocouple at 1350 mm elevation (TFS 7/17) and gas temperature (T 512) at 1360 mm between shroud and rod #20.
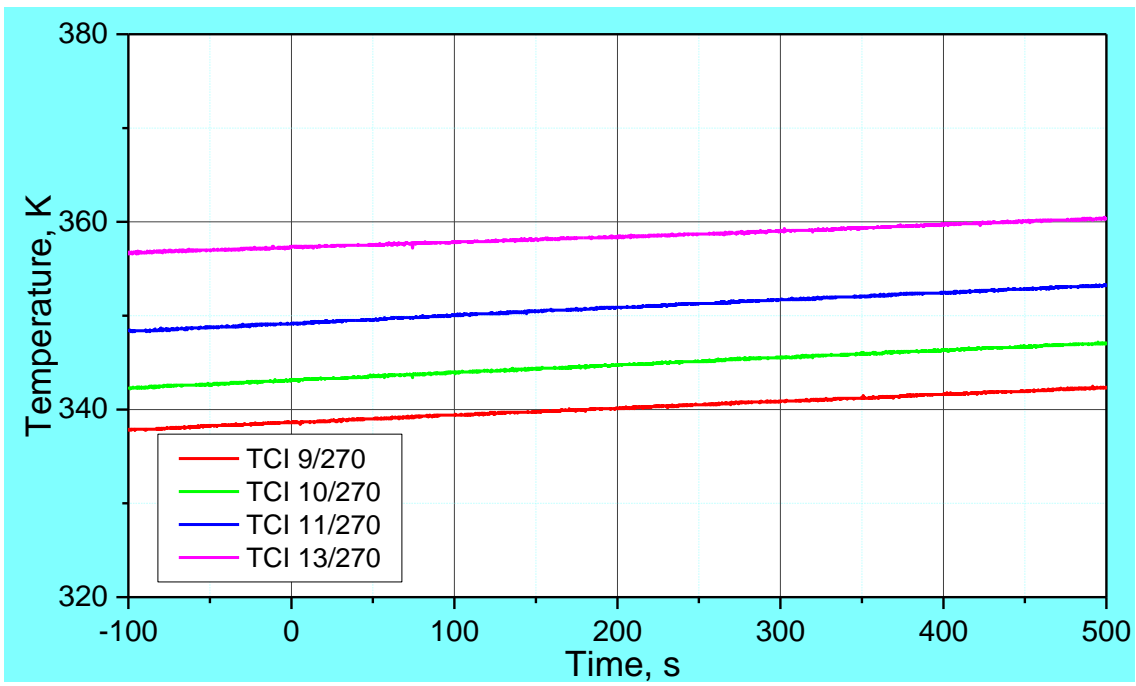
Figure 51   QUENCH-L5; Overview of the TCI (inner cooling jacket).
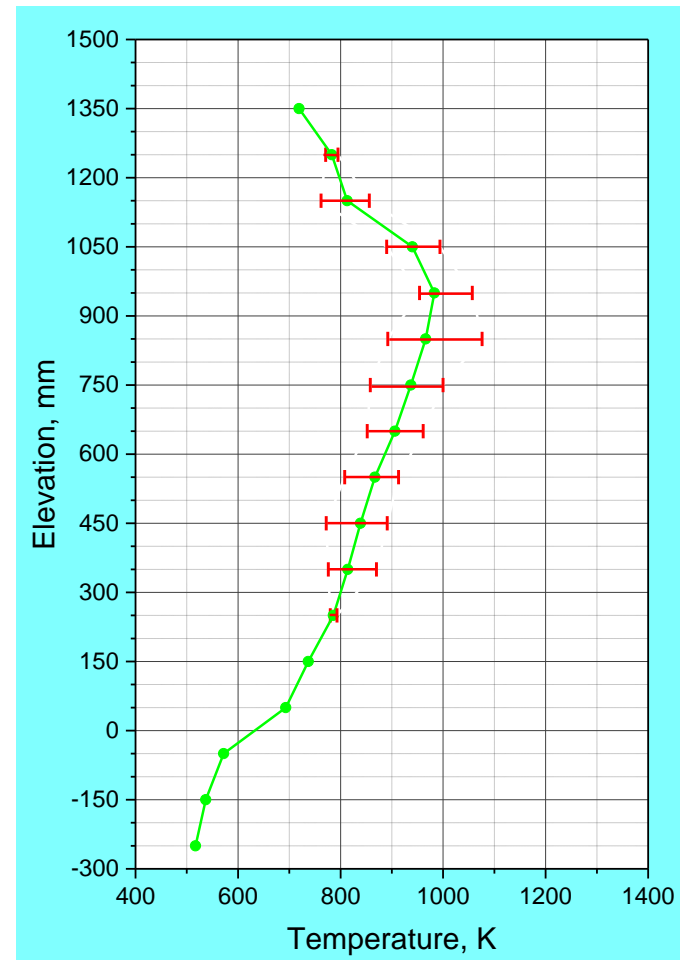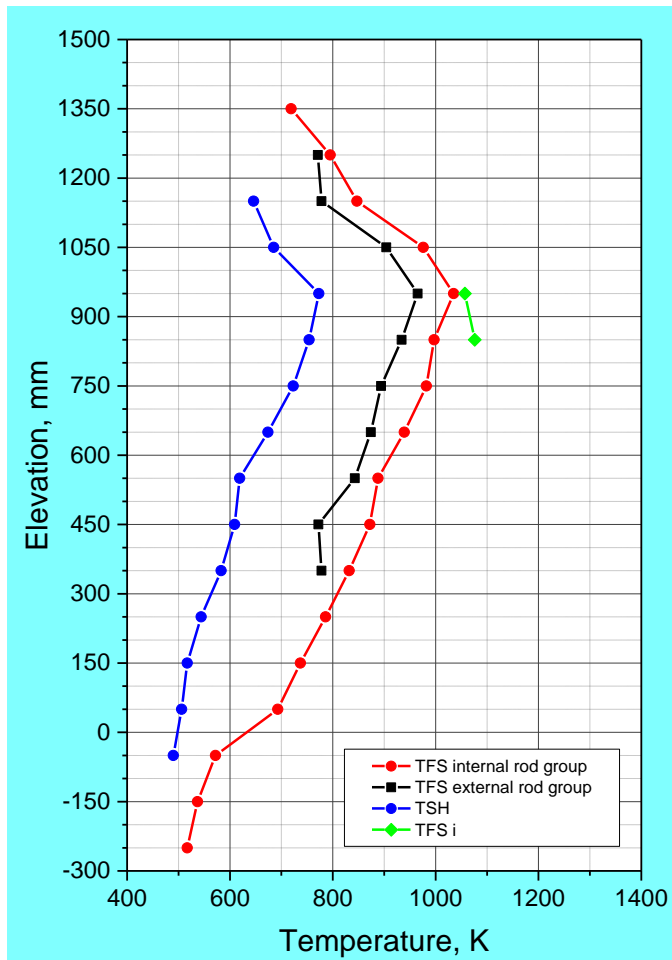
Figure 52   QUENCH-L5; Axial temperature profile TFS internal and external rod group together with TSH, left, and axial temperature profile of all TFS, right, at 50.6 s (first cladding burst).
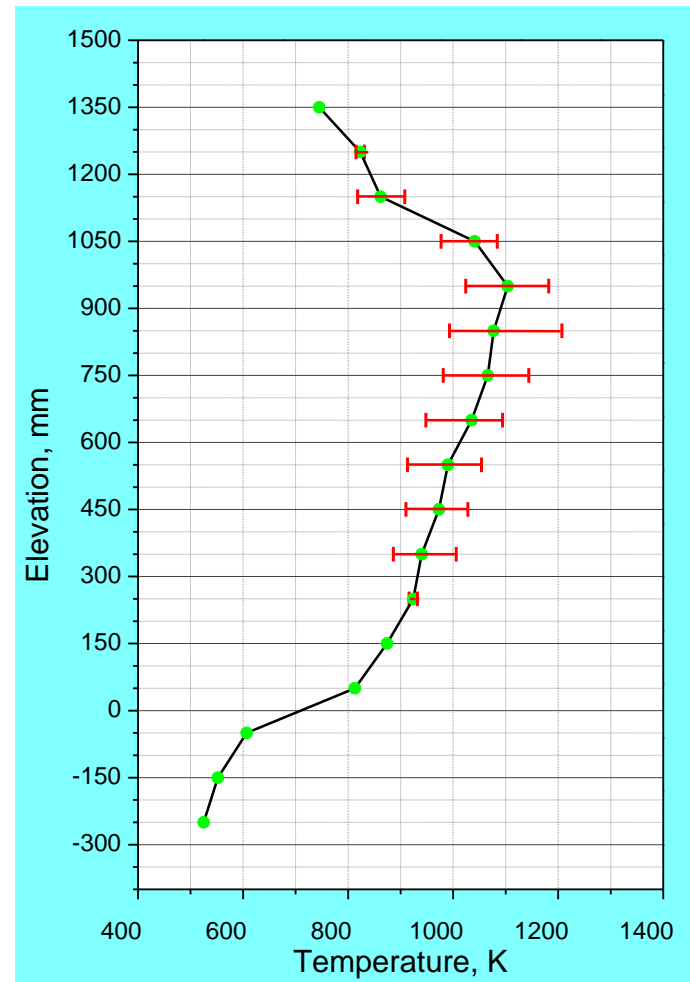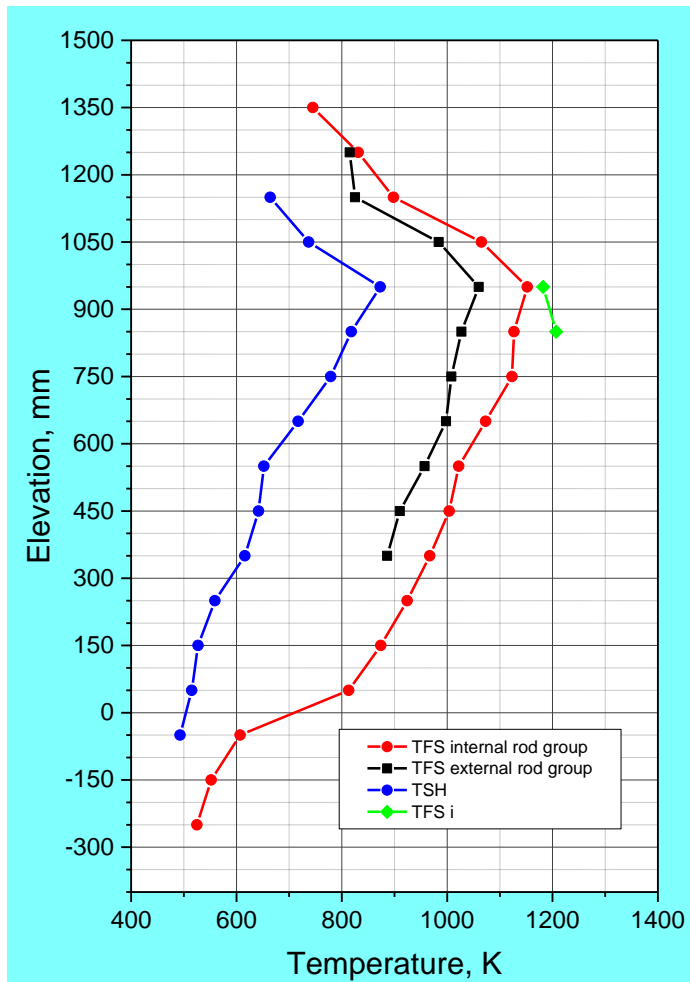
Figure 53   QUENCH-L5; Axial temperature profile TFS internal and external rod group together with TSH, left, and axial temperature profile of all TFS, right, at 73 s (last cladding burst).
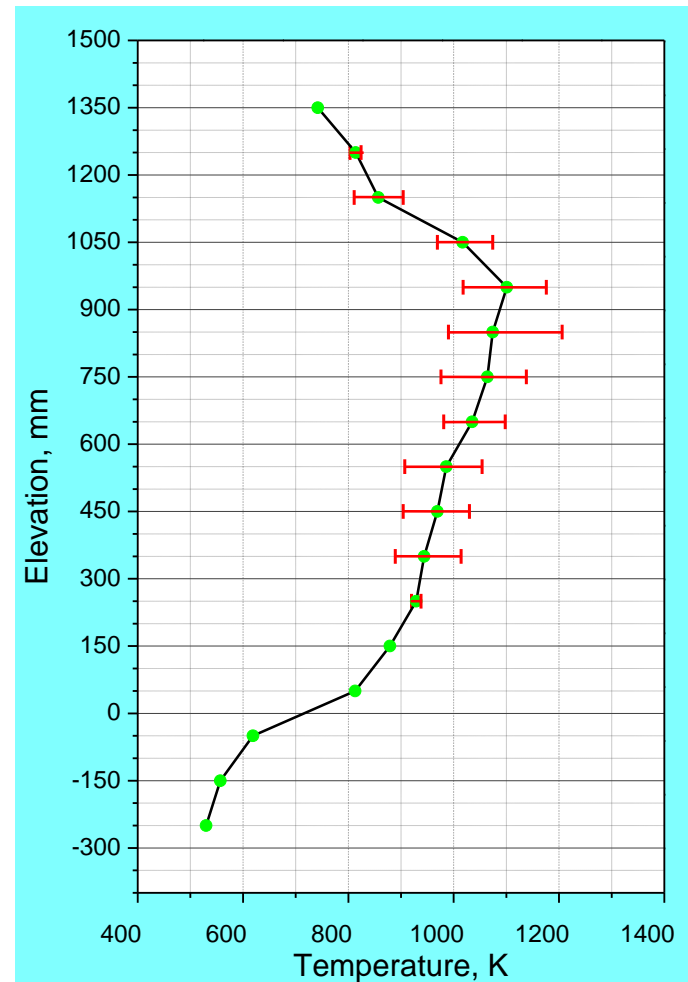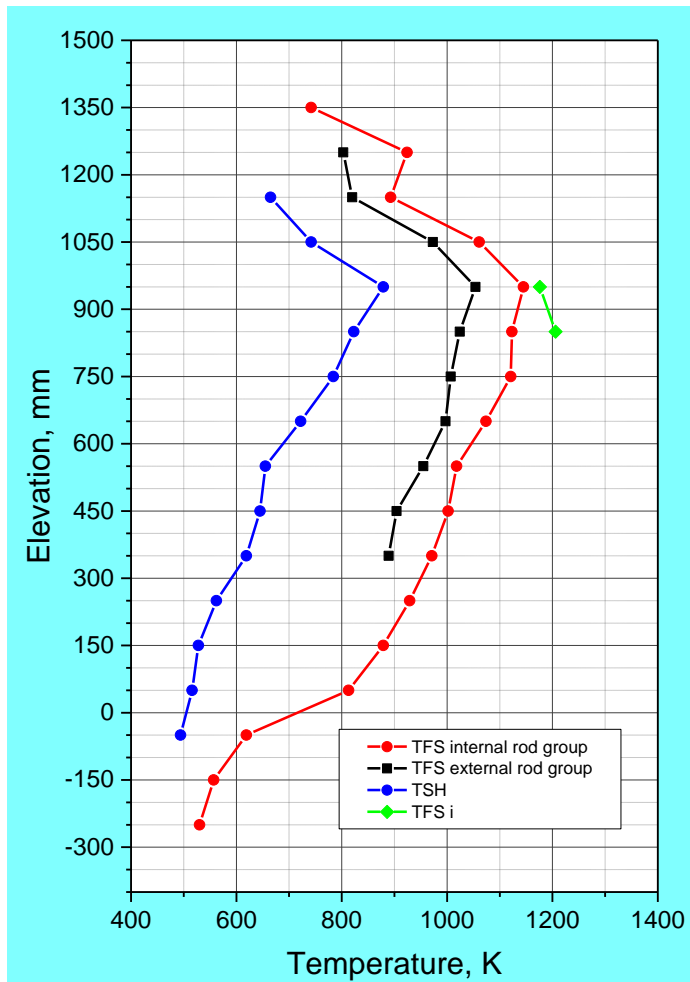
Figure 54 QUENCH-L5; Axial temperature profile TFS internal and external rod group together with TSH, left, and axial temperature profile of all TFS, right, at 74,6 s (end of transient).
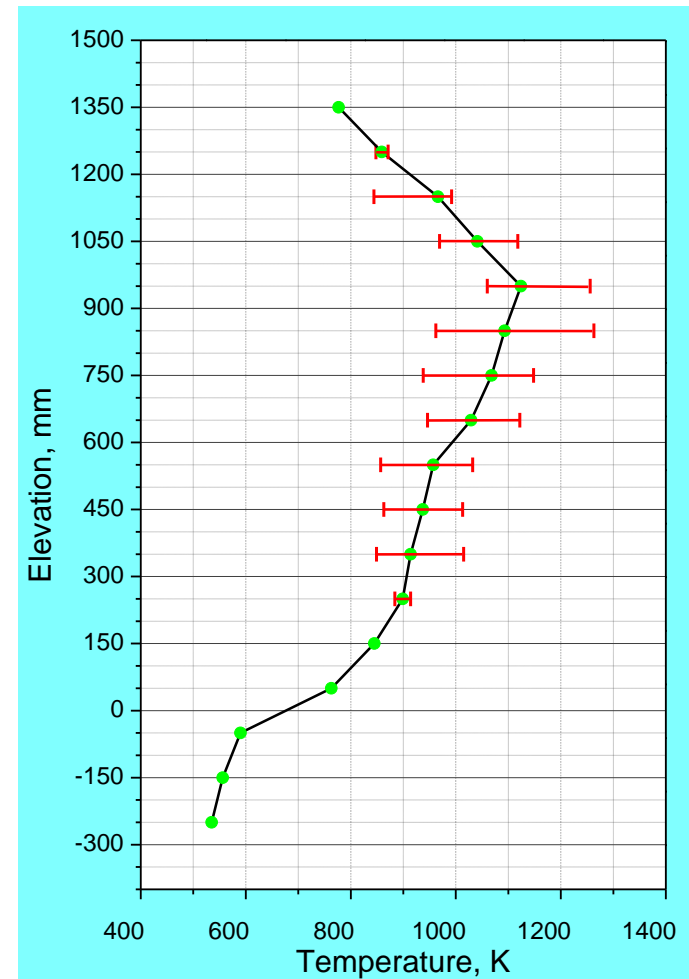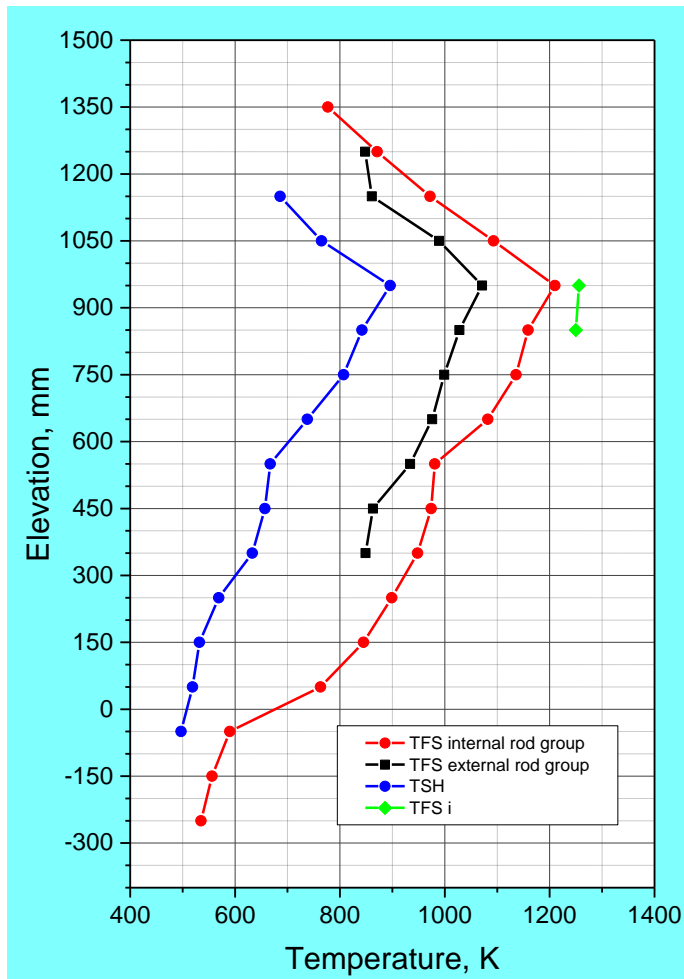
Figure 55   QUENCH-L5; Axial temperature profile TFS internal and external rod group together with TSH, left, and axial temperature profile of all TFS, right, at 81,4 s (max temperature).
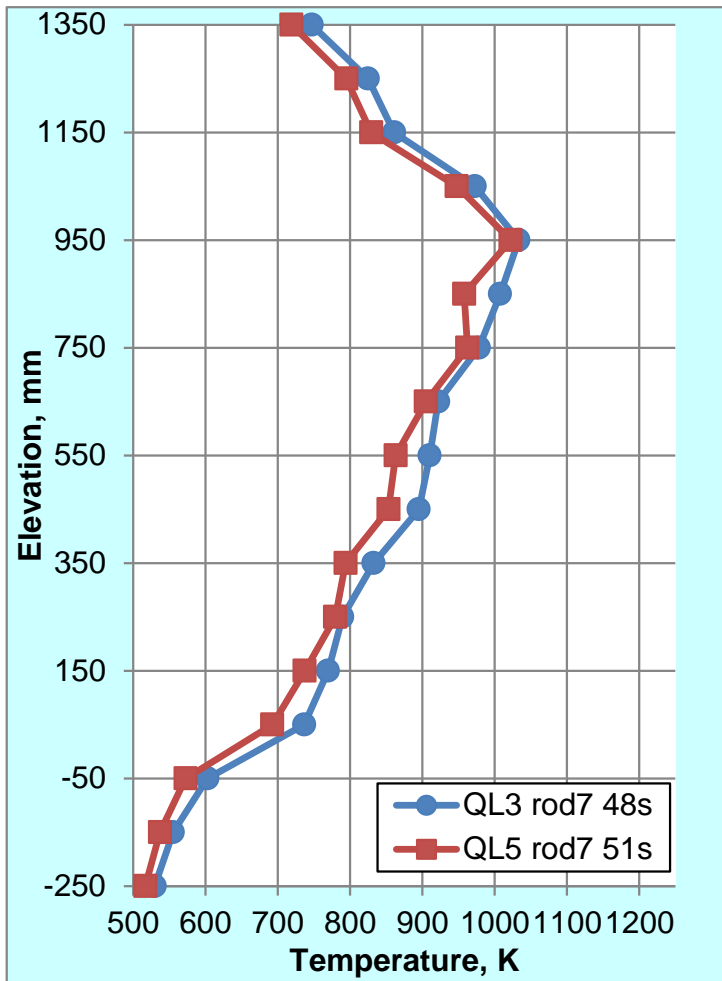
at the first cladding burst
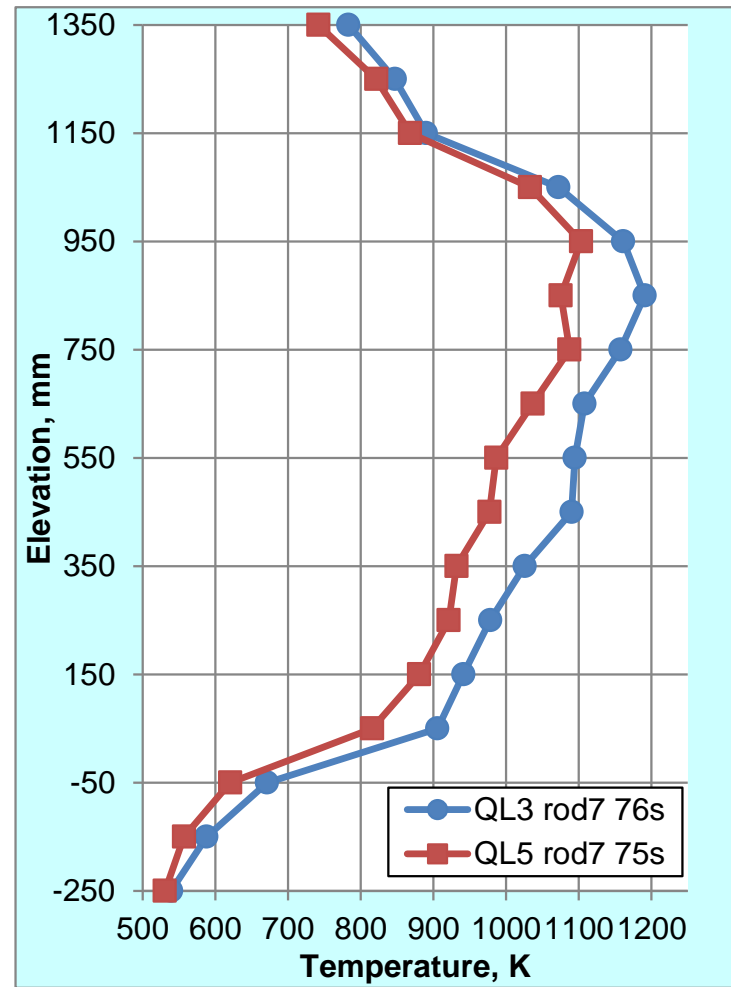
at the end of transient

Figure 56 QUENCH-L5; Comparison of axial temperature profiles of QUENCH-L3 and QUENCH-L5 during the burst occurrence.
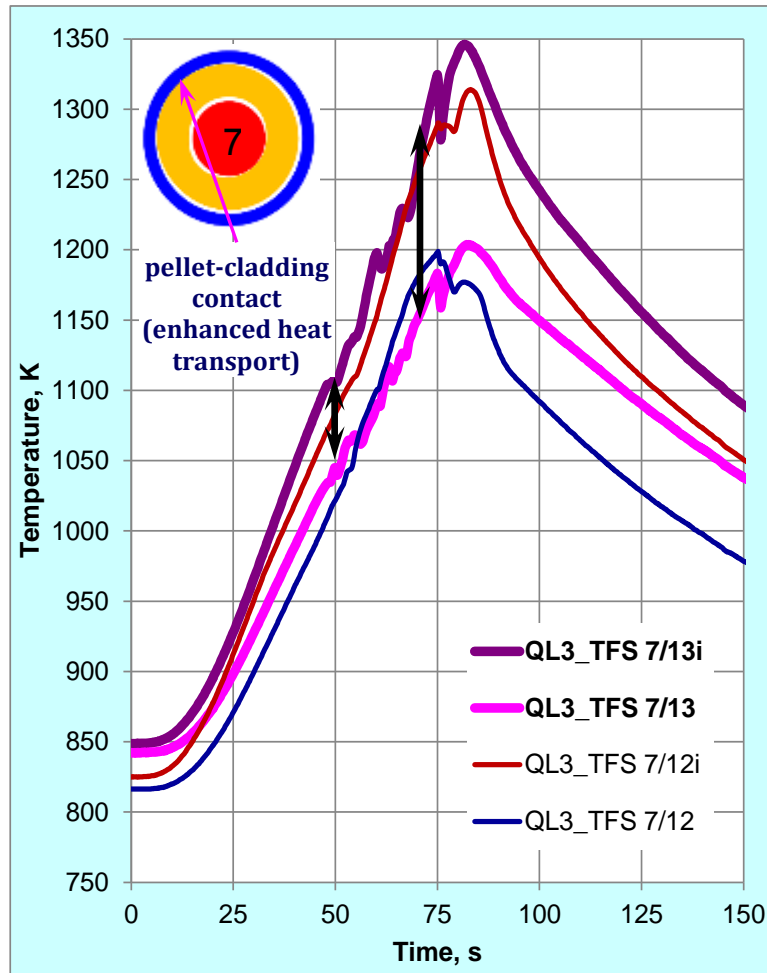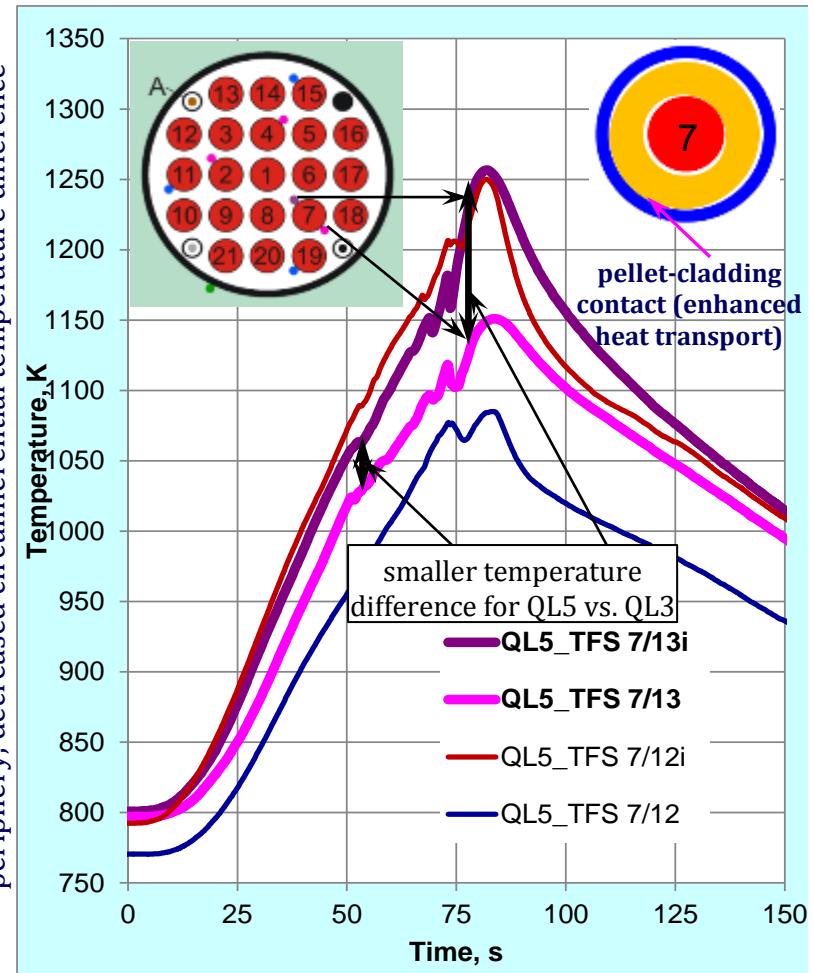
Figure 57 QUENCH-L5; Radial temperature difference during burst period as superposition of global heat loss through shroud and local pellet displacement: comparison with QUENCH-L3.
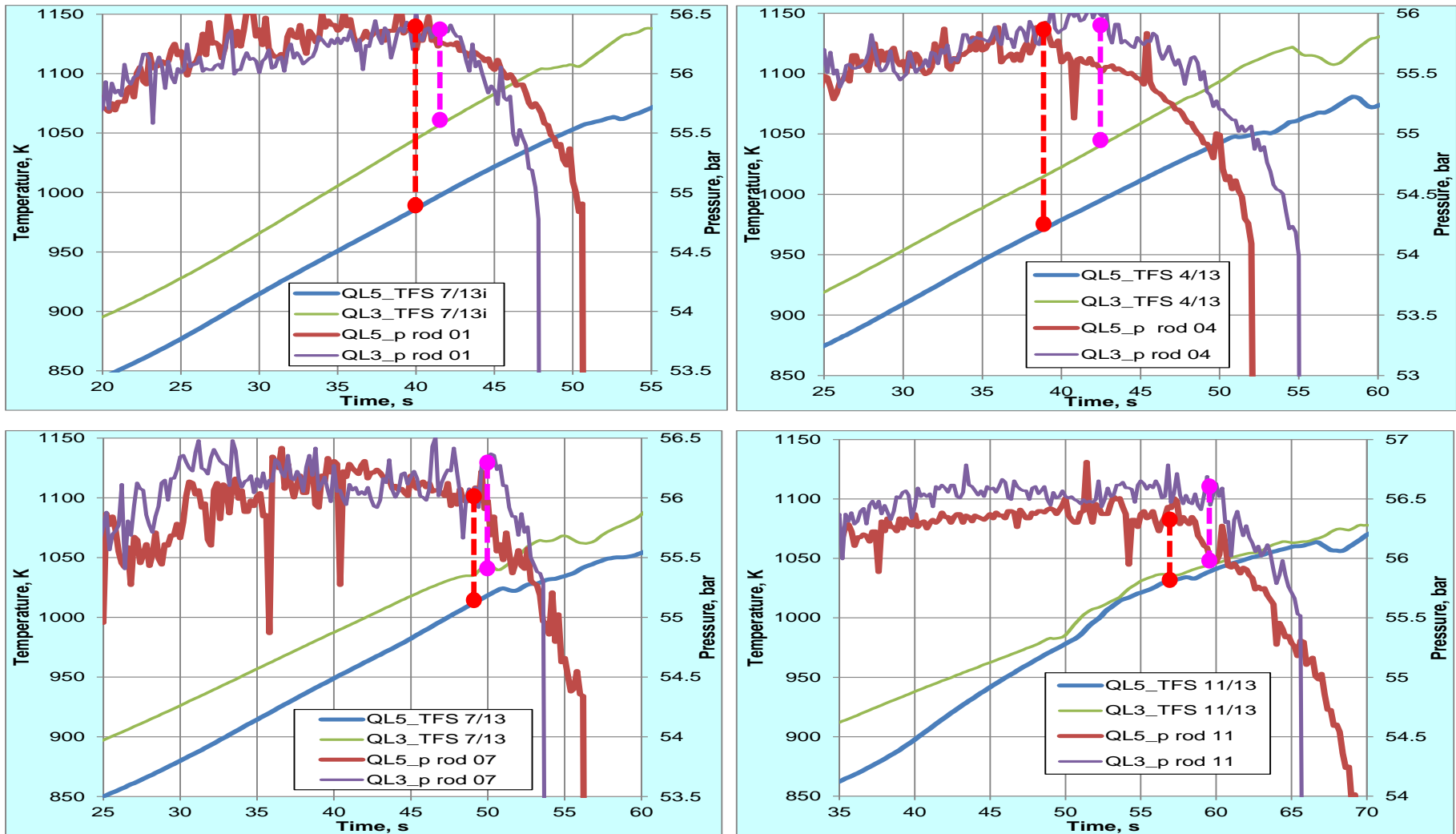
Figure 58 Pressure and temperature readings for different rods of bundles QUENCH-L3 and -L5: onset of ballooning at lower temperatures for QL-5 (Zr alloy with dissolved hydrogen will be more ductile at lower temperatures than not hydrogenated Zr alloy).
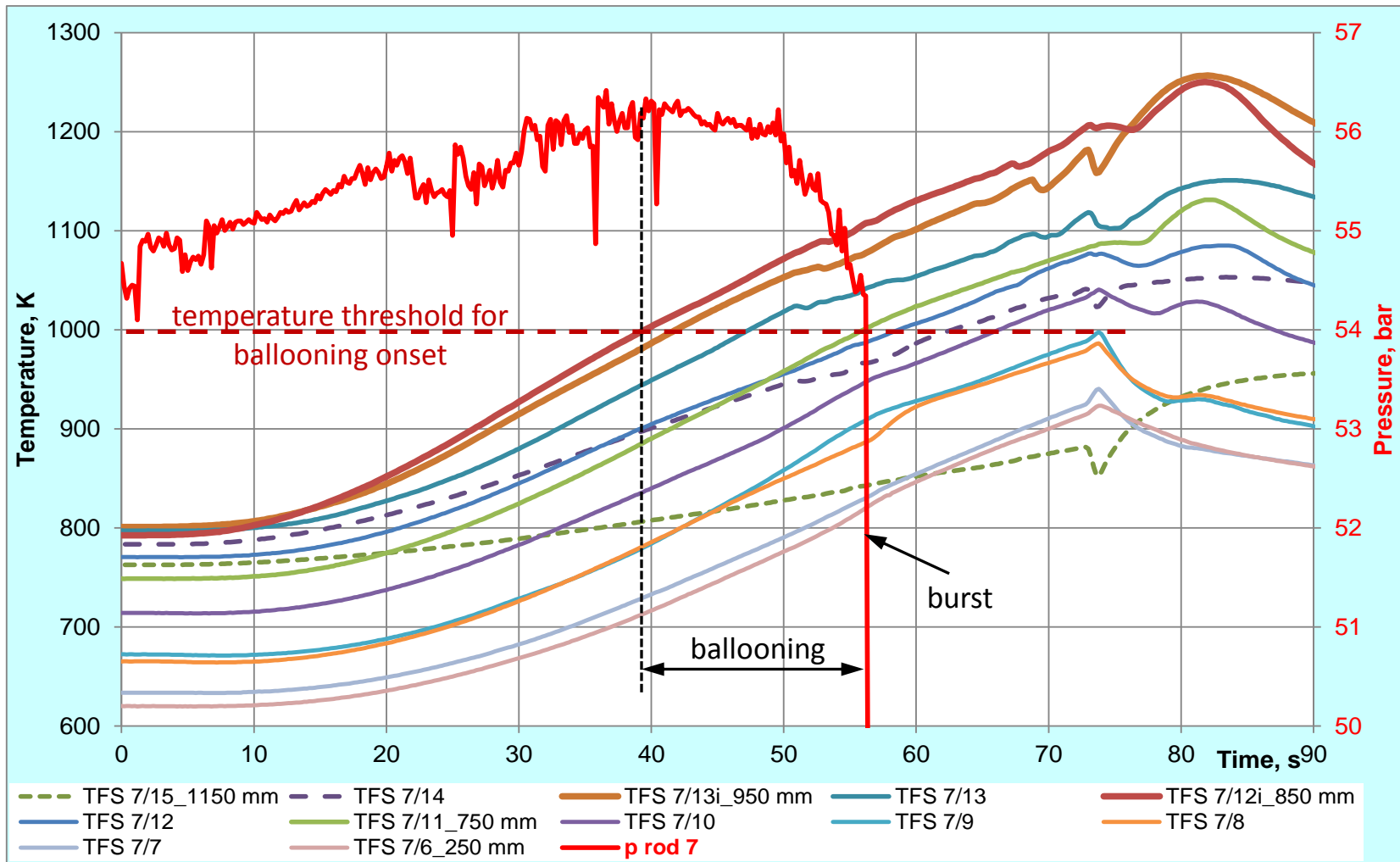
Figure 59   QUENCH-L5; sequence of ballooning onsets at different bundle elevations for rod #7 (reason of multiple ballooning regions).
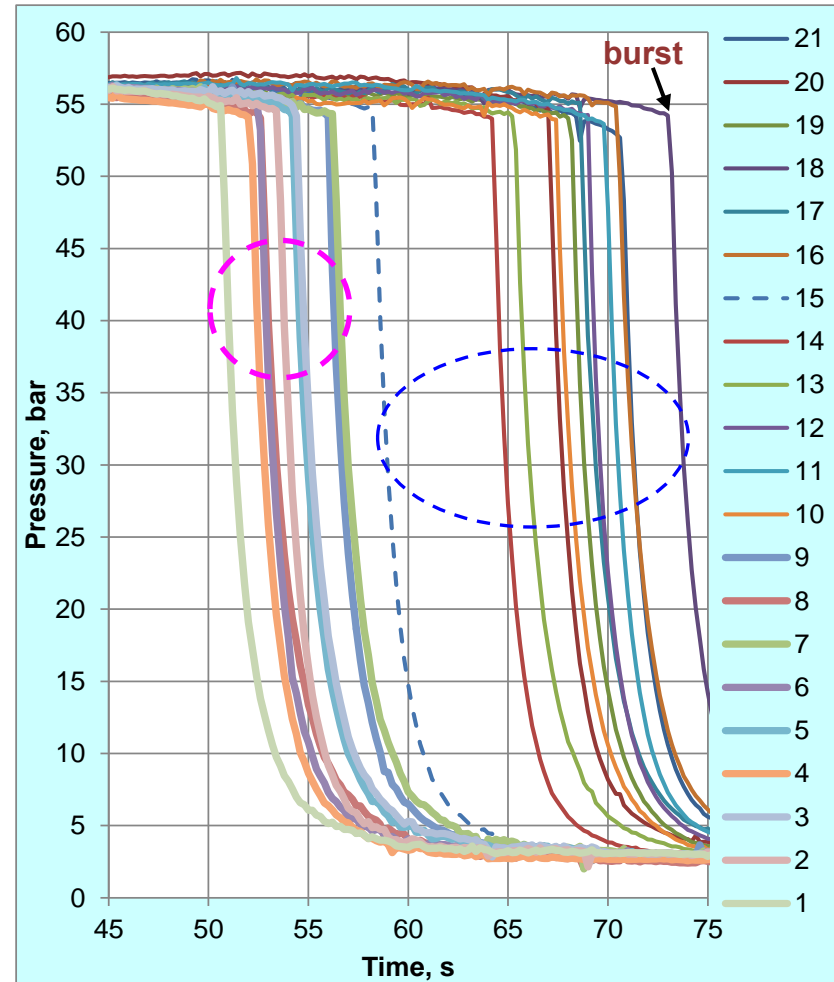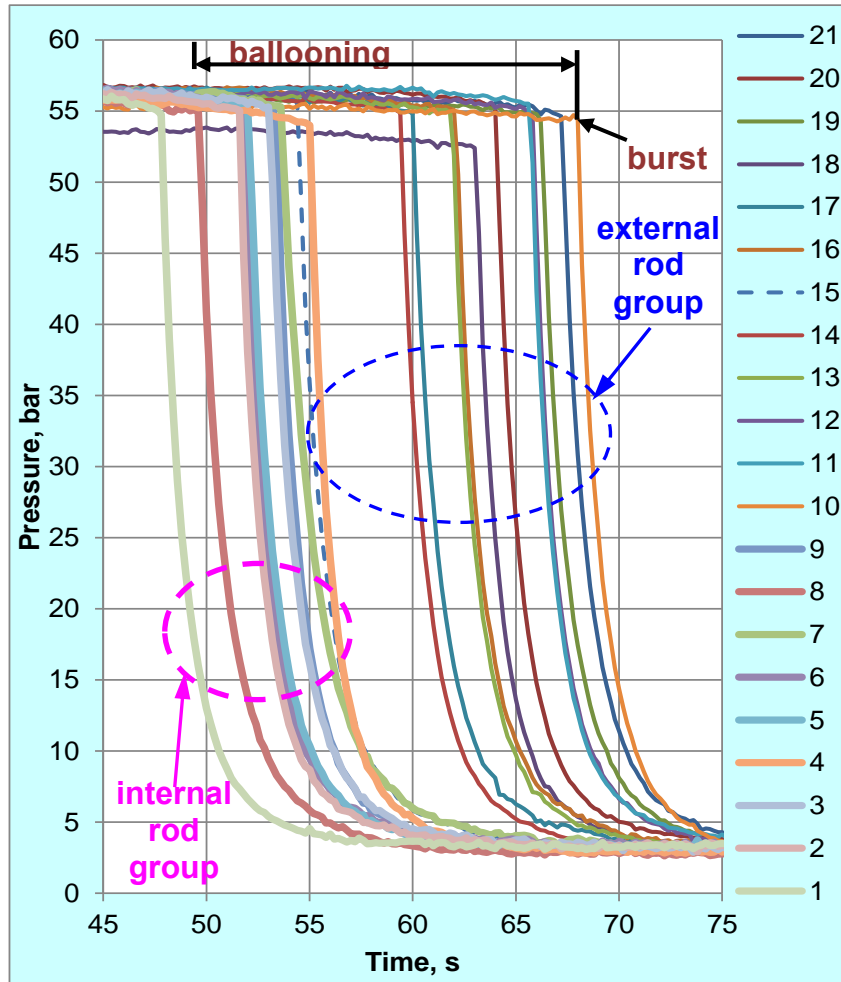
Figure 60 Rod pressure evolution during heating phase for QUENCH-L3 (left) and -L5 (right): burst time indication (rod #15 is connected electrically to internal rod group).
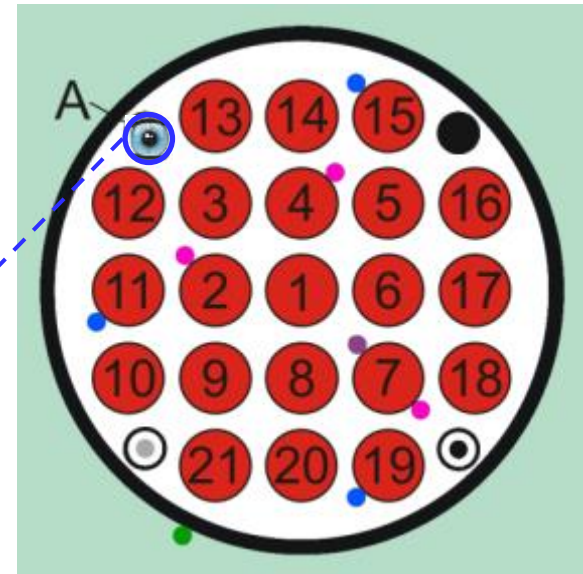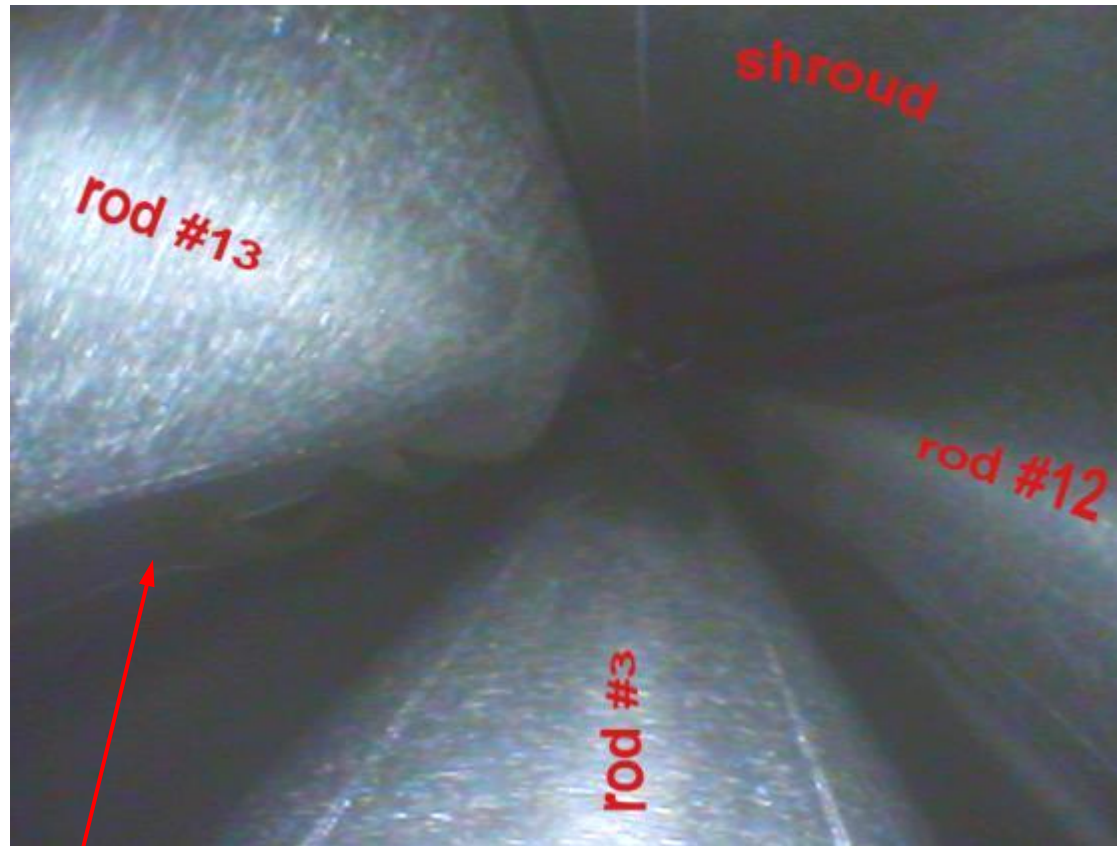
Figure 61   QUENCH-L5; videoscope observations with camera inserted from the bundle bottom at position of corner rod A.
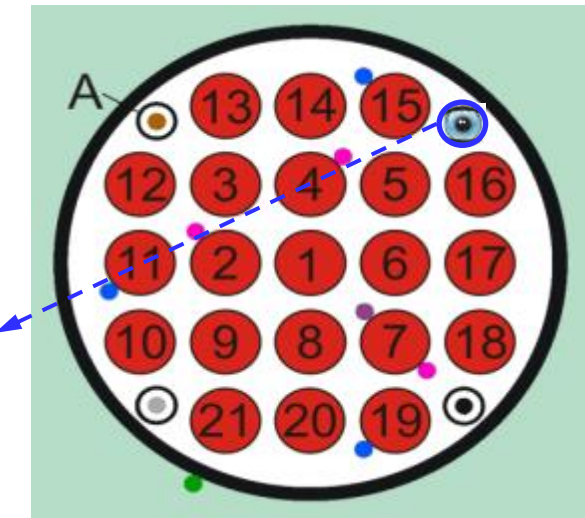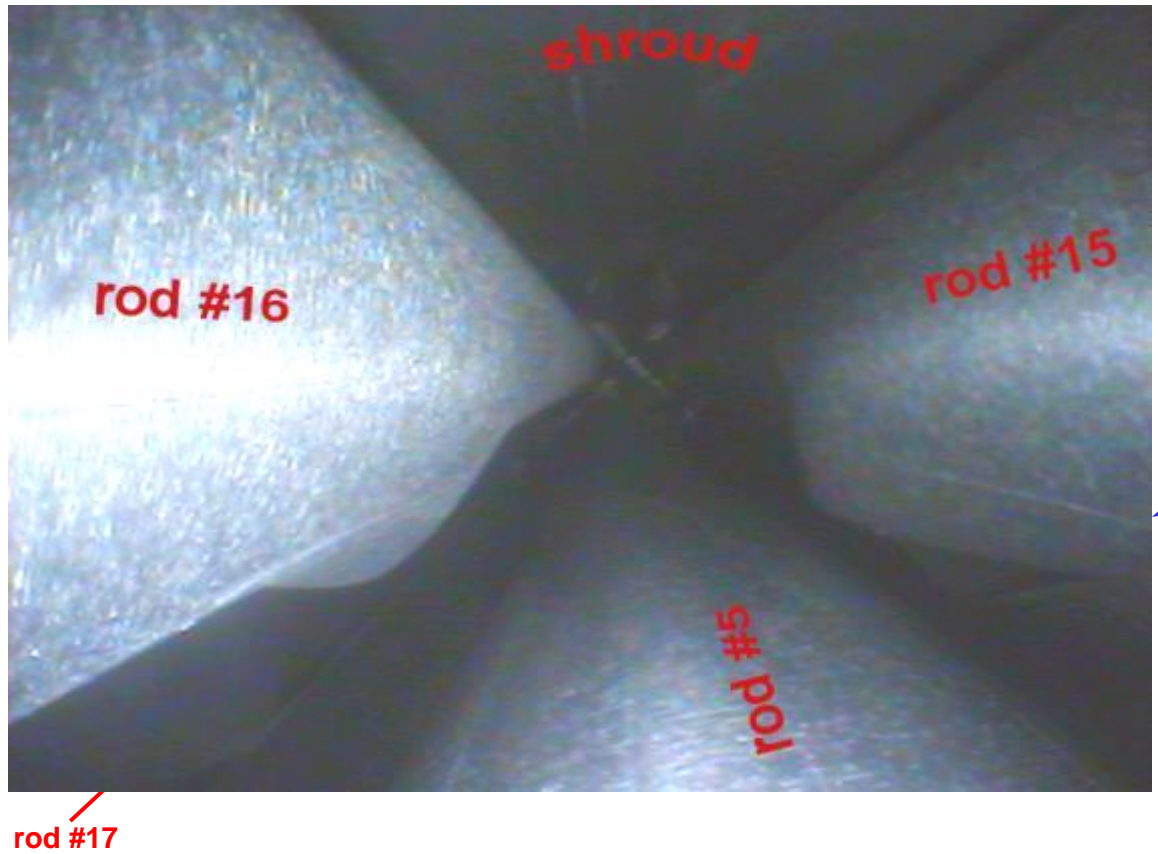
Figure 62   QUENCH-L5; videoscope observations with camera inserted from the bundle bottom at position of corner rod B.
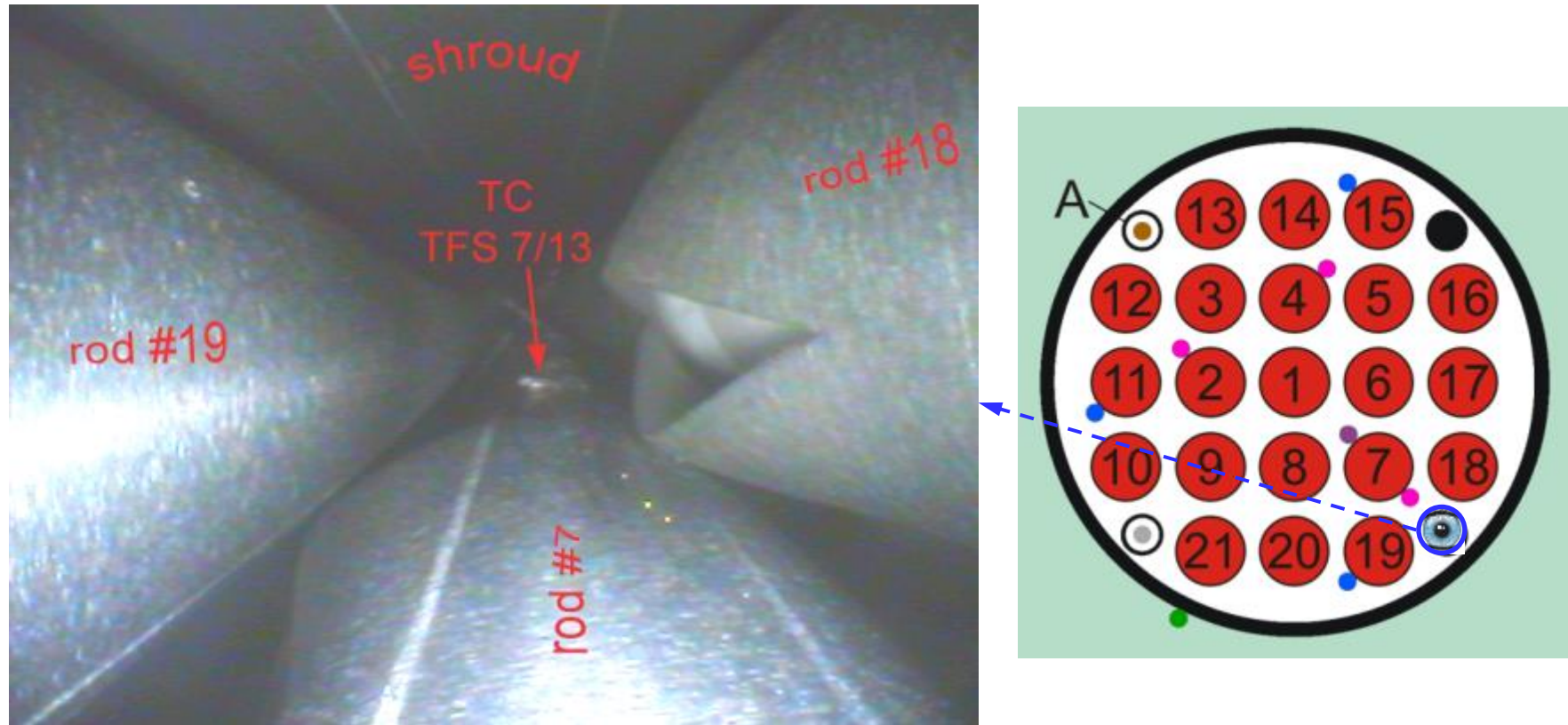
Figure 63   QUENCH-L5; videoscope observations with camera inserted from the bundle bottom at position of corner rod C.
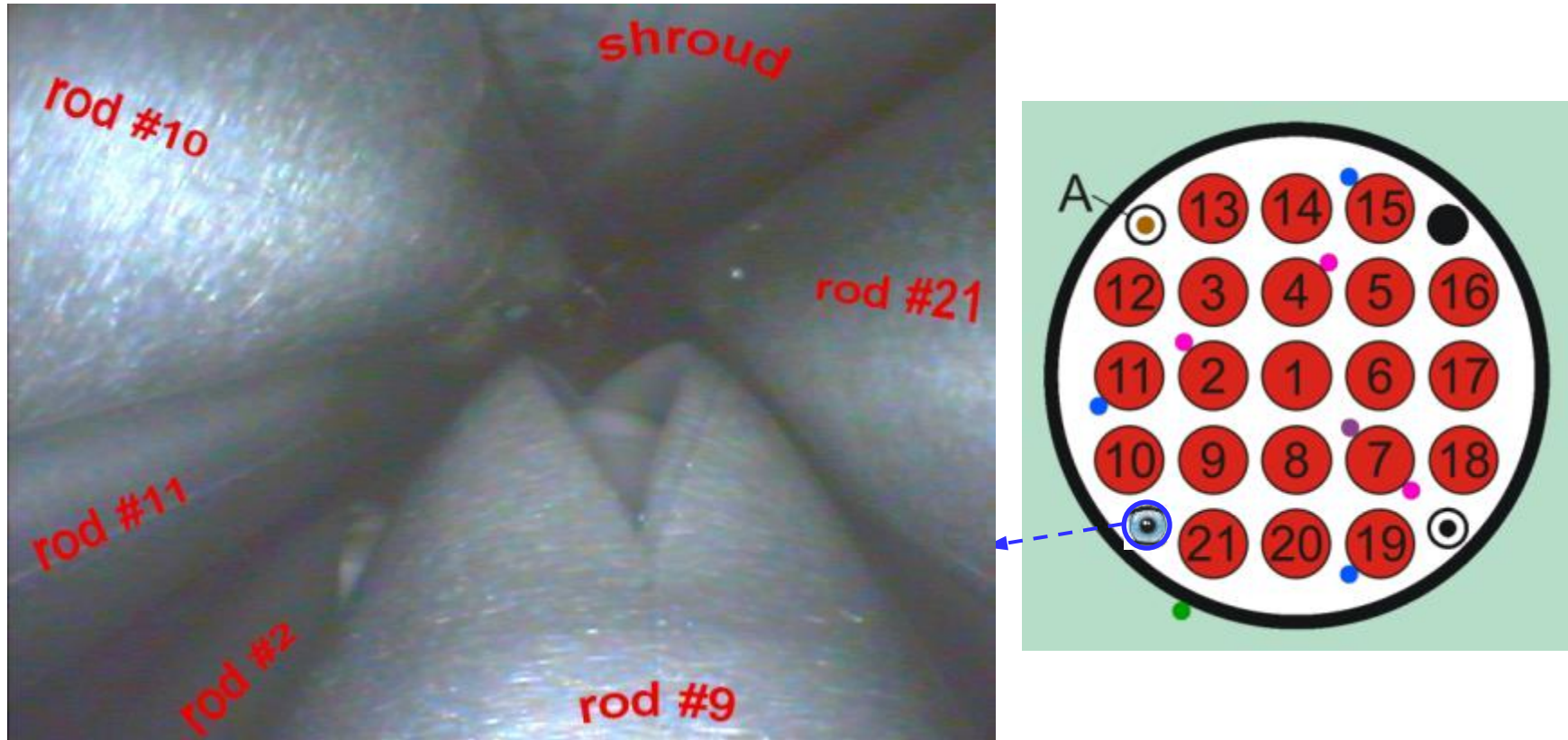
Figure 64   QUENCH-L5; videoscope observations with camera inserted from the bundle bottom at position of corner rod D.
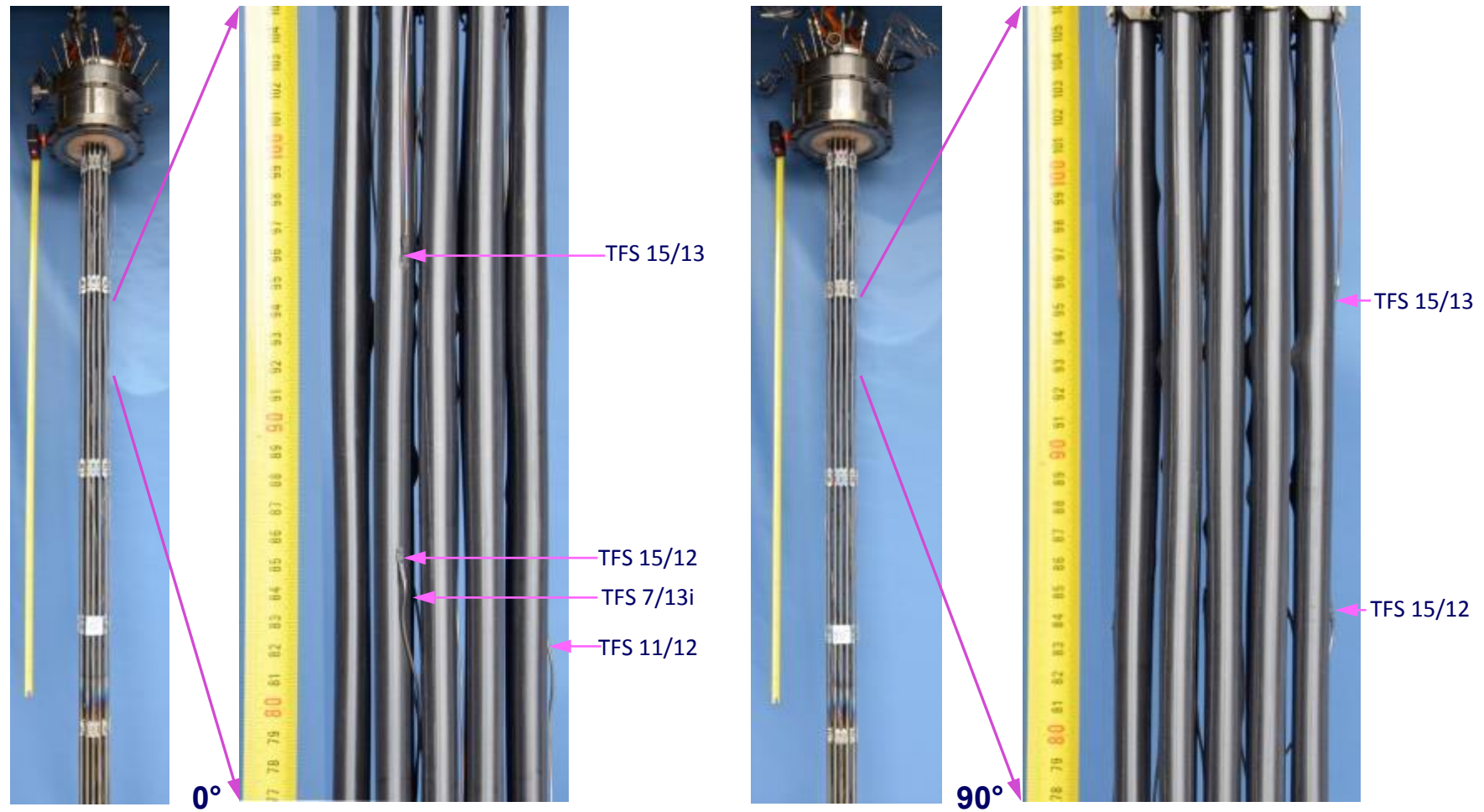
Figure 65 QUENCH-L5; Views of bundle at angle positions of 0° and 90°: negligible rod bending and intact thermocouples.
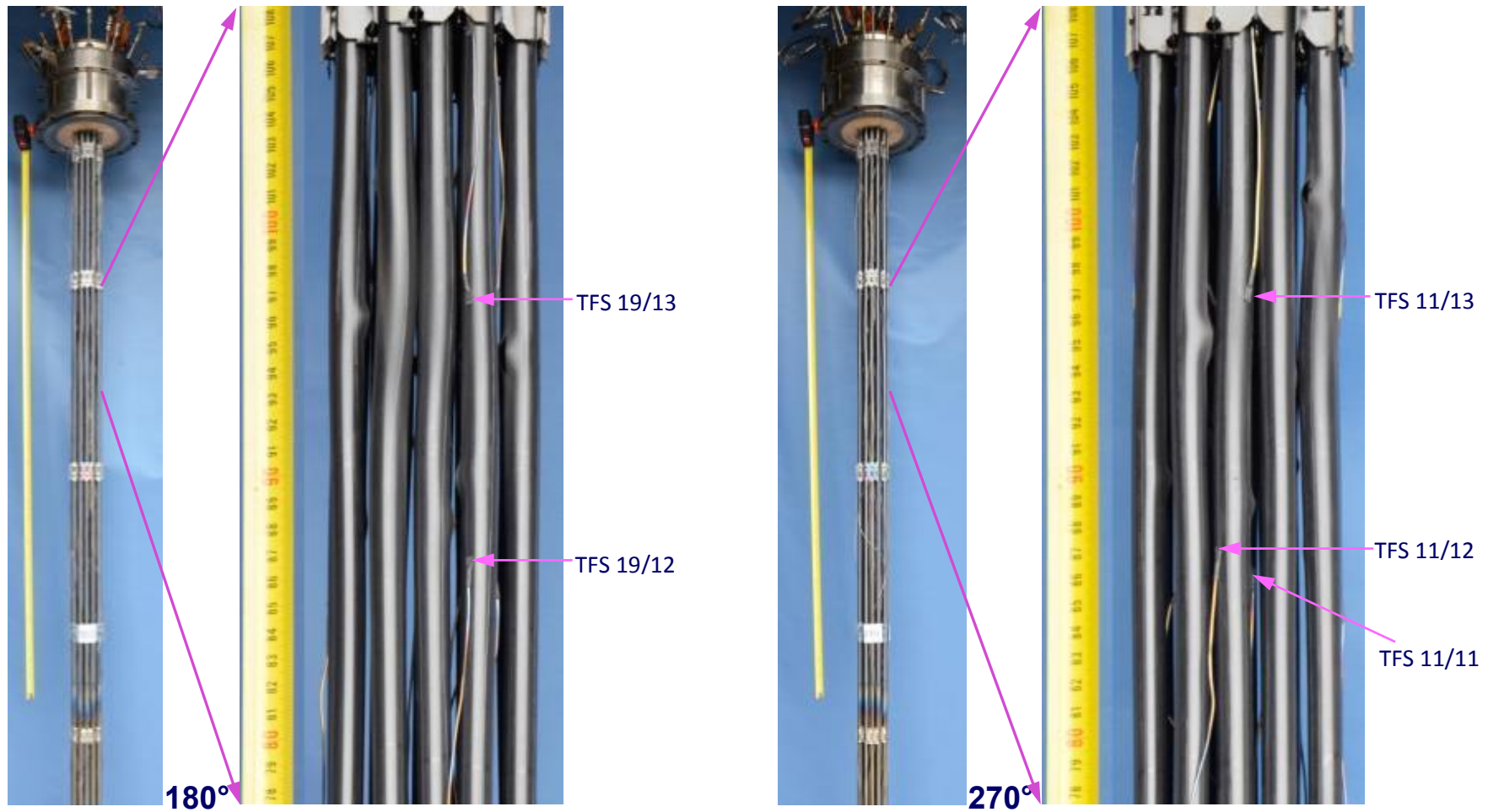
Figure 66   QUENCH-L5; Views of bundle at angle positions of 180° and 270°: negligible rod bending and intact thermocouples.
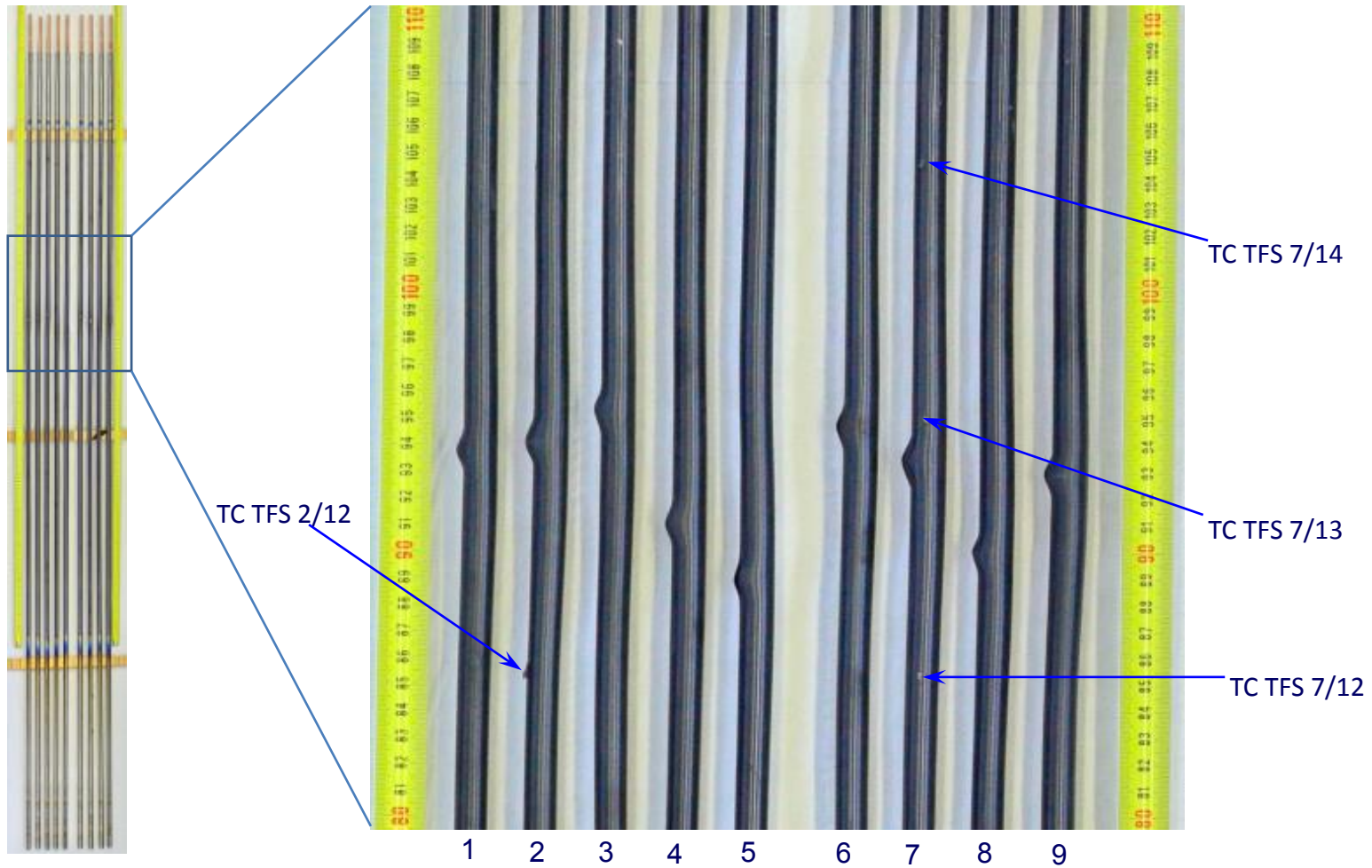
Figure 67 QUENCH-L5; post-test overview of inner rods; burst front view (left): no bending; side view (right): slight rod bending in the plane going through the burst opening, burst opening always at concave side.
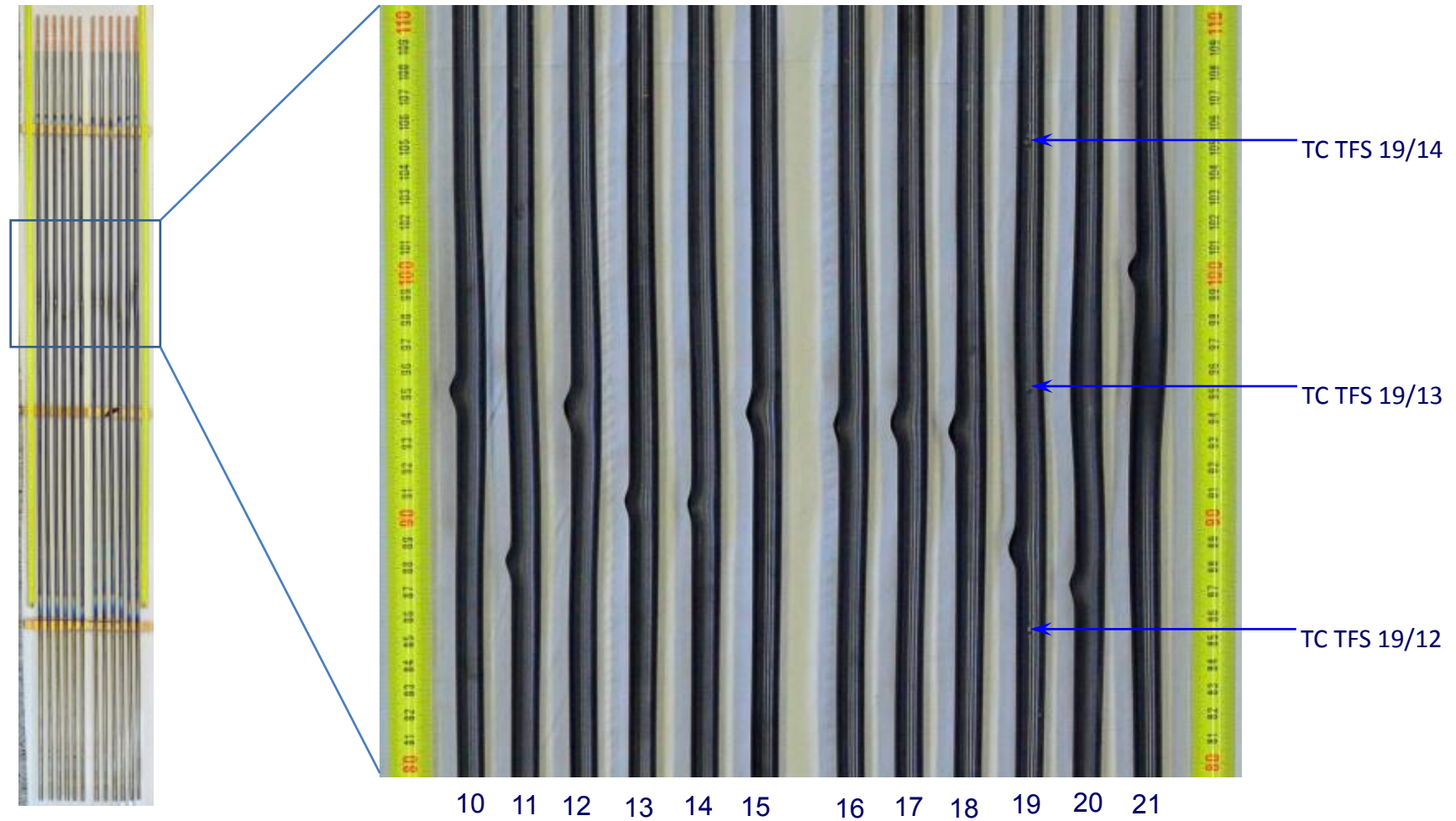
Figure 68 QUENCH-L5; post-test overview of outer rods; burst front view (left): no bending (excluding rods 20 and 21 with second ballooning); side view (right): slight rod bending in the plane going through the burst opening, burst opening always at concave side.
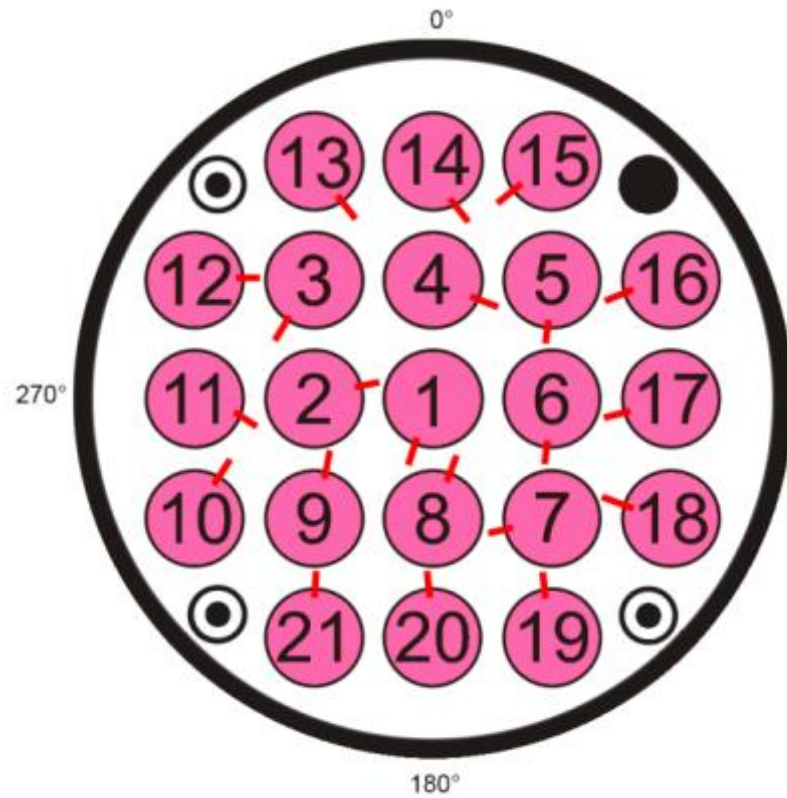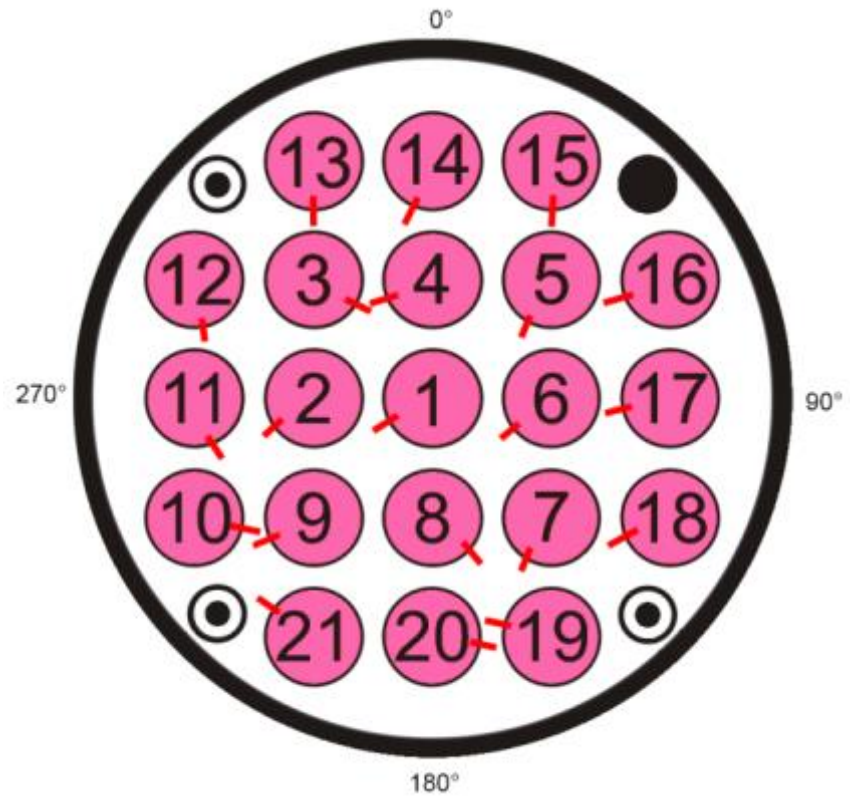
Figure 69 Burst opening orientations of QUENCH-L3 and QUENCH-L5 bundles, top view.
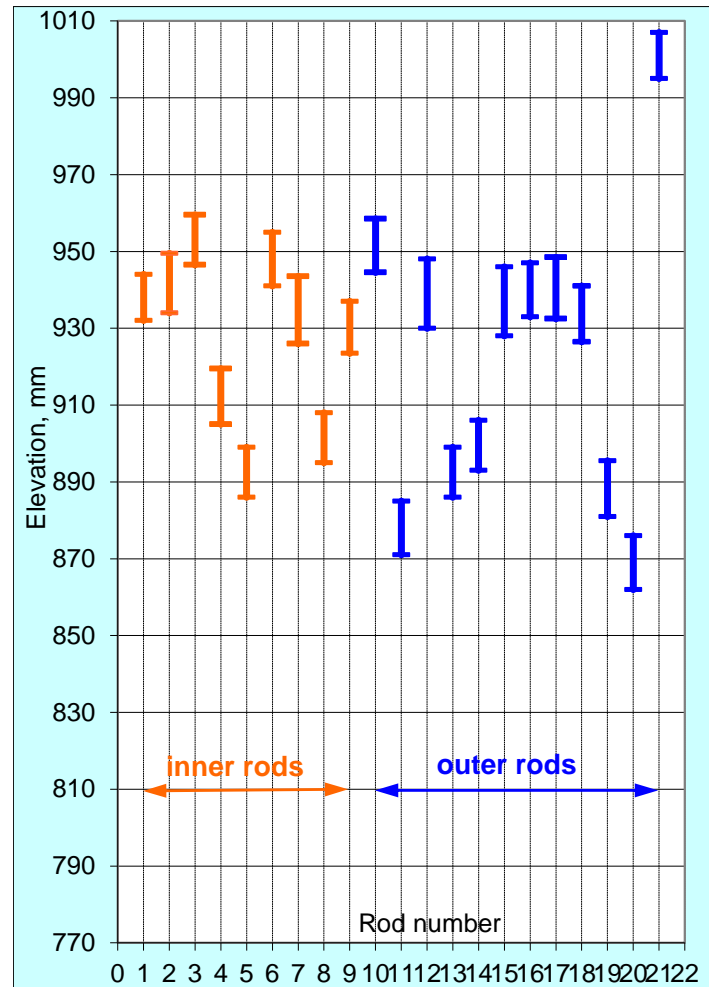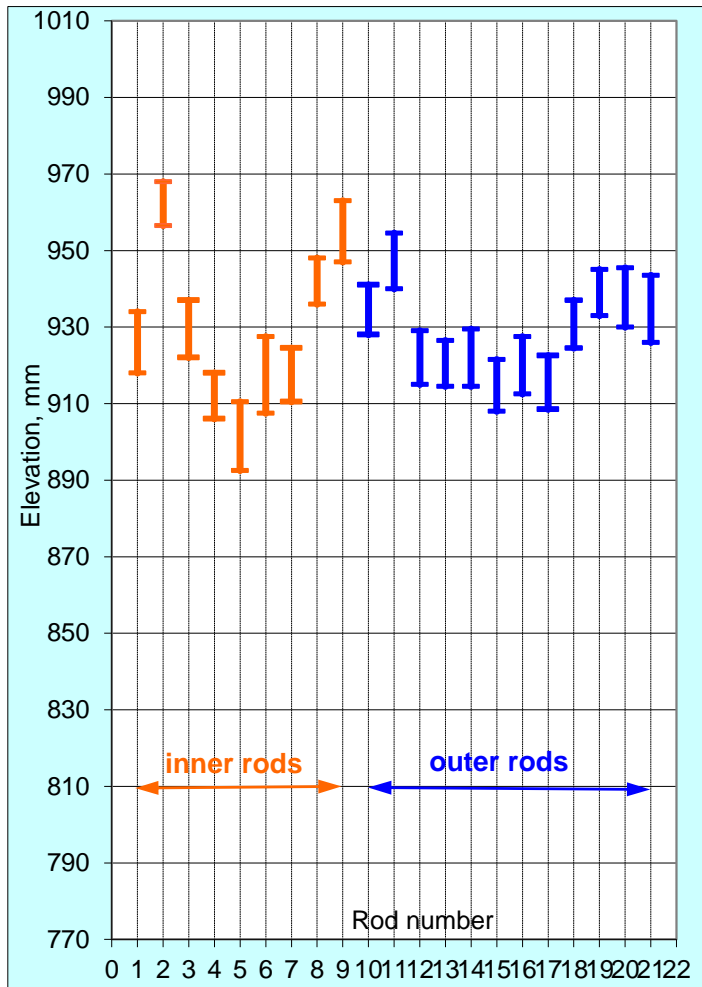
Figure 70 Vertical positions of burst openings for QUENCH-L3 (left) and QUENCH-L5 (right) bundles: scattering of opening positions is noticeable larger for QUENCH-L5.
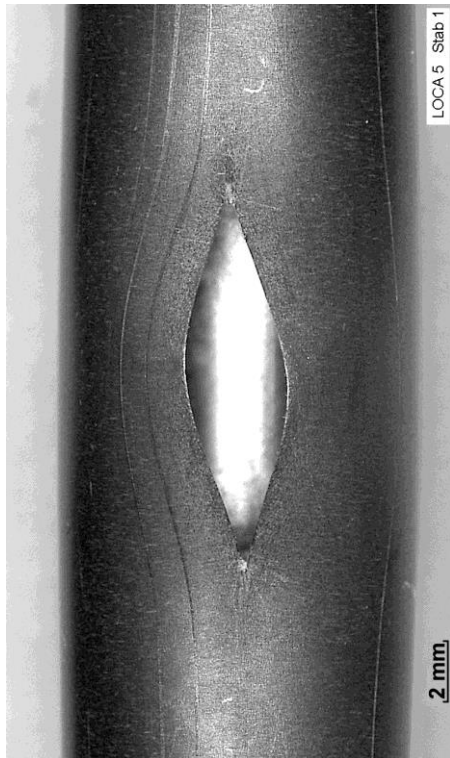
rod #1: burst at 244°; Aburst=24.2 mm²,
w=3.4 mm, h=12 mm
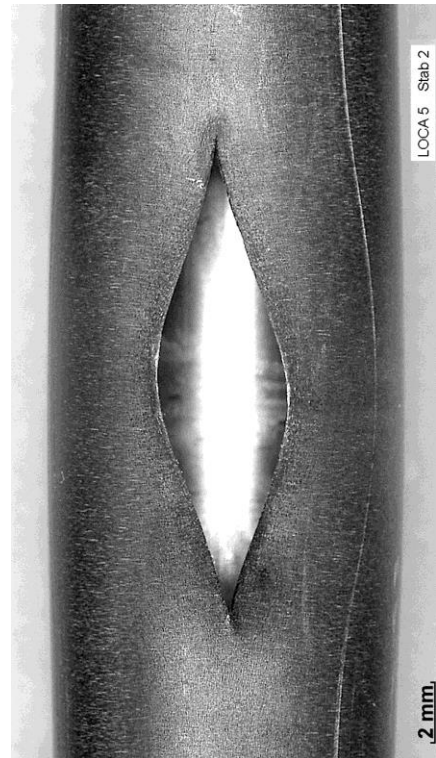
rod #2: burst at 231°; Aburst=35.1 mm²,
w=4.4 mm, h=15.5 mm
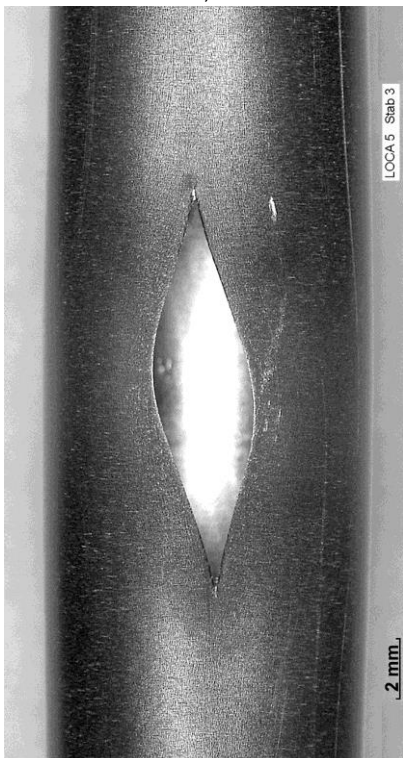
rod #3: burst at 127°; Aburst=23.4 mm²,
w=3.3 mm, h=13 mm
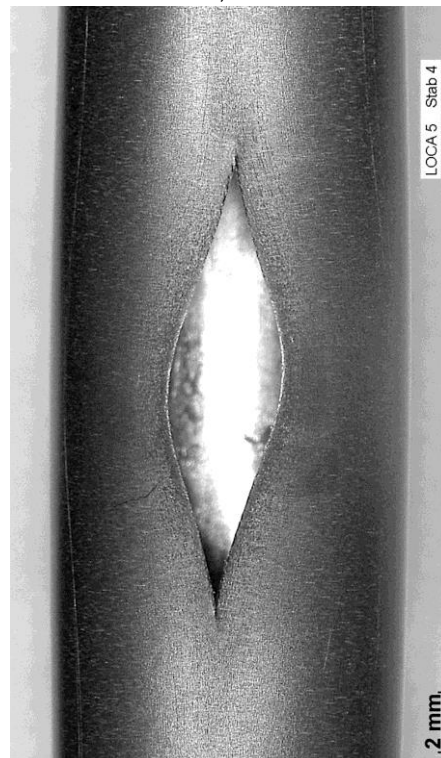
rod #4: burst at 236°; Aburst=28.8 mm²,
w=3.9 mm, h=14.5 mm

Figure 71   QUENCH-L5; overview of burst structures of rods #1 - #4.

rod #5: burst at 203°; Aburst=21 mm²,
w=3.0 mm, h=13 mm

rod #6: burst at 232°; Aburst=27 mm²,
w=3.6 mm, h=14 mm

rod #7: burst at 196°; Aburst=46 mm²,
w=4.9 mm, h=17.5 mm

rod #8: burst at 147°; Aburst=21 mm²,
w=3.2 mm, h=13 mm

Figure 72   QUENCH-L5; overview of burst structures of rods #5 - #8.
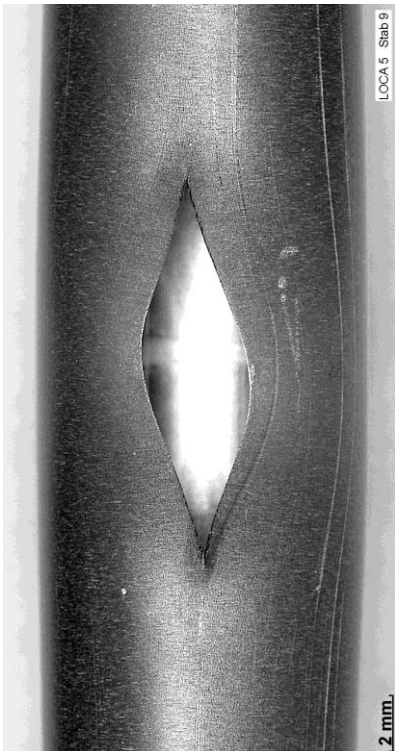
rod #9: burst at 237°; Aburst=28 mm²,
w=3.9 mm, h=13.5 mm
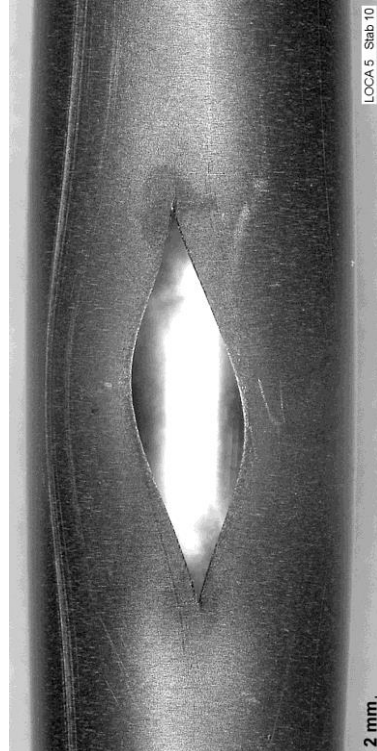
rod #10: burst at 108°; Aburst=31 mm²,
w=4.0 mm, h=14 mm
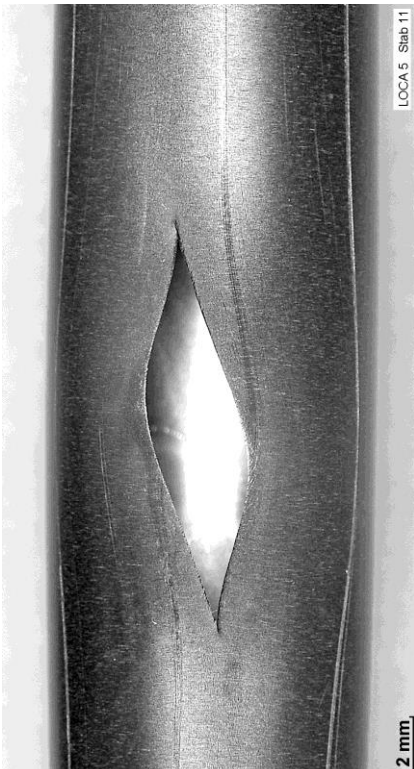
rod #11: burst at 160°; Aburst=27 mm²,
w=3.7 mm, h=14 mm

rod #12: burst at 175°; Aburst=52 mm²,
w=4.9 mm, h=18 mm

Figure 73   QUENCH-L5; overview of burst structures of rods #9 - #12.

rod #13: burst at 180°; Aburst=19 mm²,
w=2.7 mm, h=13 mm
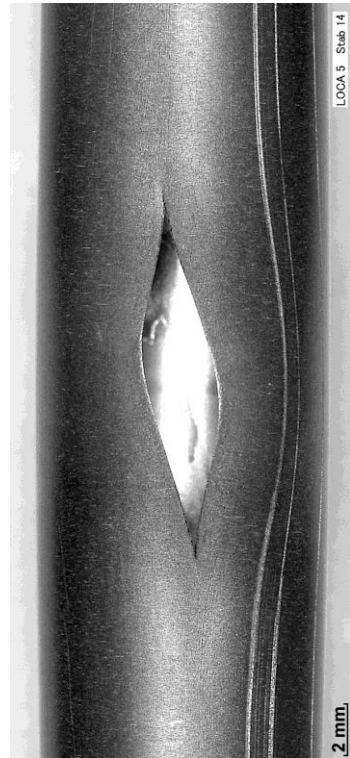
rod #14: burst at 212°; Aburst=20 mm²,
w=2.8 mm, h=13 mm

rod #15: burst at 182°; Aburst=40 mm²,
w=4.6 mm, h=18 mm

rod #16: burst at 237°; Aburst=24 mm²,
w=3.1 mm, h=14 mm

Figure 74   QUENCH-L5; overview of burst structures of rods #13 - #16.
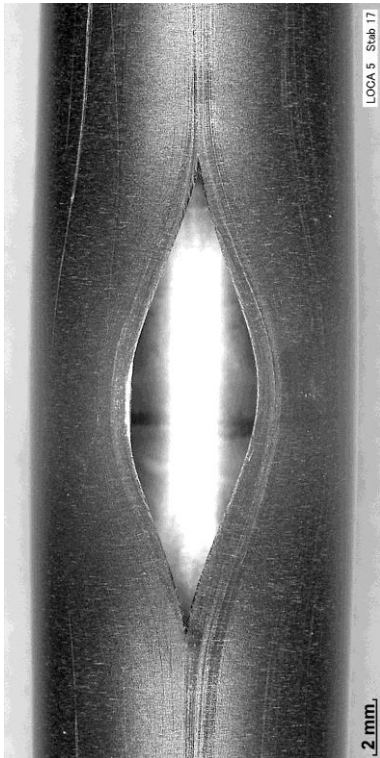
rod #17: burst at 265°; Aburst=41 mm²,
w=4.5 mm, h=16 mm

rod #18: burst at 228°; Aburst=34 mm²,
w=4.1 mm, h=14.5 mm

rod #19: burst at 280°; Aburst=29 mm²,
w=3.5 mm, h=14.5 mm

Figure 75   QUENCH-L5; overview of burst structures of rods #17 - #19.

rod #20: burst at 99°; Aburst=29 mm²,
w=3.6 mm, h=14 mm

rod #21: burst at 317°; Aburst=28 mm²,
w=3.8 mm, h=12 mm

Figure 76   QUENCH-L5; overview of burst structures of rods #20 - #21.

≈40 cracks/mm

≈20 cracks/mm
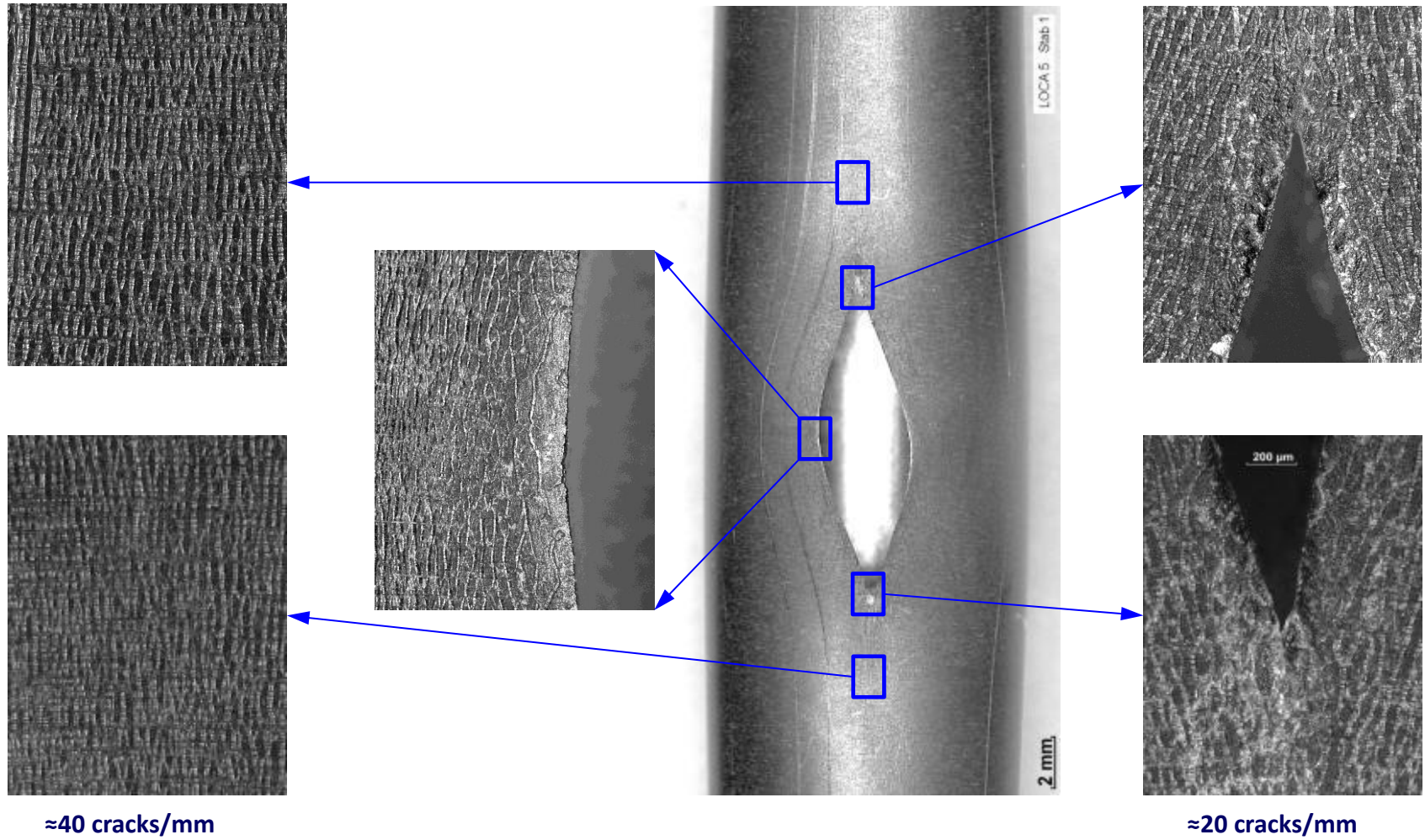
Figure 77   QUENCH-L5, Rod #1; cladding surface structure ("tree bark") formed during ballooning around the burst opening.

310°

40°

130°

circumferential
traces (mostly
tungsten) show
positions of
contacts
between pellets

burst opening

contact between pellet
and cladding
below burst opening
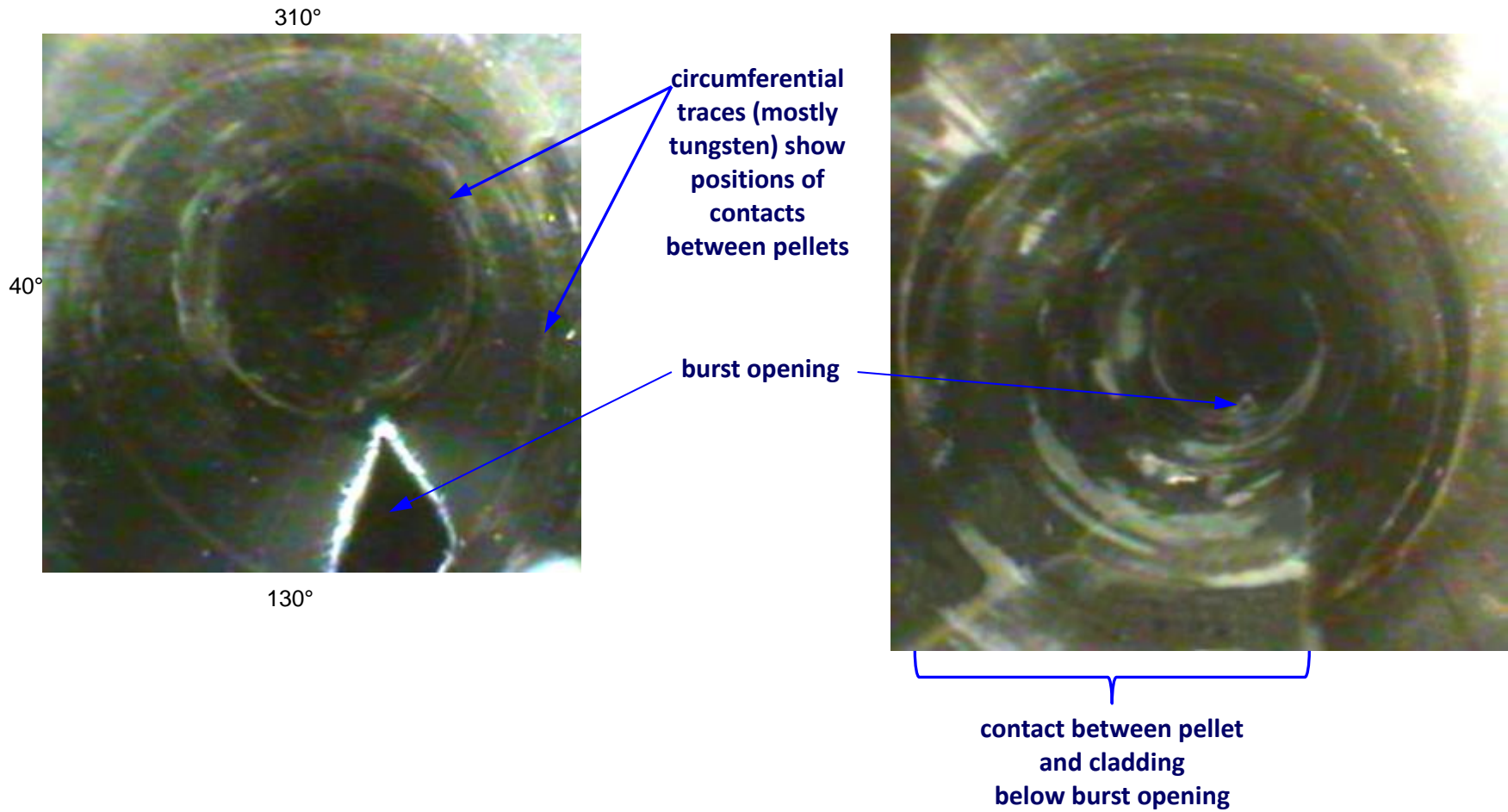
Figure 78   QUENCH-L5; videoscope observations of inner surface of cladding (rod #3, view from bottom): two phenomena of pellet influence.
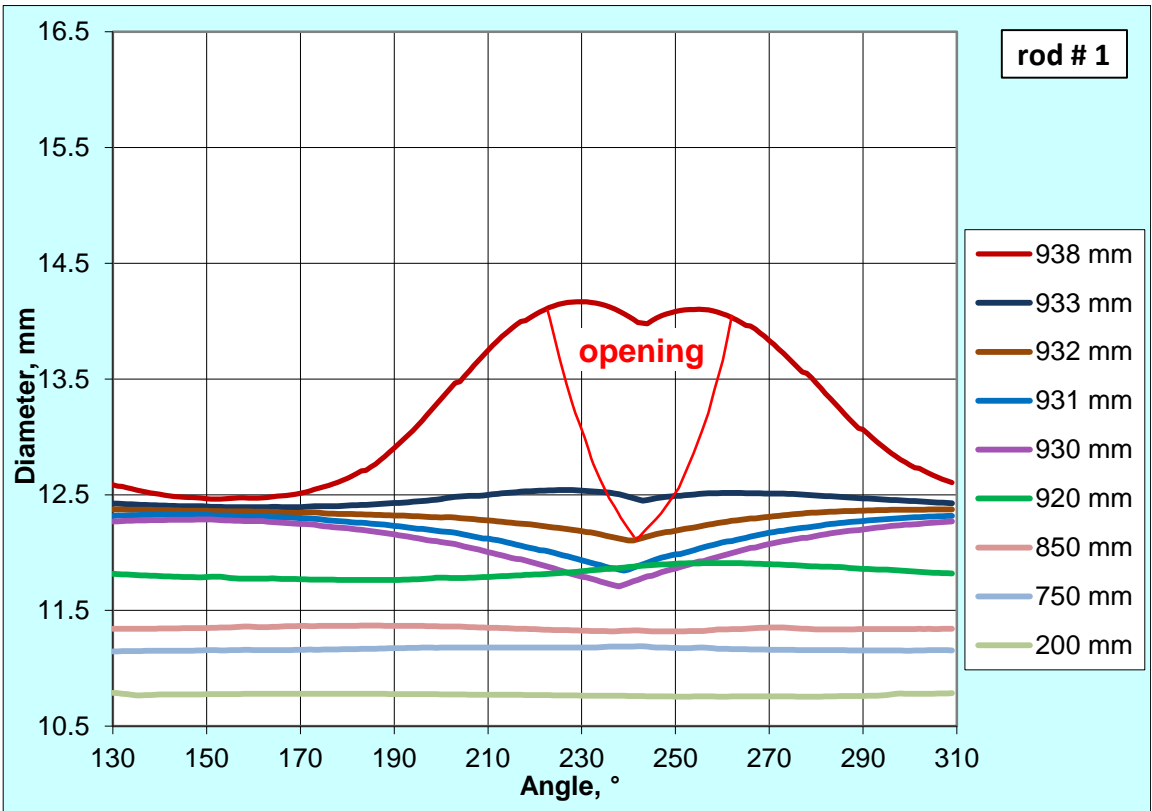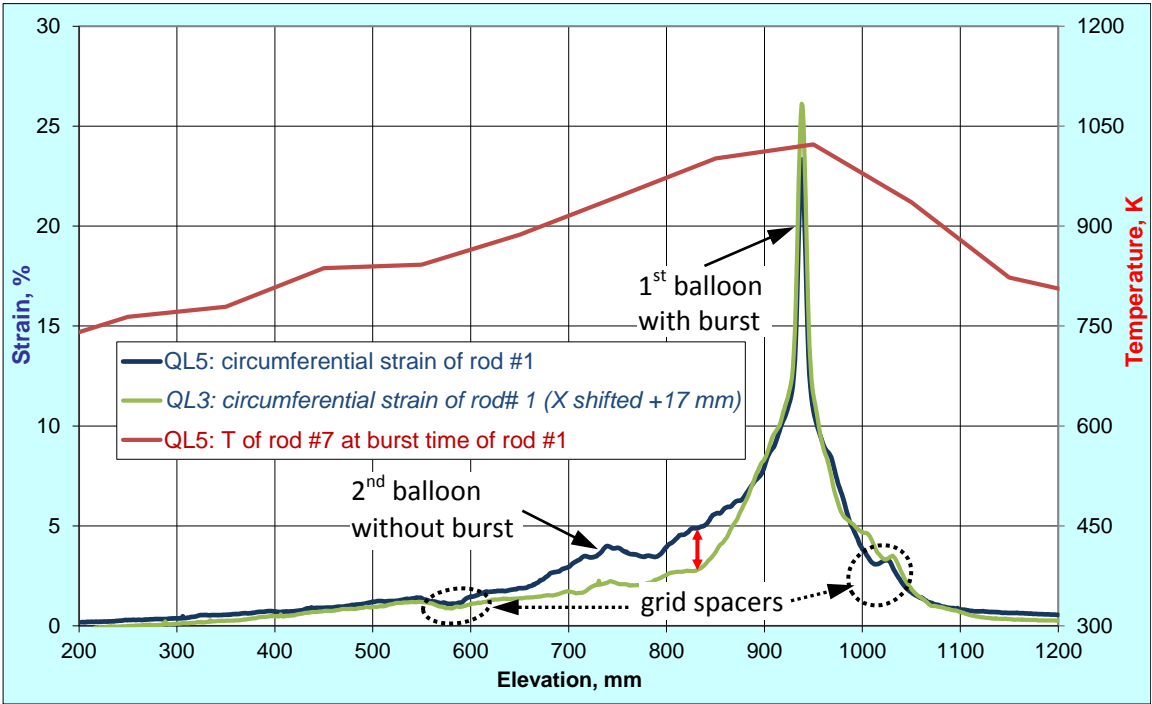
Figure 79 QUENCH-L5, Rod #1; longitudinal changing of circumferential strain (top): QL5 clad strain below main balloon exceeds corresponding strain of QL3 (red arrow); azimuthal diameter downwards from burst (bottom).
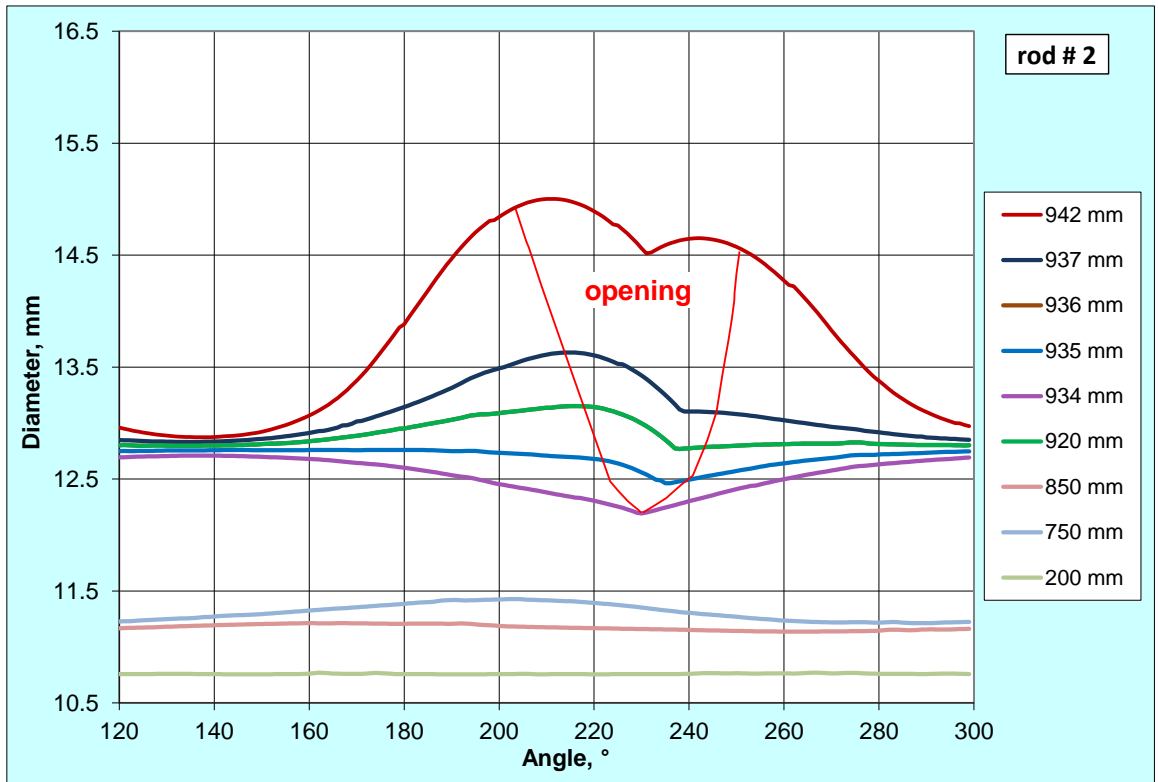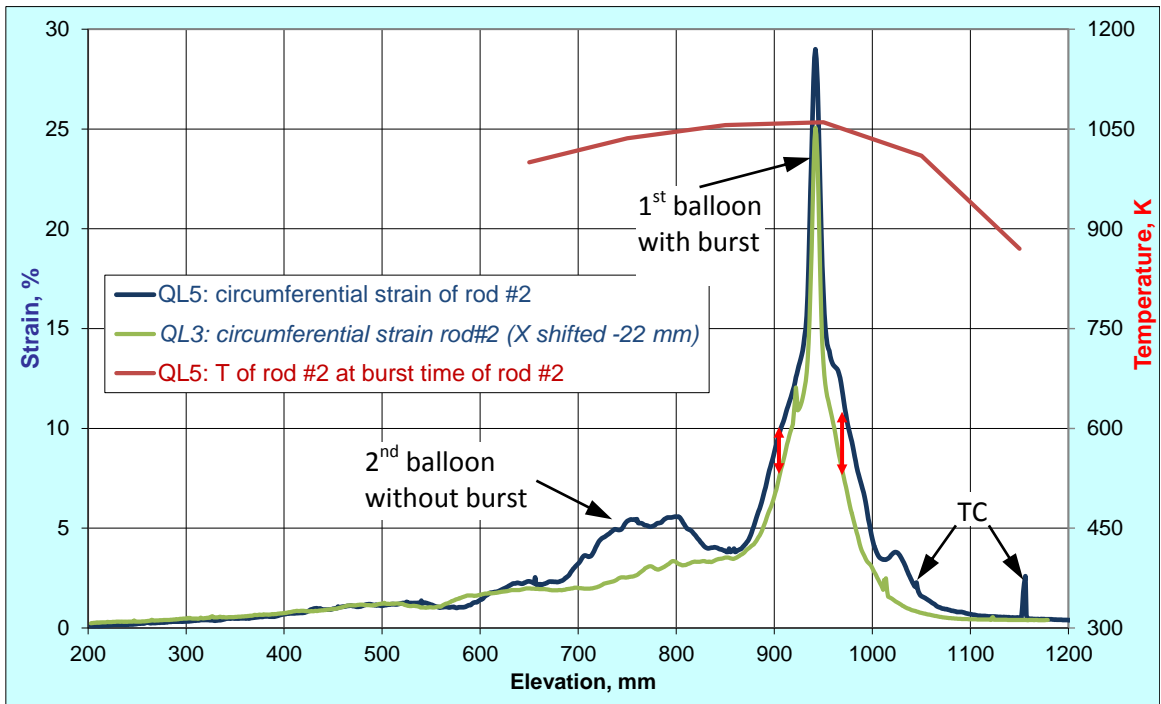
Figure 80 QUENCH-L5, Rod #2; longitudinal changing of circumferential strain (top): QL5 clad strain inside main balloon exceeds corresponding strain of QL3; azimuthal diameter downwards from burst (bottom). Spikes: thermocouples.
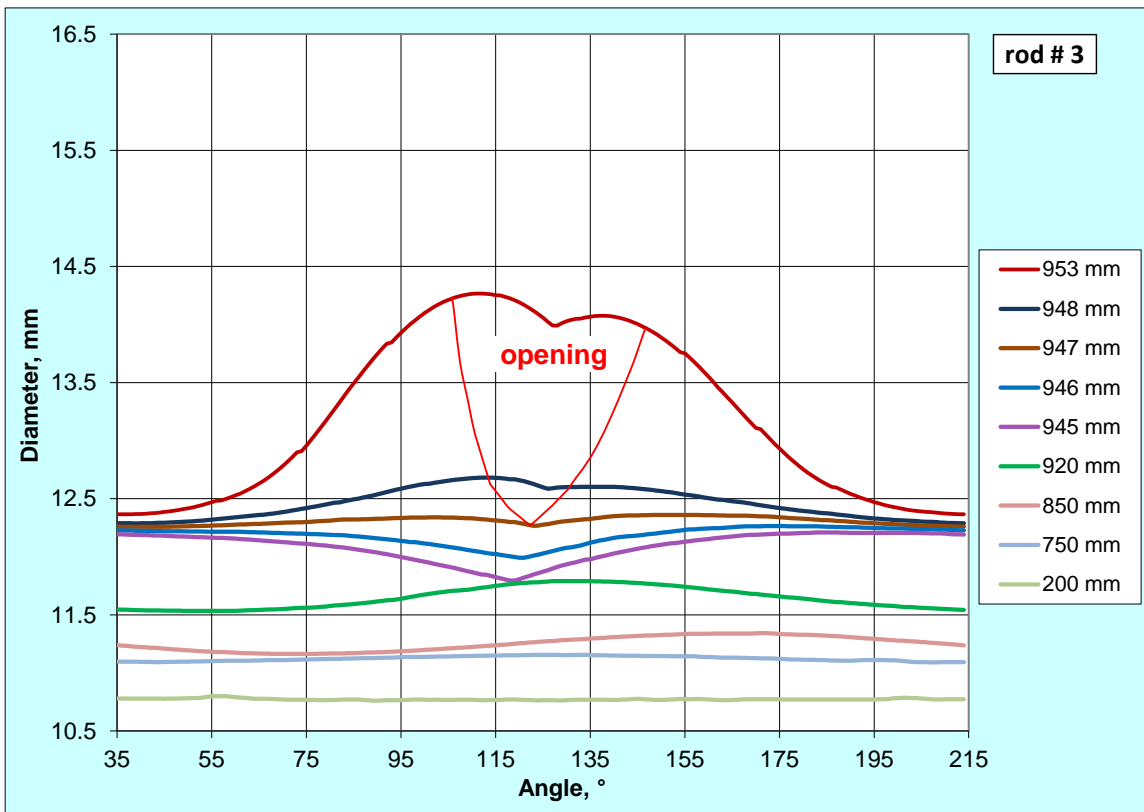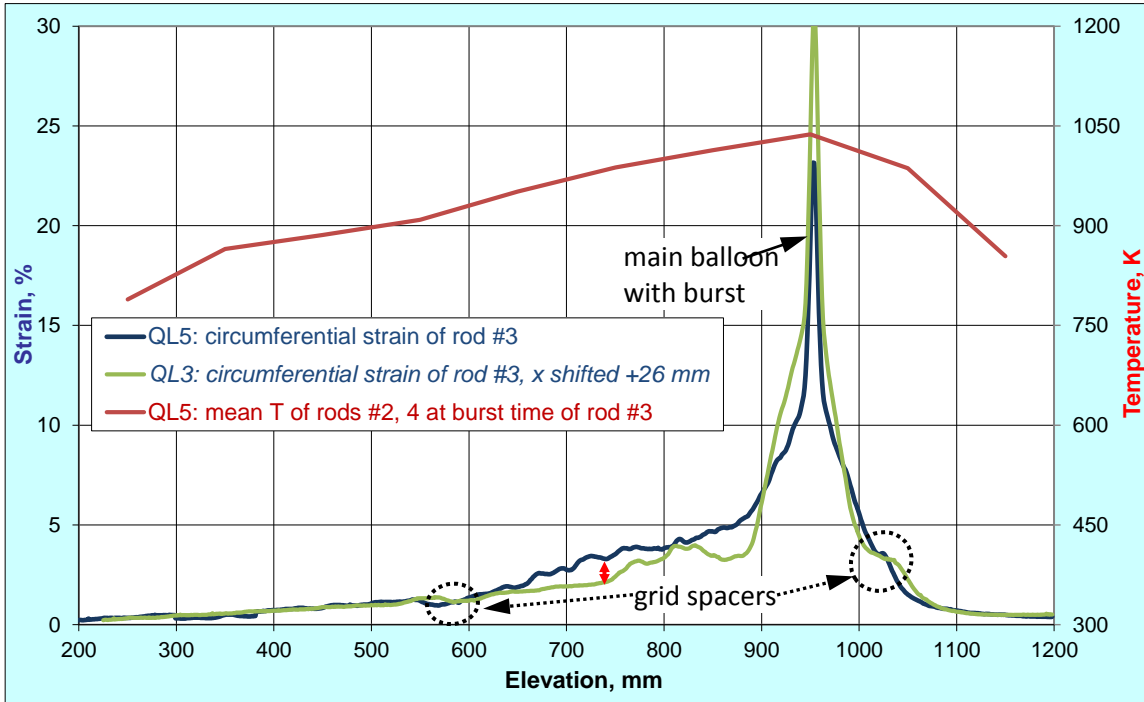
Figure 81 QUENCH-L5, Rod #3; longitudinal changing of circumferential strain (top): QL5 clad strain below main balloon exceeds corresponding strain of QL3; azimuthal diameter downwards from burst (bottom).
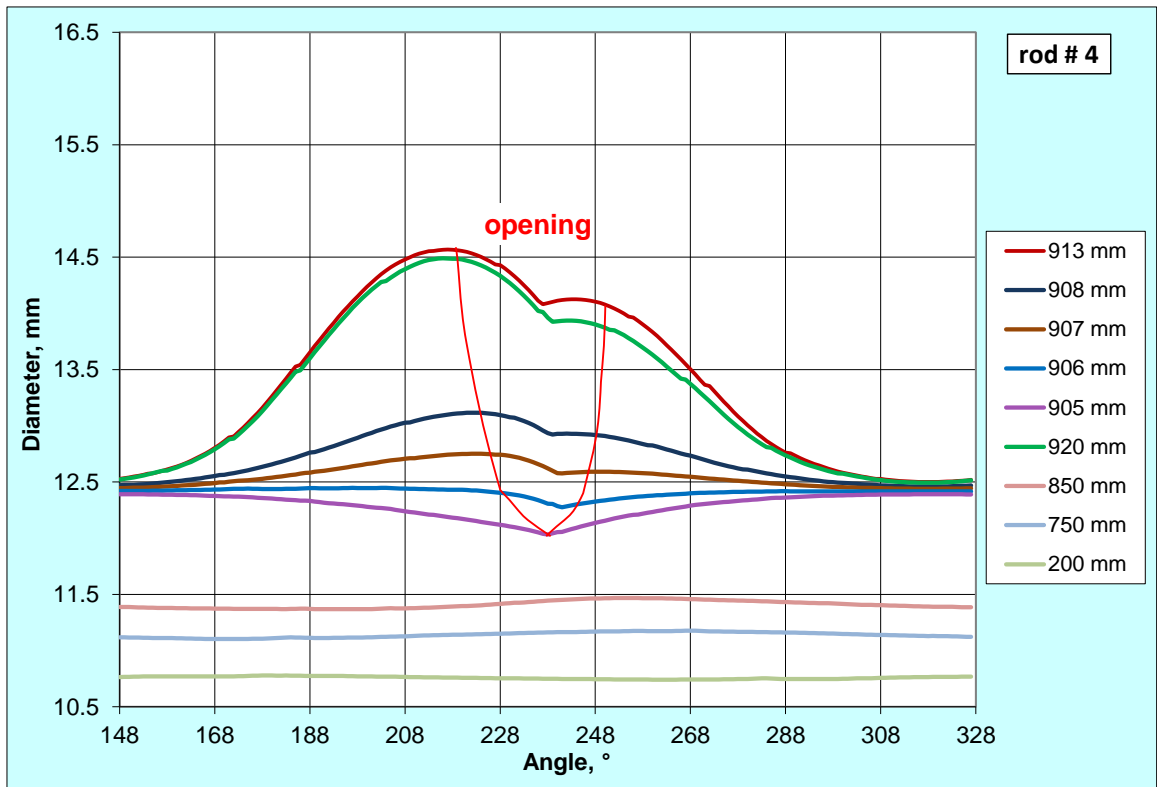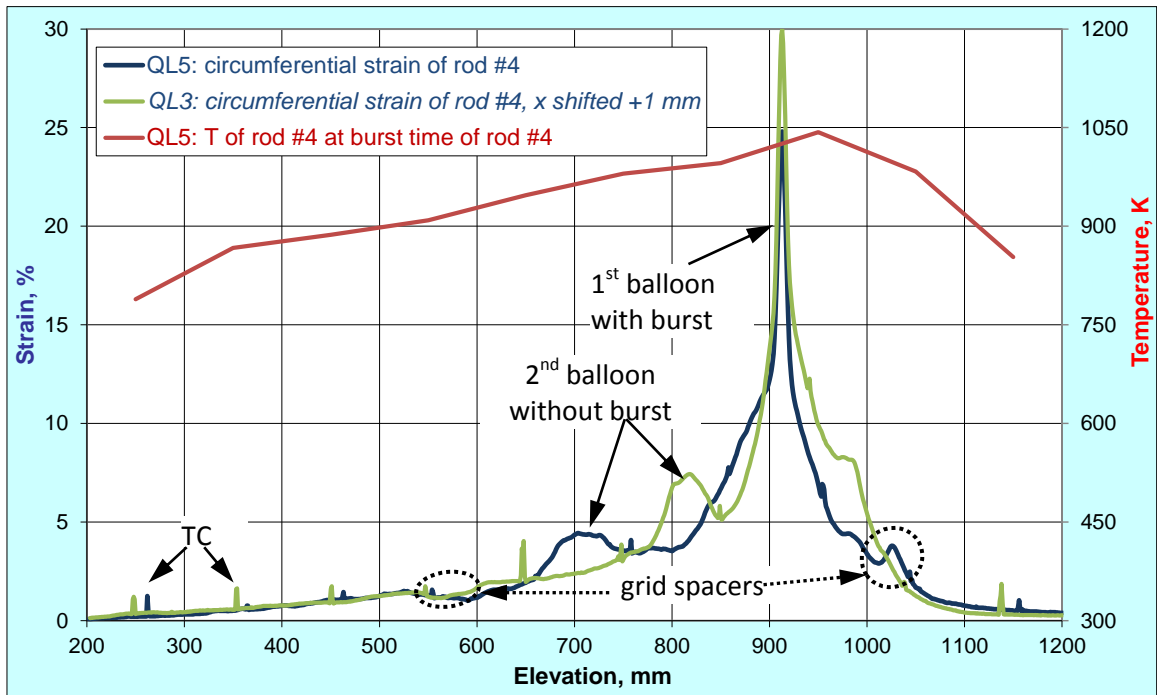
Figure 82 QUENCH-L5, Rod #4; longitudinal changing of circumferential strain (top); azimuthal diameter downwards from burst (bottom). Spikes: thermocouples.
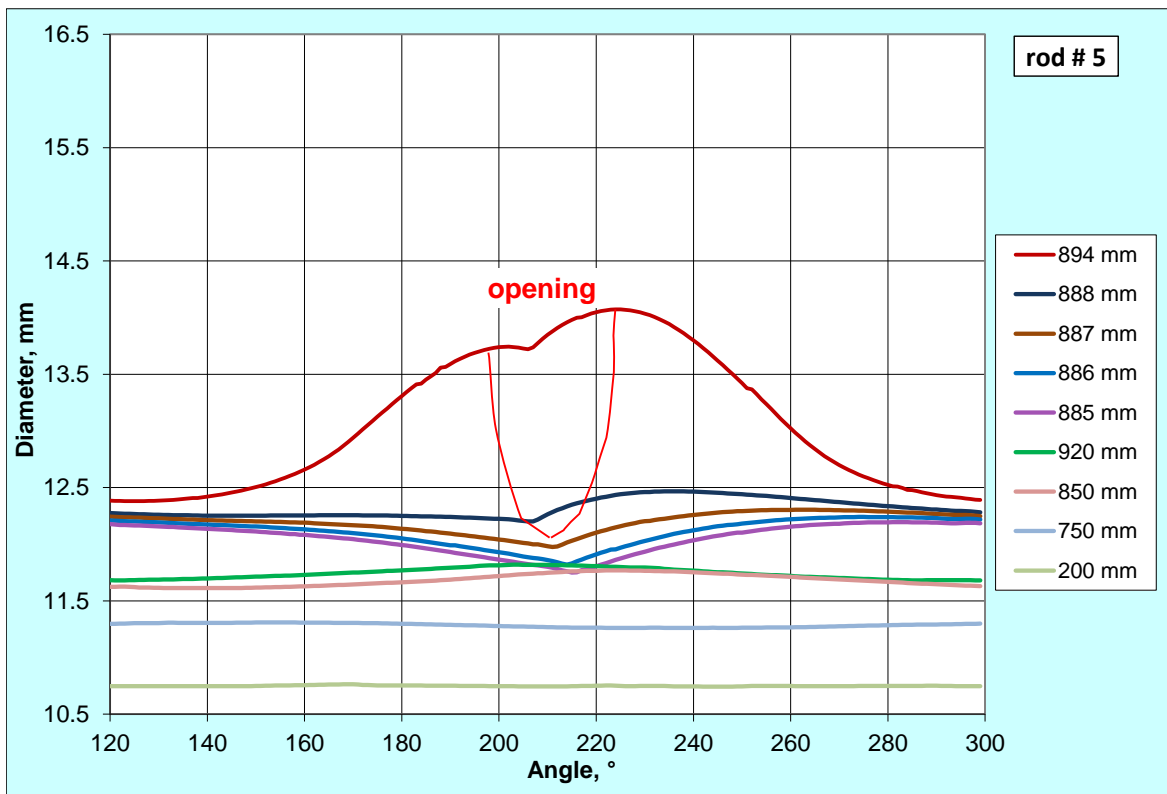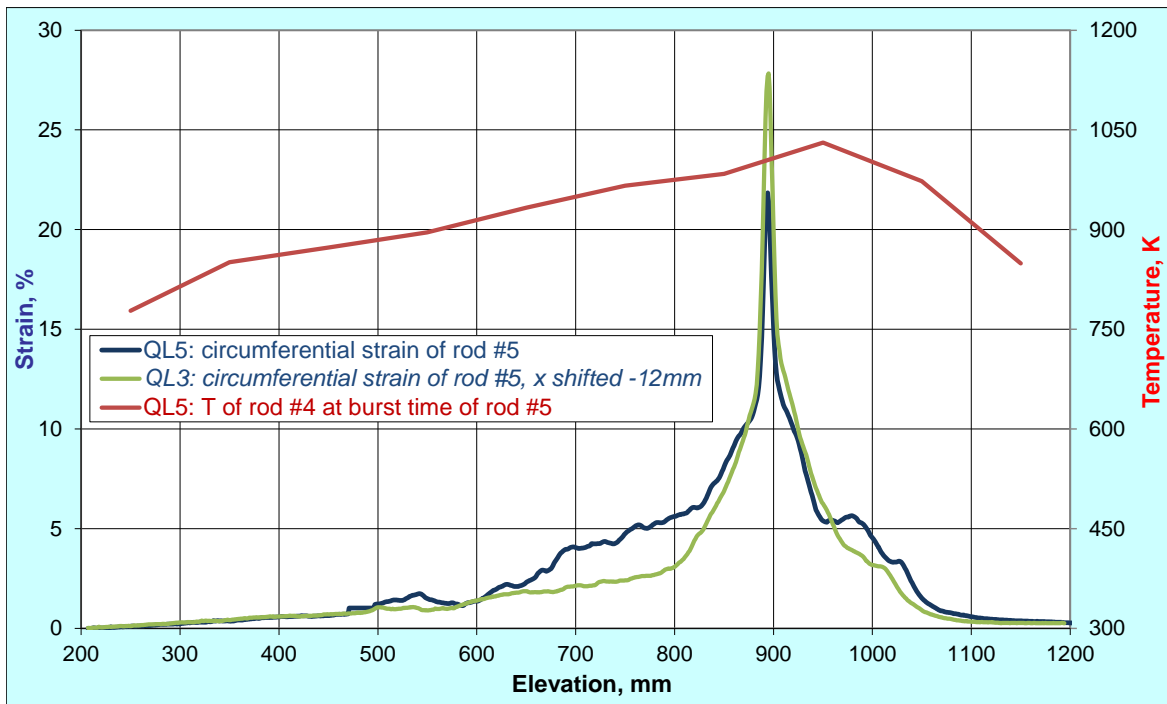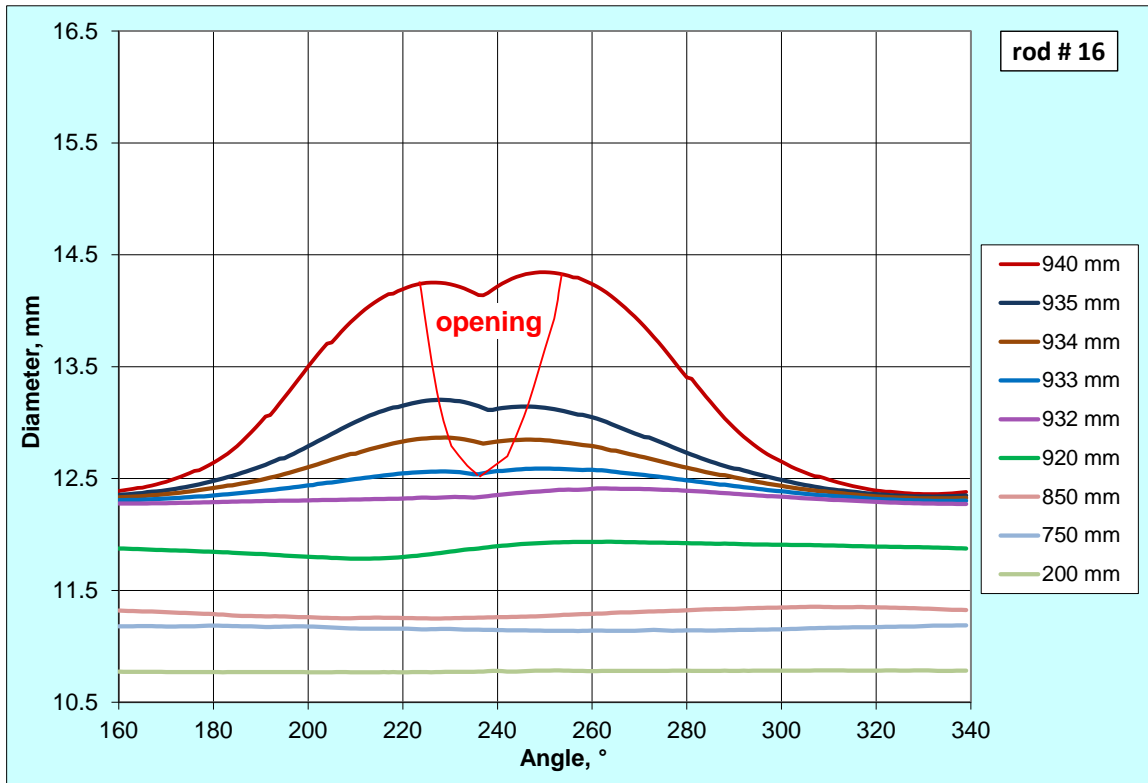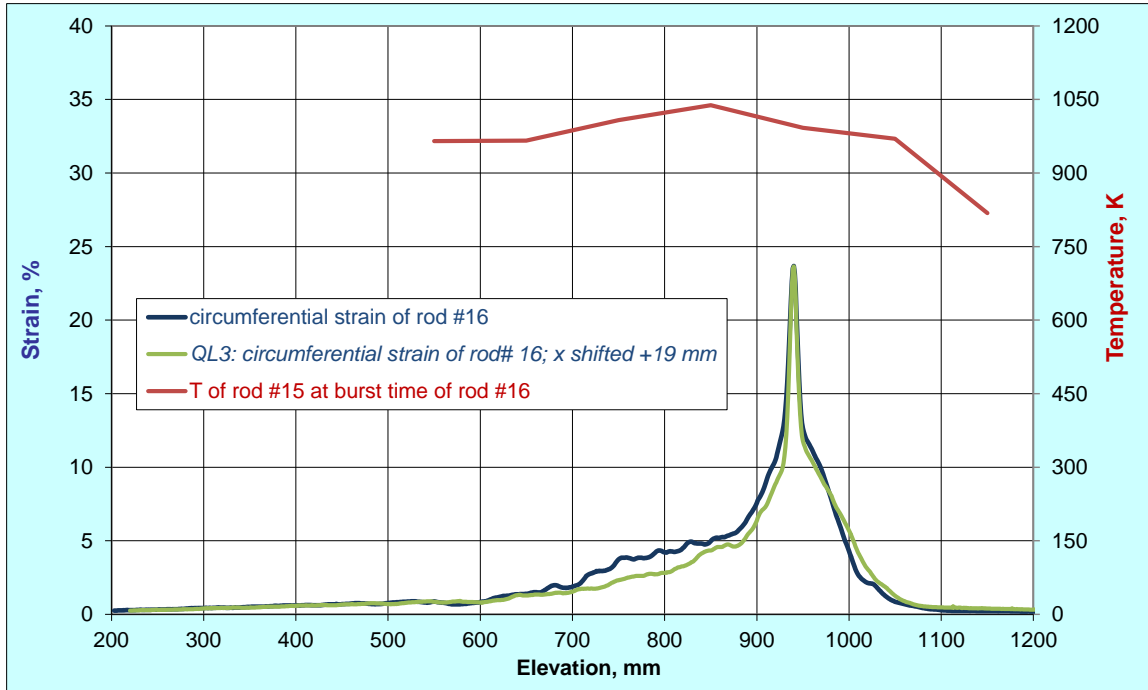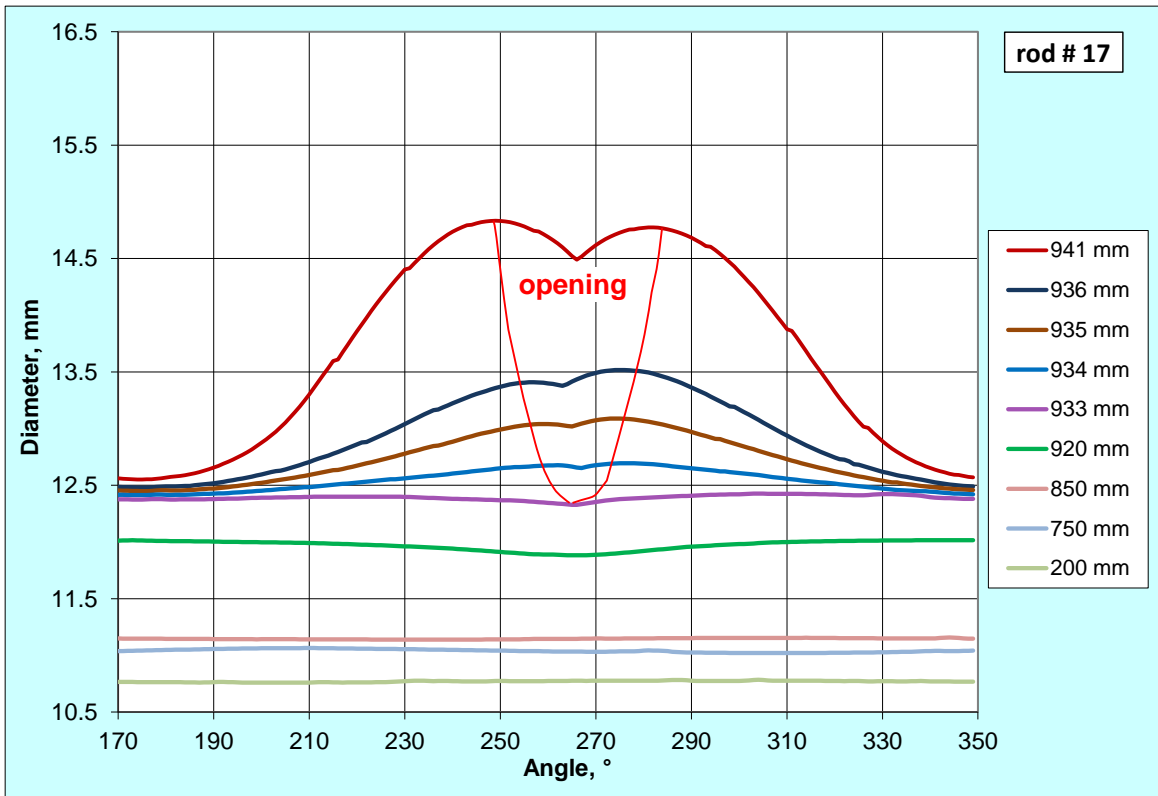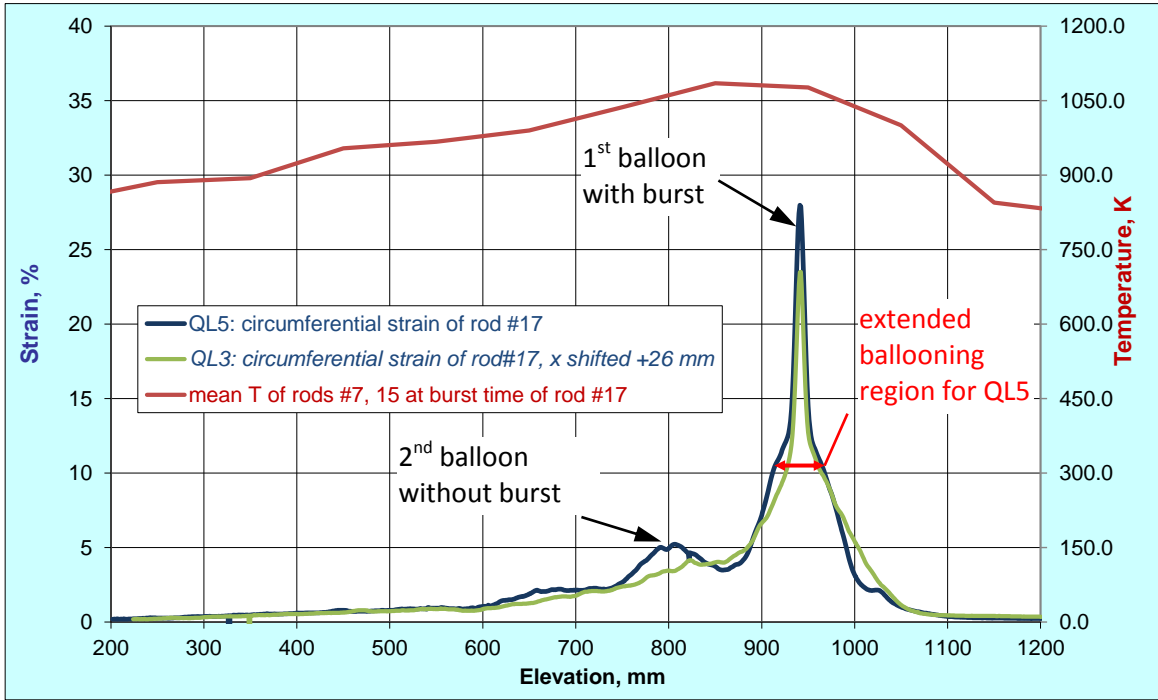
Figure 83 QUENCH-L5, Rod #5; longitudinal changing of circumferential strain (top): QL5 clad strain below main balloon exceeds corresponding strain of QL3; azimuthal diameter downwards from burst (bottom).
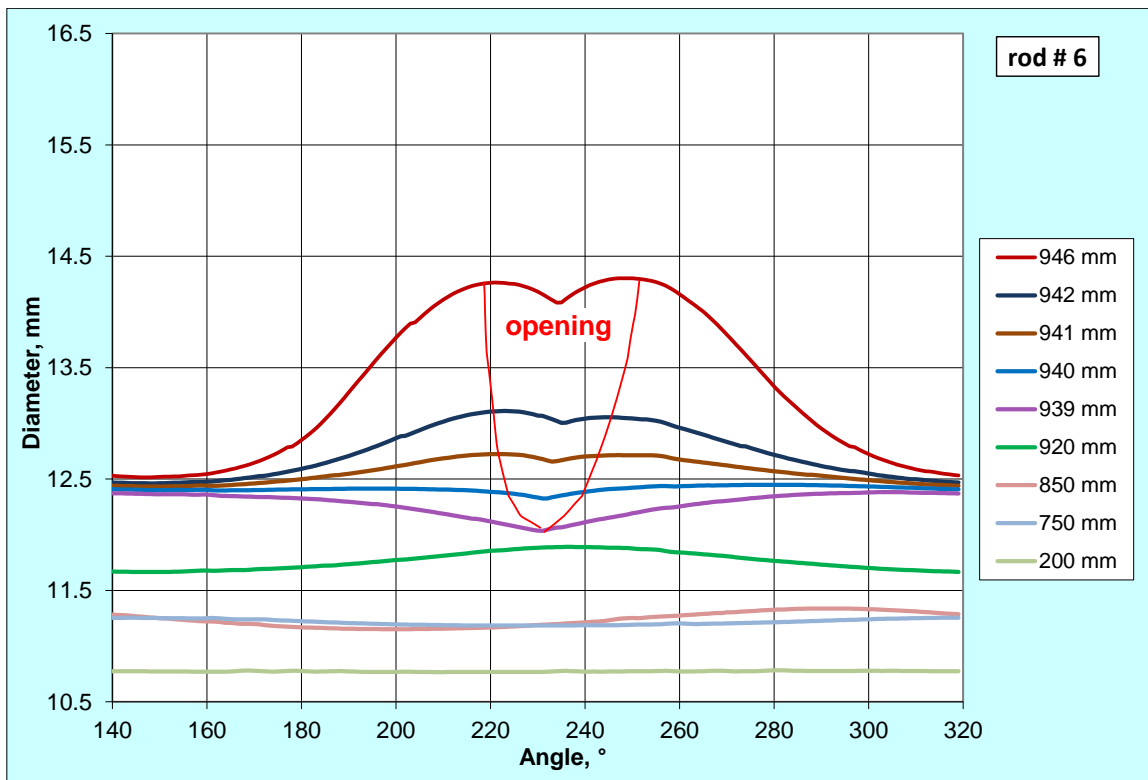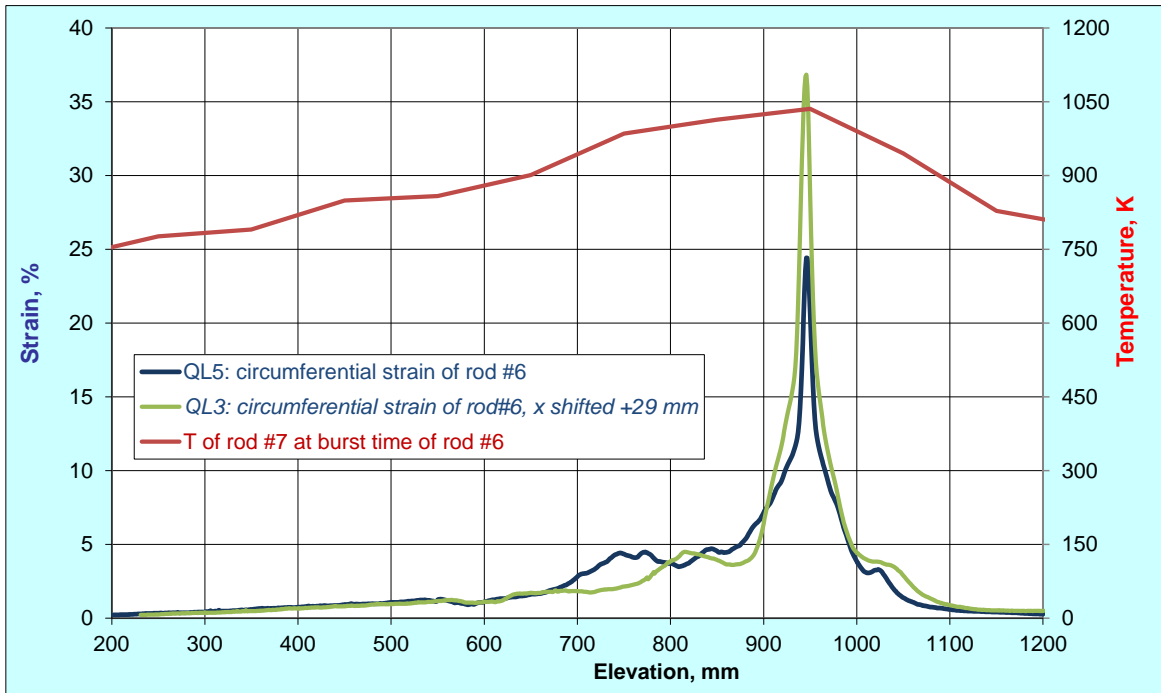
Figure 84 QUENCH-L5, Rod #6; longitudinal changing of circumferential strain (top); azimuthal diameter downwards from burst (bottom).
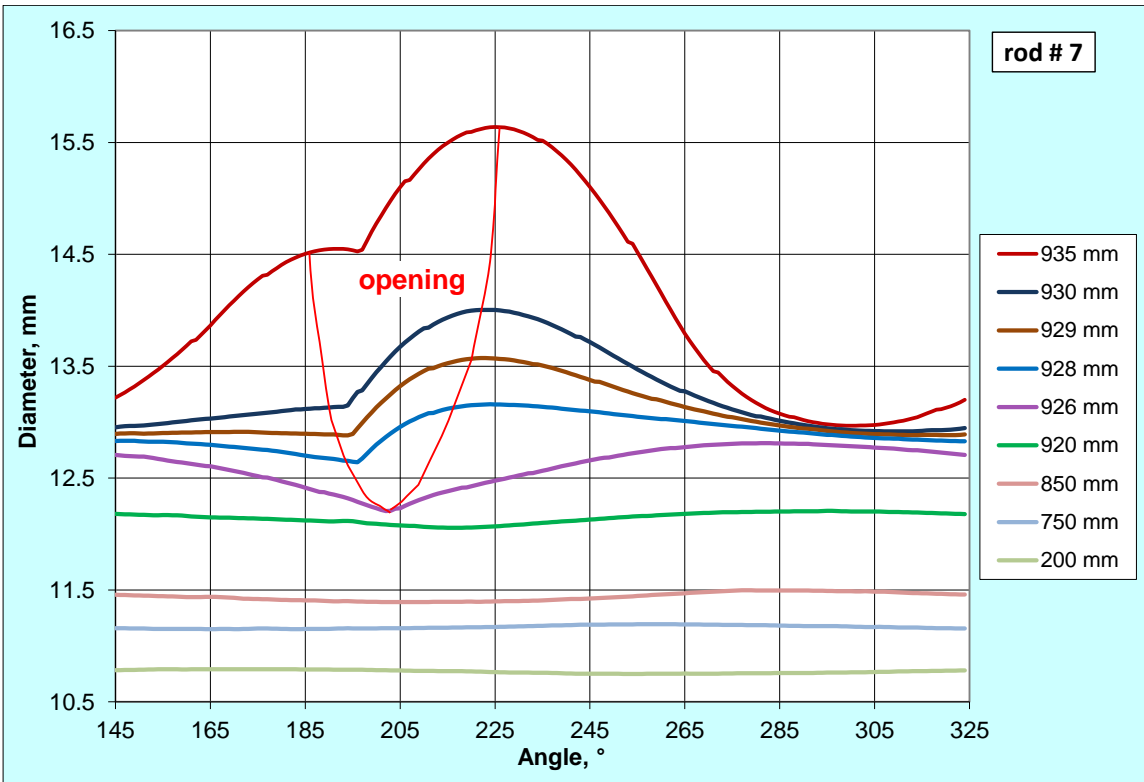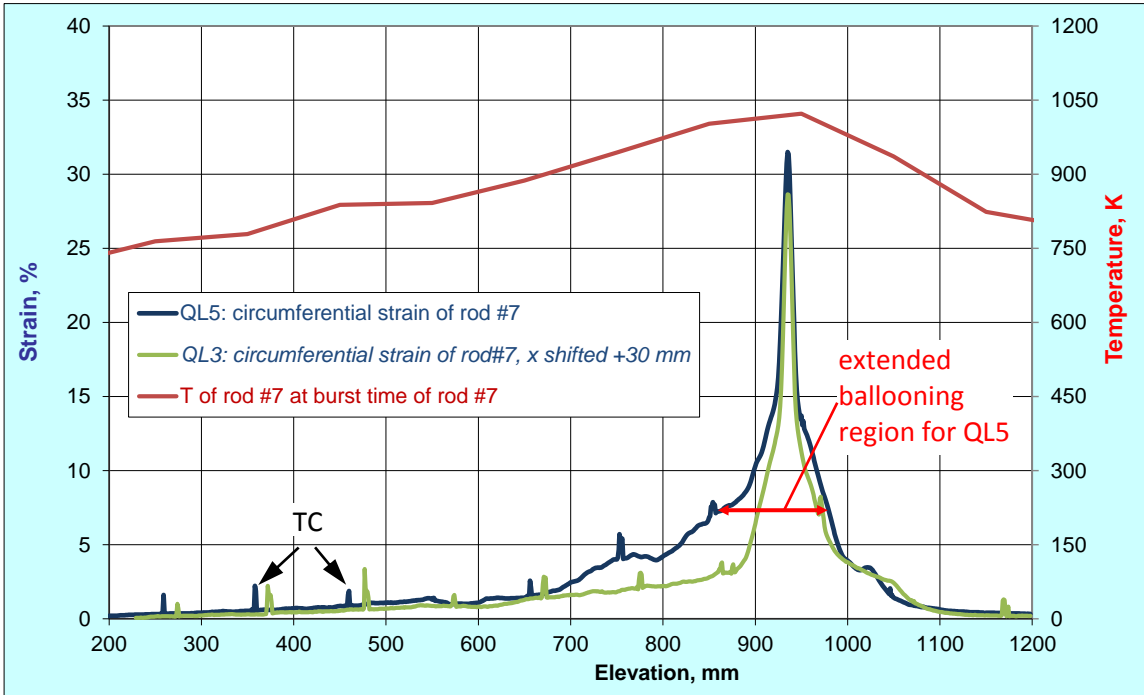
Figure 85   QUENCH-L5, Rod #7; longitudinal changing of circumferential strain (top); azimuthal diameter downwards from burst (bottom). Spikes: thermocouples.
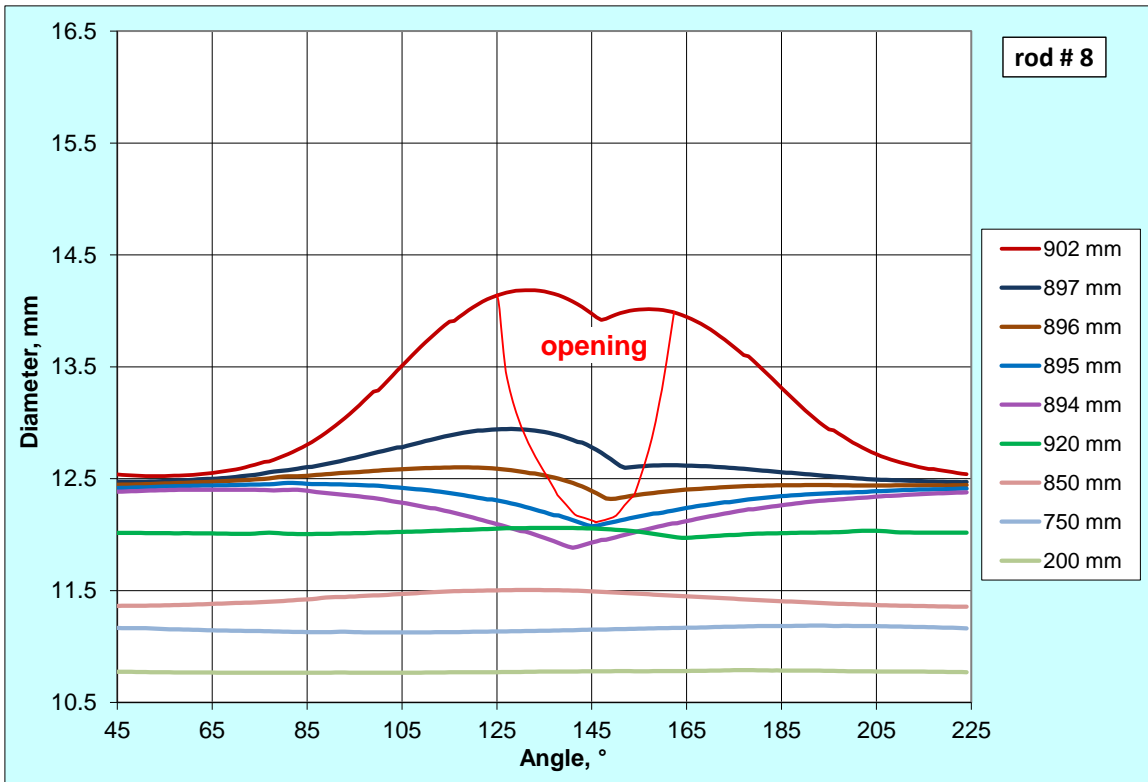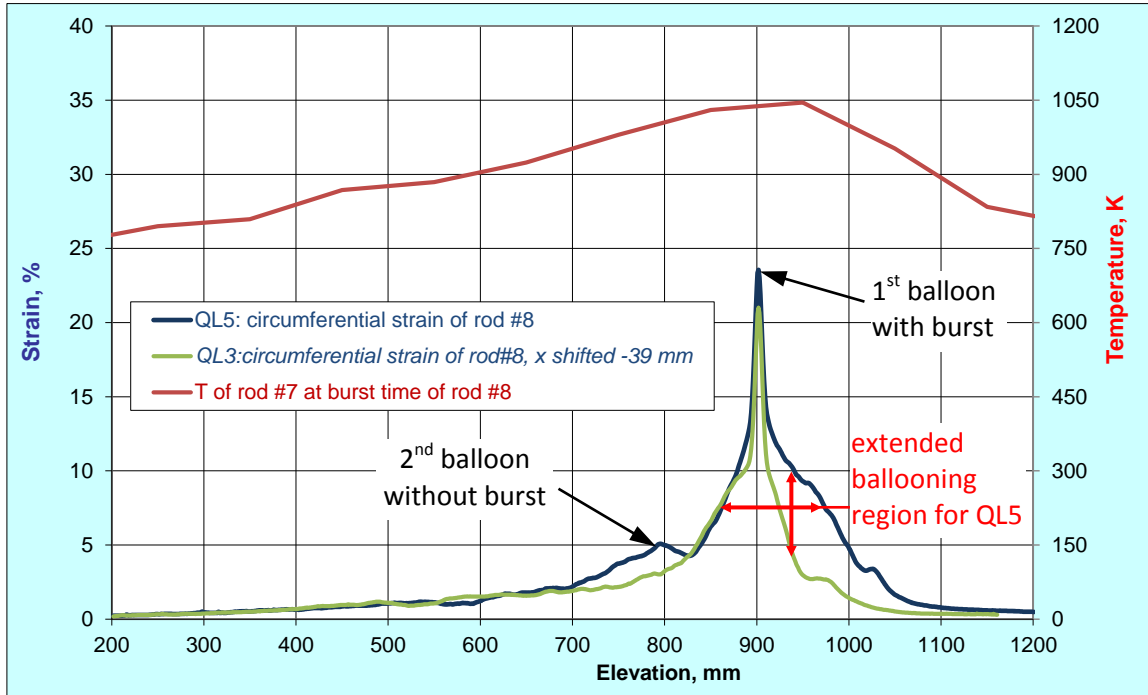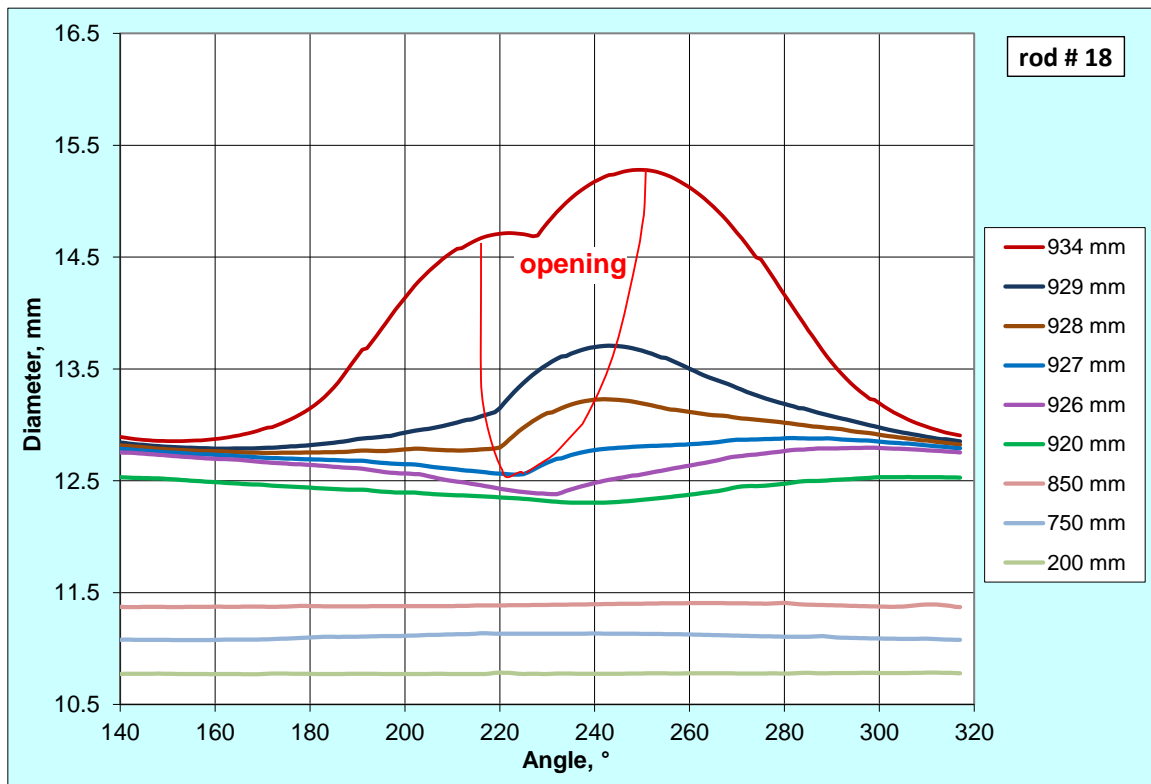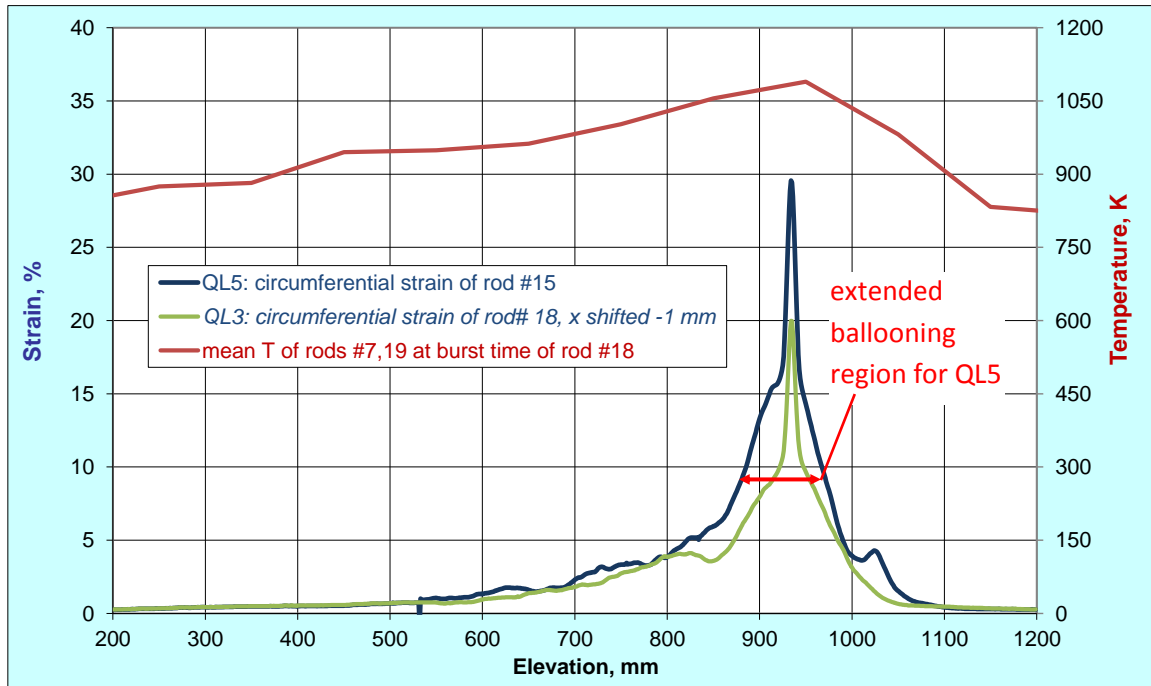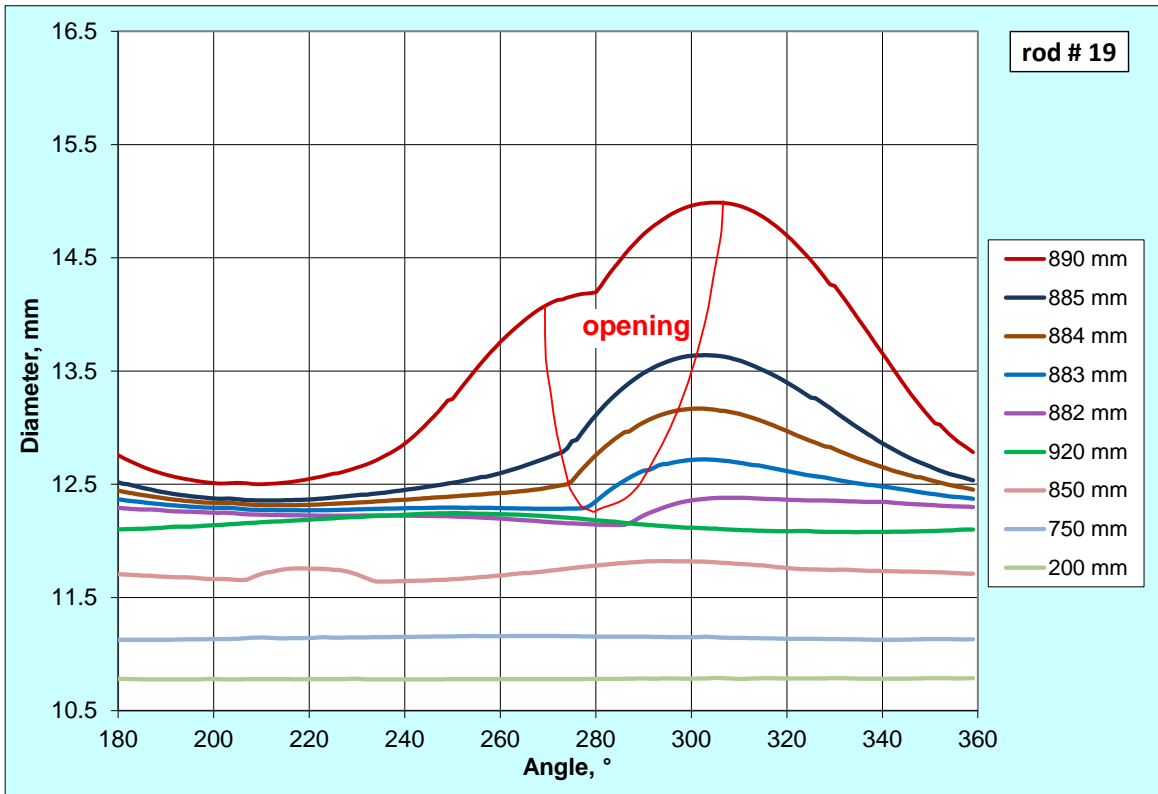
Figure 86 QUENCH-L5, Rod #8; longitudinal changing of circumferential strain (top); azimuthal diameter downwards from burst (bottom).
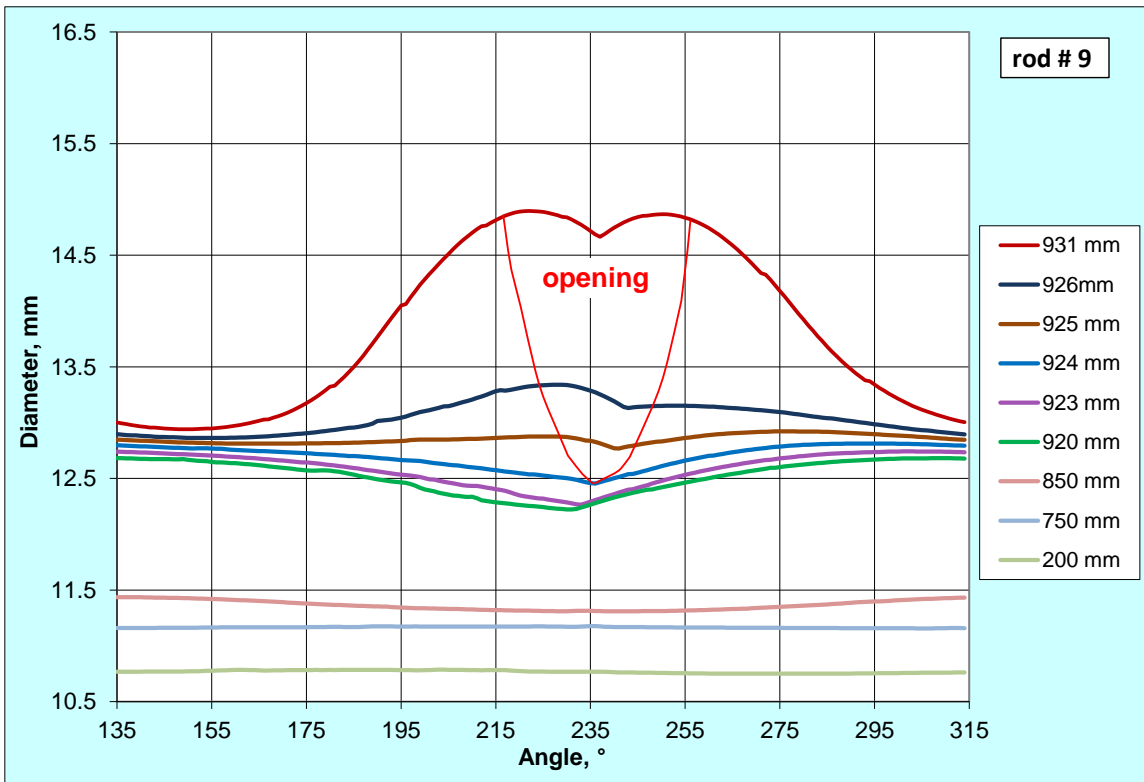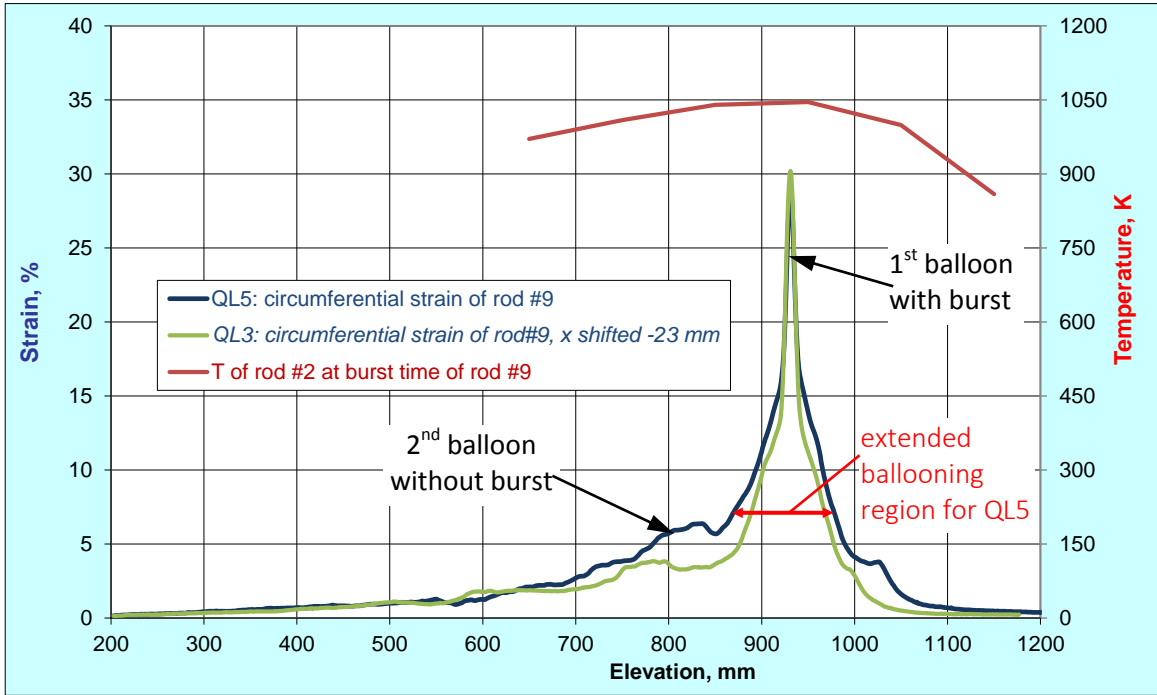
Figure 87   QUENCH-L5, Rod #9; longitudinal changing of circumferential strain (top); azimuthal diameter downwards from burst (bottom).
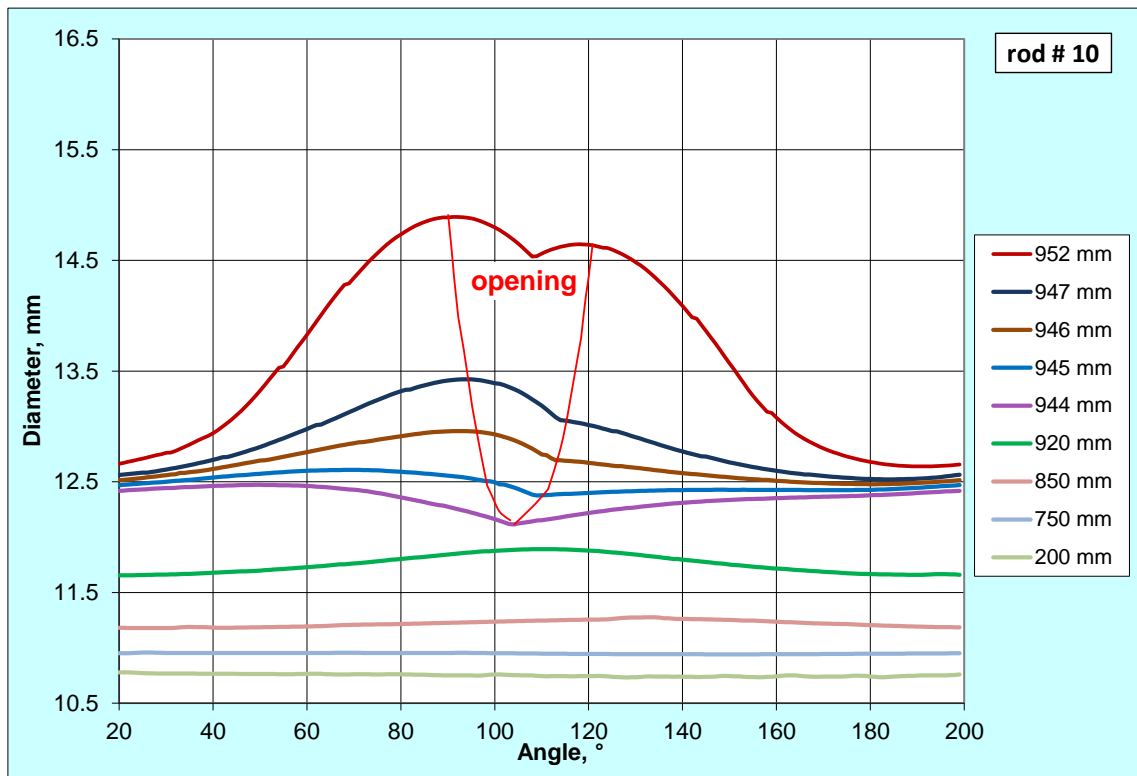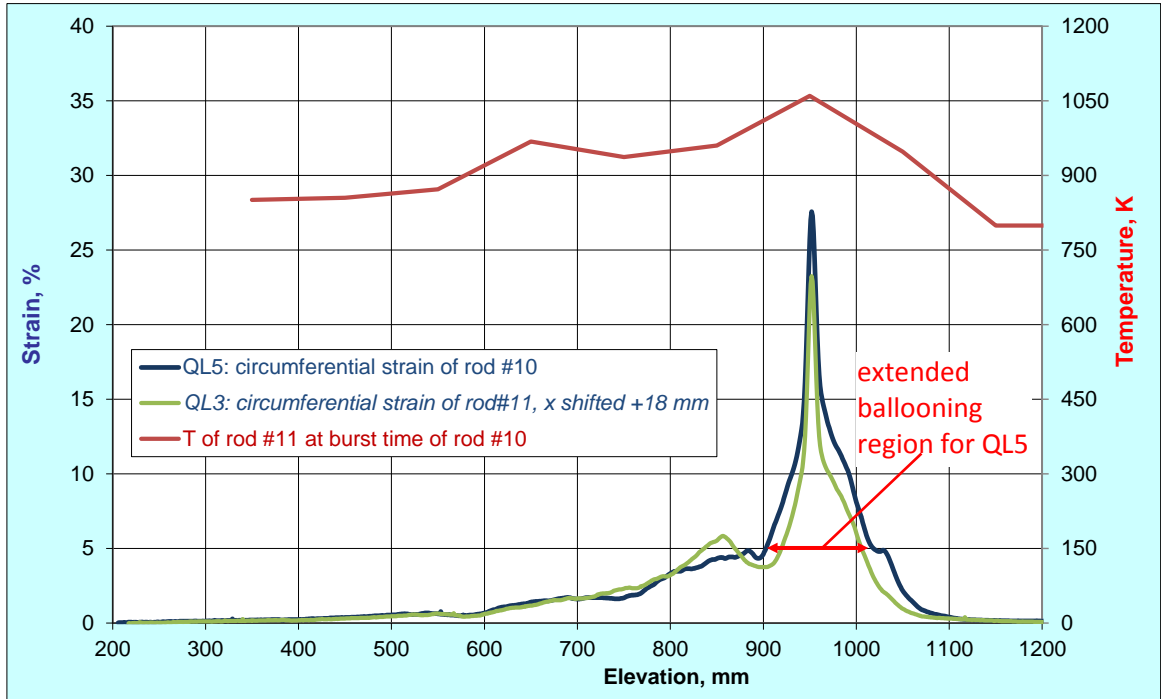
Figure 88 QUENCH-L5, Rod #10; longitudinal changing of circumferential strain (top); azimuthal diameter downwards from burst (bottom).
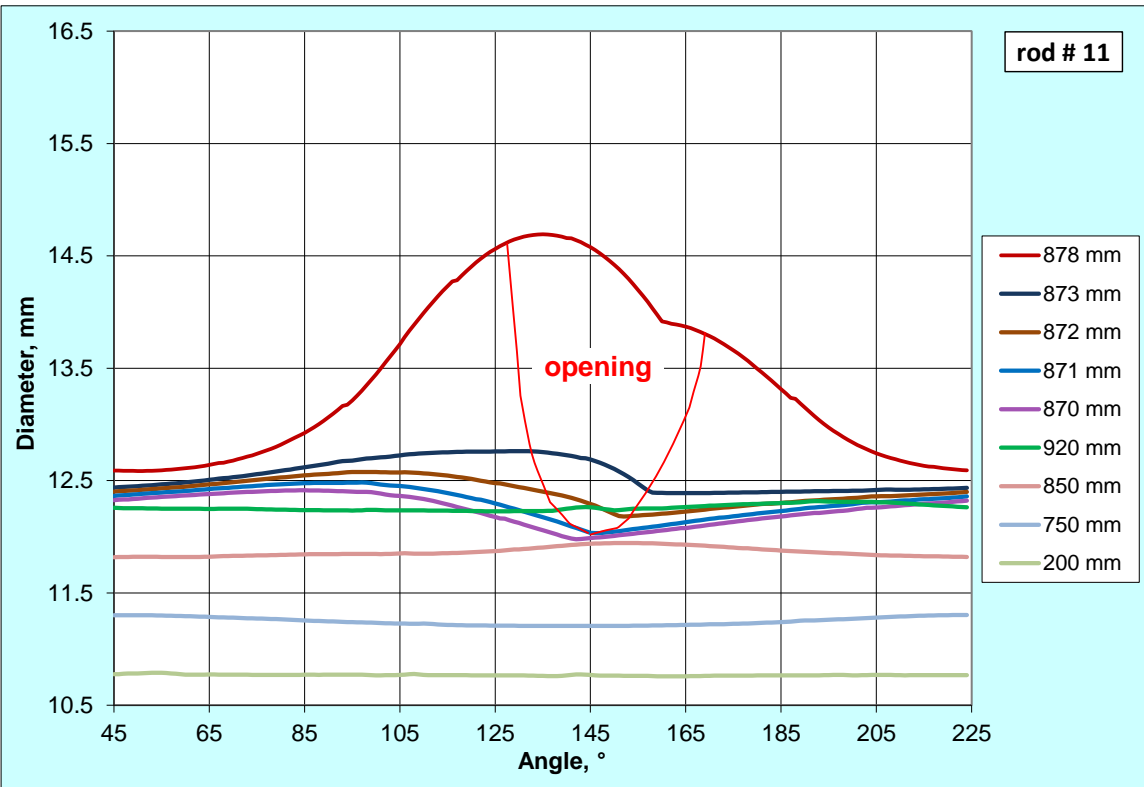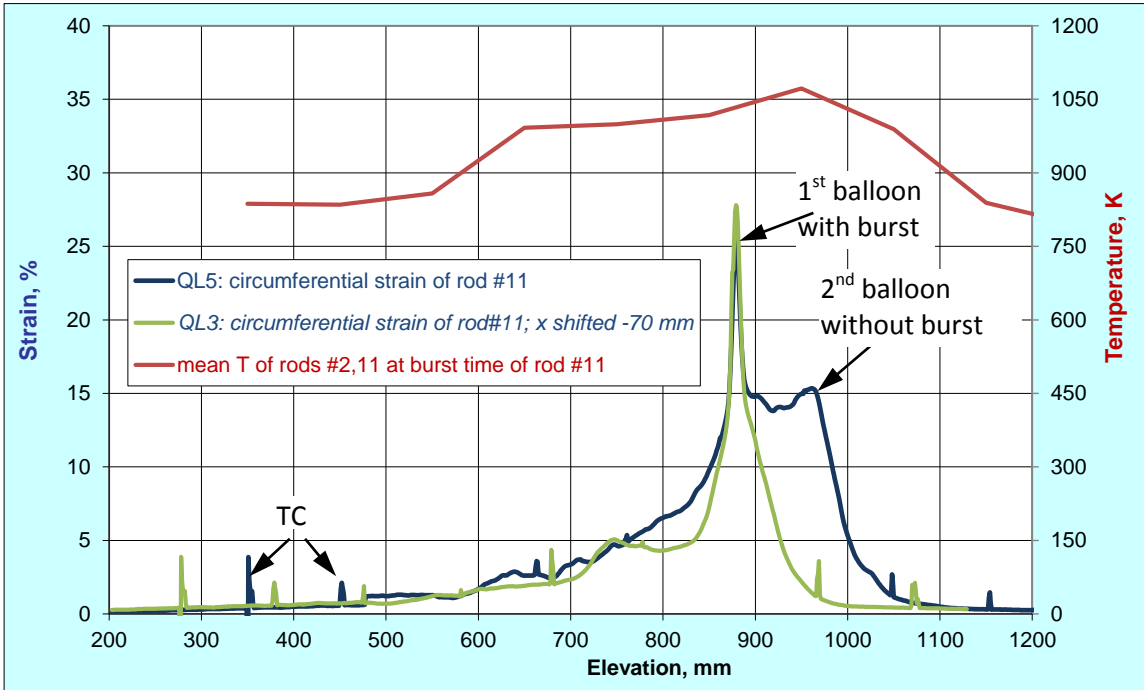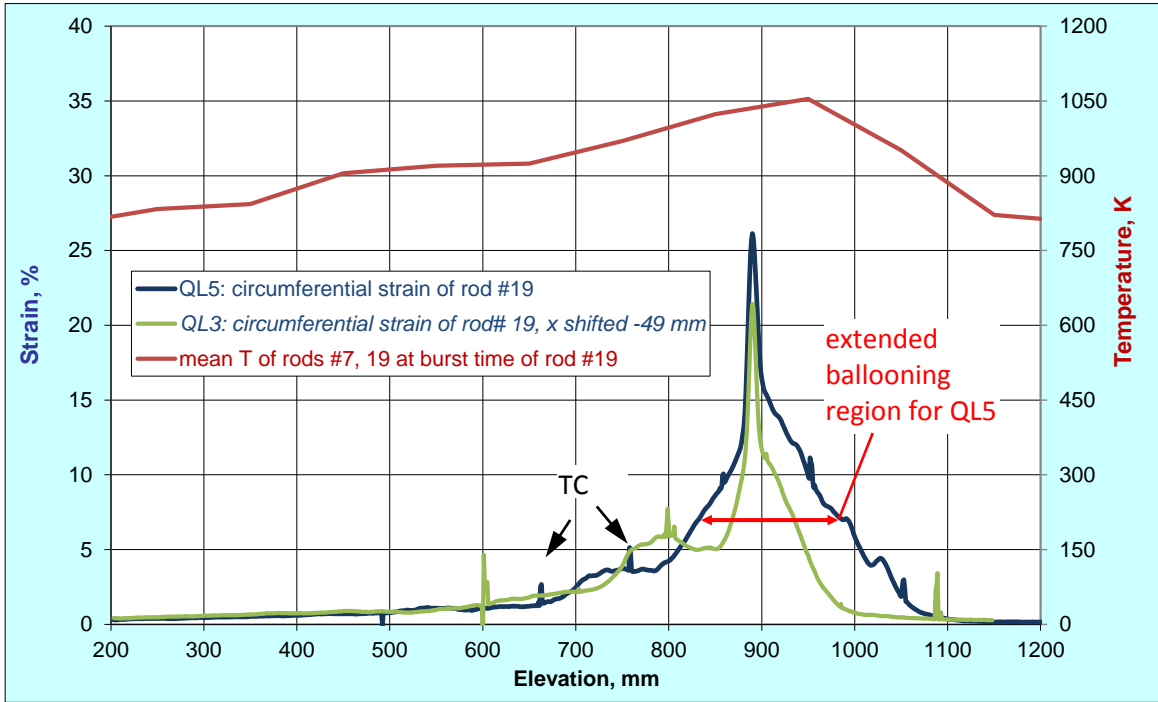
Figure 89   QUENCH-L5, Rod #11; longitudinal changing of circumferential strain (top); azimuthal diameter downwards from burst (bottom). Spikes: thermocouple.
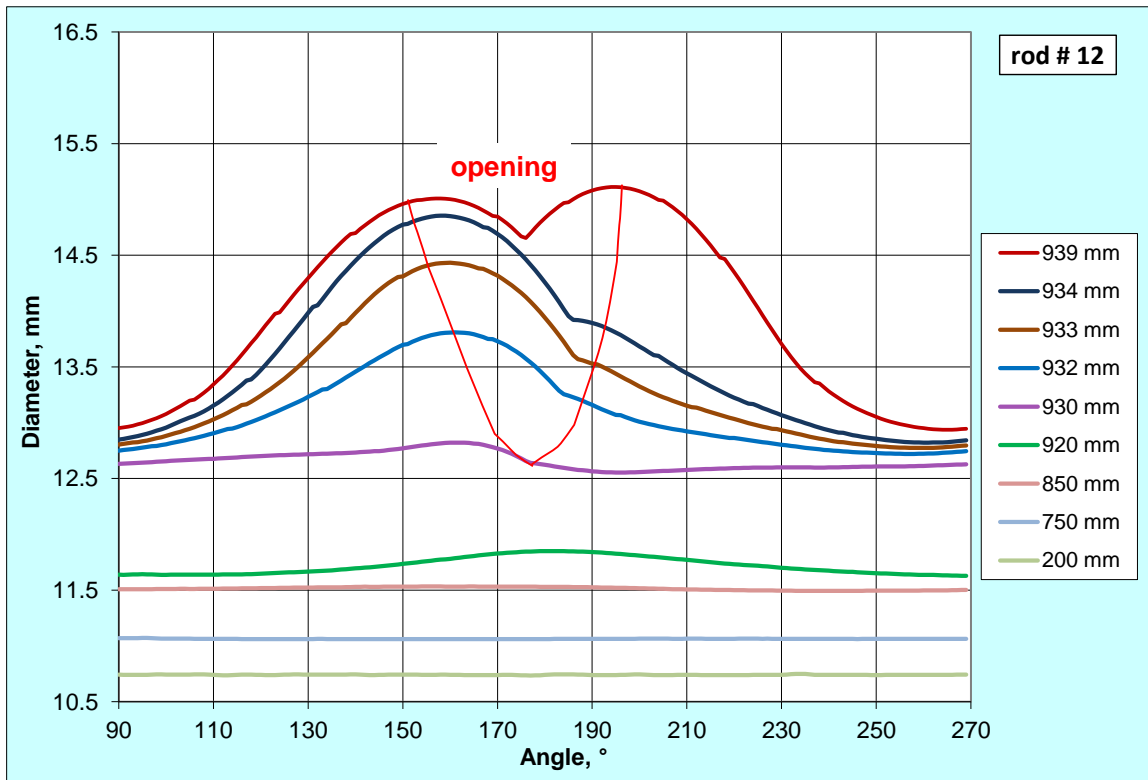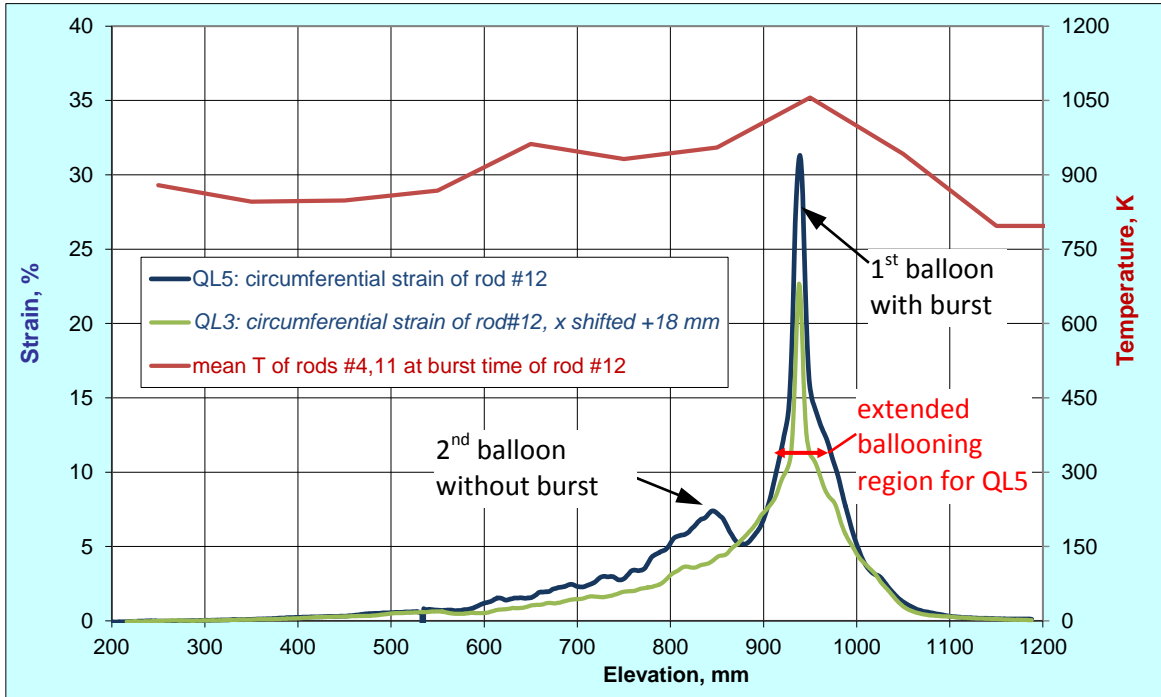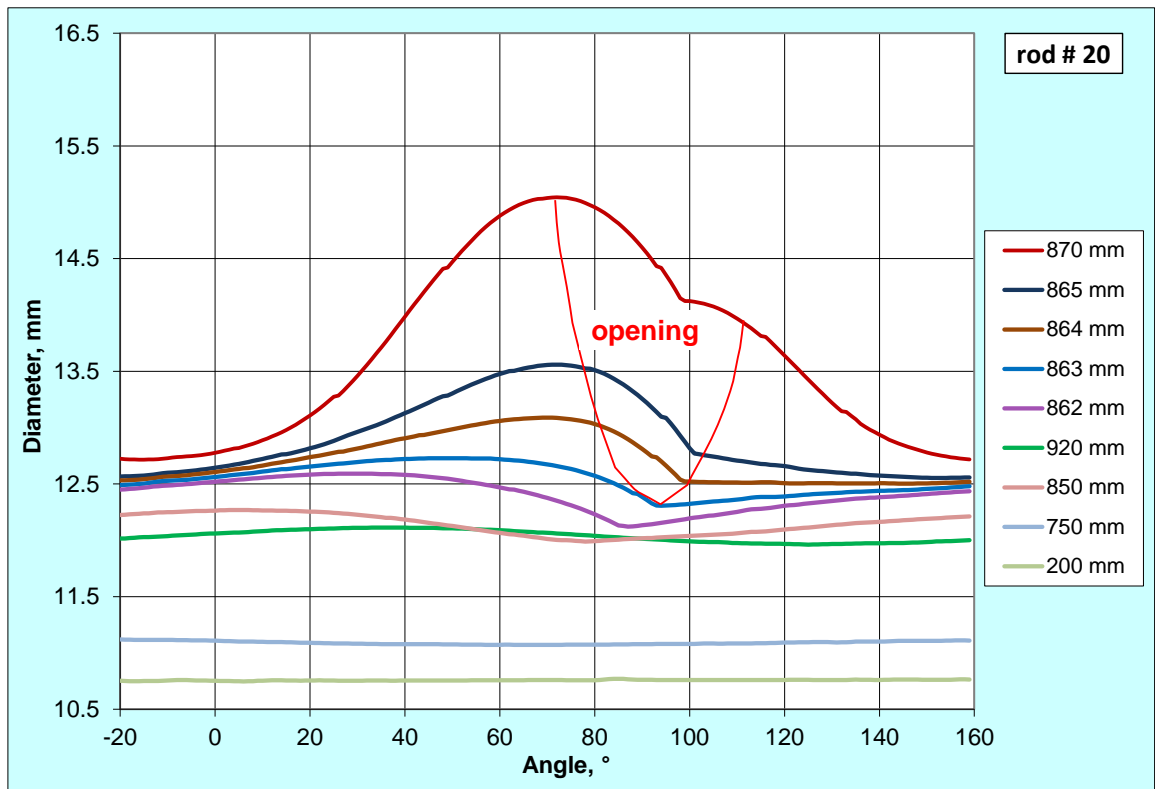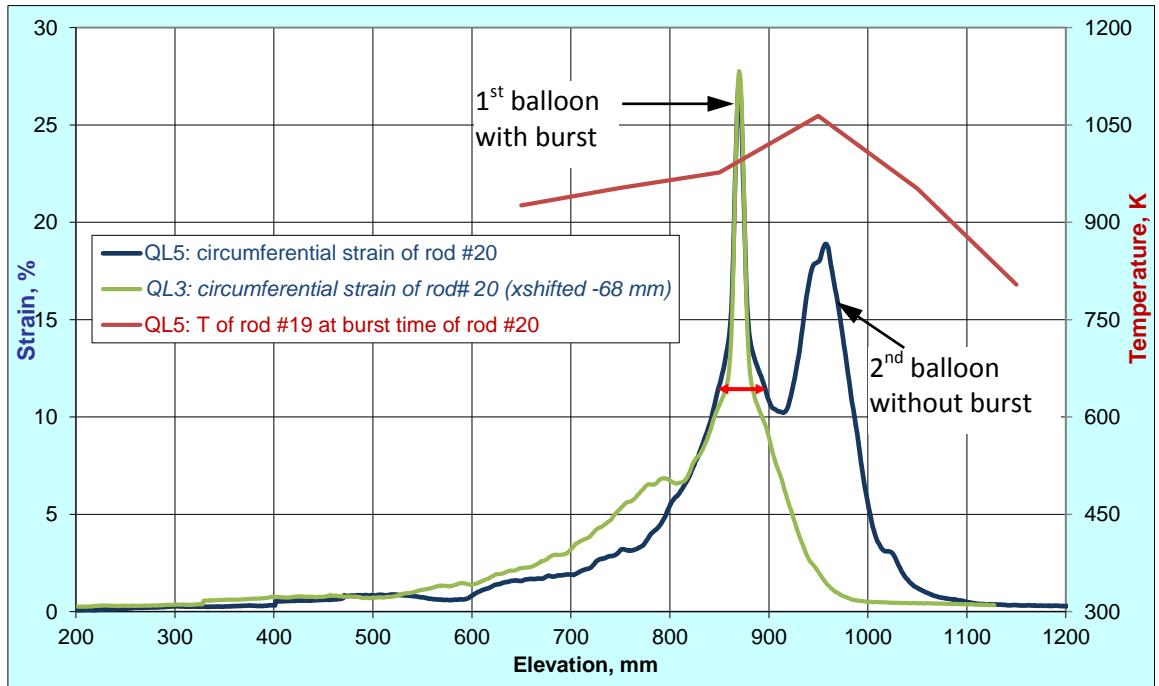
Figure 90 QUENCH-L5, Rod #12; longitudinal changing of circumferential strain (top); azimuthal diameter downwards from burst (bottom).
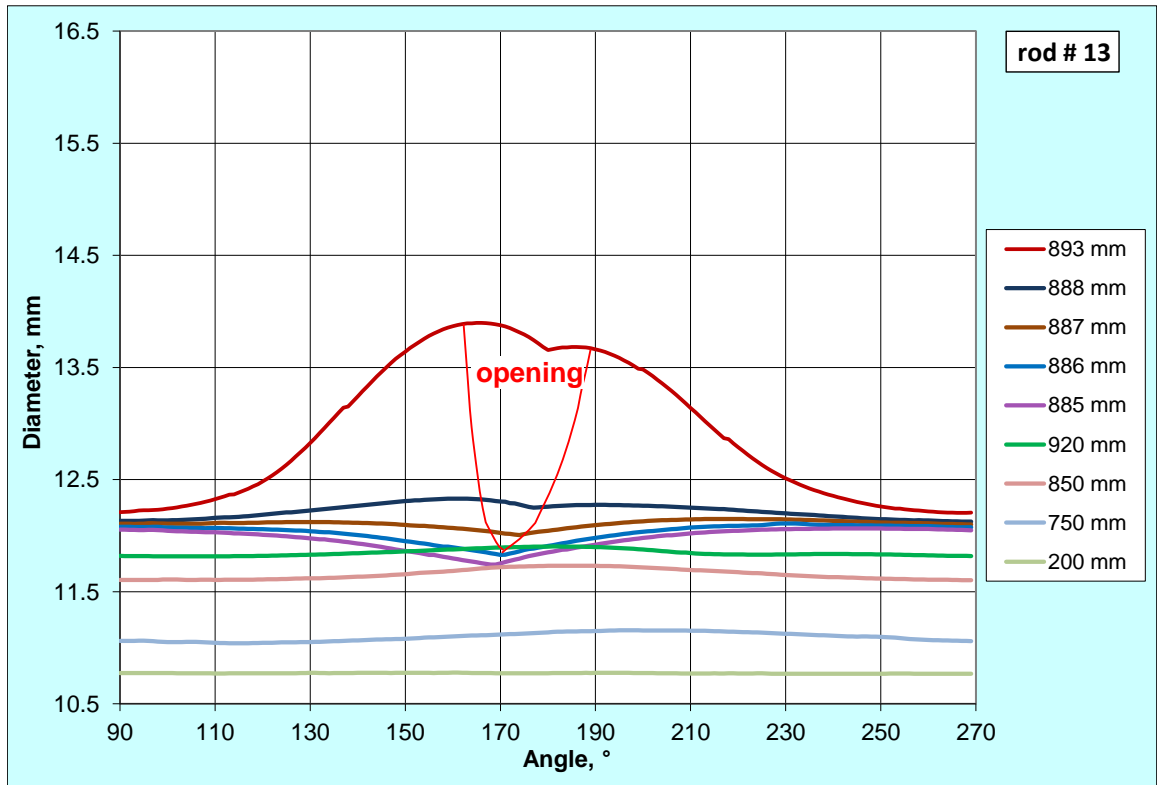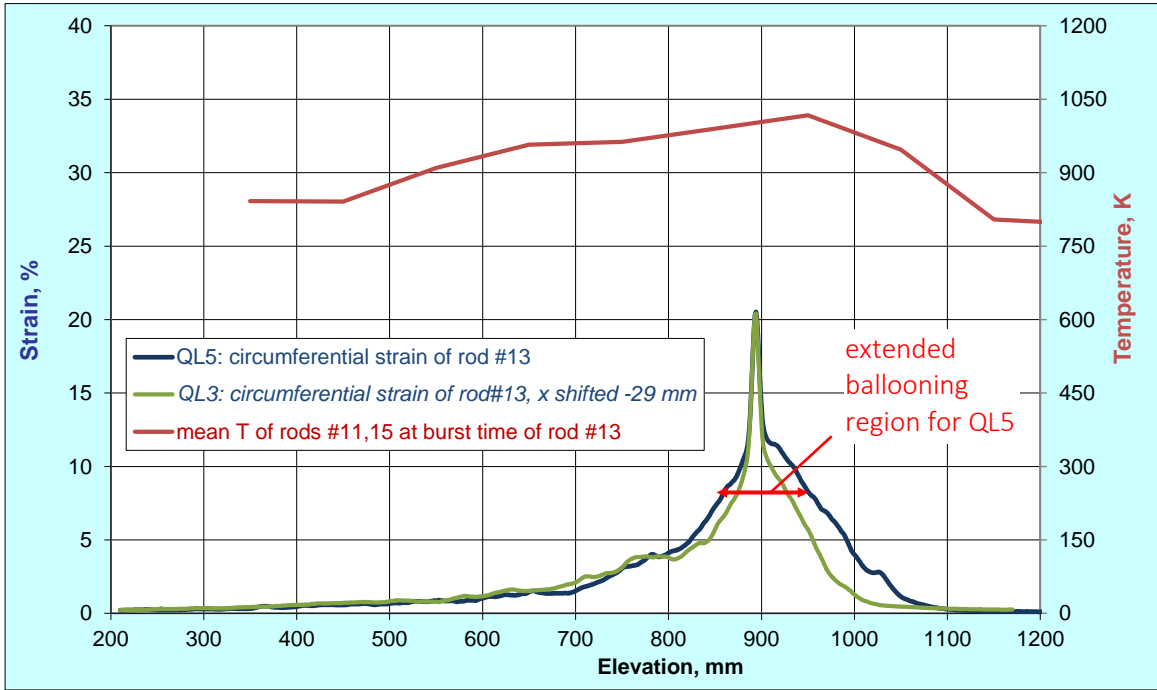
Figure 91 QUENCH-L5, Rod #13; longitudinal changing of circumferential strain (top); azimuthal diameter downwards from burst (bottom).
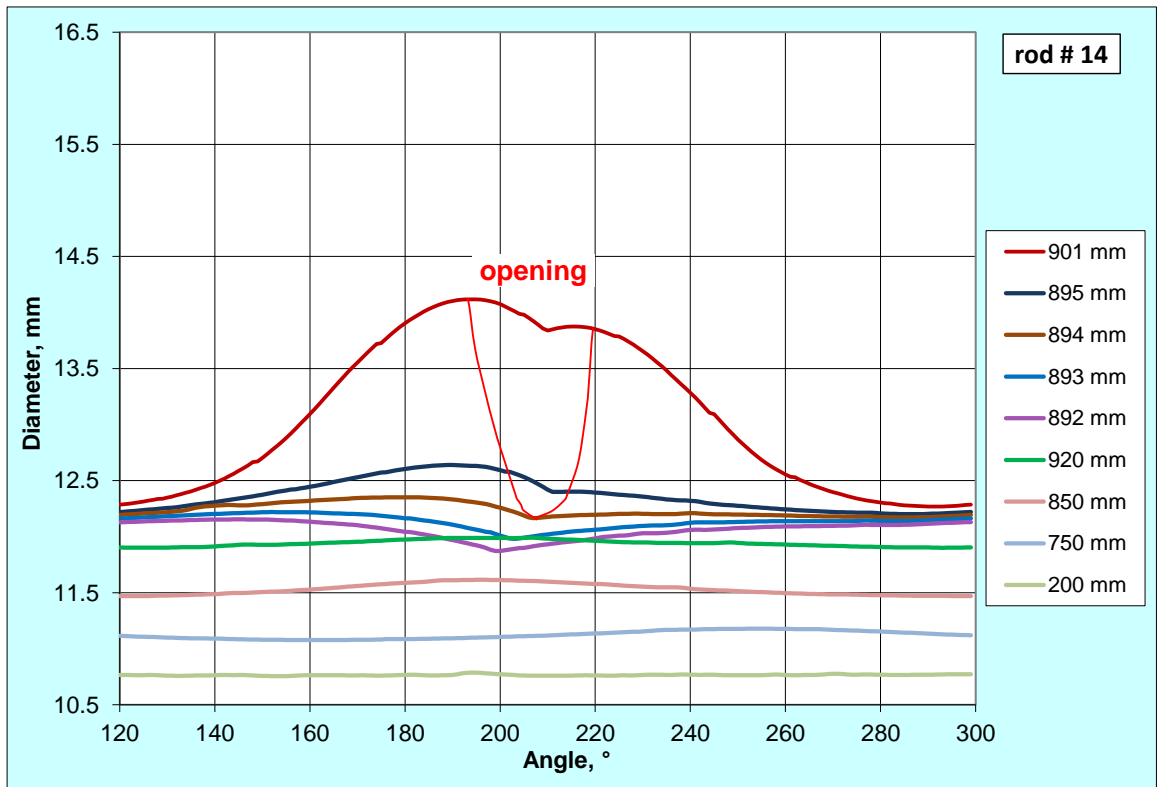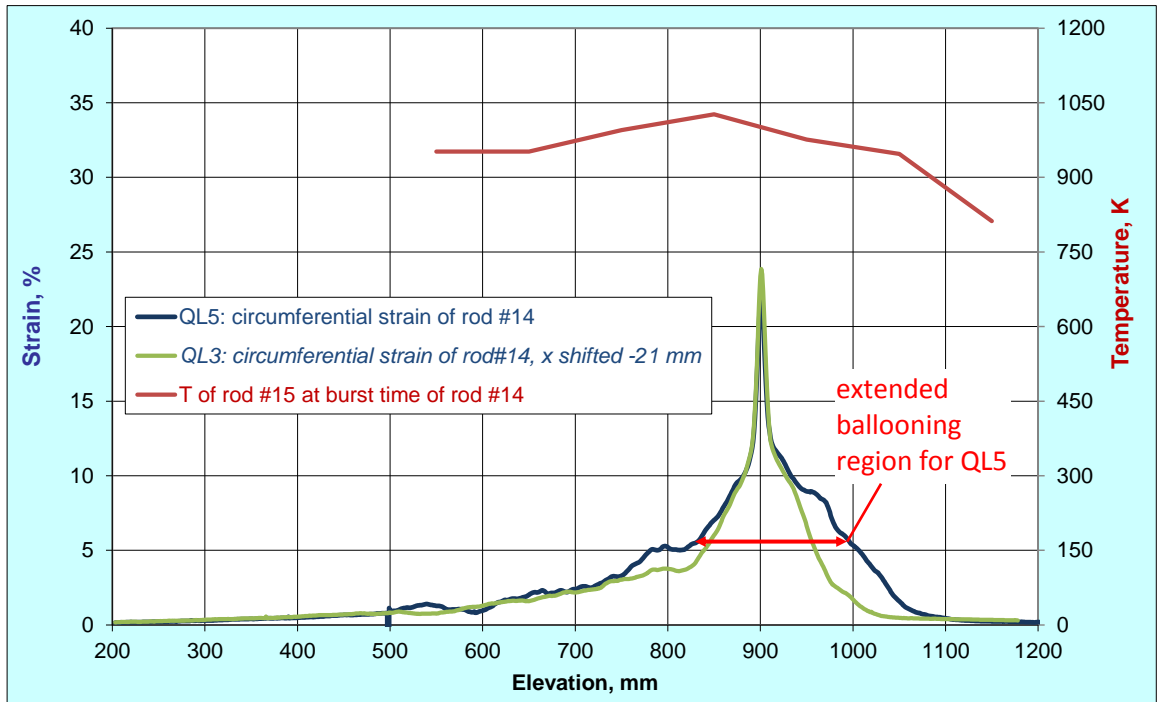
Figure 92   QUENCH-L5, Rod #14; longitudinal changing of circumferential strain (top); azimuthal diameter downwards from burst (bottom).
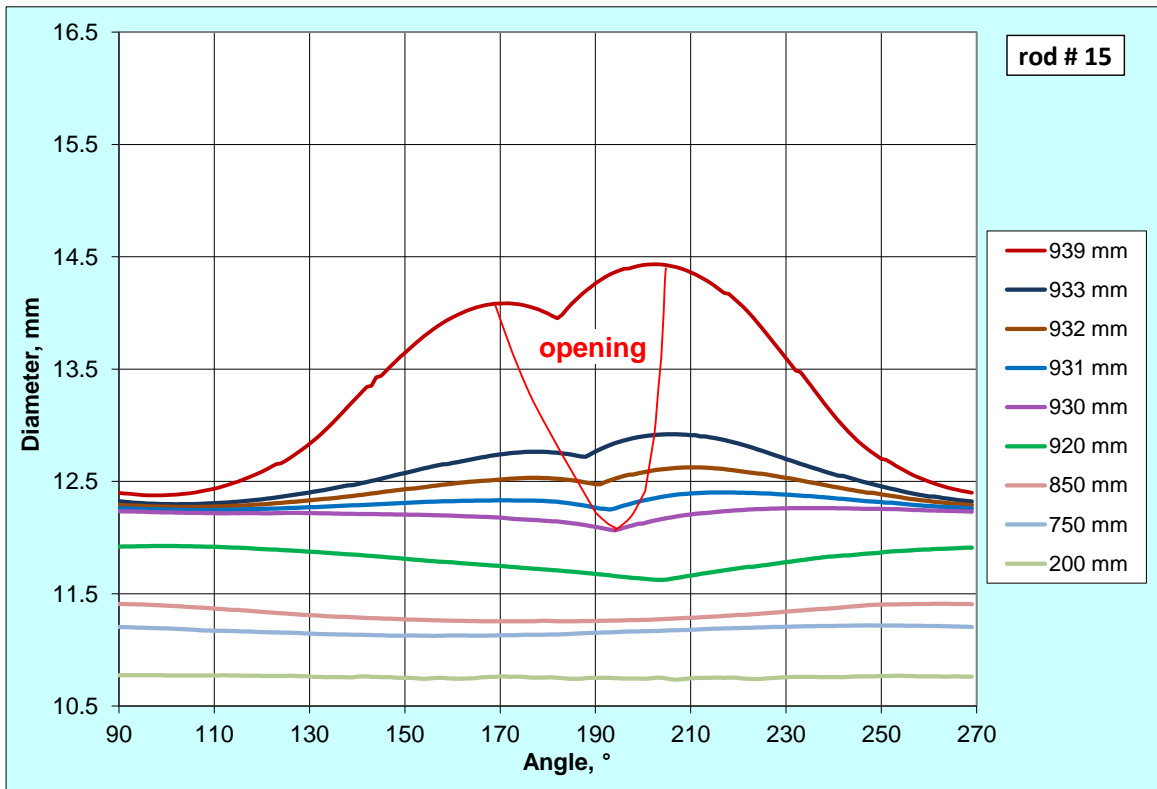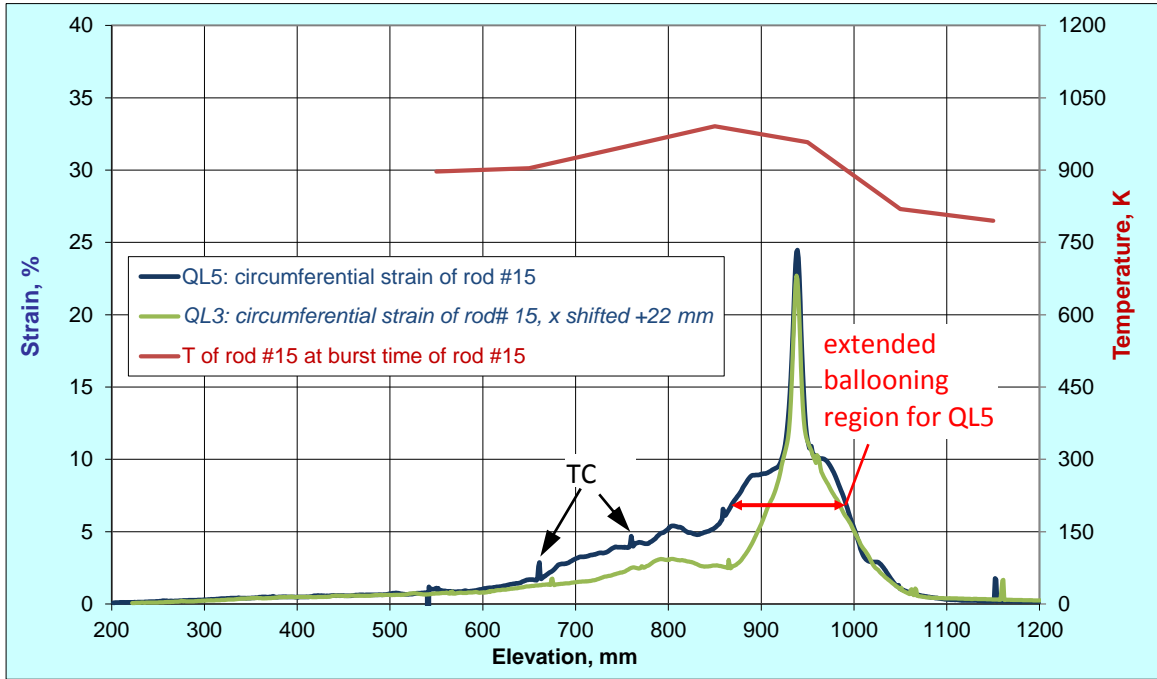
Figure 93 QUENCH-L5, Rod #15; longitudinal changing of circumferential strain (top); azimuthal diameter downwards from burst (bottom). Spikes: thermocouple.

Figure 94 QUENCH-L5, Rod #16; longitudinal changing of circumferential strain (top); azimuthal diameter downwards from burst (bottom).

Figure 95 QUENCH-L5, Rod #17; longitudinal changing of circumferential strain (top); azimuthal diameter downwards from burst (bottom).

Figure 96 QUENCH-L5, Rod #18; longitudinal changing of circumferential strain (top); azimuthal diameter downwards from burst (bottom).

Figure 97 QUENCH-L5, Rod #19; longitudinal changing of circumferential strain (top); azimuthal diameter downwards from burst (bottom).Spikes: thermocouples.

Figure 98 QUENCH-L5, Rod #20; longitudinal changing of circumferential strain (top): QL5 main balloon region is longer than QL3 one; azimuthal diameter downwards from burst (bottom).
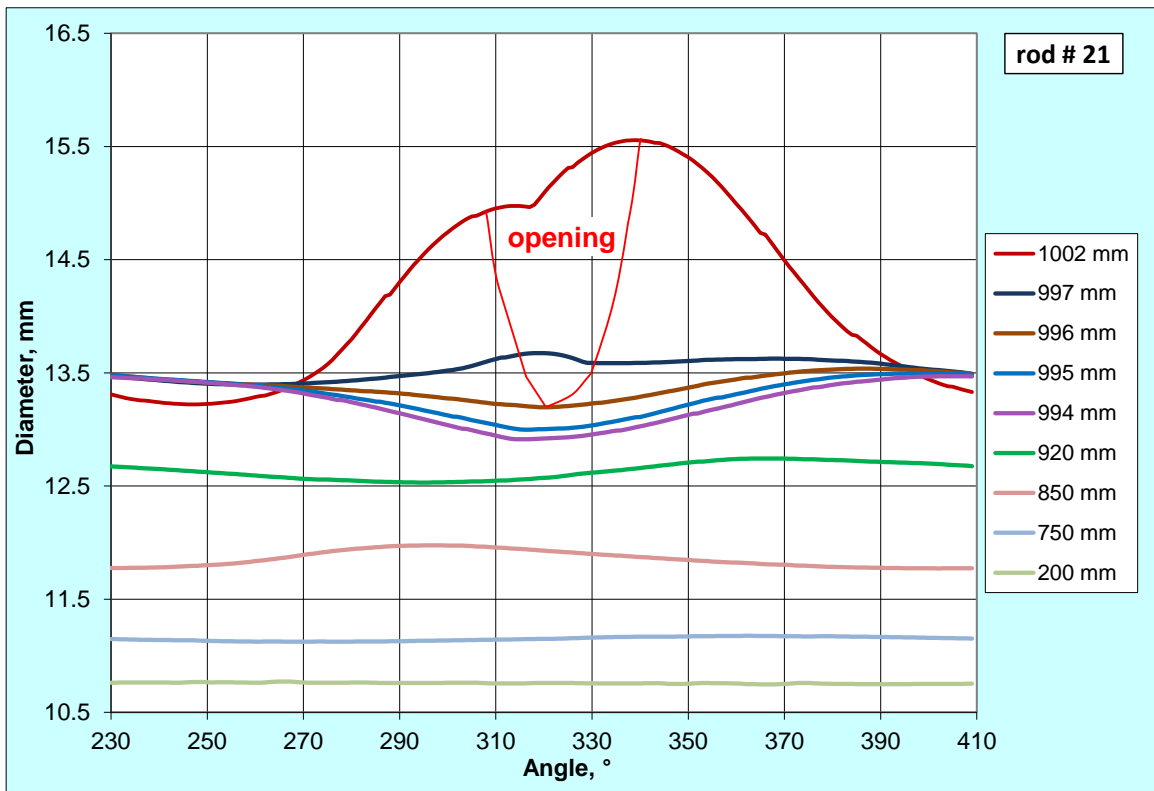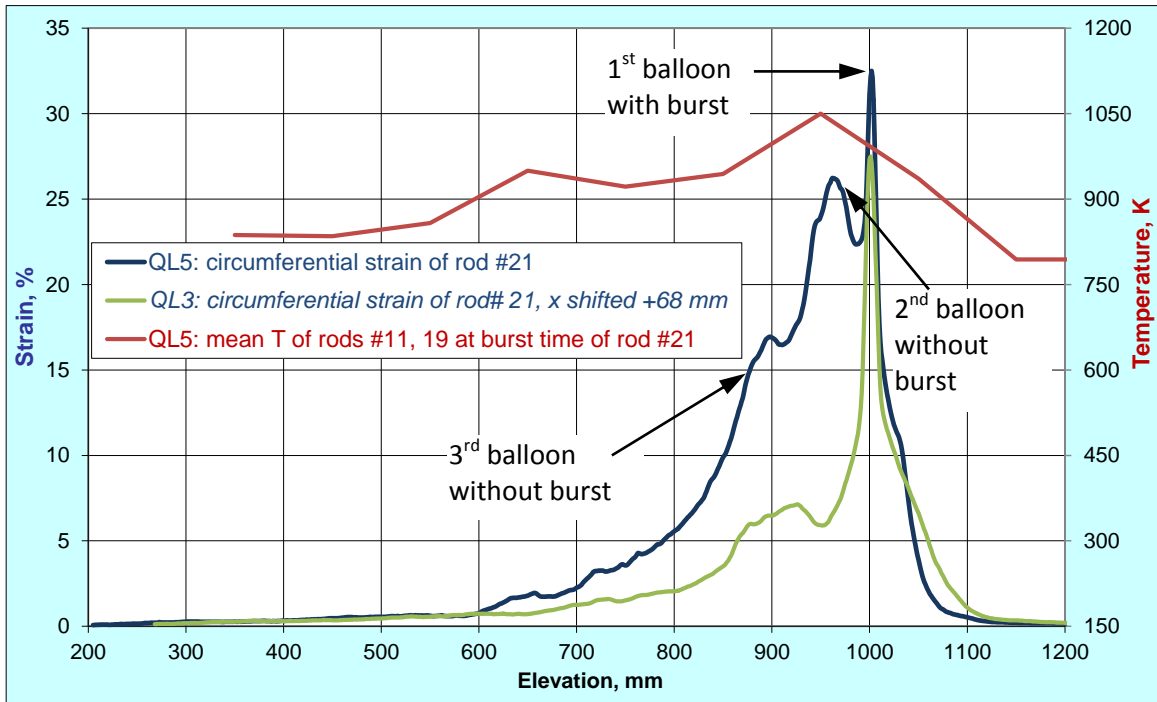
Figure 99 QUENCH-L5, Rod #21; longitudinal changing of circumferential strain (top): QL5 main balloon region is longer than QL3 one; azimuthal diameter downwards from burst (bottom).
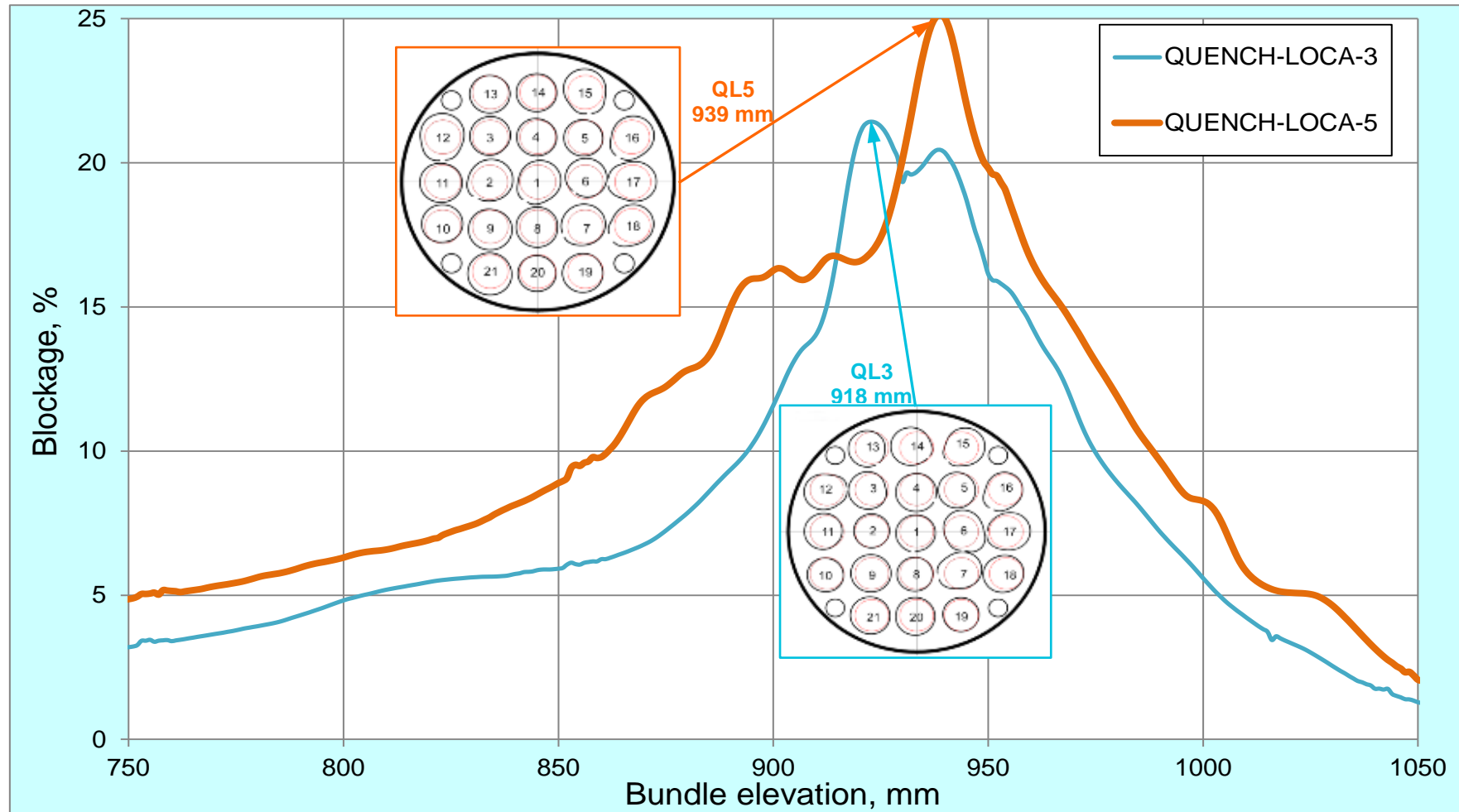
Figure 100 Axial distribution of coolant channel blockage for QUENCH-L3 and -L5 bundles.
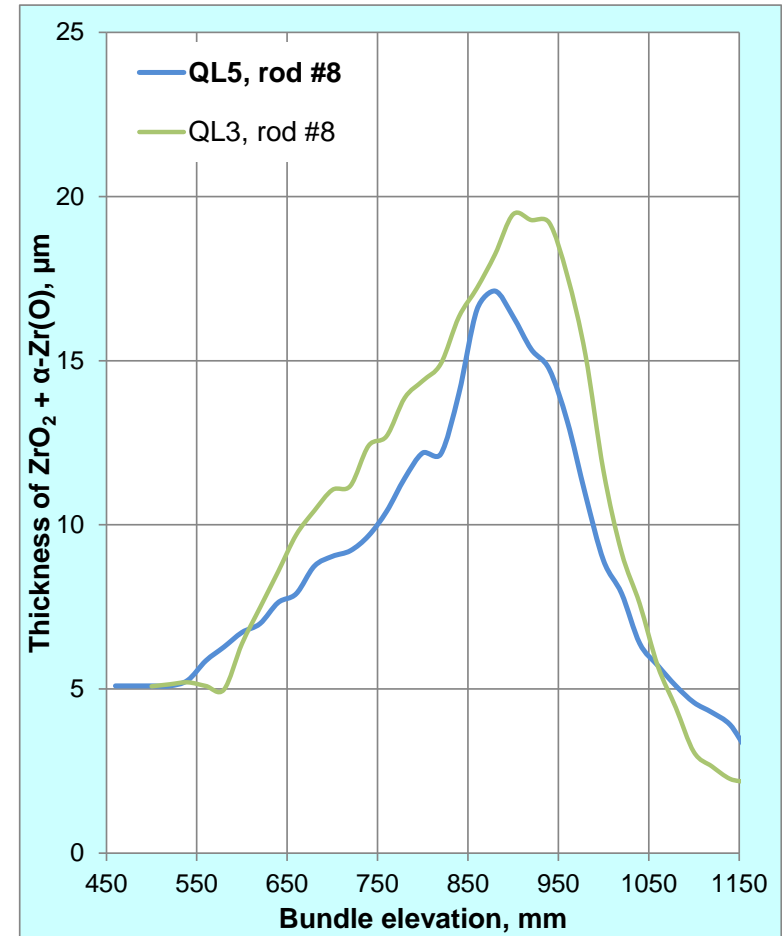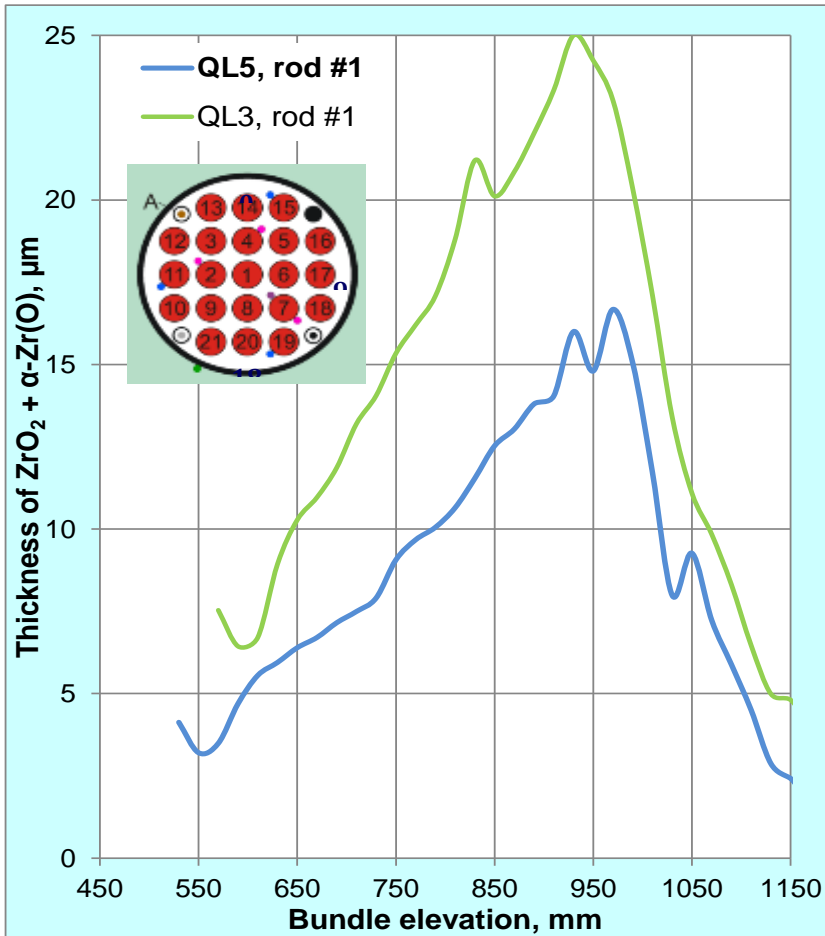
Figure 101   Comparison of cladding oxidation for bundles QUENCH-L5 and -L3 (results of eddy-current measurements averaged circumferentially for each elevation).
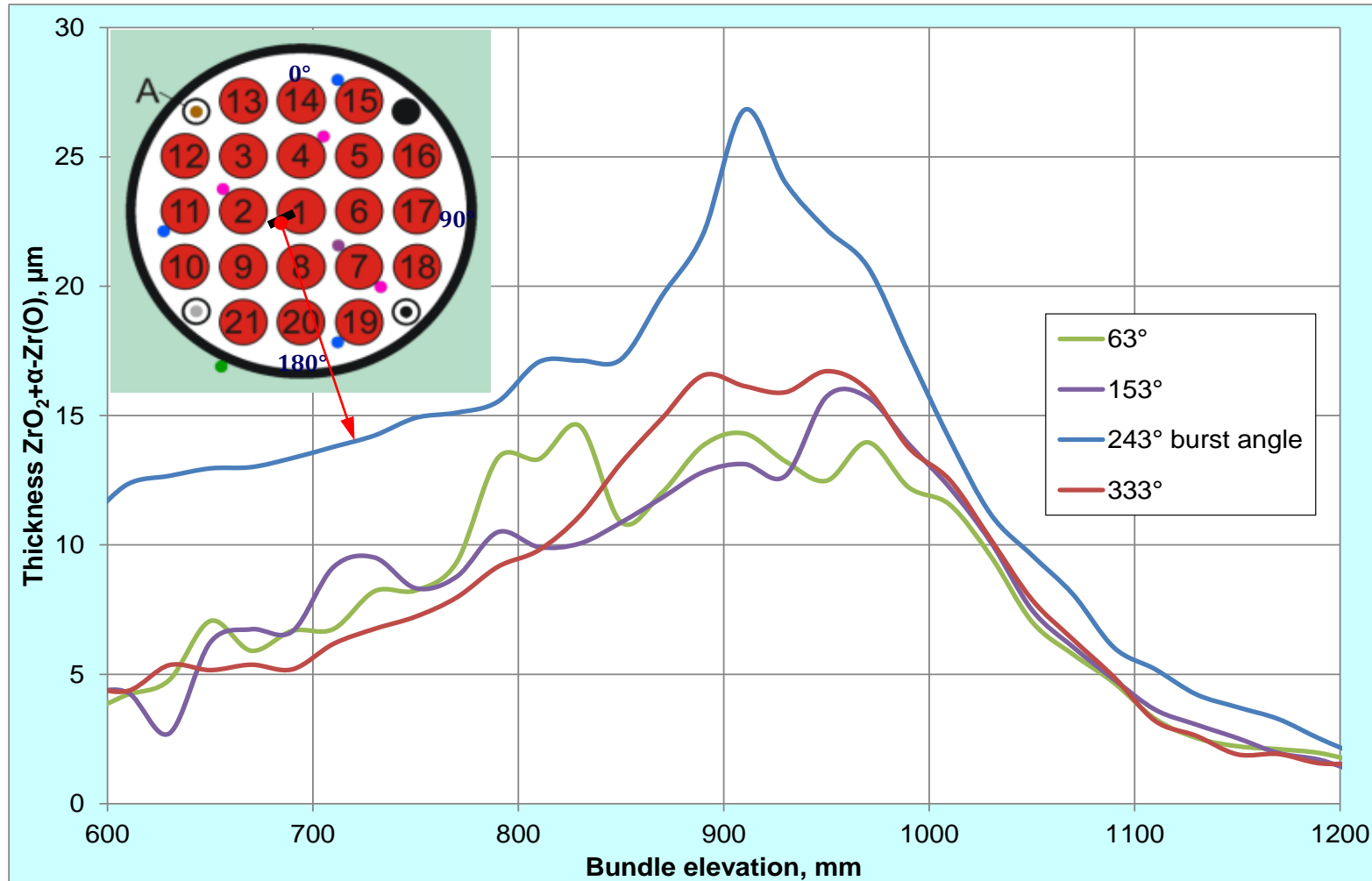
Figure 102 QUENCH-L5: results of eddy-current measurements of outer cladding layers for different circumferential positions of rod #1.
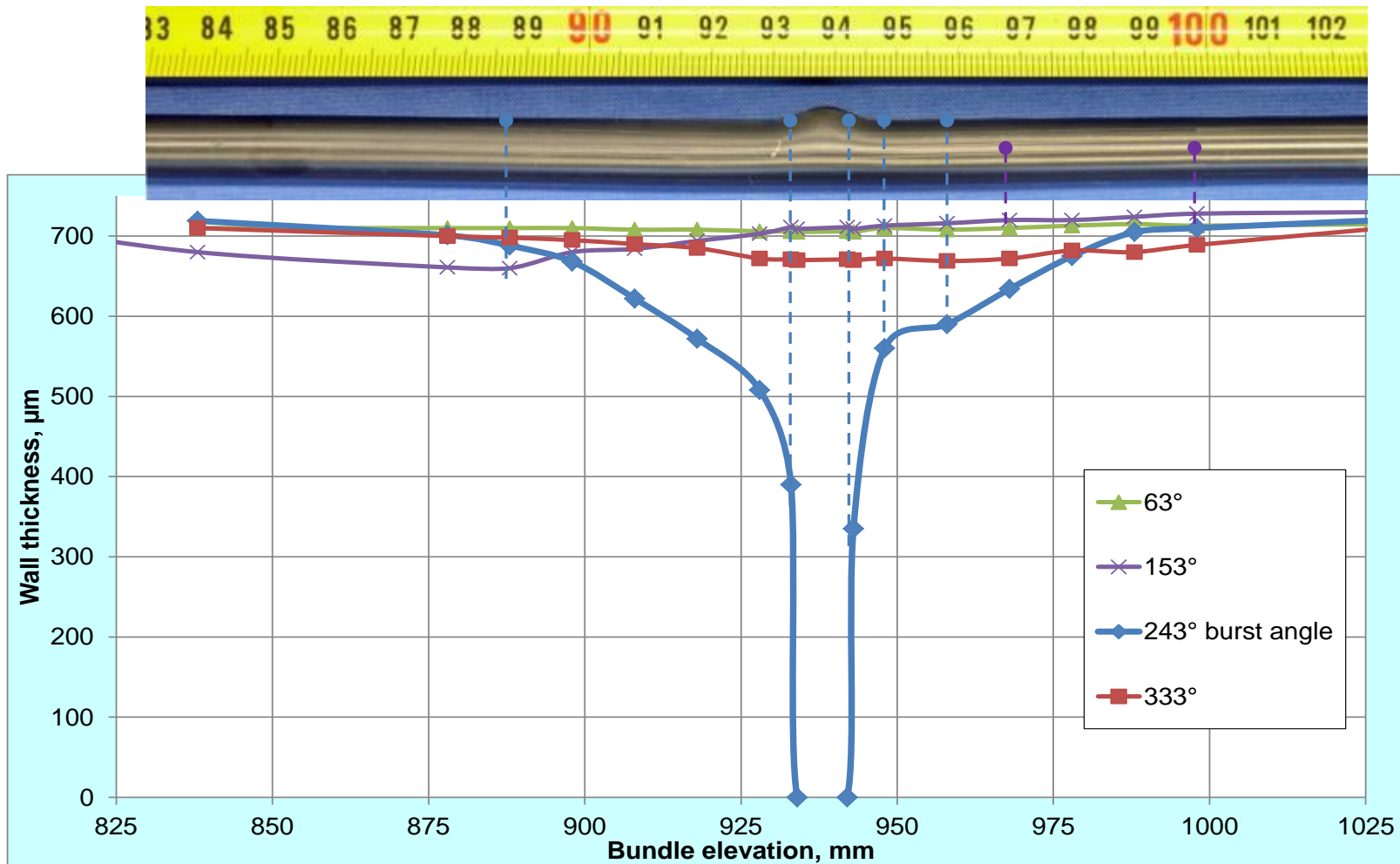
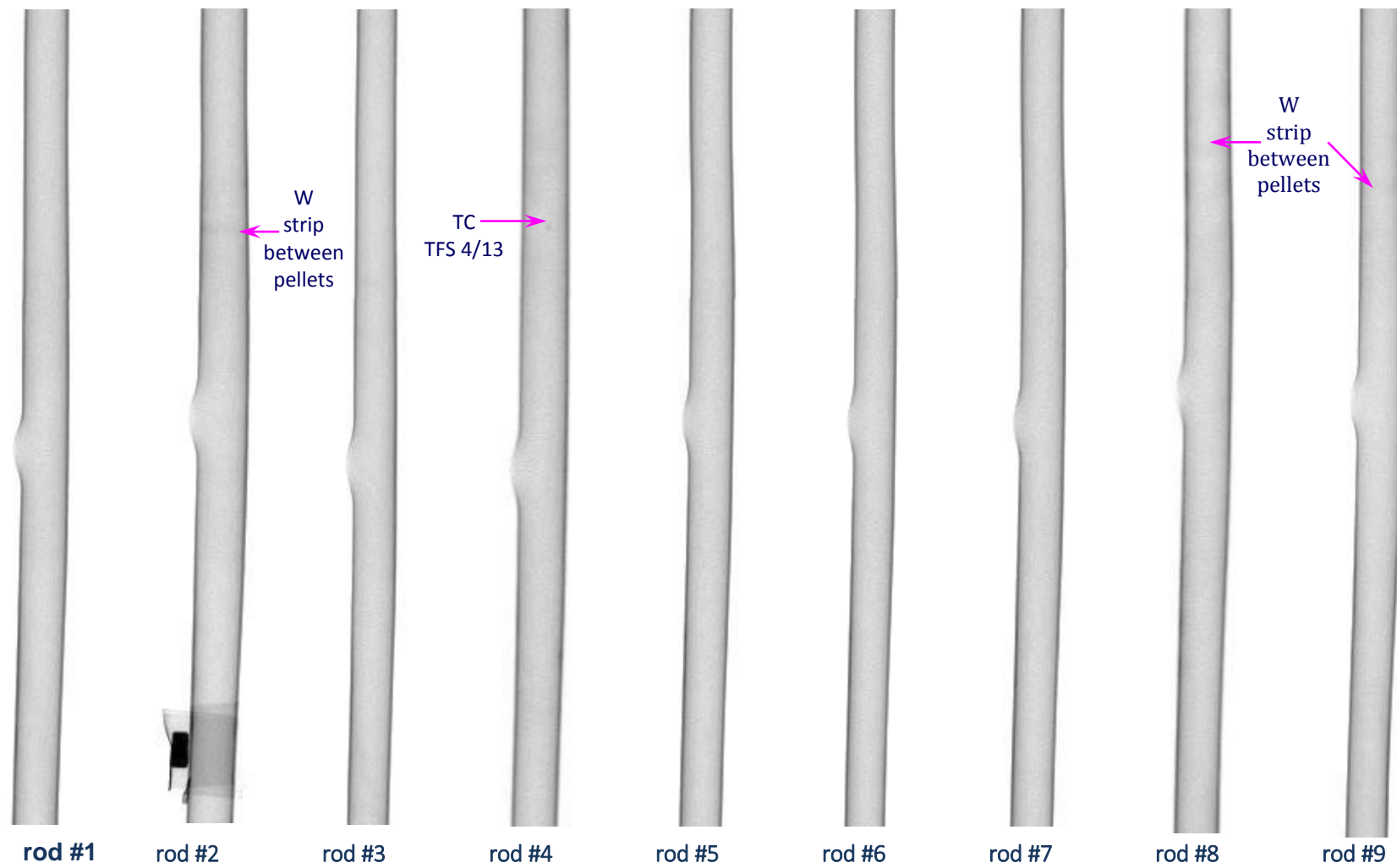**Figure 103**   QUENCH-L5; Ultrasounds measurements of cladding wall thickness for rod #1.

Figure 104 QUENCH-L5, results of neutron radiography of inner rods, no indication of secondary hydrogenation (absence of hydrogen bands)
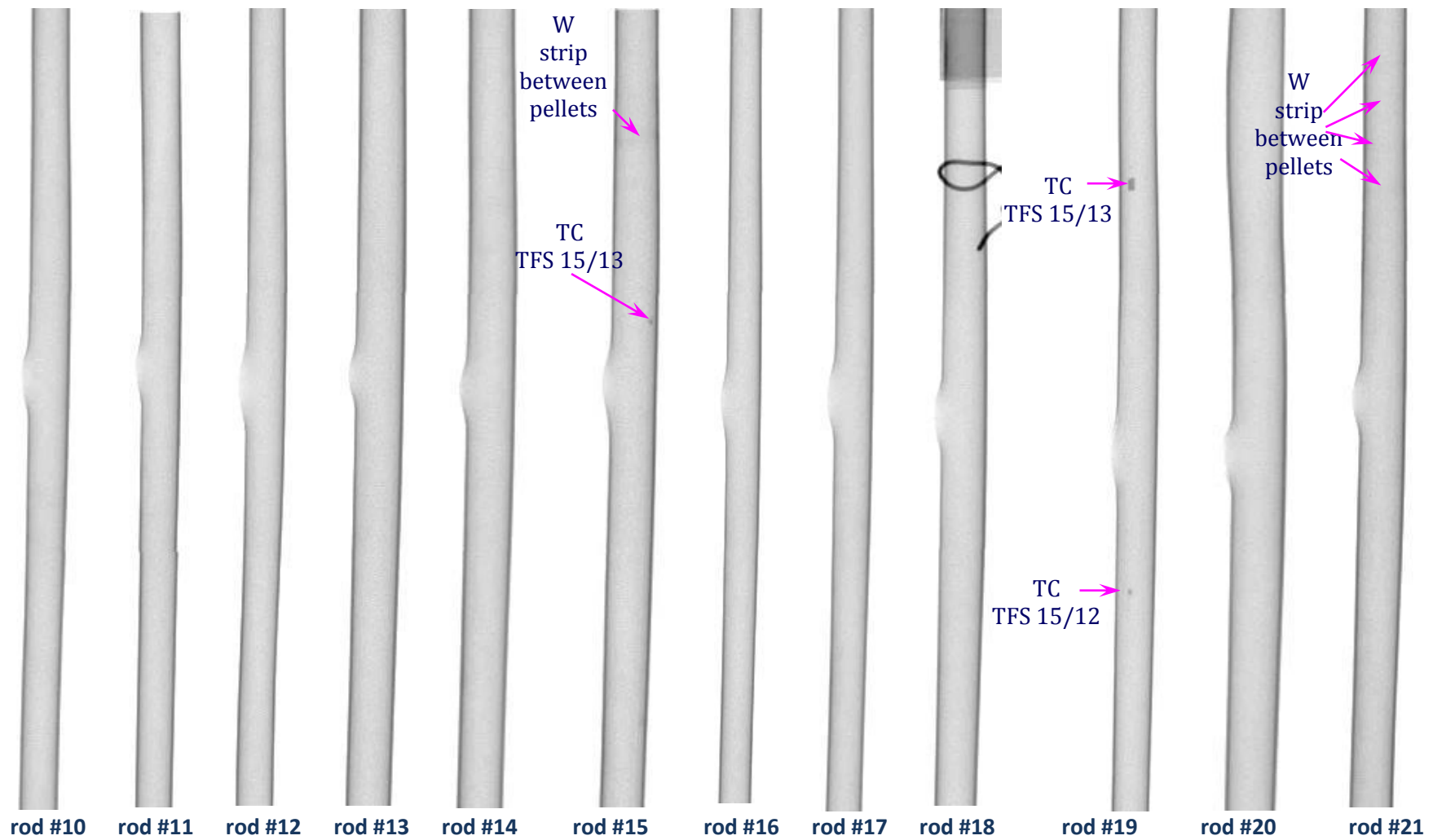
W strip between pellets

TC TFS 15/13

TC TFS 15/13

TC TFS 15/12

W strip between pellets

rod #10 rod #11 rod #12 rod #13 rod #14 rod #15 rod #16 rod #17 rod #18 rod #19 rod #20 rod #21

Figure 105 QUENCH-L5, results of neutron radiography of outer rods, no indication of secondary hydrogenation (absence of hydrogen bands).
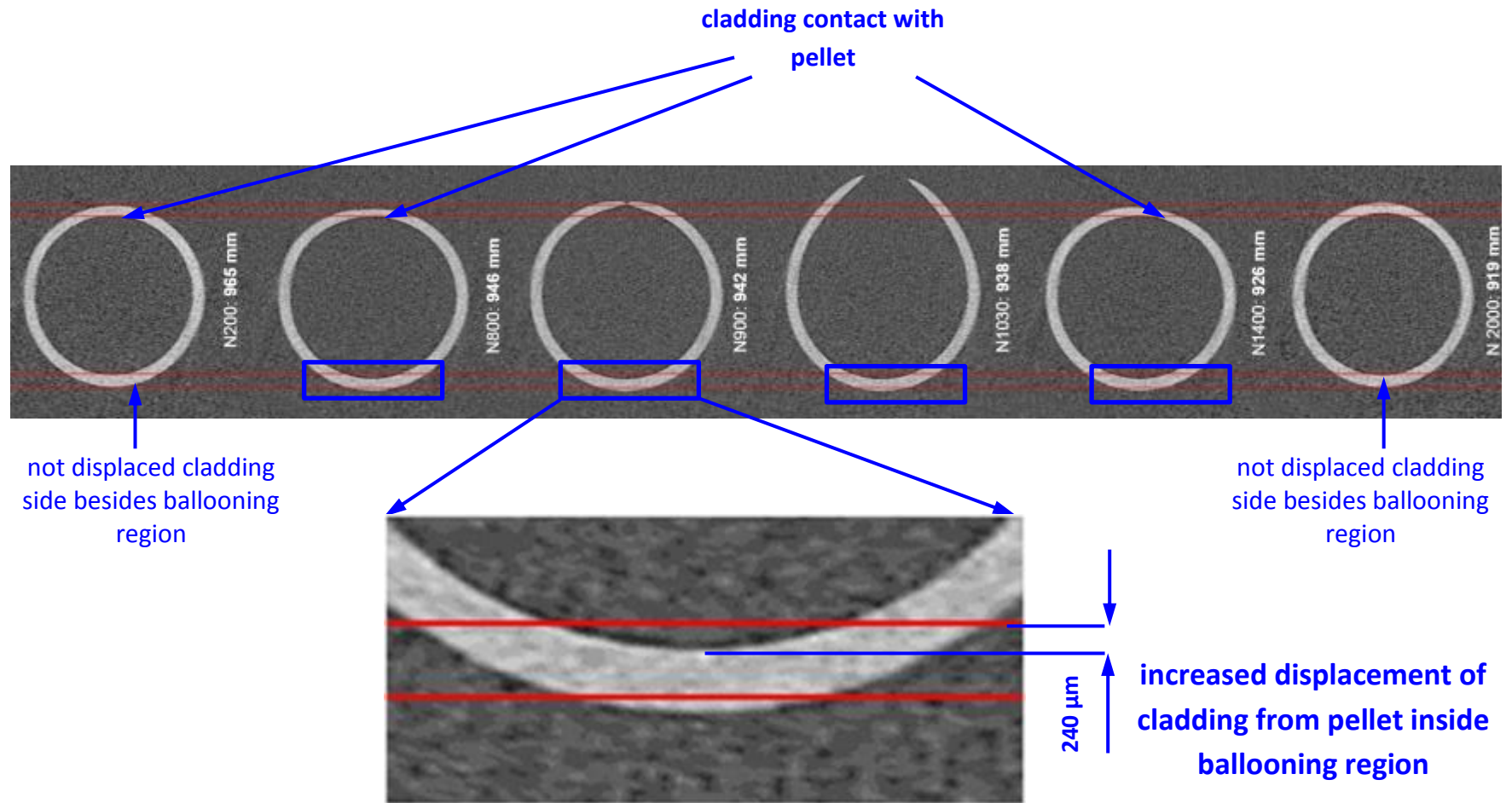
Figure 106 QUENCH-L5, Rod #1; comparison of spatial positions of cladding cross sections (neutron tomography images and corresponding bundle elevation); axial bending of cladding due to its displacement at "cold" side during ballooning.
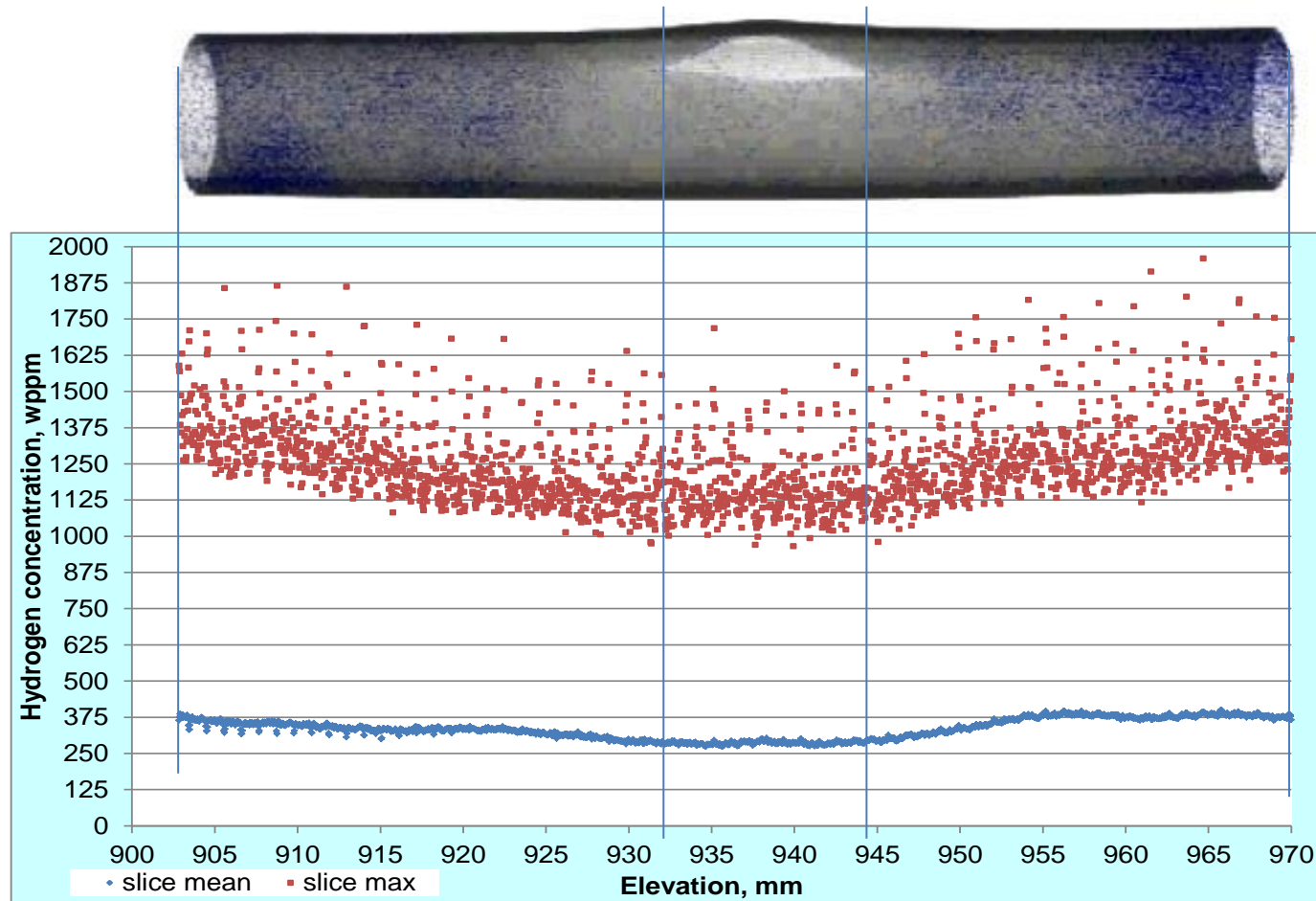
Figure 107 QUENCH-L5; correspondence between reconstruction of tomography image and plots of mean and maximal hydrogen concentrations in rod #1, plots adjusted to edges of burst opening.
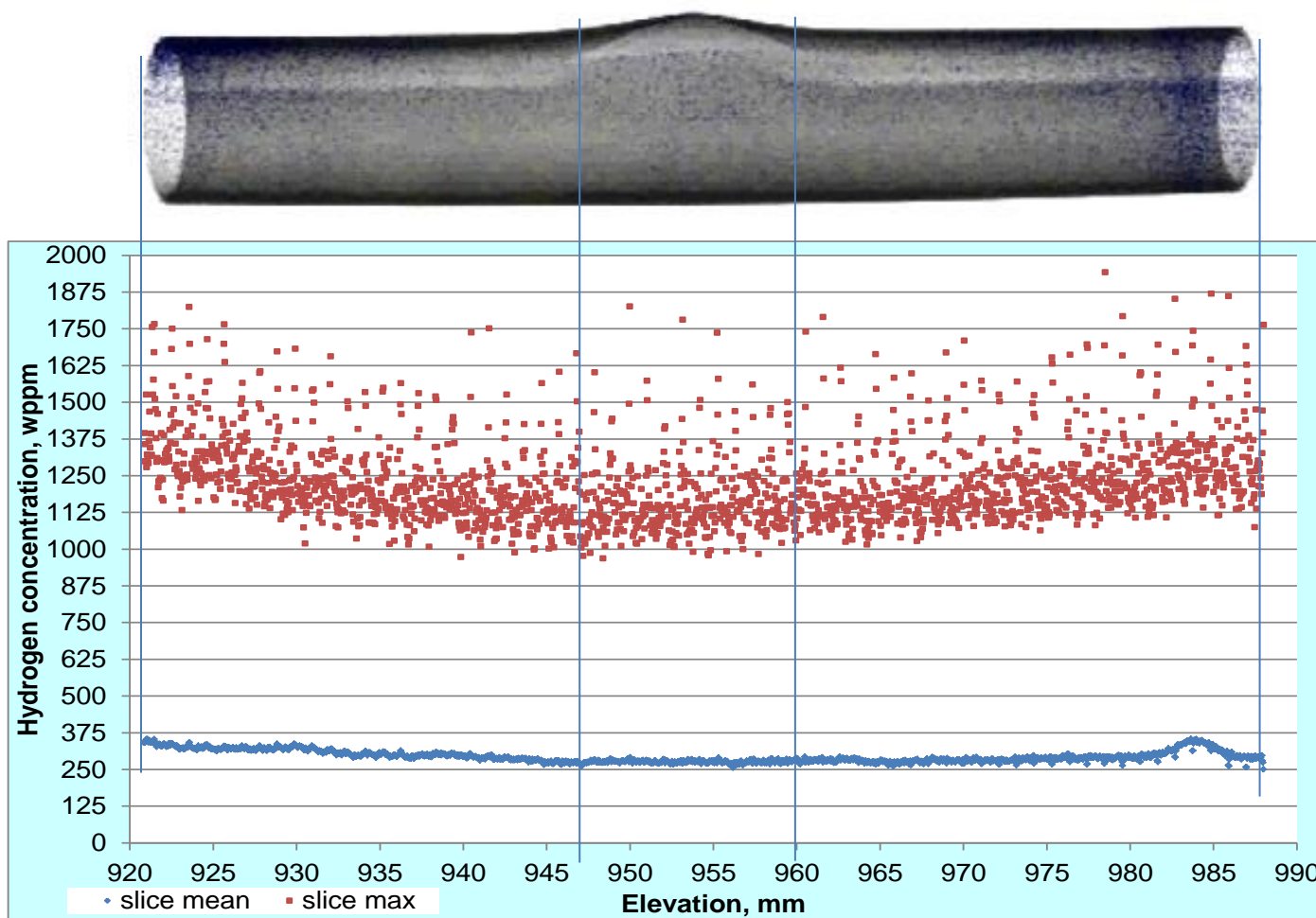
Figure 108 QUENCH-L5; correspondence between reconstruction of tomography image and plots of mean and maximal hydrogen concentrations in rod #3, plots adjusted to edges of burst opening.

Figure 109   QUENCH-L5; correspondence between reconstruction of tomography image and plots of mean and maximal hydrogen concentrations in rod #5, plots adjusted to edges of burst opening.
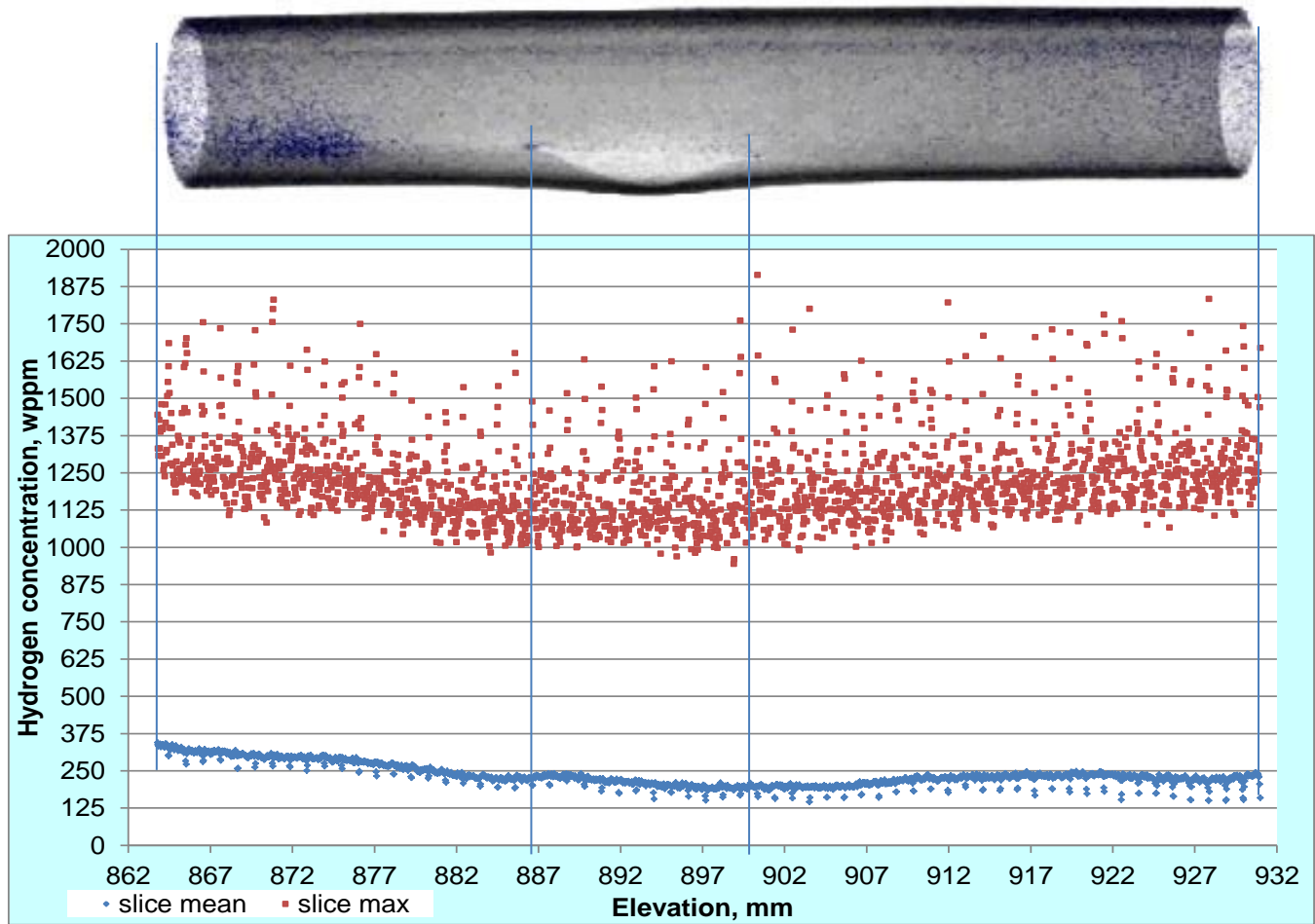
Figure 110   QUENCH-L5; correspondence between reconstruction of tomography image and plots of mean and maximal hydrogen concentrations in rod #7, plots adjusted to edges of burst opening.
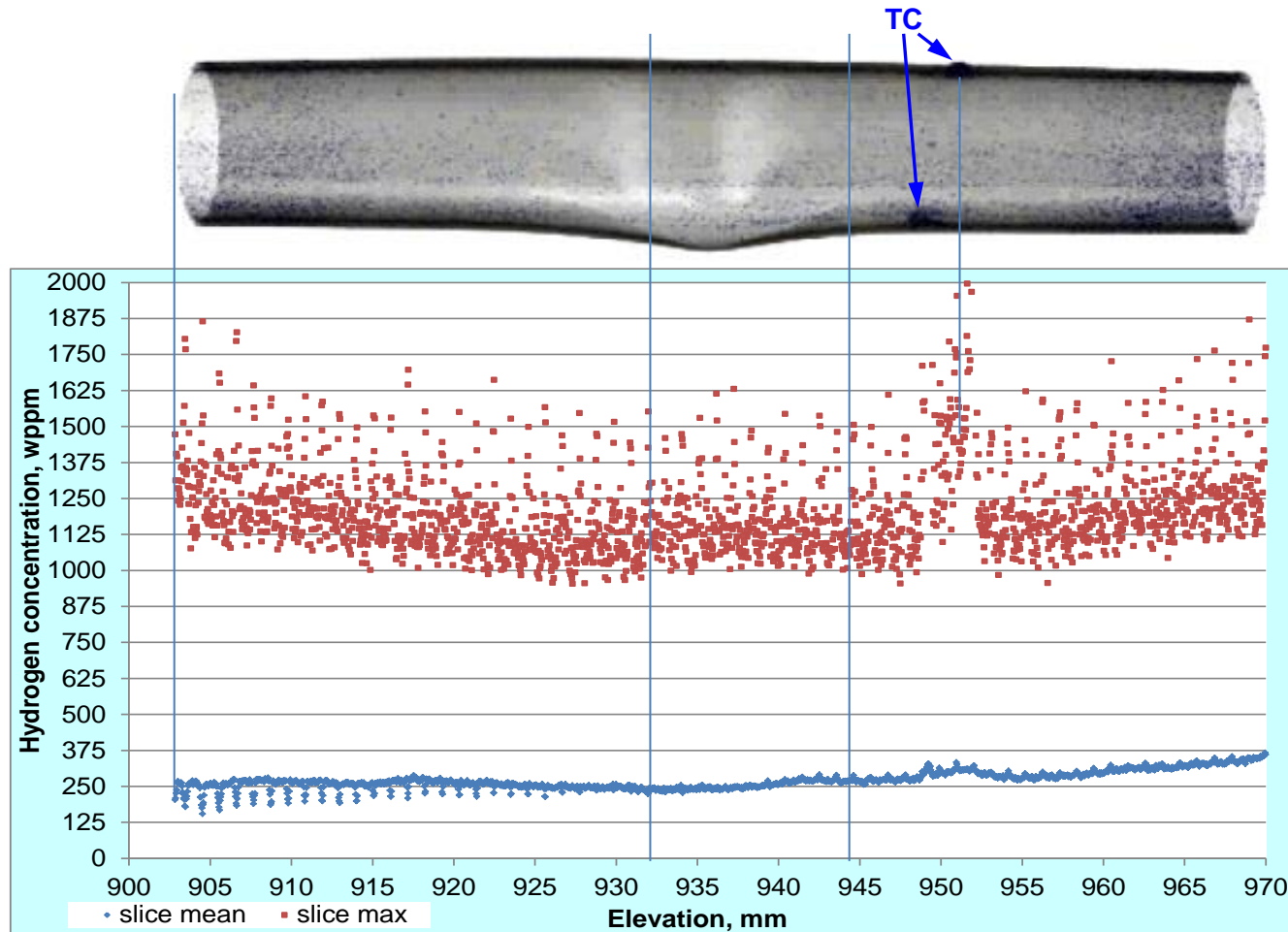
Figure 111 QUENCH-L5; correspondence between reconstruction of tomography image and plots of mean and maximal hydrogen concentrations in rod #9, plots adjusted to edges of burst opening.
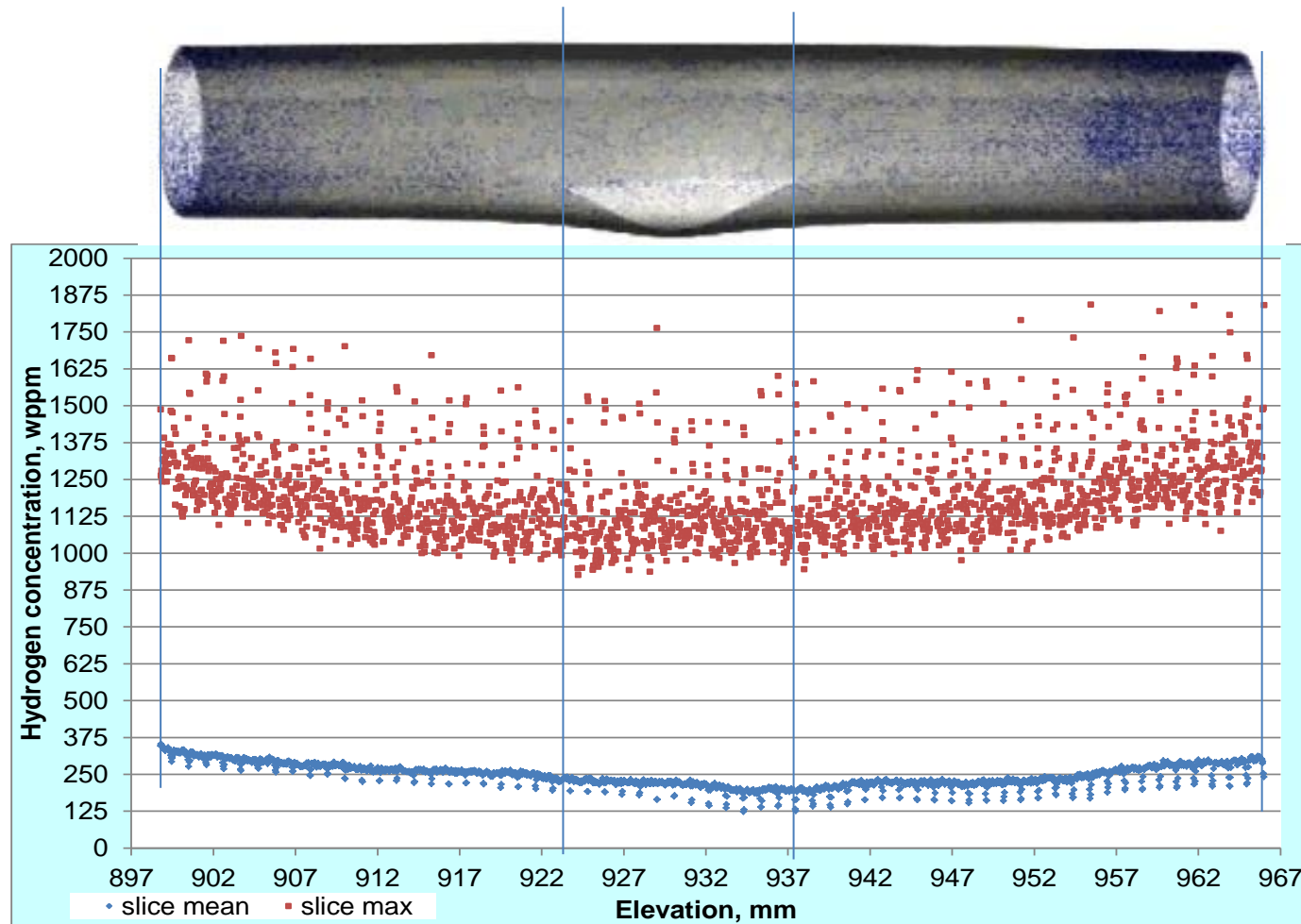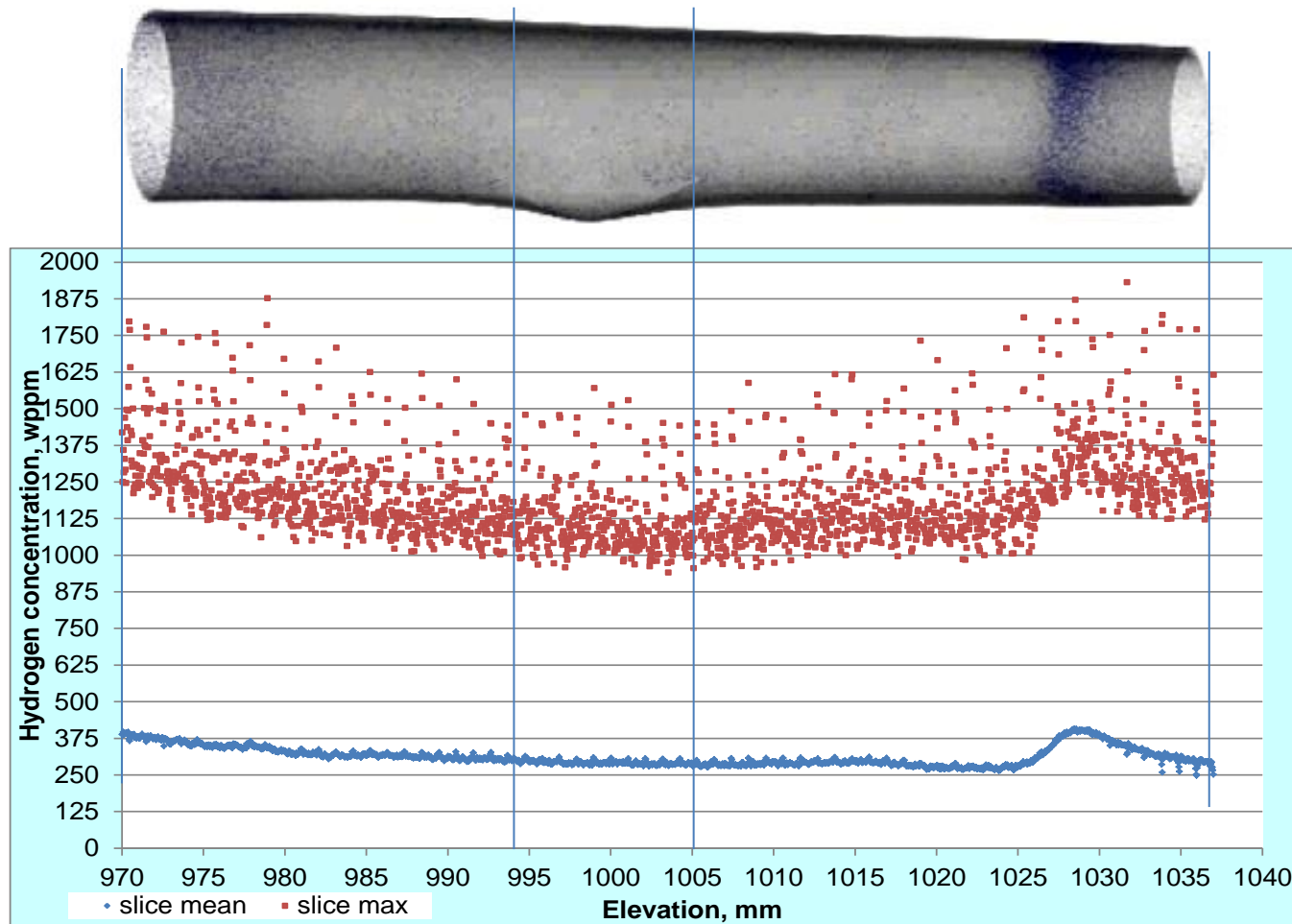
Figure 112 QUENCH-L5; correspondence between reconstruction of tomography image and plots of mean and maximal hydrogen concentrations in rod #21, plots adjusted to edges of burst opening.
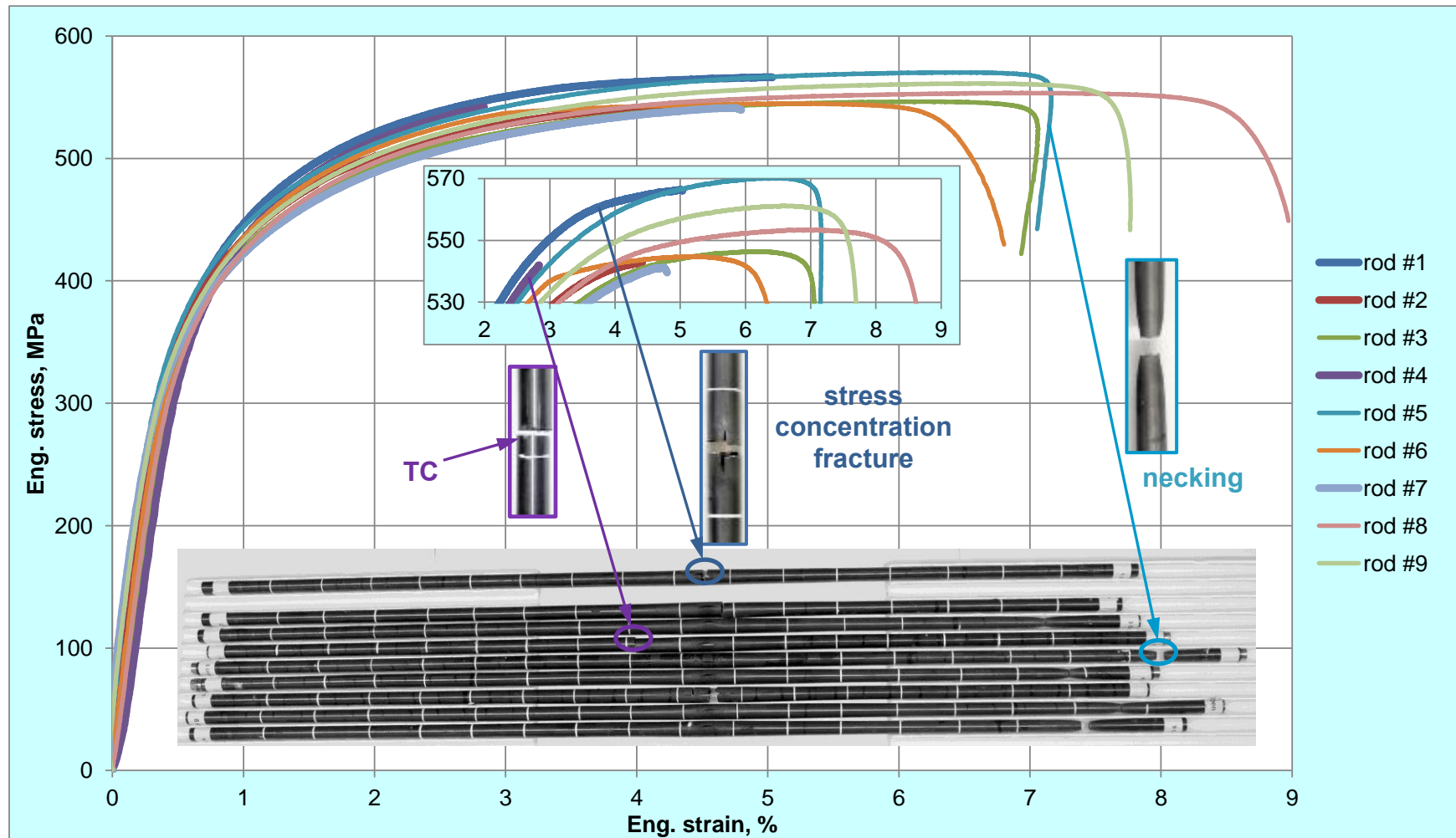
Figure 113   QUENCH-L5; results of tensile tests with claddings of the inner rod group.
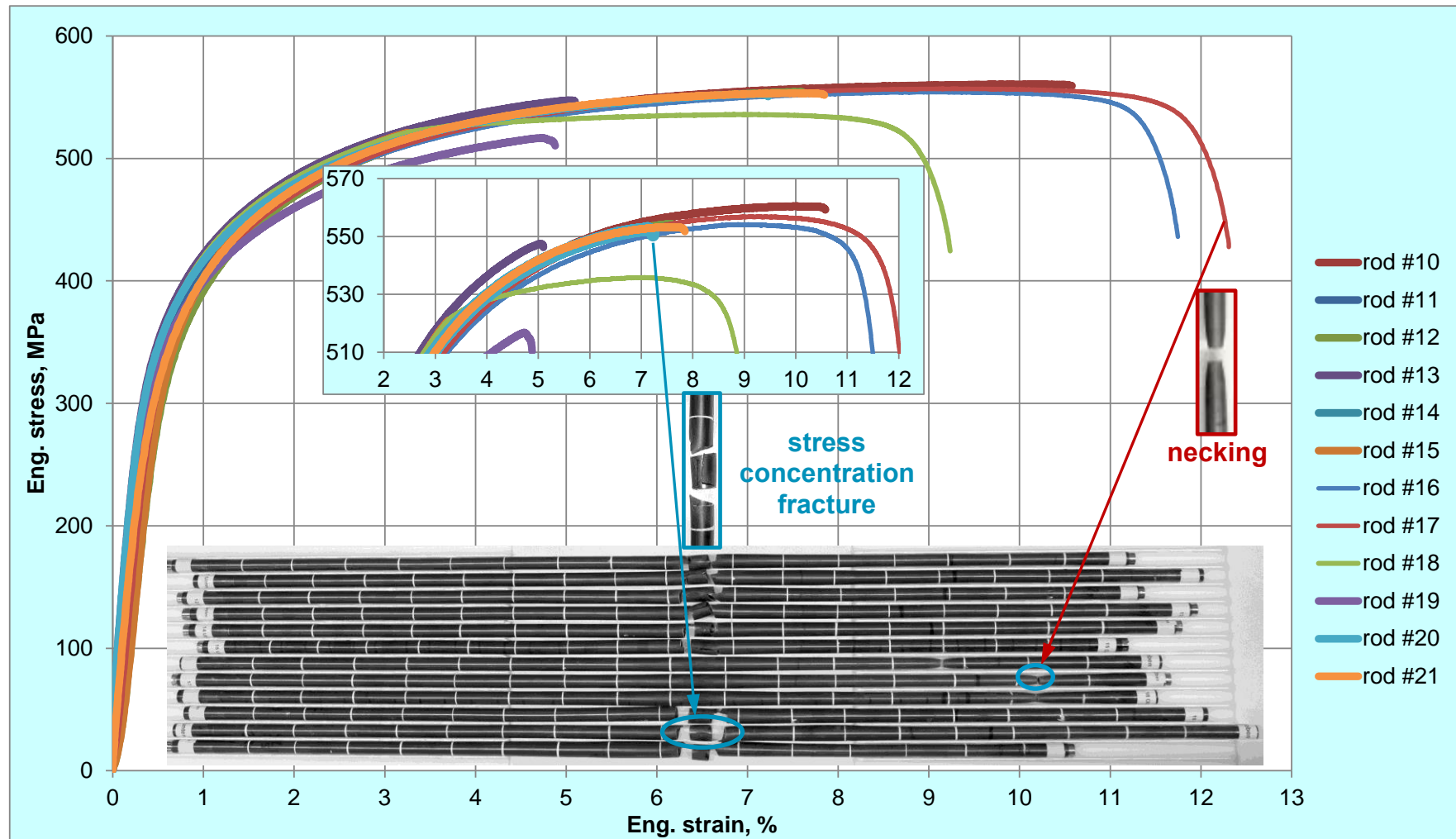
Figure 114 QUENCH-L5; results of tensile tests with claddings of the outer rod group

Appendix Hydrogenation of opt. ZIRLO samples at 600 °C to concentrations between 60 and 10860 wppm H and corresponding XRD analysis

A series of hydrogenation tests at 600 °C were performed to 1) determine the corresponding kinetics rate, and 2) check the sensitivity of XRD methods concerning the determination of zirconium hydrides.

The tube samples were charged to different hydrogen contents using an Ar + H_2 gas mixture with hydrogen partial pressure of 0.1 bar. Each hydrogenation test was performed in four stages: 1) the LORA vertical tube furnace (HTM Reetz GmbH, Berlin) was heated up to the work temperature; 2) the as-received sample was inserted while argon flowing through the furnace and the furnace was stabilized over 300 s; 3) hydrogen flow was initiated, which lasted between 18 and 240 s to reach the desired hydrogenation degree; 4) the sample was withdrawn after achieving the required hydrogenation amount and cooled to room temperature with an initial cooling rate of 5 K/s. The data for mass gain was used to calculate the hydrogen content of the hydrogenated samples. The mass gain of the slightly oxidised samples after the same temperature treatment but without hydrogen (annealed in pure argon and cooled in air) was taken as a correction parameter for a given temperature and this weight gain subtracted from the total mass of the hydrogenated sample. If there were any mass gain due to impurities in the furnace gas mixture, they would automatically be included in the subtracted mass and thus would not impact the hydrogen content estimation. The mass gain of the hydrogenated specimen was not less than ten times higher than the specimen annealed in Ar and cooled in air. The greater was the amount of absorbed hydrogen the less important was the correction value.

The test matrix is presented in Table A1. The corresponding parabolic increase of hydrogen content is showed in Fig. A1. The trend fitting line estimated by regression analysis (least square method) has high coefficient of determination R^2, but started delayed at t=20 s. The reason for this delay is a latent time necessary for dissolution of a thin surface oxide layer.

Some samples were investigated by XRD analysis to reveal hydride phases. Fig. A2 shows the corresponding results. One can see that XRD measurements cannot determine hydrides at very low hydrogen content. The δ hydrides can be detected first at hydrogen contents more than 700 wppm, and γ hydrides will be detectable at hydrogen concentration above 2000 wppm.

Table A1   Hydrogenation of opt. ZIRLO samples at 600 °C: test matrix

| sample	hydrogenation time, s	square root of time, s1/2	content of absorbed hydrogen, wppm
H4 ZIRLO	23	4.8	59
H2 ZIRLO	18	4.28	170
H3 ZIRLO	26	5.1	400
H1 ZIRLO	37	6.1	780
H7 ZIRLO	60	7.7	2867
H5 ZIRLO	120	10.95	5322
H6 ZIRLO	240	15.5	10864
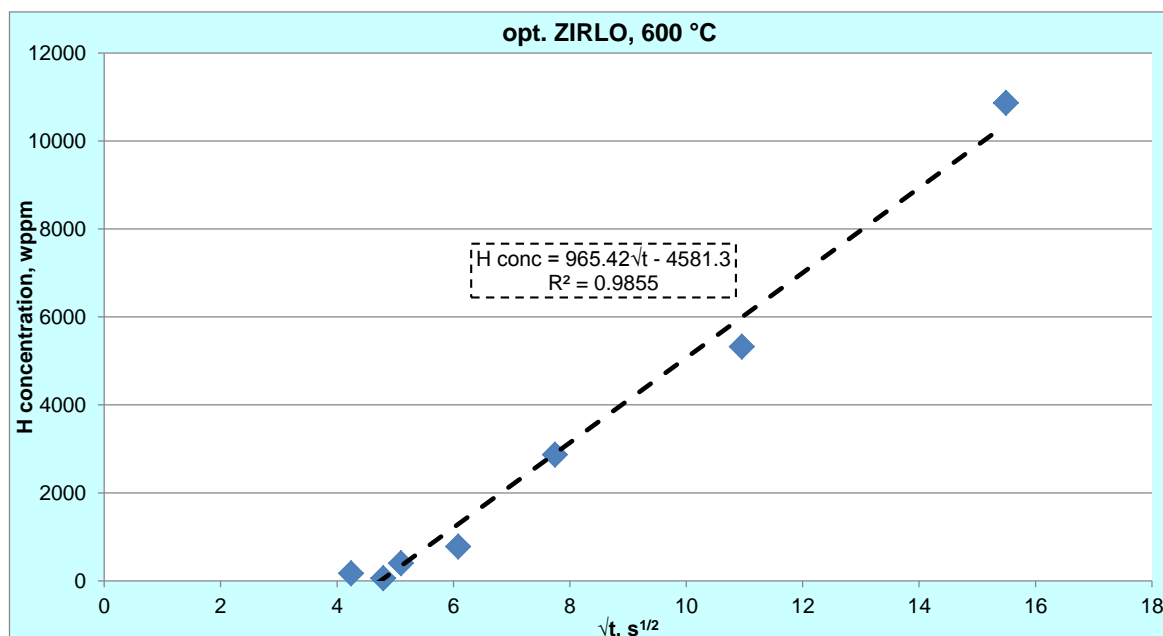
Parabolic increase of hydrogen content; first 20 s are needed for oxide layer dissolution (layer thickness about 100 nm)
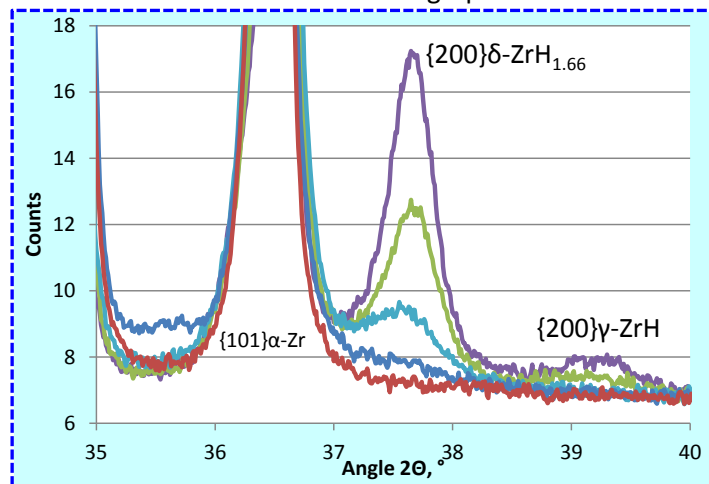
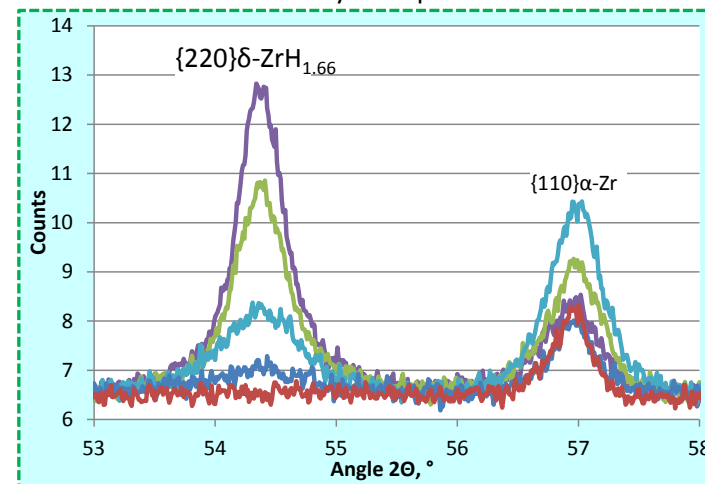Figure A1   Dependence of hydrogen absorption from hydrogenation duration at 600 °C
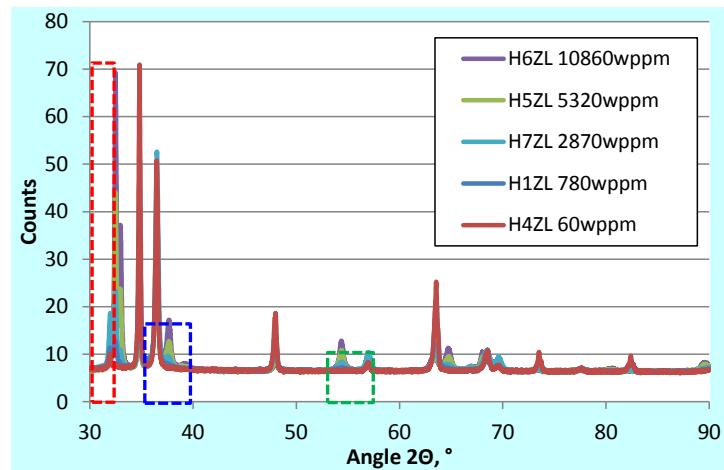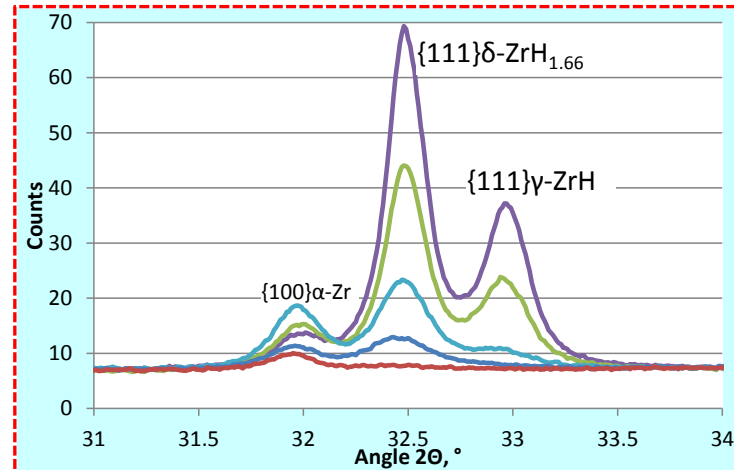
Figure A2   XRD analysis of opt. ZIRLO samples hydrogenated to 60…10860 wppm.

The QUENCH-L5 experiment was performed in the framework of the QUENCH-LOCA test series. The overall objective of this bundle test series is the investigation of ballooning, burst, degree of oxidation and secondary hydrogen uptake of the cladding under representative design-basis accident conditions and their influence on the mechanical properties. For the QUENCH L5 test, optimised ZIRLO™ claddings pre-loaded with approximately 300 wppm hydrogen (high burn-up simulation) and with an outside diameter of 10.75 mm have been used. Like in all experiments of the QUENCH LOCA series, all 21 electrical heated fuel rod simulators were separately pressurized with krypton to 55 bar. According to a temperature/time scenario typical for a LBLOCA in a German PWR, the test was performed with similar test parameters as the QUENCH-L3 test with as-received opt. ZIRLO claddings: similar time schedule, maximal heat-up rate 8 K/s, cooling phase lasted 120 s and terminated with 3.3 g/s/rod water flooding. The maximum peak cladding temperature reached on the end of the heat-up phase at elevation 950 mm was 1250 K: lower in comparison to 1350 K for QUENCH-L3 due to lower temperature on the transient start. The circumferential temperature difference at individual claddings was up to 90 K at burst onset. The maximum thickness of oxide and alpha layers at outer cladding surface was 16 μm. During quenching, following the high-temperature test stages, no fragmentation of claddings was observed indicating that the residual strengths and ductility was sufficient.

Some rods have up to three ballooning regions. Due to the low ballooning degree the maximum blockage ratio of the cooling channel was 25% at 940 mm. Cladding wall thinning from 725 μm to 450 μm due to ballooning was observed at the burst side along 50 mm below and above burst opening. The cladding burst occurred at temperatures between 1027 and 1151 K (QUENCH-L3: 1064 and 1188 K). The average burst temperature of 1081 K for QUENCH-L5 is lower than for QUENCH-L3 (1117 K) due to lower α-Zr→β-Zr phase transition temperature. The average burst opening parameters were: width 3.8, length 14.3 mm. No secondary hydrogenation was indicated for the QUENCH-L5 claddings due to very short high temperature period. Tensile tests at room temperature showed cladding fracture mostly due to stress concentration in the region of burst opening.